
Theses and Dissertations

Spring 2012

A study of optimization-based predictive dynamics method for digital human modeling

Mahdiar Hariri
University of Iowa

Follow this and additional works at: <https://ir.uiowa.edu/etd>



Part of the [Mechanical Engineering Commons](#)

Copyright 2012 Mahdiar Hariri

This dissertation is available at Iowa Research Online: <https://ir.uiowa.edu/etd/2886>

Recommended Citation

Hariri, Mahdiar. "A study of optimization-based predictive dynamics method for digital human modeling." PhD (Doctor of Philosophy) thesis, University of Iowa, 2012.
<https://doi.org/10.17077/etd.si5cwye>

Follow this and additional works at: <https://ir.uiowa.edu/etd>



Part of the [Mechanical Engineering Commons](#)

A STUDY OF OPTIMIZATION-BASED PREDICTIVE DYNAMICS METHOD FOR
DIGITAL HUMAN MODELING

by

Mahdiar Hariri

An Abstract

Of a thesis submitted in partial fulfillment
of the requirements for the Doctor of
Philosophy degree in Mechanical Engineering
in the Graduate College of
The University of Iowa

May 2012

Thesis Supervisors: Professor Karim Abdel-Malek
Professor Jasbir S. Arora

ABSTRACT

This study develops theorems which generalize or improve the existing predictive dynamics method and implements them to simulate several motion tasks of a human model. Specifically, the problem of determination of contact forces (non-adhesive) between the environment and the digital human model is addressed. Determination of accurate contact forces is used in the calculation of joint torques and is important to account for human strength limitations in simulation of various tasks. It is shown that calculation of the contact forces based on the distance of the contact areas from the Zero Moment Point (ZMP) leads to unrealistic values for some of the forces. This is the approach that has been used in the past. In this work, necessary and sufficient constraints for modeling the non-adhesiveness of a contact area are presented through the definition of NCM (Normal Contact Moment) concepts. NCM point, constraints and stability margins are the new theoretical concepts introduced. When there is only one contact area between the body and the environment, the ZMP and the NCM point coincide. In this case, the contact forces and moments are deterministic. When there are more than one contact areas, the contact forces and moments are indeterminate. In this case, an optimization problem is defined based on the NCM constraints where contact forces and moments are treated as the unknown design variables. Here, kinematics of the motion is assumed to be known. It is shown that this approach leads to more realistic values for the contact forces and moments for a human motion task as opposed to the ZMP based approach. The proposed approach appears to be quite promising and needs to be fully integrated into the predictive dynamics approach of human motion simulation.

Some other insights are obtained for the predictive dynamics approach of human motion simulation. For example, it is mathematically proved and also validated that there is a need for an individual constraint to ensure that the normal component of the resultant

global forces remains compressive for non-adhesive contacts between the body and the environment. Also, the ZMP constraints and stability margins are applicable for the problems where all the contacts between the environment and the body are in one plane; however, the NCM constraints and stability margins are applicable for all types of arbitrary contacts between the body and the environment.

The ZMP and NCM methods are used to model the motion of a human (soldier) performing several military tasks: Aiming, Kneeling, Going Prone and Aiming in Prone Position. New collision avoidance theorems are also presented and used in these simulations.

Abstract Approved: _____
Thesis Supervisor

Title and Department

Date

Thesis Supervisor

Title and Department

Date

A STUDY OF OPTIMIZATION-BASED PREDICTIVE DYNAMICS METHOD FOR
DIGITAL HUMAN MODELING

by

Mahdiar Hariri

A thesis submitted in partial fulfillment
of the requirements for the Doctor of
Philosophy degree in Mechanical Engineering
in the Graduate College of
The University of Iowa

May 2012

Thesis Supervisors: Professor Karim Abdel-Malek
Professor Jasbir S. Arora

Copyright by
MAHDIAR HARIRI
2012
All Rights Reserved

Graduate College
The University of Iowa
Iowa City, Iowa

CERTIFICATE OF APPROVAL

PH.D. THESIS

This is to certify that the Ph.D. thesis of

Mahdiar Hariri

has been approved by the Examining Committee for the thesis requirement for the Doctor of Philosophy degree in Mechanical Engineering at the May 2012 graduation.

Thesis Committee: _____
Karim Abdel-Malek, Thesis Supervisor

Jasbir S. Arora, Thesis Supervisor

Shaoping Xiao

Nicole M. Grosland

Jia Lu

To family and friends

Time discovers truth.

- Seneca (Roman philosopher, 4 BC to 65 AD)

ACKNOWLEDGMENTS

First of all, I would like to thank my advisor, Professor Karim Abdel-Malek for helping me come to the VSR Lab and for his support during these years. It has been an honor for me to be his student. Before coming here, I admired his comprehensive approaches in treating scientific problems in his many outstanding publications. Now after several years, I admire the same approach that he is encouraging in the lab as the director of the lab. I think being in VSR has improved me academically, personally and professionally.

I would like to thank my co-advisor Professor Jasbir Arora for his guidance during my thesis research. It has been an honor for me to work under his supervision. As a well known author, I had read his books on optimization before knowing about Iowa. I have learned many lessons from him in the presentation of scientific works as well as the process of logical reasoning. I think his insistence on clear presentation of scientific works has helped me understand my own research better.

I also thank Professor Shaoping Xiao, Professor Jia Lu and Professor Nicole Grosland for serving in my thesis committee.

I would also like to thank my co-workers in the predictive dynamics group including Yujiang Xiang, Rajan Bhatt, Hyun-Joon Chung and Jun Hyeak Choi and all the students and staff in VSR Lab including Rich Lineback, Tim Marler, Steve Beck, Mohammad Bataineh, John Meusch, Kim Farrell and Anith Mathai for the various ways that they have helped me during the past years.

Last but not least, I would specially like to thank all my dear friends in Iowa City who helped me keep up my spirit, think better and continue my efforts throughout my PhD study. My other special thanks goes to my parents and siblings in Iran and Sweden for their love and support.

ABSTRACT

This study develops theorems which generalize or improve the existing predictive dynamics method and implements them to simulate several motion tasks of a human model. Specifically, the problem of determination of contact forces (non-adhesive) between the environment and the digital human model is addressed. Determination of accurate contact forces is used in the calculation of joint torques and is important to account for human strength limitations in simulation of various tasks. It is shown that calculation of the contact forces based on the distance of the contact areas from the Zero Moment Point (ZMP) leads to unrealistic values for some of the forces. This is the approach that has been used in the past. In this work, necessary and sufficient constraints for modeling the non-adhesiveness of a contact area are presented through the definition of NCM (Normal Contact Moment) concepts. NCM point, constraints and stability margins are the new theoretical concepts introduced. When there is only one contact area between the body and the environment, the ZMP and the NCM point coincide. In this case, the contact forces and moments are deterministic. When there are more than one contact areas, the contact forces and moments are indeterminate. In this case, an optimization problem is defined based on the NCM constraints where contact forces and moments are treated as the unknown design variables. Here, kinematics of the motion is assumed to be known. It is shown that this approach leads to more realistic values for the contact forces and moments for a human motion task as opposed to the ZMP based approach. The proposed approach appears to be quite promising and needs to be fully integrated into the predictive dynamics approach of human motion simulation.

Some other insights are obtained for the predictive dynamics approach of human motion simulation. For example, it is mathematically proved and also validated that there is a need for an individual constraint to ensure that the normal component of the resultant

global forces remains compressive for non-adhesive contacts between the body and the environment. Also, the ZMP constraints and stability margins are applicable for the problems where all the contacts between the environment and the body are in one plane; however, the NCM constraints and stability margins are applicable for all types of arbitrary contacts between the body and the environment.

The ZMP and NCM methods are used to model the motion of a human (soldier) performing several military tasks: Aiming, Kneeling, Going Prone and Aiming in Prone Position. New collision avoidance theorems are also presented and used in these simulations.

TABLE OF CONTENTS

LIST OF TABLES	xiii
LIST OF FIGURES	xvi
LIST OF EXAMPLES	xxvi
LIST OF SYMBOLS	xxvii
LIST OF ABBREVIATIONS	xxix
CHAPTER 1. INTRODUCTION	1
1.1 Definition of Some Common Terms	1
1.2 Objectives of Research	5
1.2.1 Environmental Contact	6
1.2.2 Motion Stability	6
1.3 Motivation	7
1.3.1 Environmental Contact	7
1.3.2 Motion Stability in Predictive Dynamics	9
1.3.3 The ZMP Concepts	11
1.4 Scope of Research	12
CHAPTER 2. DIGITAL HUMAN MODEL: KINEMATICS AND DYNAMICS	14
2.1 Introduction	14
2.2 Affine Transformations and Homogeneous Coordinates in Robotics	14
2.3 Denavit-Hartenberg Method and Forward Kinematics	16
2.4 Kinematic Modeling of the Digital Human	19
2.5 Predictive Dynamics	23
2.6 Backward Recursive Dynamics (Recursive Lagrangian)	24
2.7 Kinematic and Dynamic Calculations for the Digital Human	26
CHAPTER 3. REVIEW OF ZERO MOMENT POINT (ZMP) CONCEPTS	28
3.1 Introduction to Zero Moment Point (ZMP)	28
3.2 The ZMP Constraint - Simplified Definition	31
3.3 The ZMP Constraint - Exact Definition	40
3.4 The ZMP Stability Margins and the ZMP Stability Criterion	45
3.5 A Literature Review of ZMP Concepts	48
3.6 Summary and Conclusion	52

CHAPTER 4. A THEORETICAL STUDY OF THE ZMP CONCEPTS IN PREDICTIVE DYNAMICS	53
4.1 Introduction	53
4.2 Theorems on the ZMP Constraint	55
4.2.1 ZMP Constraint and the Unilaterality of Ground Reaction Forces	57
4.2.2 ZMP Location and the Location of Ground Reaction Forces	66
4.3 Application and the Significance of the ZMP Constraint in Predictive Dynamics	72
4.4 Ground Contact Modeling in the ZMP Method	73
4.5 General Algorithms for Ground Contact Modeling in ZMP Method	74
4.6 Calculation of Ground Reaction Forces and Moments	79
4.7 Summary and Conclusion	84
CHAPTER 5. DYNAMIC SIMULATION OF A SOLDIERS' MOTION USING THE ZMP METHOD: KNEELING AND AIMING TASKS	86
5.1 Introduction	86
5.2 A Literature Review of Modeling Military Tasks	87
5.3 Marksmanship	88
5.3.1 Principles of Aiming	89
5.3.2 Natural point of Aim (NPOA)	89
5.4 Kneeling Task	90
5.5 Environment Contact Modeling for Kneeling	91
5.6 Initial Efforts: Lower Body Motion Prediction for Kneeling	93
5.7 Passive Joint Angle Limits (Expanded Ranges of Motion)	94
5.8 The Natural Point of Aim (NPOA)	97
5.9 The Target Engagement Constraint in Aiming Tasks	100
5.9.1 Input Parameters for the Target Engagement Constraint	100
5.9.2 The Target Engagement Constraint	103
5.10 NPOA and the Target Engagement Constraints	105
5.11 Joint Discomfort Objective Function	107
5.12 Problem Formulation for Kneeling	110
5.12.1 Kneeling Then Aiming Task	112
5.12.2 Aiming While Kneeling Task	113
5.13 Motion Prediction Results for Kneeling	114
5.13.1 Results for Engaging Targets at Different Positions	114
5.13.2 Cause and Effect Study for Adding Armor	115
5.13.3 Effect of Changing Avatars	117
5.14 Problem Formulation for Aiming While Standing	119
5.15 Motion Prediction Results for Aiming While Standing	121
5.15.1 Results for Engaging Targets at Different Positions	121

5.15.2	Effect of Changing Avatars	122
5.16	Validation of the Predicted NPOA in Kneeling and Aiming Tasks	124
CHAPTER 6. DYNAMIC SIMULATION OF A SOLDIERS' MOTION USING THE ZMP METHOD: STAND-PRONE-AIM TASK		126
6.1	Introduction	126
6.2	The Stand-to-Prone-to-Aim Task	127
6.3	The Going Prone Subtask	129
6.4	Problem Formulation for Going Prone	130
6.5	Motion Prediction Results for Going Prone	133
6.6	The Aim While Prone Subtask	137
6.7	Attachment of Rifle to the Avatar	138
6.8	Problem Formulation for Aim While Prone	140
6.9	Rifle Motion in the Aim While Prone Task	144
6.10	Collision Avoidance Implementation in Aim While Prone	147
6.11	Motion Prediction Result for Aim While Prone	151
6.11.1	Results for Changing Target Engagement Inputs	152
6.11.2	Results for Changing the Rifle Stock Length	154
6.12	Validation of the Predicted NPOA and the Motion	156
CHAPTER 7. NCM (NORMAL CONTACT MOMENT) CONCEPTS		157
7.1	Introduction	157
7.2	Motivation for NCM Constraints	157
7.3	Definitions for Environment Contact Modeling	158
7.4	Replacing Distributed Contact Forces by Concentrated Equivalents	159
7.5	Replacing Concentrated Contact Forces by Distributed Equivalents	160
7.6	Definitions of NCM Point and NCM Force System	161
7.7	Unilaterality Constraints via NCM Concepts	164
7.7.1	NCM Constraint and the Unilaterality of Distributed Contact Forces	164
7.7.2	NCM Point Location and the Location of Distributed Contact Forces	174
7.8	Coulomb Friction Constraints via NCM Concepts	179
7.9	Summary and Conclusion	186
CHAPTER 8. ZMP VERSUS NCM CONSTRAINTS		188
8.1	Introduction	188
8.2	NCM as the Physical Reasons for the ZMP Constraint	188
8.3	Mathematical Relationship Between ZMP and NCM Constraints	190
8.4	Inaccuracies of the ZMP Method in Chapter 4	195
8.4.1	Logical Pitfall in the ZMP method in Chapter 4	196

8.4.2	Mathematical Impossibility of Uniform Partitioning	197
8.4.3	A Re-Examination of the Basis for the Uniform Partitioning Assumption	205
8.4.4	Partitioning of the Vertical Component of GRF in NCM versus ZMP Method	208
8.5	Uniform Partitioning of GRF versus Uniform Pressure on Contact Areas	217
8.6	A Discussion of the Applicability and Drawbacks of NCM versus ZMP Constraints	222
8.6.1	Applicability of NCM versus ZMP Constraints	222
8.6.2	Drawbacks of the ZMP versus NCM Constraints	223
8.7	Summary and Conclusion	223
CHAPTER 9. PREDICTIVE DYNAMICS SIMULATIONS USING THE NCM METHOD		226
9.1	Introduction	226
9.2	Initial Values of GRF in the ZMP Method	227
9.3	GRF Re-Partitioning Based on the NCM method	239
9.4	Values of GRF after Re-Partitioning	245
9.5	Comparison of GRF and Joint Torques Before and After Re-Partitioning	251
9.6	Effect of Re-Partitioning on the Optimality of the Kinematics of the Motion Prediction Results	256
9.7	Improvement of GRF for a Walking Simulation in Predictive Dynamics Using NCM Method	257
9.7.1	Original Values of GRF for the Walking Simulation (Using ZMP Method)	258
9.7.2	Values of GRF after Re-Partitioning for Walking	262
9.7.3	Comparison of GRF Before and After Re-Partitioning	265
9.7.4	GRF Before and After Re-Partitioning versus Experimental Data	268
9.8	Summary and Conclusion	271
CHAPTER 10. NCM MARGINS OF DYNAMIC STABILITY		274
10.1	Introduction	274
10.2	Motivation for NCM Stability Concepts	274
10.3	Possibility versus the Stability of Motion	275
10.4	Contact Stability of a Dynamic System	275
10.5	Margins of Contact Stability of a Dynamic System	280
10.6	Formulation for the Margins of Dynamic Stability	284
10.6.1	Individual Contact Forces and Moments as Design Variables	285

10.6.2	The margins of dynamic stability as linear optimization problems	287
10.7	Summary and Conclusion	290
CHAPTER 11.	GENERALIZATION OF ZMP CONSTRAINT USING NCM CONCEPTS	291
11.1	Introduction	291
11.2	Motivation for the Generalization of ZMP Constraint	291
11.3	Overview of the Chapter	293
11.4	Possibility of IGE Forces and Moments in the Real World in the Most General Case of Contact Areas	294
11.5	Using NCM Constraints To Generalize the ZMP Constraint	297
11.6	The 2D ZMP-Like Constraint for the Case of Non-Coplanar but Parallel Contact Areas	301
11.7	ZMP-like Constraints in the General Case of Non-Coplanar, Inclined Contact Areas	321
11.8	Summary and Conclusion	321
CHAPTER 12.	SUMMARY, DISCUSSION AND FUTURE RESEARCH	323
12.1	Summary and Conclusions	323
12.2	Future Research	329
APPENDIX A.	OPTIMIZATION-BASED COLLISION AVOIDANCE USING SPHERES, FINITE CYLINDERS AND FINITE PLANES	333
A.1	Introduction	333
A.2	Literature Review	334
A.3	Formulations	336
A.3.1	Constraints for Collision Avoidance Between Two Primitives	337
A.3.1.1	Sphere-to-Sphere Collision Avoidance Constraint	337
A.3.1.2	Sphere-to-Infinite Cylinder Collision Avoidance Constraint	341
A.3.1.3	Sphere-to-Infinite Plane Collision Avoidance Constraint	343
A.3.1.4	Infinite Cylinder-to-Infinite Cylinder Collision Avoidance Constraint	346
A.3.2	Constraints for Collision Avoidance Between Two Compound Primitives	348
A.3.2.1	Sphere-to-Finite Cylinder Collision Avoidance Constraint	348
A.3.2.2	Sphere-to-Finite Plane Collision Avoidance Constraint	349
A.3.2.3	Finite Cylinder-to-Finite Cylinder Collision Avoidance Constraint	351

A.3.2.4	Finite Cylinder-to-Finite Plane Collision Avoidance Constraint	353
A.3.2.5	Finite Plane-to-Finite Plane Collision Avoidance Constraint	356
A.4	Test Results	357
A.5	Conclusion	359
A.6	Theorems on Optimization-Based Collision Avoidance	360
APPENDIX B.	COMPARISON OF JOINT TORQUES BEFORE AND AFTER RE-PARTITIONING IN THE SAMPLE TASK IN CHAPTER 9	365
APPENDIX C.	KINEMATIC EFFECTS OF FEEDING THE GRF RATIOS OF NCM METHOD BACK INTO THE ZMP METHOD IN THE GOING PRONE TASK (CHAPTER 9)	372
APPENDIX D.	GRF RATIOS FOR WALKING IN NCM VERSUS EXPERIMENTAL DATA	379
REFERENCES		381

LIST OF TABLES

Table

4.1. Changes of ground contact conditions for the "Kneeling" task	76
4.2. Changes of ground contact conditions for the "Going Prone" task	77
4.3. Changes of ground contact conditions for the "Aim While Prone" task	78
5.1. Changes of ground contact conditions for the "Kneeling" task	92
5.2. Problem formulation for lower body motion prediction of "Kneeling"	93
5.3. Passive joint angle limits (expanded ranges of motion)	95
5.4. Problem formulation for prediction of "Kneeling"	111
5.5. Problem formulation for prediction of "Aiming"	120
6.1. The stages defined for modeling the going prone subtask.....	129
6.2. Formulation for the first optimization problem of going prone.....	131
6.3. Formulation for the second optimization problem of going prone	132
6.4. List of time grid points corresponding to each motion stage of going prone task.....	134
6.5. The value of ground reaction forces and moments for the first subtask of going prone.....	135
6.6. The value of ground reaction forces and moments for the second subtask of going prone.....	136
6.7. The stages defined for modeling the "Aim While Prone" subtask	137
6.8. Different types of rifle attachment in aiming, kneeling, going prone, aim while prone tasks	139
6.9. Formulation for the first part of "Aim While Prone"	141
6.10. Formulation for the second part of "Aim While Prone"	142
6.11. Formulation for the third part of "Aim While Prone"	143
6.12. Comparison of the stage 2 of "Aim While Prone" in the real world with our simulations.....	145

6.13. Comparison of the stage 3 of "Aim While Prone" in the real world with our simulations.....	146
6.14. Results of "Aim While Prone" for variable rifle stock length (shoulder armor plate thickness).....	155
9.1. List of time grid points corresponding to each motion stage of "Going Prone" task.....	229
9.2. The net value of IGE forces and moments for the first subtask of "Going Prone"	230
9.3. The net value of IGE forces and moments for the second subtask of "Going Prone"	230
9.4. The value of ground reaction forces and moments for the first subtask of "Going Prone" (The highlighted values violate the NCM constraints).....	232
9.5. The value of ground reaction forces and moments for the second subtask of going prone (The highlighted values violate the NCM constraints)	234
9.6. A sample ground reaction force system for the first subtask of going prone	237
9.6. IGE Forces and Moments for the first Subtask of Going Prone after GRF Re-Partitioning.....	245
9.7. IGE Forces and Moments for the second Subtask of Going Prone after GRF Re-Partitioning	245
9.8. IGE forces and moments for the second subtask of "Going Prone" after GRF Re-Partitioning	246
9.9. GRF for the first subtask of "Going Prone" after GRF Re-Partitioning	247
9.10. GRF for the second subtask of "Going Prone" after GRF Re-Partitioning	249
9.10. GRF for the second subtask of "Going Prone" after GRF Re-Partitioning	249
9.11. List of time grid points corresponding to each motion stage of the "Walking" task.....	259
9.12. The net value of IGE forces and moments for the "Walking" task in ZMP method	260
9.13. Ground reaction forces and moments for the "Walking" task in ZMP method.....	261
9.14. The net value of IGE forces and moments for the "Walking" task in NCM method	263
9.15. Ground reaction forces and moments for the "Walking" task in NCM Method.....	264

A.1. Determining region of the location of the sphere with respect to the finite cylinder.....	349
A.2. Determining region of the location of the sphere with respect to the finite plane	350
D.1. Experimental Data (Winter, 2009).....	379
D.2. Results of Repartitioning of GRF Using NCM Method (Continuation of Table 9.14).....	380

LIST OF FIGURES

Figure	
2.1. Depiction of the D-H parameters.....	19
2.2. Branch and joint definitions for the digital human	21
2.3. Coordinate frames for the digital human	22
2.4. Depiction of the forward kinematics and backward dynamics for the digital human	27
3.1. Illustration of definitions for Example 3.1: A two dimensional problem in which a box is located on the ground. The magnitude of the external force F is slowly increased and the ZMP concepts are analyzed for each value of F	29
3.2. Illustration of the first configuration of system in Example 3.1: the bottom of the box is in contact with the ground. Acceleration of the system is assumed to be zero for this configuration. ZMP location varies between the projection of center of mass on the ground and point A.....	32
3.3. Illustration of the second configuration of system in Example 3.1: the bottom of the box is in contact with the ground. The box is about to pivot about point A and the acceleration of the system is assumed to be non-zero. ZMP location coincides with point A.....	36
3.4. Illustration of the third configuration of system in Example 3.1: only one point A of the box (system) is in contact with the ground. The box is pivoting about point A and the acceleration of the system can be either zero or non-zero. ZMP location coincides with point A.....	38
4.1. Schematic of the contact areas, the convex hull of all the contact points and the ZMP in a motion frame in the "Aiming While Kneeling" task.....	56
4.2. Distributed contact forces and the net force and moment of inertial, gravitational and external forces at the ZMP	58
4.3. Proving statement 2 when ZMP is inside the convex hull, but not a contact point.....	60
4.4. Part (B-1) of the proof: proving that it is impossible for ZMP to be outside the convex hull if contact forces are non-adhesive	65

4.5. Distributed contact forces and the net force and moment of inertial, gravitational and external forces at the ZMP on an edge of the convex hull of all contact points.....	67
4.6. Part (A-2) of the proof: proving that if ZMP is on an edge of the convex hull of contact points, then no contact force can exist outside that edge	68
4.7. Part (B-1) of the proof: proving that if all contact forces are on an edge then ZMP is on that edge.....	70
4.8. Frames of Motion for the "Kneeling" task (considering the removal of feet from the ground).....	76
4.9. Frames of Motion for the "Going Prone" task	77
4.10. Frames of Motion for the "Aim While Prone" task	78
4.11. Calculation of ground reaction forces and moments based on the ZMP location in a sample motion frame in an "Aiming While Kneeling" task.....	79
4.12. Walking measurement data from Winter (2009), approximately matching the proportionality of the vertical ground reaction forces (F_y) on the feet to the inverse of the ZMP distances from them (subscripts L and R refer to left foot and right foot).....	82
5.1. Frames of motion for the "Kneeling" task (considering the removal of feet from the ground).....	92
5.2. Lower body motion prediction for "Kneeling" (frozen upper body).....	96
5.3. Definition of input parameters for an arbitrary posture	100
5.4. Examples of two "Kneeling" tasks with predicted "Left Foot Azimuth Angle" values.....	102
5.5. Example of an "Aiming While Prone" task with predicted "Body Azimuth Angle" values	102
5.6. Points of interest in Target engagement.....	103
5.7. Unsuitable kneeling position caused by enforcing unsuitable "Left Foot Azimuth Angle". Target located at (0, 0.2, 3), "Azimuth Flag =1" and "Left Foot Azimuth Angle =20"	105

5.8. Suitable kneeling position when optimization predicts the "Left Foot Azimuth Angle". Target located at (0,2,3) and "Azimuth Flag =0"	106
5.9. An extreme case: Target located at (-1,1,-3), "Azimuth Flag =1" and "Azimuth Angle =110"	107
5.10. Plots of the joint discomfort objective function for k=5 (left) and k=10 (right)	109
5.11. Final kneeling position with "Dynamic Effort" as the only objective function (without the "Joint Discomfort Objective Function")	109
5.12. Final kneeling position using the "Joint Discomfort Objective Function" along with the "Dynamic Effort Objective Function"	110
5.13. "Kneeling Then Aiming" task (Stage 1: Kneeling from Standing)	112
5.14. "Kneeling Then Aiming" task (Stage 2: Aiming from Kneeling)	113
5.15. Results of kneeling for "Azimuth Flag = 0" and target located at A(0,-1,3) and B(-1,1.5,1).....	114
5.16. Results of kneeling for "Azimuth Flag = 0" and target located at A(-1,1,-1) and B(-1,7,2).....	115
5.17. Kneeling prediction with two armor chiclets reducing right knee's range of motion.....	116
5.18. Kneeling prediction with armor chiclets reducing right knee's range of motion considerably	117
5.19. Slides of the results of "Kneeling then Aiming" motion prediction for different avatars (a) "Sophia" avatar (b) "Santos A" avatar	118
5.20. Results of "Aiming While Kneeling" motion prediction for different avatars: (a) "Santos C" avatar (b) " Santos A" avatar	118
5.21. Solution of an avatar played on a different avatar intentionally to show the sensitivity of "Kneeling" task to input parameters (a) Solution of "Sophia" incorrectly played on "Santos A" (b) Solution of "Santos A" incorrectly played on "Sophia"	119
5.22. Results of aiming for "Azimuth Flag = 0" and target located at A(0,1.5,1.5) and B(-3,0,0).....	121
5.23. Aiming with "Azimuth Flag = 0" and target located at A(0,2,1.5), B(0,5,1), C(0,3,1.5).....	122

5.24. Results of "Aiming" for different avatars. Left to right: "Santos D", "Santos A", "Sophia"	123
5.25. Solution of an avatar played on a different avatar intentionally to show the sensitivity of "Aiming" task to input parameters (a) Solution of "Sophia" incorrectly played on "Santos D" (b) Solution of "Santos D" incorrectly played on "Sophia"	123
5.26. Predicted angle between the left foot of avatar and the target line in predictive dynamics for motion tasks: (a) Aiming and (b) Aiming While Kneeling	124
6.1. Motion prediction results for the "Going Prone" subtask.....	133
6.2. Penetration of rifle into the avatar without collision avoidance constraints.....	147
6.3. Modeling of rifle for collision avoidance with one finite cylinder.....	148
6.4. Preventing the interference of rifle with the avatar using collision avoidance constraints.....	149
6.5. Comparison of the results with and without collision avoidance: Collision avoidance constraints change the avatar's motion to prevent the penetration of the rifle with the avatar.....	149
6.6. Modeling of rifle for collision avoidance with 5 finite cylinders and 2 finite planes.....	150
6.7. Motion prediction results for the "Aim While Prone" subtask.....	152
6.8. Comfortable "Aim While Prone" motion with predicted "Body Azimuth Angle".....	153
6.9. Uncomfortable "Aim While Prone" motion with enforced "Body Azimuth Angle=-10°"	153
6.10. Results of "Aim While Prone" for target located at Left: (0,20,100), Right: (0,1,100)	154
6.11. Predicted angle between the body line and target line to minimize joint discomfort.....	156
7.1. A schematic of the general environmental contact problem.....	159
7.2. The NCM force system equivalent to F, M	161

7.3. Distributed forces on a contact area and their equivalent concentrated force and moment and NCM point	165
7.4. Distributed forces on a contact area and their equivalent NCM force system.....	165
7.5. Proving statement 2 when NCM point is inside the convex hull, but not a contact point	167
7.6. Part (B-1) of the proof: proving that it is impossible for NCM point to be outside the convex hull if the contact area is non-adhesive	168
7.7. Method for checking the NCM constraints.....	172
7.8. Distributed forces and the NCM point being on an edge of a contact area	175
7.9. Part (A-2) of the proof: proving that contact forces are only on an edge of the contact area if NCM point is on that edge.....	176
7.10. Part (B-1) of the proof: proving that that if all contact forces are on an edge then NCM point is on that edge.....	178
7.11. Finding the largest line segment in the convex hull with NCM point as its midpoint.....	181
7.12. The value of R for an irregular pentagon - Left: Perspective view, Right: Top View	182
7.13. The value of R for a regular hexagon - Left: Perspective view, Right: Top View	182
7.14. The value of R for a rectangle - Left: Perspective view, Right: Top View	183
7.15. The value of R for a disk - Left: Perspective view, Right: Top View	183
7.16. The value of R for a triangle - Left: Perspective view, Right: Top View.....	183
7.17. A loose constraint on the frictional moment which is linear	185
8.1. Relation of NCM points to the ZMP point in a sample motion frame in the "Aiming While Kneeling" task.....	191
8.2. Effect of uniform partitioning of GRF at an arbitrary point H on the NCM point locations	198

8.3. Walking measurement data from Winter (2009), approximately matching the proportionality of the vertical ground reaction forces (F_y) on the feet to the inverse of the ZMP distances from them (subscripts L and R refer to left foot and right foot).....	207
8.4. Walking measurement data from Winter (2009), showing disparity of the proportionality of the frictional ground reaction forces (F_x) on the feet to the inverse of the ZMP distances from them.....	207
8.5. Walking measurement data from Winter (2009), showing disparity of the value of contact moment of right foot at ZMP (normalized by dividing it by the vertical force) vs. the ratio of the distances of ZMP from the feet.....	208
8.6. Sample problem of finding the locus of the ZMP for different values of r_2 is depicted for two convex hulls Υ_1 and Υ_2 of two contact areas. The locus denoted by Areas Λ_{r_2} is shown for several values of r_2 (0, 0.25, 0.5, 0.75, 1).....	210
8.7. The procedure for constructing Areas Λ_{r_2} for the value of is depicted in detail for $r_2 = 0.75$ and in brief for other values of r_2 . Boundaries of Λ_{r_2} are shown by continuous lines. Boundaries of Π_i are shown by dotted lines. For each r_2 , points E_i are connected by dashed lines.	212
8.8. Apollonian Circles for different ratio of distances from points A,B. The picture is borrowed from Kunkel (2011).....	215
8.9. An example for the locus of the ZMP for different r_2 based on the ZMP method with linear GRF partitioning (locus are the points on the red curves - Apollonian Circles) and NCM method with GRF as design variables (locus are the points inside the Λ_{r_2} shapes).	216
8.10. An example to show the difference between "Uniform Pressure" and "Uniform Partitioning" assumptions for GRF partitioning	218
8.11. Results of GRF by using the "Uniform Partitioning" assumptions	220
9.1. Motion slides for the "Going Prone" subtask	228
9.2. A simplified ground contact area to check NCM constraints for a sample motion frame	238

9.3. Calculation of ground reaction forces and moments based on the ZMP method and its correction by the NCM method	240
9.4. The values obtained for M_x/F_y and M_z/F_y at the Left Foot by ZMP versus NCM Methods.....	252
9.5. The values obtained for M_x/F_y and M_z/F_y at the Right Foot by ZMP versus NCM Methods.....	252
9.6. The values obtained for M_x/F_y and M_z/F_y at the Left Knee by ZMP versus NCM Methods.....	253
9.7. The values obtained for M_x at the Left Foot by ZMP versus NCM Methods.....	254
9.8. The values obtained for M_z at the Left Foot by ZMP versus NCM Methods.....	254
9.9. The values obtained for M_x at the Right Foot by ZMP versus NCM Methods.....	254
9.10. The values obtained for M_z at the Right Foot by ZMP versus NCM Methods.....	255
9.11. The values obtained for M_x at the Left Knee by ZMP versus NCM Methods.....	255
9.12. The values obtained for M_z at the Left Knee by ZMP versus NCM Methods.....	255
9.13. Motion stages (motion segments) for the "Walking" task	259
9.14. The Values Obtained for M_x/F_y and M_z/F_y at the Left Foot by ZMP versus NCM Methods.....	266
9.15. The Values Obtained for M_x/F_y and M_z/F_y at the Right Foot by ZMP versus NCM Methods.....	266
9.16. The Values Obtained for M_x at the Left Foot by ZMP versus NCM Methods.....	267
9.17. The Values Obtained for M_z at the Left Foot by ZMP versus NCM Methods.....	267
9.18. The Values Obtained for M_x at the Right Foot by ZMP versus NCM Methods.....	268
9.19. The Values Obtained for M_z at the Right Foot by ZMP versus NCM Methods.....	268
9.20. Ratio of the vertical forces acting on Left and Right feet versus the ratio of their distances from ZMP for walking task. Measurement data is compared to the results of the NCM and ZMP methods.....	270

9.21. Ratio of the frictional forces acting on Left and Right feet versus the ratio of their distances from ZMP for walking task. Measurement data is compared to the results of the NCM and ZMP methods.....	270
9.22. Contact moment of right foot at ZMP (normalized by dividing it by the vertical force) versus the ratio of the distances of ZMP from the feet for walking task. Measurement data is compared to the results of the NCM and ZMP methods.	271
10.1. Stability criteria for a dynamic system with coplanar contact areas.....	276
10.2. Stability criteria for a general dynamic system with non-coplanar contact areas.....	278
10.3. Margins of contact stability for a general dynamic system with non-coplanar contact areas	281
10.4. Effect of allowing changes in contact forces in determination of stability margins: (a) A 2D avatar in the original (unperturbed) condition (b) Perturbed case, preventing any change in contact forces – No Solution (c) Perturbed case, allowing changes in contact forces - Solvable.....	286
11.1. A schematic of the general problem	298
11.2. Area Π for a stair climbing case	304
11.3. Area Π for 3 arbitrary contact areas.....	304
11.4. Constructing Areas Λ_v for different values of r_1 for two contact areas	309
11.5. Shapes for Areas Λ_f for $o_{23} = 0.2$, $\mu = 0.5$, $r_1 = 0, 0.1, \dots, 1$ as labeled in the figures with (11.5.a) $\mathfrak{S}_1 = 0.2$, $\mathfrak{S}_2 = -0.1$ and (11.5.b) $\mathfrak{S}_1 = -0.2$, $\mathfrak{S}_2 = 0.4$	311
11.6. Shapes for Area Π (dark yellow) and Area Λ (green) for $o_{23} = 0.2$, $\mu = 0.5$, $\mathfrak{S}_1 = 0.2$, $\mathfrak{S}_2 = -0.1$. Areas Λ_f are the same as calculated in Figure 11.5.a.	314
11.7. Shapes for Area Π (dark yellow) and Area Λ (green) for $o_{23} = 0.2$, $\mu = 0.5$, $\mathfrak{S}_1 = -0.2$, $\mathfrak{S}_2 = 0.4$. Areas Λ_f are the same as calculated in Figure 11.5.b.	314

11.8. The conventional ZMP area (red) is shown in (a). Shapes for Area Π (dark yellow) and Area Λ (green) for different values of $o_{23}, \mu, \mathfrak{S}_1, \mathfrak{S}_2$ are shown in figures (b) to (h). In (b) to (e), we have $o_{23} = 0.2, \mu = 0.5$ and (b) $\mathfrak{S}_1 = 0.32, \mathfrak{S}_2 = -0.32$, (c) $\mathfrak{S}_1 = 0, \mathfrak{S}_2 = -0.4$, (d) $\mathfrak{S}_1 = -0.4, \mathfrak{S}_2 = 0$, (e) $\mathfrak{S}_1 = 0, \mathfrak{S}_2 = 0$. In (f) to (h), we have $o_{23} = 0.2, \mu = 1$ and (f) $\mathfrak{S}_1 = 0, \mathfrak{S}_2 = 0$, (g) $\mathfrak{S}_1 = 0.4, \mathfrak{S}_2 = -0.5$, (h) $\mathfrak{S}_1 = -0.7, \mathfrak{S}_2 = -0.5$	315
11.9. Avatar having non-coplanar contact areas.....	316
11.10. The conventional ZMP area (red) is shown in (a). Shapes for Area Π (dark yellow) and Area Λ (green) for $o_{23} = 1.2, \mu = 0.5$ and different values of $\mathfrak{S}_1, \mathfrak{S}_2$ are shown in Figures (b) to (f). Values of $\mathfrak{S}_1, \mathfrak{S}_2$ in each figure are: (b) $\mathfrak{S}_1 = 0, \mathfrak{S}_2 = 0$, (c) $\mathfrak{S}_1 = 0.25, \mathfrak{S}_2 = -0.2$, (d) $\mathfrak{S}_1 = 0.25, \mathfrak{S}_2 = -0.35$, (e) $\mathfrak{S}_1 = 0.45, \mathfrak{S}_2 = -0.1$, (f) $\mathfrak{S}_1 = -0.1, \mathfrak{S}_2 = -0.45$	317
11.11. Avatar being able to lean back without falling due to non-coplanar contact areas.....	318
11.12. Samples of the applicability of the proposed ZMP-Like constraints in the analysis of motions: (a) Horizontal stairs (b) Parallel external contact areas (c) Inclined stairs.....	320
A.1. Sphere-to-Sphere collision.....	338
A.2. Collision avoidance of a sphere with an infinite cylinder.....	342
A.3. Collision avoidance of a sphere with an infinite plane.....	344
A.4. The collision avoidance of two infinite cylinders.....	346
A.5. Smoothed finite cylinder, regions defined around it and its collision avoidance with a sphere.....	348
A.6. Smoothed finite plane with the regions defined around it.....	349
A.7. Finite plane (smoothed) to sphere collision avoidance.....	350
A.8. The collision avoidance of two finite cylinders.....	351
A.9. The collision avoidance of a finite cylinders with a finite plane.....	354
A.10. The test task with sphere to sphere self collision avoidance.....	357

A.11. Result of simulation without imposing obstacle avoidance constraints	358
A.12. Result of simulation after imposing obstacle avoidance constraints	358
A.13. An edged box (unsuitable), a finite plane, a 1-sided finite plane, a box (smoothed).....	359
A.14. Continuity of witness points positions as a result of surface convexity	363

LIST OF EXAMPLES

Example

3.1	Introduction and Definition of the ZMP.....	29
3.2	Validity of ZMP Constraint in all Types of Motion.....	32
3.3	Dynamic Equilibrium Equations vs. the ZMP Constraint.....	41
3.4	ZMP Stability Margin and ZMP Stability Criterion	46
8.1	Uniform Pressure versus Uniform Partitioning (Special Case).....	217
8.2	Uniform Pressure versus Uniform Partitioning (General Case).....	221
9.1	Analysis of a Sample GRF.....	237
11.1	Constructing Areas Λ_v for Two Contact Areas: a Pentagon and a Triangle	309

LIST OF SYMBOLS

Denavit Hartenberg Method:

${}^i\mathbf{T}_{m,b}$	The 4×4 homogeneous transformation matrix from coordinate frame number m to coordinate frame number m in branch b .
${}^0\mathbf{T}_{m,b}$	The 4×4 homogeneous transformation matrix from coordinate frame number m in branch b to the global coordinate frame.
q_i	Joint angle variables in the D-H structure of the digital human.
τ_i	Joint actuation torques.

NCM Concepts:

Υ_α	Contact area (number α) of a dynamic system with the environment.
σ_α	Plane on which Υ_α is located.
$\mathbf{e}_{1\alpha}, \mathbf{e}_{2\alpha}, \mathbf{e}_{3\alpha}$	Unit vectors for a local coordinate frame on Υ_α .
\mathbf{f}_c	A sample distributed contact force acting on a dynamic system.
\mathbf{F}_α	Force vector of the force system equivalent to the forces \mathbf{f}_c on Υ_α .
\mathbf{M}_α	Moment vector of the force system equivalent to the forces \mathbf{f}_c on Υ_α .

\mathbf{p}_α	Point of effect of the force system equivalent to the forces \mathbf{f}_c on Υ_α (often).
\mathbf{v}_α	Location of the NCM point for Υ_α .

ZMP Concepts:

Υ_{Total}	Convex hull of all the contact points.
\mathbf{z}	Location of the ZMP (often).
\mathbf{F}_{ige}	Net force of IGE forces at a point fixed in global coordinate frame.
\mathbf{M}_{ige}	Net moment of IGE forces about a point fixed in global coordinate frame.
\mathbf{F}_{ige}^{zmp}	Net force of IGE forces at the ZMP.
\mathbf{M}_{ige}^{zmp}	Net moment of IGE forces about the ZMP.

LIST OF ABBREVIATIONS

ZMP	Zero Moment Point
NCM	Normal Contact Moment
IGE (forces)	Inertial, Gravity and External (forces)
GRF	Ground Reaction Force
CoM	Center of Mass
D-H (Method)	Denavit-Hartenberg (Method)
NPOA	Natural Point of Aim

CHAPTER 1

INTRODUCTION

There is an increasing demand in industry to evaluate the human aspect of designs within the digital environment. Therefore, digital human modeling and simulation has attracted considerable attention in recent years. One of its main applications is to make an ergonomic evaluation of the human interface of a product in a digital environment at a very early stage of design (prototyping stage). The cost of developing prototypes is considerably reduced when digital prototyping is implemented.

Predictive dynamics, developed recently (Xiang, 2007), is a novel approach for simulating human motion in the digital human modeling field. In this research, certain aspects of the predictive dynamics approach are studied with the objective of gaining further insights into the formulation and improve the simulation capability of the method.

1.1 Definition of Some Common Terms

In this section, some common terms that are used in this research are briefly defined. More complete definition of some of these terms will be given in appropriate chapters.

Definition 1.1: Environmental Contact

In this research, the environment refers to a set of physical objects that may have contact with the dynamic system. The contact of a dynamic system (such as a robot or a digital human) with the environment is referred to as the “environmental contact” of that dynamic system.

Definition 1.2: Environmental (or External) Contact Areas (of a System)

The contact of a dynamic system (such as a robot or a digital human) with the environment occurs through one or more contact areas. Each of them is referred to as an environmental (or external) contact area of the system. Throughout this thesis, it is assumed that the effect of the deformation of these contact areas on the location of contact forces is negligible. In other words, these contact areas are assumed to be rigid for the purpose of dynamic calculations.

Definition 1.3: Non-adhesive Contact Area

Non-adhesiveness is a property of a contact area of the system with the environment. It means that the specified contact area can only exert compressive distributed forces on the dynamic system and also coulomb friction constraints limit the amount of frictional forces that can be exerted on the dynamic system from that contact area.

Definition 1.4: Unilaterality of a Distributed Set of Forces

In general "unilaterality" is a property relating to, or affecting one side of an object (from Merriam-Webster Dictionary). A unilateral vector is generally defined with respect to a surface. So, if the vector always points to one side of this surface, the vector is said to be unilateral with respect to that surface. In this thesis we are only dealing with flat contact surfaces (planes). For any flat contact surface, if the contact area is non-adhesive, then "unilaterality" will be an inherent property of distributed forces on them. It means that on a flat and non-adhesive contact area, all the distributed contact forces have components in the same direction along the axis perpendicular to that contact area.

Definition 1.5: Reaction Force System (on a Ground/Surface Contact Area)

In this research, we replace the effect of distributed forces exerted on the dynamic system (such as a robot or a digital human) from a ground/surface contact area by equivalent concentrated force and moment vectors acting on the system from that contact area. We refer to that concentrated force and moment as the reaction force system on the segment that is in contact with the environment.

Definition 1.6: Possible/Impossible System Property (in Nature)

In this research, the terms possible/impossible are sometimes used in conjunction with a property of a dynamic system (such as its motion or some of its reaction forces). The meaning is that the given value for that specified property can/cannot exist in the nature. In other words, it is possible/impossible for that dynamic system to have that value for such a property in the real world.

Definition 1.7: Feasible/Infeasible System Property in an Optimization Problem

In this case, the meaning of “infeasible” is that the given value for that system property violates the constraints defined in the optimization problem. Therefore, any solution for the dynamic system that has that value for that system property will not satisfy the optimization constraints.

Definition 1.8: Coplanar/Non-Coplanar Environmental Contact Areas

If two environmental contact areas of a system are on the same plane, they are said to be coplanar, otherwise they are non-coplanar.

Definition 1.9: Zero Moment Point (ZMP)

ZMP exists only for a system in which all its environmental contact areas are only on the ground (or coplanar in Definition 1.8) and are all non-adhesive. For such a system, ZMP is defined as that point on the ground (plane) at which the net moment of the inertial, gravity and external (IGE) forces acting on a dynamic system (such as a robot or a digital human) has no component along the two horizontal (planar) axes (Vukobratović, 2004; Sardain, 2004).

Definition 1.10: ZMP Constraint

The ZMP constraint states that during any motion of the system (either stable or unstable), the ZMP should be inside or on the boundary of the convex hull of all the ground contact areas. If a calculated motion for the system does not obey the ZMP constraint, then that motion is impossible.

Definition 1.11: ZMP Method (in Predictive Dynamics)

By ZMP Method in predictive dynamics, we refer to a method which uses the ZMP constraint to ensure the possibility of motion and calculates the contact forces based on their distances to the ZMP.

Definition 1.12: Contact Instability of System (during motion)

In general, the contact instability of the system during motion is defined as the condition when the contact area of the dynamic system with the environment reduces to a line or a point. In more technical words, it is defined as a condition, where at least one out of the six components of the IGE (inertial, gravity, external) forces or moments acting on the system cannot either increase beyond or

decrease below its current value. In other words the contact instability occurs if distributed contact forces are not able to cancel the IGE forces and moments if one component of the IGE forces and moments increases beyond or decreases below its current value. However, this inability never occurs (because dynamic equilibrium equations can never be violated). Instead the system may acquire a sudden acceleration to change the values for the inertial components of IGE forces and moments and limit them in their possible ranges.

Definition 1.13: Contact Stability Margin of System (during motion)

The contact stability margin of the system during a motion is defined as the maximum amount of perturbation in the external forces acting on the system during the motion before it becomes unstable. In other words, it is defined as the maximum possible amount of perturbation in the six components of the IGE (inertial, gravity, external) forces or moments acting on the system. A motion with stability margins which are all non-zero is referred to as a stable motion.

1.2 Objectives of Research

This thesis aims to advance the predictive dynamics method and propose improvements in several different aspects in order to model dynamic tasks more precisely. The most notable aspect involves a new methodology for incorporating and considering the contact of digital human with the environment. This methodology can also evaluate the dynamic stability of the predicted motion. It also contributes to the generalization of the Zero-Moment-Point (ZMP) concepts to be applicable to dynamic systems with non-coplanar environmental contact areas. Conventionally, the ZMP

concept has been developed and used in generating the walking motion of humanoid robots. Therefore, the major problems to be addressed in this research are stated as follows:

- 1- Environmental contact of the digital human model – where the problem of predicting generalized contact forces will be studied.
- 2- Stability of the predicted motion – where stability aspects of the motion will be studied.

1.2.1 Environmental Contact

The digital human model can come into contact with the environment at several locations. These contacts may be in the same plane or in different planes. The major challenges with environmental contacts are:

- Determine whether the requested motion can be produced (for example: can the digital human bend forward and have zero acceleration, while only his toes are touching the ground? or, can a digital human run on ice at a given speed (acceleration)?)
- For the requested motion, how to calculate the generalized contact forces for each of the contact areas?

1.2.2 Motion Stability

Stability of motion can also be referred to as the dynamic stability of the digital human. The intent is to determine whether a predicted motion is stable against tipping over or slipping in different directions.

In this research, methods are developed to evaluate the margins of dynamic stability at any instant of time against tipping over or slipping in different directions

based on environmental contact areas, which may be coplanar or non-coplanar at that instant of time.

1.3 Motivation

The study of the background and detailed literature review of each of the subtopics will be presented in later chapters. However, in this section, we present a brief literature overview of each of the subtopics that motivate the proposed study.

1.3.1 Environmental Contact

Traditionally, a method referred to as the “ZMP method” has been used in predictive dynamics to model the contact of the digital human with the environment. Examples can be seen in Xiang et al. (2007, 2009), Kim et al. (2008), and Bhatt et al. (2008). In the ZMP method for predictive dynamics, a force vector and a moment vector are considered to act on the digital human from each contact area. In the simulation process, all the forces which are the inertial, gravitational and external (IGE) forces are known except for the contact forces. The possibility of generation of any requested motion by using the given contact areas is ensured by using the ZMP constraint. ZMP constraint requires the ZMP to be inside the convex hull of all contact points. When ZMP constraint is satisfied, it is possible to find unilateral distributed contact forces on the contact areas to equilibrate the IGE forces and moments, if enough friction exists between the contacting bodies. Then, the contact reaction force and moment vectors at each contact area are calculated. This calculation assumes that the global equivalent contact forces and moments (which should cancel IGE forces and moments to ensure dynamic equilibrium) are partitioned on contact areas based on the distances of the

contact areas from the ZMP. The problems encountered in using the ZMP method are listed as follows:

- Using the ZMP method, it is only possible to model motions in which all the contact areas of the digital human with the environment are only in one plane and also all the contact areas have unilateral (non-grasping) contact with the environment. Only motions which satisfy these contact requirements can be modeled by the ZMP method. In this research, we propose to develop methods in which more general cases of environmental contact can be addressed. The reason is to be able to model tasks with contact areas which are not co-planar or if we have some contact areas with non-unilateral contact conditions (such as grasping) and some with unilateral contact conditions. Examples are numerous, such as walking on uneven terrain, climbing an object (such as stair climbing, ladder climbing, climbing a wall, climbing an obstacle, climbing into a vehicle), leaning against a wall, touching the environment with hand while the foot is on the ground,
- Even for motions which satisfy the above conditions, the ground reaction force and moment vector on each contact area are calculated based on an assumption. The assumption is that the components of the global equivalent contact forces and moments (which should cancel IGE forces and moments to ensure dynamic equilibrium) are partitioned uniformly on contact areas based on the distances of the contact areas from the ZMP. This assumption has not been proved to be mathematically exact. This assumption is based on several measurement data, which suggest that the vertical component of the ground reaction force (1 component out of the 6 components of the ground reaction forces and moments) can be approximately partitioned linearly on the ground

contact areas based on the distances of those contact areas from the ZMP location (see Ren, 2005, 2007; Winter, 1990, 2009). Based on those measurement data, this approximation is not exact and only holds for 1 component of the GRF (out of the 3 force and 3 moments in the 3 spatial directions). The other 5 components of GRF are also partitioned linearly on the ground contact areas based on the distances of those contact areas from the ZMP location which is done without any experimental or theoretical justification. Therefore, this issue has been an open problem and is investigated in this research. The mathematical and theoretical validity of this assumption as well as its merit as an approximation are investigated. This is an important issue because the ground reaction forces are used to calculate all the torques and forces in the digital human.

- The ZMP method also assumes that infinite amount of friction could be exerted from the contact areas on the digital human. In this research, we incorporate the effect of friction in motion prediction models.

1.3.2 Motion Stability in Predictive Dynamics

ZMP stability margins are used in predictive dynamics to evaluate the stability of the motion. The distance of the ZMP in each horizontal direction to the edges of the convex hull can be considered as a stability margin against tipping over in that direction. The stability margin is expressed by a number or several numbers for each instant of motion. These numbers define how stable the digital human is at that instant of motion against a perturbation, which can make it tip over (ZMP approach cannot evaluate the margins of stability against slipping). These numbers are normally referred to as the margins of dynamic stability. This fact was mentioned in the original work on ZMP

(Vukobratović, 1972), and has been used implicitly by many researchers. Explicit definition of this ZMP stability margin can be seen, for example, in Huang (2001). The ZMP stability criterion states that a motion of the system is dynamically stable if and only if the ZMP is strictly inside (not on the boundary) the convex hull of all the contact points (Goswami, 2004). In brief, stability criterion is satisfied if the margins of stability are positive numbers. Instability occurs if one of these numbers is zero. These numbers can never be negative.

However, the ZMP stability margins do not offer a perfect criterion for evaluating the stability of motion, because of the following reasons:

- ZMP stability margins are only defined when all the contact areas of the digital human with the environment are only in one plane. In this research, we develop methods that can evaluate the motion stability in more general cases of environmental contact. The reason is that we want to be able to evaluate stability in tasks with contact areas which are not co-planar. Examples are numerous, such as walking on non-even terrain, climbing an object (such as stair climbing, ladder climbing, climbing a wall, climbing an obstacle, climbing into a military tank), leaning against a wall, touching the environment with hand while the foot is on the ground, etc.
- ZMP stability margins only define the margins of dynamic stability against tipping over. They cannot be used to evaluate the margins of dynamic stability against slipping. In this research, we develop methods that can evaluate the motion stability against slipping. The reason is that we want to be able to evaluate “Slipping” stability margins too. A motion which is on the verge of instability against “Slipping” may be very stable against “Tipping Over”. The extra

information given by the “Slipping” stability margins are essential in evaluating the stability of a motion.

- ZMP stability margins cannot define the amount of perturbations in terms of external forces or moments that the system can tolerate without becoming unstable.

We develop different stability margins to overcome these drawbacks.

1.3.3 The ZMP Concepts

Advances in the area of ZMP-based biped robots have been witnessed in the recent decades. Examples can be seen in Gienger (2001), and Park (2006). However, the conventional ZMP concept is only applicable in the cases where all contact areas are on the same plane. Other efforts have addressed the ZMP method for both parallel and non-parallel contact areas on different planes. Harada (2003) proposed an approximate method to generalize ZMP to several cases of arm/leg coordination tasks for humanoid robots. Saida (2003) suggests a new criterion instead of ZMP called FSW (Feasible Solution of Wrench) that shows the feasible condition of forces applied to the robot on rough terrain. However, an exact, general method is still lacking to check the possibility of a motion or find the margins of dynamic stability of a motion in the general cases of contact surfaces. In this research, we generalize the ZMP concepts to apply to the most general cases of contact areas (coplanar or non-coplanar contact areas which are horizontal or inclined or parallel or non-parallel).

1.4 Scope of Research

Part I of this work consisting of Chapters 1, 2 and 3 includes the introduction and background material for this research. In Chapter 2, we introduce the basics of the predictive dynamics method. Chapter 3 is a review of the ZMP concepts existing in the literature.

Part II of this study is a study of the ZMP method for modeling environmental contact. Chapter 4 presents a theoretical study of the ZMP method. In that chapter, the ZMP concepts in predictive dynamics are used to design general algorithms which model the exact changes of the transient ground contact areas during the motion and calculate ground reaction forces. In Chapter 5 and 6, the modules based on the ZMP method introduced in Sections 4.3 and 4.4 are used to model the motion of a human (soldier) performing several military tasks: aiming, kneeling, going prone and aiming in prone position.

Part III of this study is a study of NCM method for modeling environmental contact. Chapter 7 and 8 are theoretical chapters in which we introduce the new concept of Normal Contact Moment (NCM) constraints and compare them to the ZMP constraint. In those chapters, we show that unlike ZMP, the NCM constraints are valid in the most general cases of contact conditions. We also show that it is able to improve the values calculated for ground reaction forces. In Chapter 9, previous military tasks modeled in Chapters 5 and 6 by using the ZMP method are remodeled using the NCM method and the results are compared.

In Chapter 10, we introduce the NCM stability margins. In this chapter, we show that unlike ZMP, the NCM stability margins are valid in the most general cases of contact conditions. The ZMP concepts (ZMP constraints, ZMP stability criterion and the ZMP stability margins) only apply to the cases in which the body's contact areas with the

environment are in one plane (the ground). In Chapter 11, the NCM constraints are used to generalize the ZMP constraint.

In this study, general formulas are presented to generalize all the ZMP concepts to apply to the most general cases of contact areas (coplanar or non-coplanar contact areas which are horizontal or inclined or parallel or non-parallel). We also introduce general “Slipping” stability margins similar to their “Tipping” (ZMP) counterparts.

Also, in Appendix A, we present new theorems on optimization-based collision avoidance that use other finite primitives besides the conventional spheres to model objects or limbs. This capability was needed to model self and environment collision avoidance and has been used in the dynamic simulations presented in this research.

CHAPTER 2

DIGITAL HUMAN MODEL: KINEMATICS AND DYNAMICS

2.1 Introduction

In this chapter, we first present the basic robotics conventions for the kinematic analysis of a robot. Then, we present the kinematic model of our digital human. In the next step, we introduce the predictive dynamics method to perform the kinematic and dynamic analysis of the robot. These kinematic and dynamic calculations are based on the exact and well established forward kinematics and backward dynamics methods. Therefore, by the end of this chapter, we will conclude that in predictive dynamics, for any given motion of a digital human, the kinematic and dynamic calculations can be performed with complete mathematical certainty, if and only if the ratios for the partitioning of environment contact forces are given (if all the external forces are known in the general sense). However, this is not true for a digital human, if it has more than one contact area with the environment. In that case, the equivalent ground reaction force and moment exerted on each contact area of the digital human with the environment is indeterminate. The resolution of this indeterminacy is the most important objective of this thesis which will be discussed in Part II and Part III of this research.

2.2 Affine Transformations and Homogeneous Coordinates in Robotics

In linear algebra, linear transformations can be represented by matrices. If T is a linear transformation mapping R^n to R^m and \mathbf{x} is a column vector with n entries, then:

$T(\mathbf{x}) = \mathbf{Ax}$ for some $m \times n$ matrix \mathbf{A} , called the transformation matrix of T . An affine transformation T' consists of a linear transformation followed by a translation:

$$\mathbf{T}' : \mathbf{x} \rightarrow \mathbf{Ax} + \mathbf{b} \quad \text{or} \quad \mathbf{T}'(\mathbf{x}) = \mathbf{Ax} + \mathbf{b} \quad (2.2.1)$$

An affine transformation preserves:

1. The colinearity relation between points; i.e., all the points which lie on a line still lie on a line after the transformation
2. Ratios of distances along a line; e.g., the midpoint of a line segment remains the midpoint after transformation

In general, an affine transformation is composed of linear transformations (rotation, scaling or shear) and a translation. Several linear transformations can be combined into a single one, so that the general formula given above is still applicable. In the one-dimensional case, \mathbf{A} and \mathbf{b} are called, respectively, slope and intercept.

Ordinary vector algebra uses matrix multiplication to represent linear transformations, and vector addition to represent translations. To represent both transformations by using matrix multiplications, we must use homogeneous coordinates. This means representing a 3-vector (x, y, z) as a 4-vector $(x, y, z, 1)$, and similarly for n -vectors in n -dimensional problems. The technique requires that all vectors be augmented with a "1" at the end, and all matrices are augmented with an extra row of zeros at the bottom, an extra column—the translation vector—to the right, and a "1" in the lower right

corner. If \mathbf{A} is a matrix, then equation $\begin{bmatrix} \mathbf{y} \\ 1 \end{bmatrix} = \begin{bmatrix} \mathbf{A} & \mathbf{b} \\ 0 \dots 0 & 1 \end{bmatrix} \begin{bmatrix} \mathbf{x} \\ 1 \end{bmatrix}$ is equal to $\mathbf{y} = \mathbf{Ax} + \mathbf{b}$.

Homogeneous coordinates are found everywhere in computer graphics. Since they allow common operations such as translation, rotation, scaling and perspective projection to be implemented as matrix operations. Homogeneous coordinates are also used in the related areas of CAD/CAM (Zeid, 1991), robotics (McKerrow, 1991), surface modeling (Farin, 1990), and computational projective geometry (Kanatani, 1991).

2.3 Denavit-Hartenberg Method and Forward Kinematics

Denavit and Hartenberg (1955) suggested a systematic method to formulate the kinematics of a general 3 dimensional open loop robot, now known as the D-H method. Each of the joints in the open loop robot (open loop chain) should possess only one degree of freedom (either purely revolute or purely prismatic) to be modellable by the D-H method.

We use the D-H method in predictive dynamics to address the forward kinematics calculations of our digital human model. The Denavit-Hartenberg (D-H) method was created in the 1950's to systematically represent the relation between two coordinate systems but was only extensively used in the early 1980's with the appearance of computational methods and hardware that enable the necessary calculations. The method is currently used to a great extent in the analysis and control of robotic manipulators. The D-H method is based upon characterizing the configuration of link i with respect to link $(i-1)$ by a (4×4) homogeneous transformation matrix representing each link's coordinate system. This method represents each link coordinate system in terms of the previous link

coordinate system. The position of any point in any of the local coordinate frames can be expressed in global reference frame by the D-H method.

Assume that the global coordinate frame in the D-H method is numbered as coordinate frame 0. Consider a branched open-loop robot such as a digital human. Assume that point A is attached to a coordinate frame denoted respectively in the D-H table as coordinate frame number m in branch b of that open loop robot. Let the local position vector of point A in that local coordinate frame be given by $\mathbf{L}_A = (x_A \ y_A \ z_A \ 1)^T$. Let the global position vector of the point A be given by $\mathbf{G}_A = (X_A \ Y_A \ Z_A \ 1)^T$. Then, \mathbf{L}_A can be related to \mathbf{G}_A by the following formula:

$$\mathbf{G}_A = \begin{bmatrix} X_A \\ Y_A \\ Z_A \\ 1 \end{bmatrix} = [{}^0\mathbf{T}_{m,b}] \begin{bmatrix} x_A \\ y_A \\ z_A \\ 1 \end{bmatrix} = [{}^0\mathbf{T}_{m,b}] \mathbf{L}_A \quad (2.3.1)$$

In the above formula, $[{}^0\mathbf{T}_{m,b}]$ is the 4×4 homogeneous transformation matrix from coordinate frame number m in branch b to the global coordinate frame. $[{}^0\mathbf{T}_{m,b}]$ can be calculated from the formula:

$$[{}^0\mathbf{T}_{m,b}] = [{}^0\mathbf{T}_{1,b}] [{}^1\mathbf{T}_{2,b}] [{}^2\mathbf{T}_{3,b}] \mathbf{L} [{}^{s-1}\mathbf{T}_{s,b}] \mathbf{L} [{}^{m-1}\mathbf{T}_{m,b}] \quad (2.3.2)$$

Each transformation matrix ${}^{s-1}\mathbf{T}_{s,b}$ is given by:

$${}^{s-1}\mathbf{T}_{s,b} = \begin{pmatrix} C_{s,b} & -S_{s,b}C\alpha_{s,b} & S_{s,b}S\alpha_{s,b} & a_{s,b}C_{s,b} \\ S_{s,b} & C_{s,b}C\alpha_{s,b} & -C_{s,b}S\alpha_{s,b} & a_{s,b}S_{s,b} \\ 0 & S\alpha_{s,b} & C\alpha_{s,b} & d_{s,b} \\ 0 & 0 & 0 & 1 \end{pmatrix} \quad (2.3.3)$$

$$\text{where: } \begin{cases} S_{s,b} \equiv \sin(\theta_{s,b}) & , & C_{s,b} \equiv \cos(\theta_{s,b}) \\ S\alpha_{s,b} \equiv \sin(\alpha_{s,b}) & , & C\alpha_{s,b} \equiv \cos(\alpha_{s,b}) \end{cases}$$

The four values for the D-H parameters $\theta_{s,b}, d_{s,b}, \alpha_{s,b}, a_{s,b}$ are typically entered into a table known as the D-H Table. These transformation matrices will be used in Appendix A (Section A.3) for the derivation of collision avoidance formula. However, for the simplicity of notation in the rest of this section, let us assume only one branch and denote coordinate frame m in branch b by coordinate frame i . Therefore, the four parameters $\theta_i = \theta_{s,b}, d_i = d_{s,b}, \alpha_i = \alpha_{s,b}$ and $a_i = a_{s,b}$ (depicted in Figure 2.1) are defined as:

- 1) θ_i is the joint angle, measured from the x_{i-1} to the x_i axis about the z_{i-1} .
- 2) d_i is the distance from the origin of the coordinate frame $(i-1)$ to the intersection of the z_{i-1} axis with the x_i axis along z_{i-1} axis.
- 3) a_i is the offset distance from the intersection of the z_{i-1} axis with the x_i axis to the origin of the frame i along x_i axis.
- 4) α_i is the offset angle from z_{i-1} axis to z_i axis about the x_i axis.

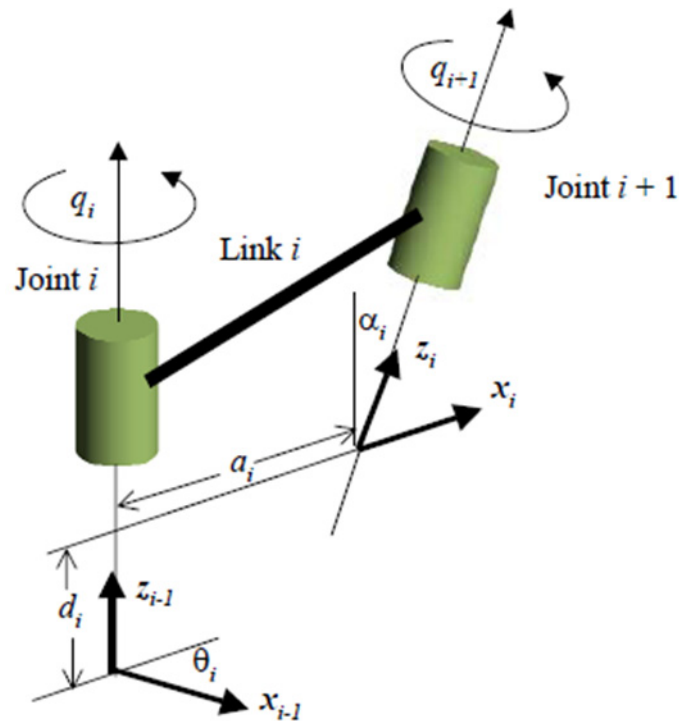


Figure 2.1. Depiction of the D-H parameters

Besides the global position, the global velocity and acceleration of each point attached to each local coordinate frame can be obtained by differentiating Equation (2.3.1) with respect to time. This is a basic concept in robotics known as “Forward Dynamics”.

2.4 Kinematic Modeling of the Digital Human

In this study, each limb of the digital human is assumed to represent a bone in the skeleton. Therefore, the motion of the skeleton completely defines the motion of all the limbs of the digital human.

The skeleton can be modeled precisely enough as a branched open loop system with 7 branches (numbered 0 to 6) as shown in Figure 2.2. In this branched open loop system (or a tree structured manipulator), branch 0 starts from the global coordinate frame and ends in the pelvis (hip) point of the digital human. Branch 0 includes 3 translational (prismatic) joints and 3 rotational (revolute) joints. So, it totally contains 6 degrees of freedom which specify the global position and orientation of the coordinate frame attached to the pelvis.

49 degrees of freedom in branches 1 to 6, represent the revolute joints which model the human joints and determine the kinematics of all the limbs of the digital human. (For some joints such as the shoulder and the clavicle there revolute joint modeling is less precise).

Branches 1, 5, 6 start from the “hip point” frame and respectively define the spine, right leg and left leg of the digital human. The spine branch ends in a local frame called the “spine end” frame. Branches 2, 3, 4 start from the “spine end” point and respectively define the right arm, left arm and the neck of the digital human.

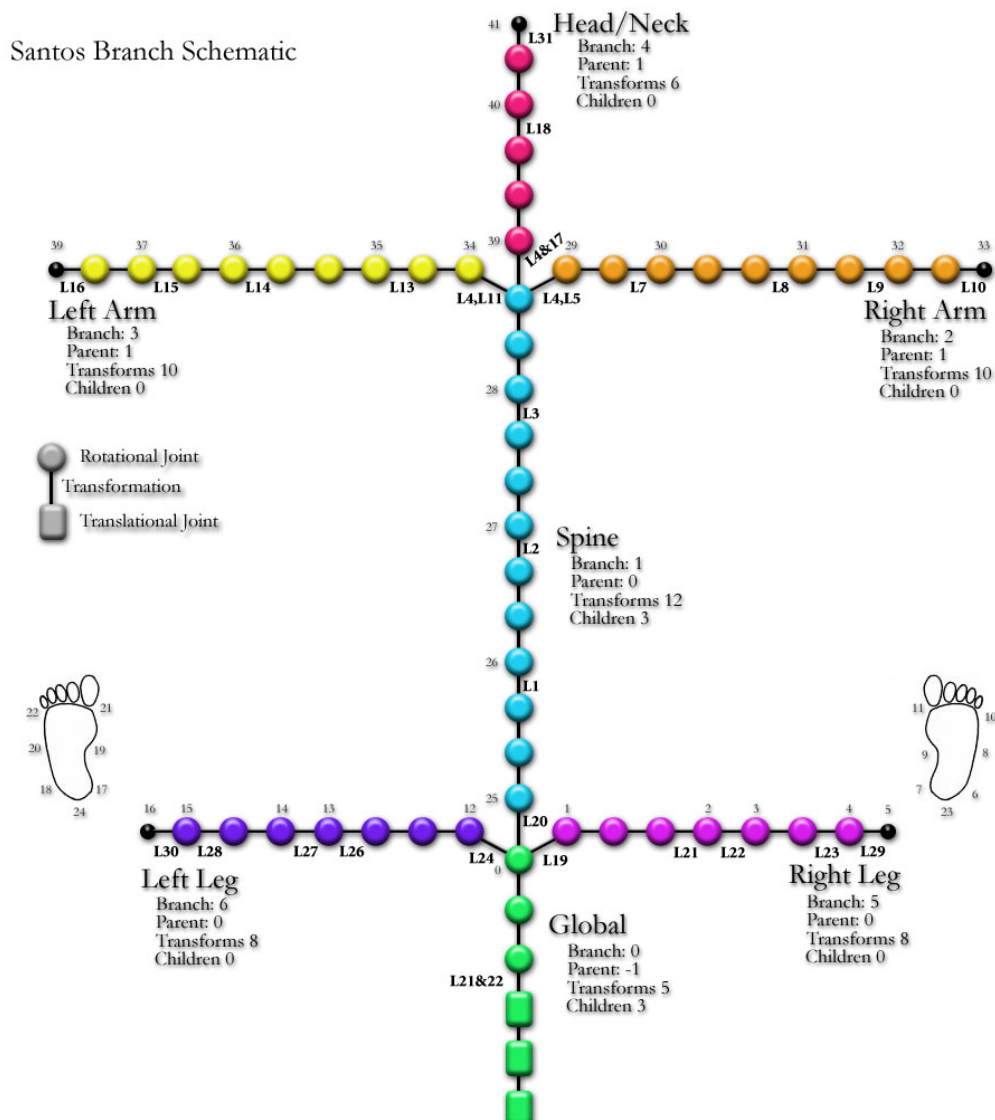


Figure 2.2. Branch and joint definitions for the digital human

The coordinate frames in the D-H table which are each attached to separate limbs of the digital human are depicted in Figure 2.3.

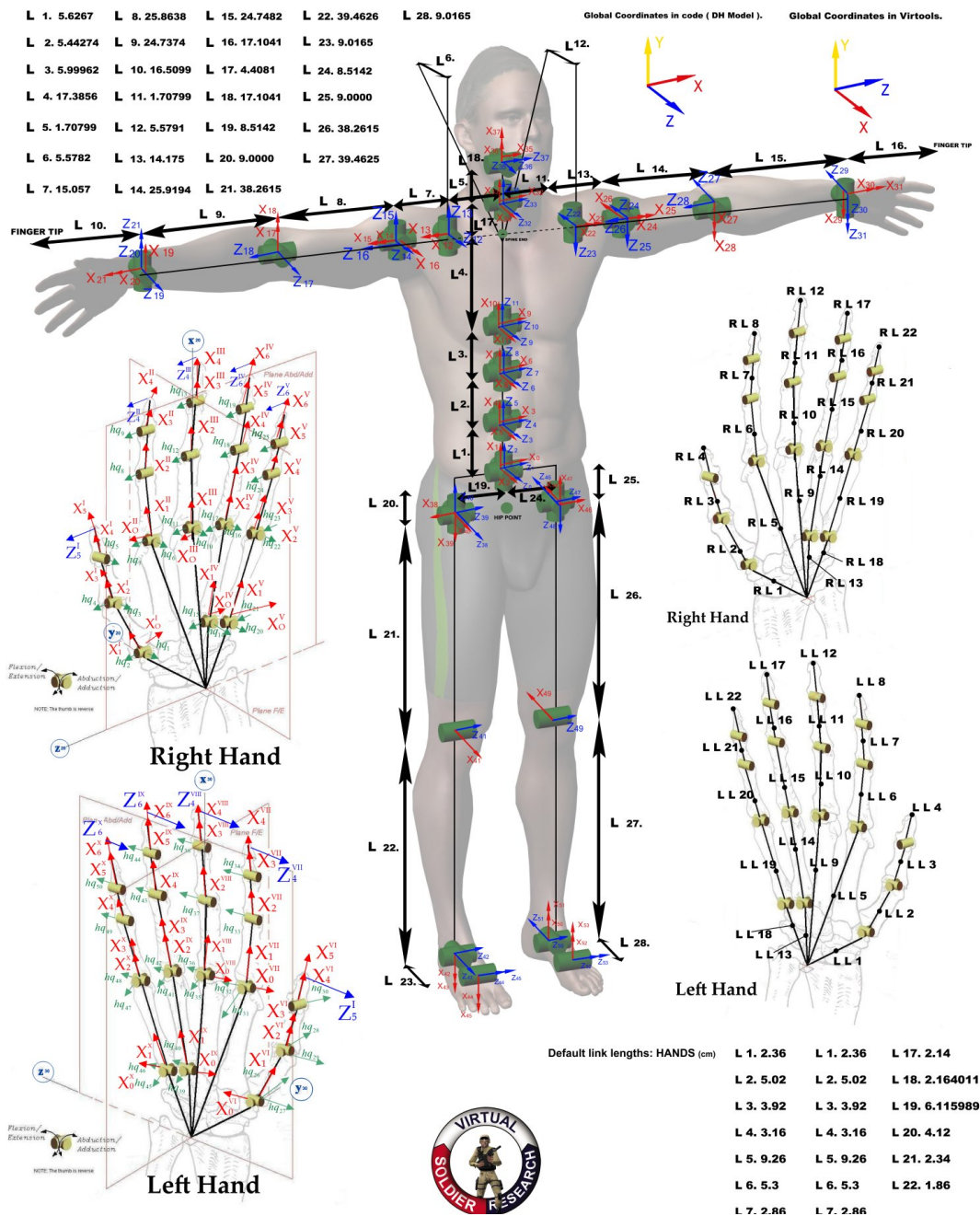


Figure 2.3. Coordinate frames for the digital human

2.5 Predictive Dynamics

As described in Section 2.4, our digital human is modeled as an open-loop robot. The conventional methods for the dynamic analysis of robots are normally classified into two different categories:

- 1- Forward Dynamics Methods: In forward dynamics methods, it is assumed that the input forces (e.g. the actuation torques at robot joints) are known and the forward dynamics method finds the response (e.g. the force exerted by the robot hand) by integrating differential equations of motion.
- 2- Inverse Dynamics Methods: In inverse dynamics methods, it is assumed that the response is known and the inverse dynamics method finds the input forces by directly evaluating the equations of motion.

However, in the study of human motion, both input forces and the response are normally unknown. In reality, humans can perform a same task in a variety of ways. Therefore, there is no unique solution for a human motion in performing a specific task. A very little amount of information is normally available in the form of equalities (i.e. exact information). They usually include: known (non-contact) external forces, boundary conditions for a motion task and some expected system response. Joint angle values, torque profiles as well as ground reaction forces (or contact forces acting on the digital human from the environment) are all unknowns. Most of the known information for modeling a human motion task such as walking, running, aiming, kneeling, going prone, etc. usually appear as inequality constraints. These constraints represent the limitations of the environment (e.g. non-adhesive contact areas), the limitations of the digital human

model (e.g. joint angle or torque limits) and the limitations of the motion task (e.g. those requirements that differentiate crawling from walking). In such cases, the concept of predictive dynamics is used to solve this type of a problem. The basic idea is to use optimization methods to reveal force and response histories based on the available information of the dynamic system.

Predictive Dynamics is a term coined to characterize the prediction of human motion in a physics-based world. The method capitalizes on a novel optimization-based approach to motion prediction. The non-contact external forces are all assumed to be known during the motion. An arbitrary motion (a set of joint angle profiles for all joint angles) of the avatar (humanoid robot) is used as an initial guess. Based on this motion, the required external contact forces and moments that should act on each separate contact area are calculated such that dynamic equilibrium equations hold. Using these contact forces and moments, the required torques at all joints are calculated. Physical constraints such as constraints on joint angles and torques are imposed. This renders a feasible (realistic and possible) motion. Best motions are selected (motion is optimized) based on human performance measures, such as speed, energy and comfort which act as objective functions in the optimization formulation. Predicting motion in this way allows one to use avatars to study how and why humans move the way they do, given a specific scenario.

2.6 Backward Recursive Dynamics (Recursive Lagrangian)

There are several methods in robotics for the calculation of torques in an open loop robot (open loop chain). For these calculations, it is always assumed that all the

external forces and the mass of the links are known. In this work, calculation of torques at joints is accomplished by the Recursive Lagrangian method. It is accomplished by defining 4×4 homogeneous transformation matrix \mathbf{D}_i and 4×1 homogeneous vectors \mathbf{E}_i , \mathbf{F}_i , and \mathbf{G}_i as follows.

Given the mass and inertia properties of each link, and the external force $\mathbf{f}_k^T = [{}^k f_x \quad {}^k f_y \quad {}^k f_z \quad 0]$ and the moment $\mathbf{h}_k^T = [{}^k h_x \quad {}^k h_y \quad {}^k h_z \quad 0]$ for the link k defined in the global coordinate system, then the joint actuation torques τ_i are computed for $i = n$ to 1 as (Xiang et al., 2008)

$$\tau_i = tr \left[\frac{\partial \mathbf{A}_i}{\partial q_i} \mathbf{D}_i \right] - \mathbf{g}^T \frac{\partial \mathbf{A}_i}{\partial q_i} \mathbf{E}_i - \mathbf{f}_k^T \frac{\partial \mathbf{A}_i}{\partial q_i} \mathbf{F}_i - \mathbf{G}_i^T \mathbf{A}_{i-1} \mathbf{z}_0 \quad (2.6.1)$$

Where:

$$\begin{cases} \mathbf{D}_i = \mathbf{I}_i \mathbf{C}_i^T + \mathbf{T}_{i-1} \mathbf{D}_{i+1} \\ \mathbf{E}_i = m_i {}^i \mathbf{r}_i + \mathbf{T}_{i+1} \mathbf{E}_{i+1} \\ \mathbf{F}_i = {}^k \mathbf{r}_f \delta_{ik} + \mathbf{T}_{i+1} \mathbf{E}_{i+1} \\ \mathbf{G}_i = \mathbf{h}_k \delta_{ik} + \mathbf{G}_{i+1} \end{cases} \quad (2.6.2)$$

With $\mathbf{D}_{n+1} = \mathbf{0}$ and $\mathbf{E}_{n+1} = \mathbf{F}_{n+1} = \mathbf{G}_{n+1} = \mathbf{0}$; \mathbf{I}_i is the inertia matrix for link i ; m_i is the mass of link i ; \mathbf{g} is the gravity vector; ${}^i \mathbf{r}_i$ is the location of center of mass of link i in the local frame i ; ${}^k \mathbf{r}_f$ is position of the external force in the local frame k ;

$\mathbf{z}_0 = [0 \ 0 \ 1 \ 0]^T$ for a revolute joint and $\mathbf{z}_0 = [0 \ 0 \ 0 \ 0]^T$ for a prismatic joint. δ_{ik} is Kronecker delta.

The first term in torque expression is the inertia and Coriolis torque, the second term denotes the torque of force due to gravity, the third term is the torque due to external force, and the fourth term represents the torque due to external moment.

2.7 Kinematic and Dynamic Calculations for the Digital Human

The D-H method based forward dynamics as explained in Section 2.3 and the recursive Lagrangian method explained in Section 2.6 are used in this work to carry out the kinematic and dynamic analyses for the 3D human model.

The forward kinematics calculates the motion from the origin towards the end of each branch along the branch as shown in Figure 2.4. This process only involves joint angle values and geometrical parameters. However, backward dynamics propagates forces from end-effector to the origin, and the mass and inertia property of the links need to be considered for dynamic analysis.

In Figure 2.4, joint (k) and joint (k+1) are connected by link (j+1) for which mass and inertia properties are defined in the local coordinate system \mathbf{z}_{i+3} . The links between coordinates \mathbf{z}_{i+3} and \mathbf{z}_{i+2} , and \mathbf{z}_{i+2} and \mathbf{z}_{i+1} have zero link length, and zero mass and inertia properties, so that the force is correctly transferred back through \mathbf{z}_{i+3} , \mathbf{z}_{i+2} , and \mathbf{z}_{i+1} for the joint (k).

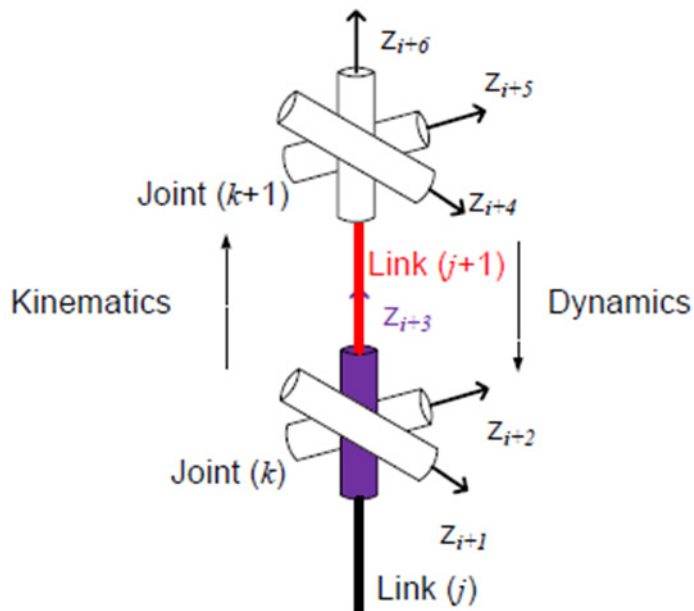


Figure 2.4. Depiction of the forward kinematics and backward dynamics for the digital human

However, there is an unsolved problem in the dynamics calculations for a digital human. The problem is that in the recursive Lagrangian method explained in Section 2.6, we assumed that all the external forces and the mass of the links are known. This is not true for a digital human, if it has more than one contact area with the environment. In that case, the equivalent ground reaction force and moment exerted on each contact area of the digital human with the environment is indeterminate. The resolution of this indeterminacy is the most important objective of this thesis. Two methods are given in Chapter 4 (ZMP Method) and Chapter 7 (NCM Method) of this thesis to address this indeterminacy. As soon as this indeterminacy is resolved, the well established Recursive Lagrangian method in Section 2.6 can be used to calculate the torques at all joint of the digital human.

CHAPTER 3

REVIEW OF ZERO MOMENT POINT (ZMP) CONCEPTS

3.1 Introduction to Zero Moment Point (ZMP)

The conventional Zero Moment Point (ZMP) concepts are defined for a system (such as a robot or a digital human) having several non-adhesive contact areas with a plane. We call them the ZMP contact areas. It is assumed that all the ZMP contact areas are coplanar (i.e., all the ZMP contact areas are on the same plane which is conventionally the ground).

The ZMP is defined as that point on the plane at which the net moment of the inertial, gravitational and external (IGE) forces acting on the system (such as a robot or a digital human) has no component along the two planar axes. From the above definition it is concluded that for a static system which has several non-adhesive contact areas with only one plane, and is under no external force, the projection of the center of mass on that plane is same as the ZMP for that system.

It should be noted that we are making a distinction between contact, gravity and external forces. It means that the contact or gravity forces should not be considered as a part of external forces (in calculating the IGE forces).

An illustrative example is used in this chapter to explain the ZMP concepts. In each section, when a new ZMP concept is introduced, we refer to this example to illustrate the concept.

Example 3.1 *Introduction and Definition of the ZMP*

Consider a box located on the ground at rest as shown in Figure 3.1. We define F as the magnitude of a horizontal external force that is applied to the box at the top of the box as shown in the figure (acting in the positive x direction). We consider all the forces and motions of the system (the box) to occur in the xy plane of the global coordinate system shown in the figure (In other words, the problem is idealized as a 2D system). Assume that the coefficient of friction between the box and the ground is very large and the height of the box is considerably larger than its length. In such a case, when F is increased beyond some value the box eventually tips and pivots about point A.

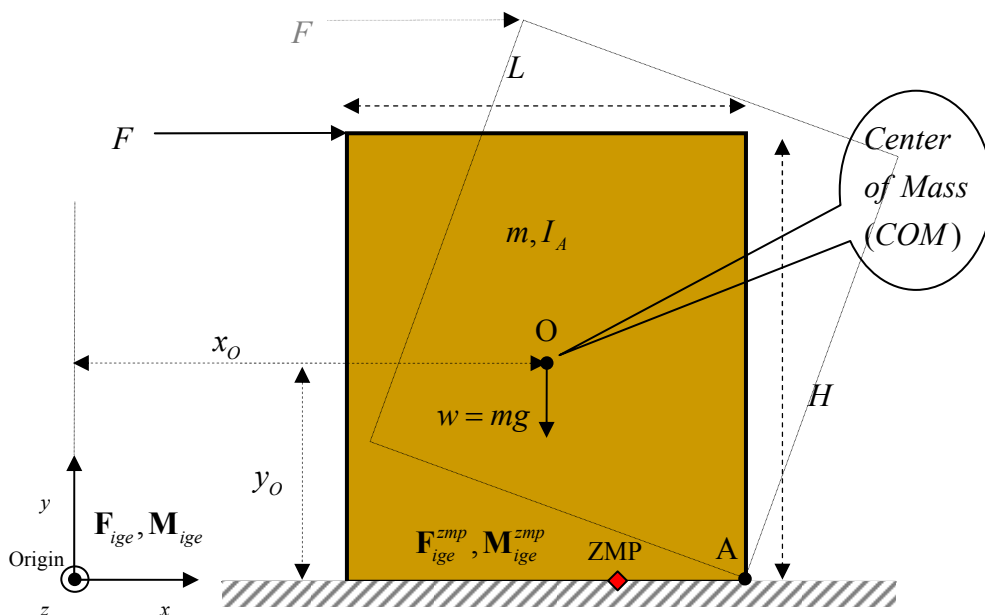


Figure 3.1. Illustration of definitions for Example 3.1: A two dimensional problem in which a box is located on the ground. The magnitude of the external force F is slowly increased and the ZMP concepts are analyzed for each value of F .

Point A is defined on the right bottom corner of the box as shown in Figure 3.1. Point A is a significant point because the box will pivot about it due to external force F as will be shown later. Also m and I_A respectively denote the mass of the box and its mass moment of inertia about point A. The center of mass of the box is assumed to be located at its geometrical center that is denoted by point O. The x and y components of the locations of points O, A, ZMP, ... in the global coordinate system are respectively given as $x_O, y_O, x_A, y_A, x_{ZMP}, y_{ZMP}, \dots$. The length and height of the box are denoted by L and H , respectively.

We slowly increase the value of F from zero, calculate the ZMP location and see what requirements the ZMP constraint imposes on the system (for the possibility of motion) and study the ZMP stability margins and stability criterion at any instant of motion. Since the ZMP location and ZMP concepts depend on the acceleration of the system and its contact points with the ground, we study the motion under three different configurations:

1. First configuration is the initial configuration of the system when the bottom of the box is in contact with the ground. The system is not pivoting about point A. Therefore, the translational and angular accelerations of the system are zero due to the large coefficient of friction that prevents the box from sliding on the ground.

2. Second configuration is when the bottom of the box is still in contact with the ground. However, the system starts to pivot about point A and the acceleration of the system is non-zero.

3. Third configuration is when the box only has contact with the ground at point A. It is pivoting about point A and the acceleration of the system can be calculated based on the magnitude of F and can be either zero or non-zero.

3.2 The ZMP Constraint - Simplified Definition

Before the exact definition, we give a simplified definition for the ZMP constraint. ZMP constraint states that for any given motion of a system, ZMP should be inside the convex hull of all the ground contact areas. Otherwise, the motion is impossible in the real world. We call this definition a simplified definition because it does not indicate what the satisfaction of the ZMP constraint ensures. As a very simple explanation, consider a system with a known mass having several contact areas with the ground. Assume that the system is at rest and no external load is applied on it. Therefore, the only forces acting on the system are the gravitational and ground contact forces. ZMP constraint states that the projection of the center of mass (which is equal to ZMP location for this static case under no external force) should be in the convex hull of all the ground contact areas. Otherwise, this configuration is impossible in the real world (i.e., the system cannot stay at rest).

In order to see whether the ZMP constraint is really valid in the real world during all types of motion, we will apply it for the system described in Example 3.1. We study the ZMP constraint for each of the three configurations defined in the previous section.

Example 3.2 *Validity of ZMP Constraint in all Types of Motion*

➤ For the First Configuration in Example 3.1:

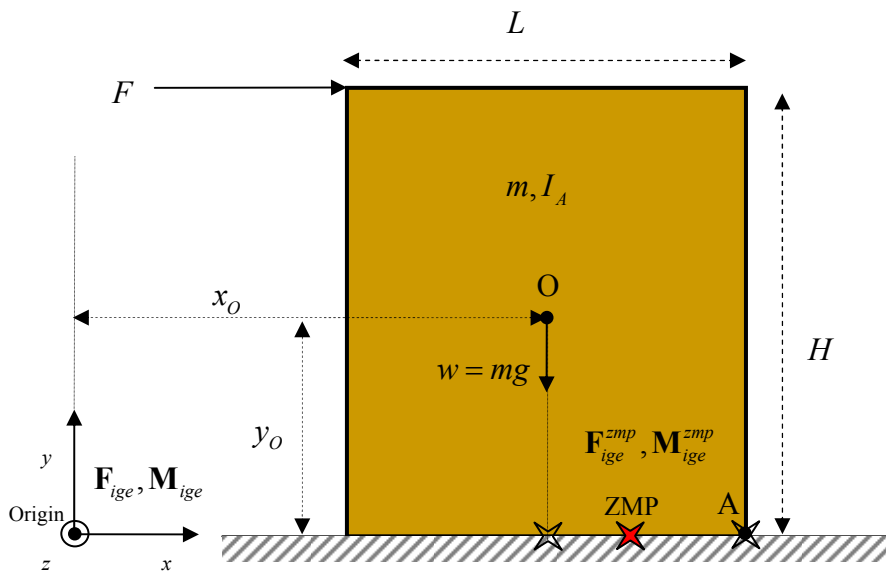


Figure 3.2. Illustration of the first configuration of system in Example 3.1: the bottom of the box is in contact with the ground. Acceleration of the system is assumed to be zero for this configuration. ZMP location varies between the projection of center of mass on the ground and point A.

We calculate the vectors \mathbf{F}_{ige} and \mathbf{M}_{ige} (moment is calculated about the Origin of the inertial reference frame) and \mathbf{F}_{ige}^{zmp} and \mathbf{M}_{ige}^{zmp} (moment is calculated about the ZMP) for this configuration of the system (system has zero acceleration):

$$\left\{ \begin{array}{l} \mathbf{F}_{ige} = F \mathbf{i} - mg \mathbf{j}, \\ \mathbf{F}_{ige}^{zmp} = \mathbf{F}_{ige} = F \mathbf{i} - mg \mathbf{j}, \end{array} \quad \begin{array}{l} \mathbf{M}_{ige} = (-FH - mgx_o) \mathbf{k} \\ \mathbf{M}_{ige}^{zmp} = (-FH + mg(x_{ZMP} - x_o)) \mathbf{k} \end{array} \right\} \quad (3.2.1)$$

ZMP is defined as that point on the ground at which the moments of IGE forces are zero about the two horizontal axes. Therefore, we should have:

$$\mathbf{M}_{ige}^{zmp} \times \mathbf{j} = \mathbf{0} \quad \stackrel{(3.2.1)}{\Rightarrow} \quad -FH + mg(x_{ZMP} - x_o) = 0 \quad \Rightarrow \quad x_{ZMP} = \frac{FH}{mg} + x_o \quad (3.2.2)$$

The ZMP constraint requires the ZMP to be inside or on the boundary of the system's contact points with the ground at any instant of motion. Otherwise, that motion (or configuration) will be an impossible motion (or configuration). Therefore:

$$\text{ZMP Constraint} \quad \Rightarrow \quad x_A - L \leq x_{ZMP} \leq x_A \quad (3.2.3)$$

$$\stackrel{(3.2.2)}{\Rightarrow} \quad x_A - L \leq \frac{FH}{mg} + x_o \leq x_A \quad \stackrel{x_A - x_o = \frac{L}{2}}{\Rightarrow} \quad -\frac{mgL}{2H} \leq F \leq \frac{mgL}{2H} \quad (3.2.4)$$

We slowly increase F from zero for the First Configuration (defined in Section 3.1) and study the ZMP location and ZMP constraint. The following cases will occur during this increase in F:

- Case I, First Configuration: $F = 0$

In this case, the ZMP location is the same as the location of the projection of the system's center of mass on the ground. This can be observed from the following calculations:

$$F = 0 \stackrel{(3.2.2)}{\Rightarrow} x_{ZMP} = \frac{0}{mg} + x_O = x_O \quad (3.2.5)$$

- Case II, First Configuration: $0 < F < \frac{mgL}{2H}$

In this case, the ZMP will be located between the projection of the system's center of mass on the ground and point A. This can be observed from the calculations that follow:

$$\begin{aligned} 0 < F < \frac{mgL}{2H} &\stackrel{(3.2.2)}{\Rightarrow} \frac{0}{mg} + x_O < x_{ZMP} < \frac{\frac{mgL}{2H} H}{mg} + x_O \\ \Rightarrow x_O < x_{ZMP} < x_A &\quad (3.2.6) \end{aligned}$$

- Case III, First Configuration: $F = \frac{mgL}{2H}$

In this case, the ZMP will coincide with point A. This can be observed from the following calculations:

$$F = \frac{mgL}{2H} \stackrel{(3.2.2)}{\Rightarrow} x_{ZMP} = \frac{\frac{mgL}{2H} H}{mg} + x_O \Rightarrow x_{ZMP} = x_A \quad (3.2.7)$$

- Case IV, First Configuration: $F > \frac{mgL}{2H}$

This case is impossible according to (3.2.4). However, in this case, the ZMP location will be beyond the point A and outside of the boundary of the system's contact points with the ground. This can be observed from the following calculations:

$$F > \frac{mgL}{2H} \stackrel{(3.2.2)}{\Rightarrow} x_{ZMP} > \frac{\frac{mgL}{2H} H}{mg} + x_O \Rightarrow x_{ZMP} > x_A \quad (3.2.8)$$

Therefore, the ZMP constraint (3.2.3) is violated and this motion (or configuration) is impossible. In other words, this value of F cannot occur in the first configuration (First Configuration is when the bottom of the box is in contact with the ground and the acceleration of the system is zero).

Therefore at least one of the assumptions of the first configuration needs to change to allow F to increase beyond $mgL/2H$. It is obvious that an instantaneous change (requiring zero time) cannot happen in the system's contact areas. So, the only possibility is that the system acquires a non-zero acceleration. It means that the ZMP constraint requires the system to have a non-zero acceleration if we increase F beyond $mgL/2H$. This exactly falls under the assumptions of the Second Configuration (defined in Section 3.1). So, we will study this case under the Second Configuration.

❖ Thus, the effect of ZMP constraint in the first configuration is to show the limitations on the magnitude of F for this configuration to exist. These limitations shown by inequality (3.2.4) seem logical according to the explanation given in Case IV in the first configuration. However, where the ZMP constraint exactly comes from will be explained in Section 3.3.

➤ For the Second Configuration in Example 3.1:

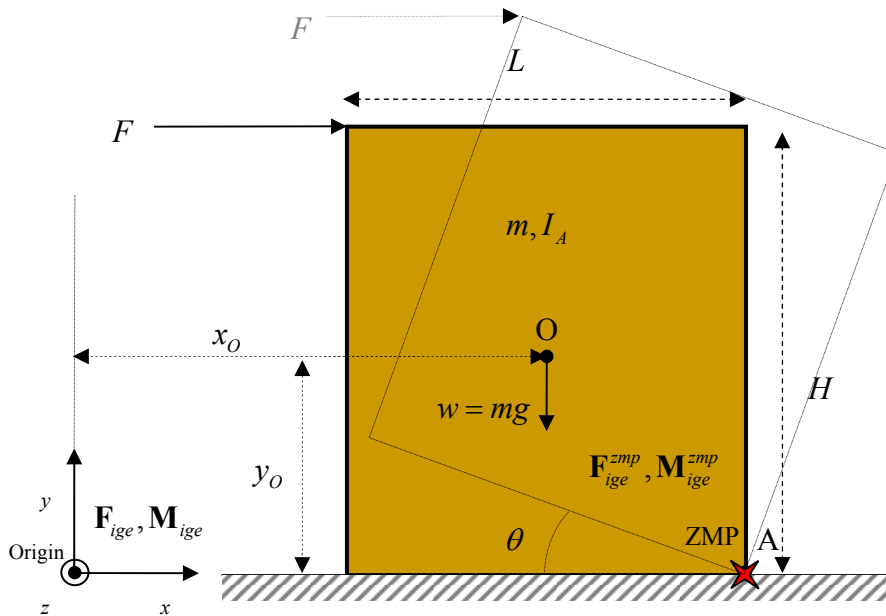


Figure 3.3. Illustration of the second configuration of system in Example 3.1: the bottom of the box is in contact with the ground. The box is about to pivot about point A and the acceleration of the system is assumed to be non-zero. ZMP location coincides with point A.

The ZMP constraint requires the ZMP to be inside or on the boundary of the system's contact points with the ground at any instant of motion. Otherwise, that motion (or configuration) will be impossible. Therefore:

$$\text{ZMP Constraint} \quad \Rightarrow \quad x_{ZMP} = x_A \quad (3.2.9)$$

The ZMP constraint in its general form is an inequality constraint. However, as seen in equation (3.2.9), for this case it has turned into an equality constraint (or, the

inequality constraint has become active) since the system's contact area with the ground has reduced to a point. We calculate the vector \mathbf{M}_{ige}^{zmp} for this configuration of the system:

$$\mathbf{M}_{ige}^{zmp} = \left(-FH + I_A \ddot{\theta} + mg \frac{L}{2} \right) \mathbf{k} \quad (3.2.10)$$

ZMP is defined as that point on the ground at which the moment of the IGE forces is zero about the two horizontal axes. Therefore, ZMP constraint actually imposes the following constraint on the system:

$$\begin{aligned} \mathbf{M}_{ige}^{zmp} \times \mathbf{j} = \mathbf{0} & \stackrel{(3.2.10)}{\Rightarrow} -FH + I_A \ddot{\theta} + mg \frac{L}{2} = 0 \\ & \Rightarrow FH - mg \frac{L}{2} = I_A \ddot{\theta} \end{aligned} \quad (3.2.11)$$

❖ Thus in the second configuration, the ZMP constraint (3.2.11) (which is an equality here) gives the equation of dynamic equilibrium. However, where ZMP constraint exactly comes from will be explained in Section 3.3.

➤ For the Third Configuration in Example 3.1:

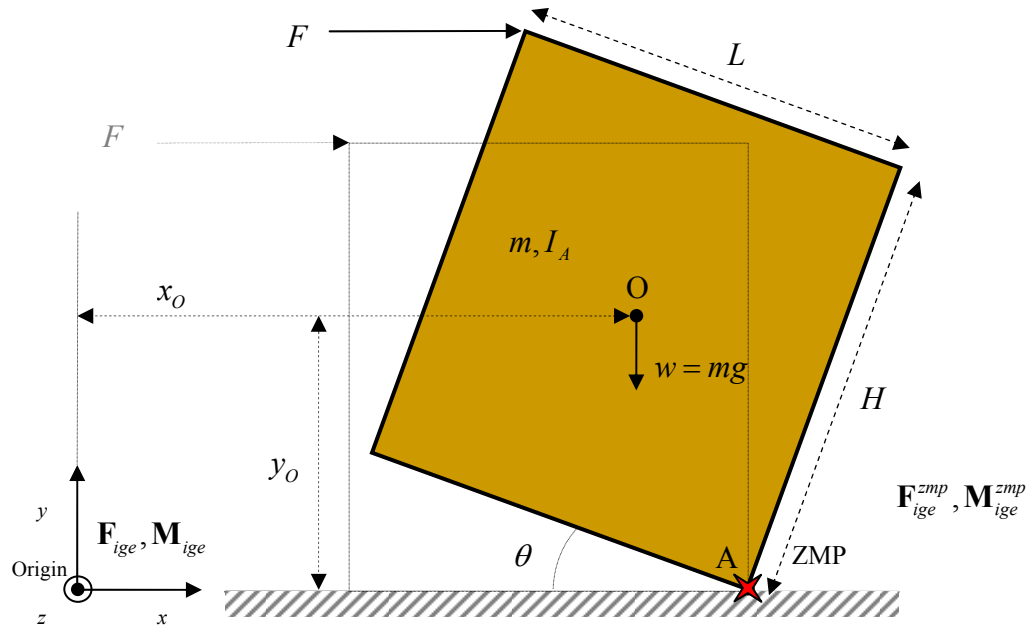


Figure 3.4. Illustration of the third configuration of system in Example 3.1: only one point A of the box (system) is in contact with the ground. The box is pivoting about point A and the acceleration of the system can be either zero or non-zero. ZMP location coincides with point A.

The ZMP constraint requires the ZMP to be inside or on the boundary of the system's contact points with the ground at any instant of motion. Otherwise, that motion (or configuration) is impossible. Therefore:

$$\text{ZMP Constraint} \quad \Rightarrow \quad x_{ZMP} = x_A \quad (3.2.12)$$

We calculate the vector \mathbf{M}_{ige}^{zmp} for this configuration of the system:

$$\mathbf{M}_{ige}^{zmp} = \left(-F(H\cos\theta + L\sin\theta) + I_A\ddot{\theta} + mg\frac{L\cos\theta - H\sin\theta}{2} \right) \mathbf{k} \quad (3.2.13)$$

ZMP is defined as that point on the ground at which the moment of IGE forces are zero about the two horizontal axes. Therefore, ZMP constraint actually imposes the following constraint on the system:

$$\begin{aligned} \mathbf{M}_{ige}^{zmp} \times \mathbf{j} = \mathbf{0} & \stackrel{(3.2.13)}{\Rightarrow} -F(H\cos\theta + L\sin\theta) + I_A\ddot{\theta} + mg\frac{L\cos\theta - H\sin\theta}{2} = 0 \\ \Rightarrow F(H\cos\theta + L\sin\theta) - mg\frac{L\cos\theta - H\sin\theta}{2} & = I_A\ddot{\theta} \end{aligned} \quad (3.2.14)$$

❖ Thus in the third configuration, the ZMP constraint (3.2.14) (which is an equality here) gives the equation of dynamic equilibrium.

A less important issue to note is that for a same angular acceleration, the force required to cause the system to proceed to fall is actually less than the force that was required in the second configuration to initiate the pivoting of the system about point A.

This can be seen in the following calculations:

$$(3.2.14) \Rightarrow F_{Third\ Configuration} = \frac{mg(L\cos\theta - H\sin\theta) + 2I_A\ddot{\theta}}{2(H\cos\theta + L\sin\theta)} \quad (3.2.15)$$

$$(3.2.11) \Rightarrow F_{Second\ Configuration} = \frac{mgL + 2I_A\ddot{\theta}}{2H} \quad (3.2.16)$$

$$For\ 0 < \theta < \frac{\pi}{2} \quad : \quad \begin{cases} L\cos\theta - H\sin\theta < L \\ H\cos\theta + L\sin\theta > H \end{cases} \quad (3.2.17)$$

$$(3.2.15), (3.2.16), (3.2.17) \Rightarrow F_{Third\ Configuration} < F_{Second\ Configuration} \quad (3.2.18)$$

Goswami (1999) correctly points out that there has been a confusion in the interpretation of the meaning of the ZMP constraint. He states that contrary to what was incorrectly implied in several papers: “the ZMP location may never leave the support polygon (convex hull of the ZMP contact areas)” even during unstable or falling motions. In fact, ZMP constraint can be used very well to simulate unstable and falling motions. In falling motions, it will enforce the system to have the exact correct acceleration. Goswami (1999) also states that: “ZMP constraint has no inherent relationship with a dynamically stable gait as had been incorrectly stated in several papers”. As was shown in Example 3.2, ZMP constraint ensures “possible motion”, not necessarily “stable motion”. Later, we will define the ZMP stability margin which is a different part of the ZMP concepts and claim that if it is non-zero (ZMP location not on the boundary of the convex hull) then we have “stable motion”.

3.3 The ZMP Constraint - Exact Definition

The simplified definition of ZMP constraint given in Section 3.2 only indicates that its violation is impossible for systems in the real world such as online control problems (but in simulations or offline control problems it may be violated; therefore the ZMP constraint should be imposed in such problems to match the reality). What does the ZMP constraint exactly ensure if it is satisfied and where does it come from? In order to find out what the ZMP constraint exactly ensures, we will study the equations that ZMP constraint imposes on the system in Example 3.1:

Example 3.3: *Dynamic Equilibrium Equations vs. the ZMP Constraint*

➤ For the first configuration in Example 3.2:

As stated before, the effect of ZMP constraint in the first configuration is to show the limitations on the magnitude of F in this configuration. These limitations are shown by inequality (3.2.4).

It turns out that we can study such limitations by writing the equations of equilibrium for the system in the first configuration (Figure 3.2). To do that, we replace the distributed ground reaction forces on the system in the first configuration by one upward force acting on the bottom of the box at the location x_{GRF} . Then, it is obvious that:

$$x_A - L \leq x_{GRF} \leq x_A \quad (3.3.1)$$

The equation of static equilibrium of the moments for the system at point A about z direction can be expressed as:

$$\begin{aligned} \sum M_z &= 0 \\ \Rightarrow -FH + mg \frac{L}{2} - mg(x_A - x_{GRF}) &= 0 \\ \Rightarrow FH &= mg \left(-x_A + x_{GRF} + \frac{L}{2} \right) \end{aligned} \quad (3.3.2)$$

We evaluate x_{GRF} from the equilibrium equations (3.3.2) and substitute it into inequality (3.3.1):

$$\begin{aligned}
(3.3.1), (3.3.2) \quad &\Rightarrow \quad mg \left(-x_A + (x_A - L) + \frac{L}{2} \right) \leq FH \leq mg \left(-x_A + x_A + \frac{L}{2} \right) \\
\Rightarrow \quad &-mg \frac{L}{2H} \leq F \leq mg \frac{L}{2H} \quad (3.3.3)
\end{aligned}$$

Equation (3.3.3) can be viewed as conversion of the equation of equilibrium of moments about z into an inequality by removing the contact forces acting on the system (here, by using Equation (3.3.1)). As it is seen, it is exactly same as Equation (3.2.4) which is the ZMP constraint.

➤ For the second and third configurations in Example 3.2:

As stated before, the ZMP inequality constraint turns into equality constraints (3.2.11) and (3.2.14) in the second and third configurations which look similar to equations of dynamic equilibrium.

For the second configuration, the equations of dynamic equilibrium of the moments for the system at point A about z direction can be expressed as (see Figure 3.3):

$$\begin{aligned}
\sum M_z + I_A \ddot{\theta} &= 0 \\
\Rightarrow \quad -FH + mg \frac{L}{2} + I_A \ddot{\theta} &= 0 \quad \Rightarrow \quad FH - mg \frac{L}{2} = I_A \ddot{\theta} \quad (3.3.4)
\end{aligned}$$

For the third configuration, the equations of dynamic equilibrium of the moments for the system at point A about z direction can be expressed as (see Figure 3.4):

$$\begin{aligned}
& \sum M_z + I_A \ddot{\theta} = 0 \\
\Rightarrow & -F(H\cos\theta + L\sin\theta) + mg \frac{L\cos\theta - H\sin\theta}{2} + I_A \ddot{\theta} = 0 \\
\Rightarrow & F(H\cos\theta + L\sin\theta) - mg \frac{L\cos\theta - H\sin\theta}{2} = I_A \ddot{\theta} \quad (3.3.5)
\end{aligned}$$

As it is seen, Equations (3.3.4) and (3.3.5) which are the general equations of dynamic equilibrium of moment about z direction for the second and third configurations are exactly same as Equations (3.2.11) and (3.2.14) which are the ZMP constraints for those configurations. Actually, for any dynamic system, whenever the contact forces are absent (have no role in) from these two equilibrium equations, they will be same as the ZMP constraints.

ZMP constraint in its general form is an inequality constraint. Based on the observations made in Example 3.3, we can claim that: *The ZMP constraint can be considered as a conversion of the two equations of the general dynamic equilibrium (out of the 6 force and moment equilibrium equations for the whole system) into inequalities by removing the contact forces acting on the system from the equations. These two equations are the dynamic equilibrium of all moments exerted on the whole system about the horizontal axes.*

The above claim holds for all the three configurations in Example 3.1. For example, this claim holds precisely for the first configuration if we consider that the system is static and has no acceleration, therefore dynamic equilibrium equations are the same as the static equilibrium equations. For the second and third configurations, because

the contact area of the system with the ground has reduced to a point, the ZMP constraint becomes an equality and exactly matches the dynamic equilibrium equations for moments about the horizontal axes.

In general, the ZMP constraint specifies the range of values for the tipping (horizontal) components of the net moment of the IGE forces (about any fixed point such as the origin) that are possible in the real world for a dynamic system. In other words, in a dynamic system, the ZMP constraint implies that the moment of IGE forces at the origin about the horizontal axes are within certain bounds. For example, Equations (3.2.4) and (3.2.1) result in:

$$\begin{aligned}
 (3.2.4) \quad & \Rightarrow \quad mg(x_A - L) \leq FH + mgx_O \leq mgx_A \\
 (3.2.1) \quad & \Rightarrow \quad \mathbf{M}_{ige} \cdot \mathbf{k} = -FH - mgx_O \\
 & \Rightarrow \quad -mgx_A \leq \mathbf{M}_{ige} \cdot \mathbf{k} \leq -mg(x_A - L)
 \end{aligned} \tag{3.3.6}$$

Even if a huge external force is applied on the dynamic system (a huge perturbation in a component of IGE forces), the moment of IGE forces will not exceed that range and the ZMP will not exit the convex hull in the real world. That is because the ZMP constraint will require the system to fall with a huge acceleration. For example, the ZMP constraint shown in Equations (3.2.11) and (3.2.14) requires large acceleration of falling ($\ddot{\theta}$) for a large external force (F) applied on the system. In other words, to satisfy the ZMP constraint in the simulation, when a large external force is applied to the system, the falling acceleration has to be large so that the inertial terms of IGE forces cancel the external terms. And the net moments of the IGE forces stay in the ranges specified by the

ZMP constraint and the ZMP location stays inside or on the boundary of the convex hull. This is how ZMP constraint can ensure the possibility of motion and even ensure correct accelerations during falling and unstable motions of virtual systems.

3.4 The ZMP Stability Margins and the ZMP Stability Criterion

Now, we introduce two other definitions in the ZMP concepts, which are the “ZMP stability margin” and the “ZMP stability criterion”. It can be shown that the distance of the ZMP location in each horizontal direction to the edges of the convex hull of the ZMP contact areas can be considered as a stability margin against tipping in that direction (an example is shown later in this section). For example if the ZMP location is near an edge in one direction, the robot has a small stability margin against tipping in that direction. If it is on an edge, it has zero stability margin against tipping in the direction perpendicular to that edge and towards the outside of the convex hull. It probably has a much larger stability margin against tipping in exactly the opposite direction, because it probably has a large distance to the opposite side of the convex hull.

The ZMP stability criterion states that a motion of the system is dynamically stable if and only if the ZMP location is strictly inside (not on the boundary) of the convex hull of all the contact points. In this case, “the system is stable against a perturbation in the tipping moment of IGE forces in any direction as long as the perturbation is small enough”.

Let us study the ZMP stability margins and stability criterion for all the configurations and cases in Example 3.2:

Example 3.4 *ZMP Stability Margin and ZMP Stability Criterion*

➤ For the first configuration (Figure 3.2):

- Case I, First Configuration: $F = 0$

In this case, the ZMP location is the same as the location of the projection of the system's center of mass on the ground. So, the ZMP stability margin against tipping about either positive or negative z axis is equal to $\underline{L/2}$. Therefore, the ZMP stability criterion declares the system to be stable.

- Case II, First Configuration: $0 < F < \frac{mgL}{2H}$

In this case, the ZMP is located between the projection of the system's center of mass on the ground and point A. So, the ZMP stability margins against tipping about the z axis are: $\underline{x_{ZMP} - (x_A - L)}$ and $\underline{x_A - x_{ZMP}}$. Therefore, the ZMP stability criterion declares the system to be stable.

- Case III, First Configuration: $F = \frac{mgL}{2H}$

In this case, the ZMP coincides with point A. So, the ZMP stability margins against tipping about the z axis are \underline{L} and zero. Therefore, the ZMP stability criterion declares the system to be unstable.

- Case IV, First Configuration: $F > \frac{mgL}{2H}$

As discussed in Section 3.2, this case is impossible according to the ZMP constraint. Since this motion (or configuration) is impossible, the ZMP stability criterion or ZMP stability margin for this case are meaningless.

- For the second configuration (Figure 3.3):

In this case, the ZMP coincides with point A. So, the ZMP stability margin against tipping about the z axis are L and zero. Therefore, the ZMP stability criterion declares the system to be unstable.

- For the third configuration (Figure 3.4):

In this case, the ZMP coincides with point A. So, the ZMP stability margins against tipping about the z axis is zero. Therefore, the ZMP stability criterion declares the system to be unstable.

In short, according to the ZMP constraint, the ZMP location can never exit the convex hull. The ZMP location is on an edge of the convex hull if and only if the robot is either falling or is on the verge of instability. If ZMP location is strictly inside the convex hull, then the system is stable against “a small perturbation in the tipping moment of IGE forces”.

3.5 A Literature Review of ZMP Concepts

The zero-moment point (ZMP) might be one of the most famous terms born in robotics community. The ZMP concepts have been used for improving the stability of numerous legged robots such as ASIMO, developed by Honda Motor Co. in 2000 (Hirose, *et al* 2001). There exist numerous biped robots controlled by the ZMP concepts such as seen in Takanishi, *et al* (1985), Hirose, *et al* (2001), Kaneko, *et al* (2002), Sugahara, *et al* (2004). However, normally a ZMP based motion is initially designed offline and then an online ZMP based motion control is used to modify it. In other words, an additional online feedback control is performed in order to overcome errors resulting from external perturbations. The broadest application of ZMP is in the field of offline motion planning. For offline problems such as in the motion planning of biped robots, ZMP is a very important concept to ensure that the offline calculated motions for the robot are possible and to analyze the dynamic stability of those calculated motions. For example, it has been used in Bachar (2004) as the basis for an offline gait correction algorithm. Other examples for offline motion planning can be seen in Huang, *et al* (2001), Arakawa and Fukuda (1997). Dasgupta and Nakamura (1999) propose a method of generating feasible walking of humanoid robots by converting human motion capture data to a modified version which satisfies a desired ZMP location. Similar to its application in offline problems, ZMP has also been used in the virtual reality fields and in dynamic simulation problems such as in the field of digital human modeling (Xiang, *et al* 2007, 2009; Kim, *et al* 2008; Bhatt, *et al* 2008) to simulate motions of the mechanical systems or analyze their stability.

Impressive advances in the field of ZMP-based biped robots have been witnessed in the recent decades. Examples can be seen in Gienger, Löffler and Pfeiffer (2001) and Park, *et al* (2006). The popularity of ZMP concepts has caused a requirement for their generalization and numerous articles have been published in this field (Garcia, Estremera and Gonzalez de Santos, 2002; Goswami, 1999; Hurmuzlu, G'eno and Brogliato, 2001; Vukobratović, *et al* 1997). ZMP concepts have been the subject of many diverse analyses, but a general unifying idea that offers a solid theoretical background seems to have been lacking so far. In most of the related publications, ZMP location is defined as that point on the horizontal ground at which the net moment of the inertial, gravitational and external (IGE) forces acting on the system (such as a robot or a digital human) has no component along the two horizontal axes (Vukobratović, Borovac, 2004; Sardain, Bessonnet, 2004). Since the net of contact forces equilibrates the IGE forces for dynamic equilibrium, the moment of the net of contact forces is also zero at the ZMP point along the two horizontal axes. Due to that reason, ZMP has also been denoted by the name CoP (Center of Pressure) borrowed from the field of fluid mechanics in several publications such as Sardain, Bessonnet (2004). The ZMP constraint states that during any motion of the system (either stable or unstable), the ZMP location should be inside or on the boundary of the convex hull of all the contact points.

The ZMP concepts can be used in multilegged robots similar to the biped robots. For a biped or multilegged dynamic walking robot, the distance of the ZMP location in each horizontal direction to the edges of the convex hull can be considered as a stability margin against tipping in that direction. This fact was already mentioned in the original

work on ZMP (Vukobratović, Stepanenko, 1972), and has been used implicitly by many researchers (Kalakrishnan, *et al* 2011; Moosavian, Dabiri, 2010; Jindrich, Full, 2002; Kaneko, *et al* 2002). Explicit definition of this ZMP stability margin can be seen, for example, in Huang, *et al* (2001). The ZMP stability criterion states that a motion of the system is dynamically stable if and only if the ZMP location is strictly inside (not on the boundary of) the convex hull of all the contact points (Goswami, Kallem, 2004).

Multilegged robots generally move slowly. Therefore, the net inertial effects can be ignored sometimes and the projection of the CoM (center of mass) on the ground may be considered to be a good approximation of the ZMP. Thus, it can be assumed that the robot maintains balance if the projection of the CoM falls inside the support polygon. The stability margin may be defined as the minimum distance of the vertical projection of CoM to the boundaries of the support pattern on the ground.

ZMP concepts may also be used in fields other than robotics to model the equivalent forces and moments exerted from non-adhesive contacts areas. For example, the contact stability problem has been studied in the community of mechanical assembly to design the optimal fixture, and the methods to determine stability have been proposed in which Coulomb friction is considered (Balkcom, Trinkle, 2002; Pang, Trinkle, 2000; Trinkle, *et al* 1997).

It is essential for robots to move around the conventional human-centered environments that include stairs as a major terrain. But, the conventional ZMP concept is only applicable in the cases where all contact areas are on the same plane. Only a few robots are known to be able to perform stair ascent or descent. Even the successful ones

perform such tasks too slowly (Bae, 2001) or fast enough but in an undisclosed technical manner (Hirai, *et al* 1998). Lim (2007) proposes a dynamic gait pattern suitable for stair walks. Kim, Park, Oh (2009) try to overcome the instabilities of the KHR-2 robot during the stair climbing task. They describe a stair climbing pattern generation and stair climbing stages, and then propose a real-time balance control algorithm which is composed of several online controllers.

There has been an on-going research to generalize the ZMP method for both parallel or non-parallel contact areas on different planes. Harada, *et al* (2003) proposed an approximate method to generalize ZMP to several cases of arm/leg coordination tasks for humanoid robots. Saida, Yokokoji and Yoshikawa (2003) suggest a new criterion instead of ZMP called FSW (Feasible solution of wrench) that shows the feasible condition of forces applied to the robot on rough terrain. Hirukawa, *et al* (2006) also claim that it is not suitable to generalize ZMP for cases other than coplanar contact areas. It proposes a new criterion to determine the “strong stability” and “weak stability” of the foot contact when the robot walks on an arbitrary terrain or when the hands of the robot are in contact with the terrain under the assumption that sufficient friction should exist at the contact. However, to the best of our knowledge, an exact, general method is still lacking to check the possibility or find the margin of stability of a dynamic motion in the general cases of contact surfaces.

3.6 Summary and Conclusion

In this chapter, the ZMP concepts were defined and illustrated using a simple example. It was shown that in the real world, the ZMP constraint is never violated during any motion of a dynamic system including unstable or falling motions. It was also shown that ZMP stability margins and stability criterion are very different from the ZMP constraint and their role is to evaluate the stability of a given motion. Some observations made regarding the relationship of the ZMP constraints with the dynamic equilibrium equations and the moment of IGE forces are summarized as follows:

- 1- The ZMP constraint transforms two equations of the general dynamic equilibrium (out of the 6 force and moment equilibrium equations for the whole system) into inequalities by removing from the equations the contact forces acting on the system. These equations represent the dynamic equilibrium of all the moments exerted on the whole system about the horizontal axes.
- 2- The ZMP constraint specifies the range of values for the tipping (horizontal) components of the net moment of the IGE forces (about any fixed point such as the origin) that are possible in the real world for a dynamic system.

They are important observations which will be used in later chapters.

CHAPTER 4

A THEORETICAL STUDY OF THE ZMP CONCEPTS IN PREDICTIVE DYNAMICS

4.1 Introduction

As noted in Chapter 3, the broadest application of ZMP is in the field of offline motion planning. For offline problems such as in the motion planning of biped robots, ZMP is a very important concept to ensure that the offline calculated motions for the robot are possible and to analyze the dynamic stability of the calculated motions. Similar to its application in offline problems, ZMP has also been used in the virtual reality fields and in dynamic simulation problems such as in the field of digital human modeling (Xiang, *et al* 2007, 2009; Kim, *et al* 2008; Bhatt, *et al* 2008) to simulate possible motions of the mechanical systems or analyze their stability. These works are based on the use of the ZMP concepts in the predictive dynamics method.

Also, as previously mentioned in Sections 3.3 and 3.6, the ZMP constraint is an inequality constraint which can be considered as a conversion of the two equations of the general dynamic equilibrium (out of the 6 force and moment equilibrium equations for the whole system) into inequalities by removing the contact forces acting on the system from the equations. These two are the equations of dynamic equilibrium of the moments of all the forces exerted on the whole system about the two horizontal axes. The ZMP constraint states that during any type of motion for any system, the ZMP should be inside or on the boundary of the convex hull of the ground contact areas. If the ZMP constraint is violated for a system at an instant of time during an arbitrary motion, then the tipping (horizontal) components of the net moment of the IGE (inertial, gravity, external) forces

(about any fixed point such as the origin) calculated for that motion are impossible values in the real world at that instant of time (in order for these two components to have values that are possible in the real world, the ZMP constraint should be satisfied.). Therefore, that arbitrary motion is impossible in the real world.

In predictive dynamics, for any given motion, the IGE forces acting on the system are known. These IGE forces are cancelled by the system's contact forces to ensure dynamic equilibrium of all the forces acting on the system at any instant of motion. The contact forces are initially unknown. In the ZMP method in predictive dynamics, it is first checked whether it is possible to generate such a motion by the system's contact areas by imposing the ZMP constraint. In the second step, the contact forces are calculated.

In other words, before calculating the contact forces, the ZMP constraint checks whether it is possible at all to find any set of unilateral contact forces acting from the environment on the system's contact areas to balance the given IGE forces. However, ZMP constraint alone cannot ensure that in general. In the theorems that appear in Section 4.2, we enhance the ZMP constraint by adding a complementary constraint to it which requires the vertical component of the IGE forces to be downwards. We will prove that the ZMP constraint used along with this additional constraint ensure that the given motion is possible for a system with the given contact areas (if all the system's contact areas are on a same plane and the environment can only exert unilateral distributed contact forces on them). In more exact words, the ZMP constraint used along with this additional constraint ensure that it will be theoretically possible in the second step to find unilateral contact forces acting from the environment on the system's contact areas to

balance the IGE forces. In this way, we give the ZMP constraint a more distinctive role in predictive dynamics calculations.

Sections 4.4, 4.5 and 4.6 present the general algorithms that have been initially developed to model the contact of the digital human with the ground in predictive dynamics using the ZMP concepts. The validity and accuracy of the ZMP-based approach is initially addressed in this chapter and will be further studied in Chapter 7.

4.2 Theorems on the ZMP Constraint

As explained in Chapter 3, the ZMP constraint is defined for a system (such as a robot or a digital human) having several non-adhesive contact areas with the horizontal ground. Non-adhesiveness of the contact areas means that the distributed forces on them cannot have any arbitrary value. These distributed forces have to be unilateral (compressive) and also have to obey the coulomb friction laws. It is also assumed that all the contact areas of this system with the environment considered in the ZMP approach are on one horizontal plane or the ground (it can be generalized so that it is applicable to cases of inclined contact areas which are all co-planar). ZMP is defined as that point on the ground at which the net moment of the IGE acting on the system has no component along two horizontal axes (Vukobratović, Stepanenko, 1972).

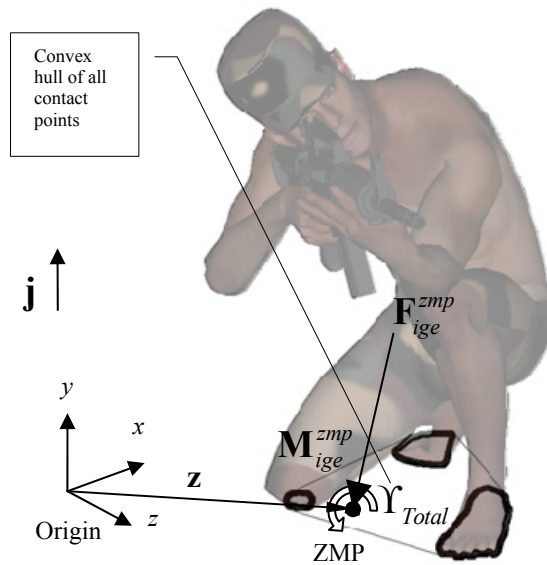


Figure 4.1. Schematic of the contact areas, the convex hull of all the contact points and the ZMP in a motion frame in the "Aiming While Kneeling" task

Figure 4.1 shows a sample frame of motion in the motion of a digital human. Let us define the global coordinate frame zxy attached to the ground with the unit vector along the y axis perpendicular to the ground ($\mathbf{j} = \mathbf{k} \times \mathbf{i}$). The symbols used in the figure are defined as follows:

- 1- The ZMP location is denoted by the vector \mathbf{z} .
- 2- \mathbf{F}_{ige}^{zmp} and \mathbf{M}_{ige}^{zmp} denote the net equivalent force and moment of IGE forces acting at the ZMP.
- 3- Γ_{Total} denotes the set of all the contact points of the dynamic system (digital human) with the ground.
- 4- Υ_{Total} denotes the convex hull of Γ_{Total} .

4.2.1. ZMP Constraint and the Unilaterality of Ground Reaction Forces

Previously, we discussed (in Sections 3.3, 3.6 and 4.1) the relation of the ZMP constraint with the dynamic equilibrium equations and the moment of IGE forces using an example. The purpose was to show the significance of the ZMP concepts regarding a given motion of a system while paying little attention to the location of environmental contact forces. Those observations will mostly be used in Chapters 9 and 10 for the generalization of ZMP concepts.

The ZMP constraint alone does not ensure the unilaterality of the vertical component of the ground reaction forces. In this section, we present a theorem which shows that an additional constraint is required besides the ZMP constraint to ensure the unilaterality of ground reaction forces. This theorem shows the role that the ZMP constraint plays in ensuring the unilaterality of ground reaction forces.

Theorem 4.1: *ZMP Constraint and the Unilaterality of Ground Reaction Forces*

Consider a system having external contact areas only with the same horizontal plane (the ground). For example, consider the problem depicted in Figure 4.1 with some of its features shown again in Figure 4.2. Let \mathbf{f}_c denote the distributed contact forces at \mathbf{r} inside Γ_{Total} (all contact areas) applied from the ground on the system (the z - x plane). For any arbitrary \mathbf{F}_{ige}^{zmp} and \mathbf{M}_{ige}^{zmp} acting on this system at the ZMP (at location \mathbf{z}), the following two statements are equivalent (they are necessary and sufficient conditions for each other, or one can conclude statement 1 from 2 and vice versa.) :

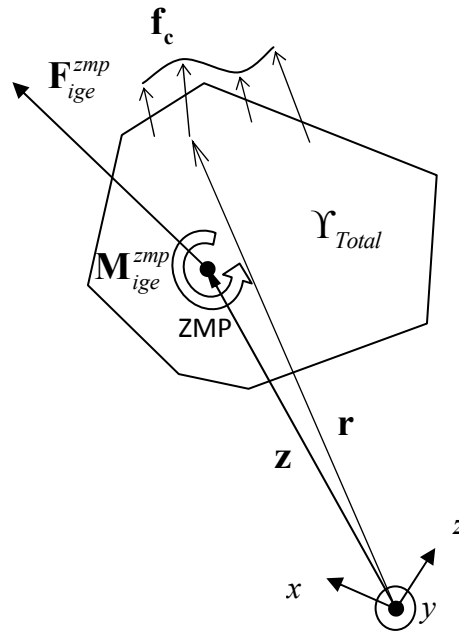


Figure 4.2. Distributed contact forces and the net force and moment of inertial, gravitational and external forces at the ZMP

- 1- The ZMP is inside the convex hull of all the contact points (Υ_{Total}) and $\mathbf{F}_{ige}^{zmp} \cdot \mathbf{j} \leq 0$.
- 2- It is possible to find unilaterally distributed contact forces \mathbf{f}_c with $\mathbf{f}_c \cdot \mathbf{j} \geq 0$ inside the set of all the contact points Γ_{Total} that can equilibrate \mathbf{F}_{ige}^{zmp} and \mathbf{M}_{ige}^{zmp} .

Proof:

Part A) Assume statement 1 holds, we prove statement 2:

The proof method we use in this part is a constructive proof, i.e. we provide a method for creating the distributed forces \mathbf{f}_c that can cancel the force system \mathbf{F}_{ige}^{zmp} and \mathbf{M}_{ige}^{zmp} acting

at the ZMP (location \mathbf{z}). We construct 3 different subsets of \mathbf{f}_c called $\mathbf{w}_a, \mathbf{w}_b, \mathbf{w}_c$. One subset (\mathbf{w}_a) is for canceling \mathbf{F}_{ige}^{zmp} without producing any equivalent moment about the ZMP and the 2 other subsets ($\mathbf{w}_b, \mathbf{w}_c$) are for canceling \mathbf{M}_{ige}^{zmp} without producing any equivalent force. These three subsets satisfy the following conditions:

$$\begin{cases} \{\mathbf{w}_a\} \cap \{\mathbf{w}_b\} = \{\mathbf{w}_a\} \cap \{\mathbf{w}_c\} = \{\mathbf{w}_b\} \cap \{\mathbf{w}_c\} = \phi \\ \{\mathbf{w}_a\} \cup \{\mathbf{w}_b\} \cup \{\mathbf{w}_c\} = \{\mathbf{f}_c\} \end{cases} \quad (4.2.1)$$

Constructing \mathbf{w}_a :

The first subset of \mathbf{f}_c called \mathbf{w}_a can be constructed as follows:

Case 1: When ZMP is a contact point (it is inside Γ_{Total} ; i.e., inside one contact area):

Assume all distributed forces \mathbf{w}_a to be concentrated at the ZMP and all have exactly opposite directions to \mathbf{F}_{ige}^{zmp} . Although there is a constraint ($\mathbf{f}_c \cdot \mathbf{j} \geq 0 \Rightarrow \mathbf{w}_a \cdot \mathbf{j} \geq 0$), it is always possible to do so because $\mathbf{F}_{ige}^{zmp} \cdot \mathbf{j} \leq 0$.

It is also obvious that it is possible to select the magnitudes of \mathbf{w}_a such that:

$$\mathbf{F}_{ige}^{zmp} + \int_{\Gamma_{Total}} \mathbf{w}_a dA = \mathbf{0} \quad (4.2.2)$$

Also because \mathbf{w}_a is located at the ZMP, \mathbf{w}_a will produce no moment about the ZMP.

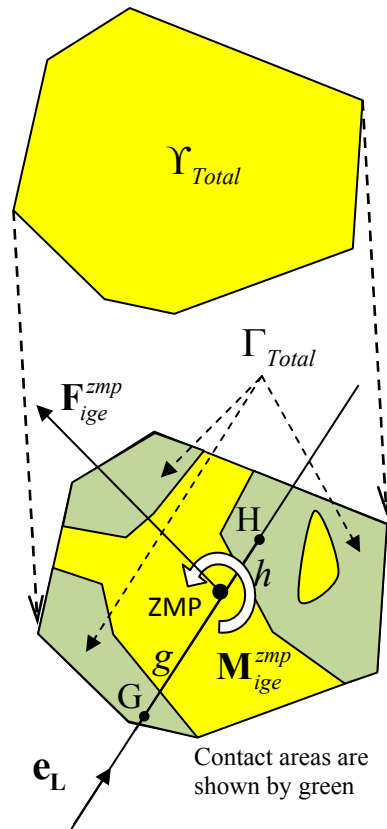


Figure 4.3. Proving statement 2 when ZMP is inside the convex hull, but not a contact point

Case 2: When ZMP is not a contact point (it is inside Y_{Total} , but not inside Γ_{Total}):

The convex hull of all contact areas Y_{Total} which was previously shown in Figure 4.2 is repeated in Figure 4.3 and identified in yellow. The set of contact areas Γ_{Total} (which are a subset of Y_{Total}) are shown by another color (green), overlaid on the yellow colored areas. Therefore, the green areas in this figure denote points that belong to both Y_{Total} and Γ_{Total} , while the yellow areas only belong to Y_{Total} but not Γ_{Total} . It is possible to find a line that passes through the ZMP and contains two arbitrary contact points G and H

in Γ_{Total} . Let us denote the unit vector along that line by \mathbf{e}_L . In this case, ZMP would be located between G and H. Let us denote the distance from the ZMP to G and H by g and h . We assume \mathbf{w}_a to be composed of two subsets \mathbf{w}_{a_G} and \mathbf{w}_{a_H} such that:

$$\{\mathbf{w}_{a_G}\} \cap \{\mathbf{w}_{a_H}\} = \phi, \{\mathbf{w}_{a_G}\} \cup \{\mathbf{w}_{a_H}\} = \{\mathbf{w}_a\} \quad (4.2.3)$$

Assume all distributed forces \mathbf{w}_{a_G} to be concentrated at the point G and all have exactly opposite directions to \mathbf{F}_{ige}^{zmp} . It is obvious that it is possible to select the magnitudes of \mathbf{w}_{a_G} such that:

$$\mathbf{F}_{ige}^{zmp} \frac{h}{g+h} + \int_{\Gamma_{Total}} \mathbf{w}_{a_G} dA = \mathbf{0} \quad (4.2.4)$$

Assume all distributed forces \mathbf{w}_{a_H} to be concentrated at the point H and all have exactly opposite directions to \mathbf{F}_{ige}^{zmp} . It is obvious that it is possible to select the magnitudes of \mathbf{w}_{a_H} such that:

$$\mathbf{F}_{ige}^{zmp} \frac{g}{g+h} + \int_{\Gamma_{Total}} \mathbf{w}_{a_H} dA = \mathbf{0} \quad (4.2.5)$$

So, the set \mathbf{w}_a exactly cancels \mathbf{F}_{ige}^{zmp} but will produce no equivalent moment about the ZMP, as shown below:

$$\begin{aligned} \mathbf{F}_{ige}^{zmp} + \int_{\Gamma_{Total}} \mathbf{w}_a dA &= \mathbf{F}_{ige}^{zmp} + \int_{\Gamma_{Total}} \mathbf{w}_{a_G} dA + \int_{\Gamma_{Total}} \mathbf{w}_{a_H} dA \\ &= \mathbf{F}_{ige}^{zmp} - \mathbf{F}_{ige}^{zmp} \frac{h}{g+h} - \mathbf{F}_{ige}^{zmp} \frac{g}{g+h} = \mathbf{0} \end{aligned} \quad (4.2.6)$$

$$\begin{aligned} \mathbf{M}_{\mathbf{w}_a, ZMP} &= g\mathbf{e}_L \times \int_{\Gamma_{Total}} \mathbf{w}_{a_G} dA - h\mathbf{e}_L \times \int_{\Gamma_{Total}} \mathbf{w}_{a_H} dA \\ &= g\mathbf{e}_L \times \mathbf{F}_{ige}^{zmp} \frac{h}{g+h} - h\mathbf{e}_L \times \mathbf{F}_{ige}^{zmp} \frac{g}{g+h} = \mathbf{0} \end{aligned} \quad (4.2.7)$$

Constructing $\mathbf{w}_b, \mathbf{w}_c$:

The second and third subsets of \mathbf{f}_c respectively called $\mathbf{w}_b, \mathbf{w}_c$ can be considered to be concentrated at two locations $\mathbf{r}_b, \mathbf{r}_c$ inside Γ_{Total} and acting along $\mathbf{j} \times (\mathbf{r}_b - \mathbf{r}_c), -\mathbf{j} \times (\mathbf{r}_b - \mathbf{r}_c)$ (in the $z-x$ plane, normal to $\mathbf{r}_b, \mathbf{r}_c$). So, they are all planar (frictional) distributed forces ($\mathbf{w}_b \cdot \mathbf{j} = 0, \mathbf{w}_c \cdot \mathbf{j} = 0$). It is possible to select the magnitudes of $\mathbf{w}_b, \mathbf{w}_c$ such that:

$$\int_{\Gamma_{Total}} \|\mathbf{w}_b\| dA = \int_{\Gamma_{Total}} \|\mathbf{w}_c\| dA = \frac{-\|\mathbf{M}_{ige}^{zmp}\|}{\|\mathbf{r}_b - \mathbf{r}_c\|} \quad (4.2.8)$$

Therefore, the distributed forces \mathbf{w}_b and \mathbf{w}_c are equivalent to a couple (same magnitude and opposite directions) that exactly cancels \mathbf{M}_{ige}^{zmp} without producing any equivalent force, as shown below:

$$\mathbf{w}_b = \|\mathbf{w}_b\| \left(\frac{\mathbf{j} \times (\mathbf{r}_b - \mathbf{r}_c)}{\|\mathbf{r}_b - \mathbf{r}_c\|} \right), \quad \mathbf{w}_c = \|\mathbf{w}_c\| \left(\frac{-\mathbf{j} \times (\mathbf{r}_b - \mathbf{r}_c)}{\|\mathbf{r}_b - \mathbf{r}_c\|} \right) \quad (4.2.9)$$

$$\mathbf{M}_{\mathbf{w}_b} + \mathbf{M}_{\mathbf{w}_c} = \mathbf{r}_b \times \int_{\Gamma_{Total}} \mathbf{w}_b dA + \mathbf{r}_c \times \int_{\Gamma_{Total}} \mathbf{w}_c dA \quad (4.2.10)$$

$$\Rightarrow \mathbf{M}_{\mathbf{w}_b} + \mathbf{M}_{\mathbf{w}_c} = \mathbf{r}_b \times \left(\int_{\Gamma_{Total}} \|\mathbf{w}_b\| \frac{\mathbf{j} \times (\mathbf{r}_b - \mathbf{r}_c)}{\|\mathbf{r}_b - \mathbf{r}_c\|} dA \right) + \mathbf{r}_c \times \left(\int_{\Gamma_{Total}} \|\mathbf{w}_c\| \frac{-\mathbf{j} \times (\mathbf{r}_b - \mathbf{r}_c)}{\|\mathbf{r}_b - \mathbf{r}_c\|} dA \right) \quad (4.2.11)$$

$$\Rightarrow \mathbf{M}_{\mathbf{w}_b} + \mathbf{M}_{\mathbf{w}_c} = \left(\left(\int_{\Gamma_{Total}} \|\mathbf{w}_b\| dA \right) \mathbf{r}_b - \left(\int_{\Gamma_{Total}} \|\mathbf{w}_c\| dA \right) \mathbf{r}_c \right) \times \left(\frac{\mathbf{j} \times (\mathbf{r}_b - \mathbf{r}_c)}{\|\mathbf{r}_b - \mathbf{r}_c\|} \right)$$

$$\Rightarrow \mathbf{M}_{\mathbf{w}_b} + \mathbf{M}_{\mathbf{w}_c} = \frac{-\|\mathbf{M}_{ige}^{zmp}\|}{\|\mathbf{r}_b - \mathbf{r}_c\|} (\mathbf{r}_b - \mathbf{r}_c) \times \left(\frac{\mathbf{j} \times (\mathbf{r}_b - \mathbf{r}_c)}{\|\mathbf{r}_b - \mathbf{r}_c\|} \right)$$

$$\Rightarrow \mathbf{M}_{\mathbf{w}_b} + \mathbf{M}_{\mathbf{w}_c} = \frac{-\|\mathbf{M}_{ige}^{zmp}\|}{\|\mathbf{r}_b - \mathbf{r}_c\|} \frac{(\mathbf{r}_b - \mathbf{r}_c) \times \mathbf{j} \times (\mathbf{r}_b - \mathbf{r}_c)}{\|\mathbf{r}_b - \mathbf{r}_c\|}$$

$$\Rightarrow \mathbf{M}_{\mathbf{w}_b} + \mathbf{M}_{\mathbf{w}_c} = \frac{-\|\mathbf{M}_{ige}^{zmp}\|}{\|\mathbf{r}_b - \mathbf{r}_c\|} \frac{\overbrace{((\mathbf{r}_b - \mathbf{r}_c) \cdot (\mathbf{r}_b - \mathbf{r}_c))}^{\|\mathbf{r}_b - \mathbf{r}_c\|^2} \mathbf{j} - \overbrace{((\mathbf{r}_b - \mathbf{r}_c) \cdot \mathbf{j})}^0 (\mathbf{r}_b - \mathbf{r}_c)}{\|\mathbf{r}_b - \mathbf{r}_c\|}$$

$$\Rightarrow \mathbf{M}_{\mathbf{w}_b} + \mathbf{M}_{\mathbf{w}_c} = \frac{-\|\mathbf{M}_{ige}^{zmp}\|}{\|\mathbf{r}_b - \mathbf{r}_c\|} \|\mathbf{r}_b - \mathbf{r}_c\| \mathbf{j} = -\|\mathbf{M}_{ige}^{zmp}\| \mathbf{j}$$

$$\text{Definition of ZMP} \Rightarrow \quad \mathbf{M}_{ige}^{zmp} \text{ is along } \mathbf{j} \Rightarrow \quad \left. \begin{array}{l} \|\mathbf{M}_{ige}^{zmp}\| \mathbf{j} = \mathbf{M}_{ige}^{zmp} \end{array} \right\}$$

$$\Rightarrow \mathbf{M}_{\mathbf{w}_b} + \mathbf{M}_{\mathbf{w}_c} = -\mathbf{M}_{ige}^{zmp} \quad (4.2.12)$$

Also,

$$\mathbf{F}_{\mathbf{w}_b} + \mathbf{F}_{\mathbf{w}_c} = \int_{\Gamma_{Total}} \mathbf{w}_b dA + \int_{\Gamma_{Total}} \mathbf{w}_c dA$$

$$\Rightarrow \mathbf{F}_{\mathbf{w}_b} + \mathbf{F}_{\mathbf{w}_c} = \int_{\Gamma_{Total}} \|\mathbf{w}_b\| \frac{\mathbf{j} \times (\mathbf{r}_b - \mathbf{r}_c)}{\|\mathbf{r}_b - \mathbf{r}_c\|} dA + \int_{\Gamma_{Total}} \|\mathbf{w}_c\| \frac{-\mathbf{j} \times (\mathbf{r}_b - \mathbf{r}_c)}{\|\mathbf{r}_b - \mathbf{r}_c\|} dA$$

$$\begin{aligned}
\Rightarrow \quad \mathbf{F}_{\mathbf{w}_b} + \mathbf{F}_{\mathbf{w}_c} &= \left(\int_{\Gamma_{Total}} \|\mathbf{w}_b\| dA - \int_{\Gamma_{Total}} \|\mathbf{w}_c\| dA \right) \left(\frac{\mathbf{j} \times (\mathbf{r}_b - \mathbf{r}_c)}{\|\mathbf{r}_b - \mathbf{r}_c\|} \right) \\
\Rightarrow \quad \mathbf{F}_{\mathbf{w}_b} + \mathbf{F}_{\mathbf{w}_c} &= \left(-\frac{\|\mathbf{M}_{ige}^{zmp}\|}{\|\mathbf{r}_b - \mathbf{r}_c\|} + \frac{\|\mathbf{M}_{ige}^{zmp}\|}{\|\mathbf{r}_b - \mathbf{r}_c\|} \right) \left(\frac{\mathbf{j} \times (\mathbf{r}_b - \mathbf{r}_c)}{\|\mathbf{r}_b - \mathbf{r}_c\|} \right) \\
\Rightarrow \quad \mathbf{F}_{\mathbf{w}_b} + \mathbf{F}_{\mathbf{w}_c} &= \mathbf{0} \tag{4.2.13}
\end{aligned}$$

Therefore, the set of distributed forces \mathbf{f}_c that we constructed by the subsets $\mathbf{w}_a, \mathbf{w}_b, \mathbf{w}_c$ cancels \mathbf{F}_{ige}^{zmp} and \mathbf{M}_{ige}^{zmp} .

Part B) Assume statement 2 holds, we prove statement 1:

Part B-1) Proving that ZMP is "not" outside the convex hull (proof by contradiction):

As shown in Figure 4.4, if ZMP is outside the convex hull of the contact areas Υ_{Total} , consider the nearest edge of the convex hull to the ZMP. Due to the definition of the convex hull, if you draw a line parallel to that edge, the line will not intersect the convex hull and the convex hull will lie on one side of the line. Now, define a unit vector \mathbf{u} perpendicular to this line and pointing from the ZMP to the convex hull. Then it is obvious that for any point Q in the convex hull, located at \mathbf{r} :

$$(\mathbf{r} - \mathbf{z}) \cdot \mathbf{u} > 0 \quad \text{and} \quad \mathbf{u} \cdot \mathbf{j} = 0 \tag{4.2.14}$$

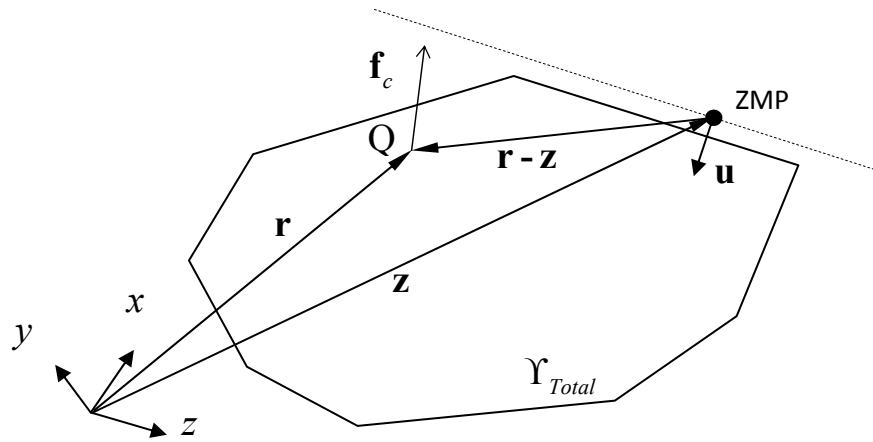


Figure 4.4. Part (B-1) of the proof: proving that it is impossible for ZMP to be outside the convex hull if contact forces are non-adhesive

$$\begin{aligned}
 \mathbf{M}_{ige}^{zmp} + \int_{Y_{Total}} (\mathbf{r} - \mathbf{z}) \times \mathbf{f}_c \, dA = \mathbf{0} \quad , \quad \mathbf{M}_{ige}^{zmp} \times \mathbf{j} = \mathbf{0} &\Rightarrow \int_{Y_{Total}} (\mathbf{r} - \mathbf{z}) \times \mathbf{f}_c \, dA \times \mathbf{j} = \mathbf{0} \\
 (4.2.14) \quad \Rightarrow \int_{Y_{Total}} \left[\underbrace{(\mathbf{j} \cdot (\mathbf{r} - \mathbf{z}))}_0 \mathbf{f}_c - (\mathbf{j} \cdot \mathbf{f}_c)(\mathbf{r} - \mathbf{z}) \right] dA = \mathbf{0} \\
 \Rightarrow \int_{Y_{Total}} (\mathbf{f}_c \cdot \mathbf{j})(\mathbf{r} - \mathbf{z}) \, dA = \mathbf{0} \\
 \stackrel{\mathbf{u}}{\Rightarrow} \int_{Y_{Total}} (\mathbf{f}_c \cdot \mathbf{j})((\mathbf{r} - \mathbf{z}) \cdot \mathbf{u}) \, dA = 0 \quad (4.2.15)
 \end{aligned}$$

For any point on Y_{Total} we have :

$$\begin{aligned}
 \left\{ \begin{array}{l} \text{Statement 2} \Rightarrow \mathbf{f}_c \cdot \mathbf{j} \geq 0 \\ (4.2.14) \Rightarrow (\mathbf{r} - \mathbf{z}) \cdot \mathbf{u} > 0 \quad (\text{If ZMP is outside the convex hull}) \end{array} \right. \\
 \Rightarrow \int_{Y_{Total}} (+)(+) \, dA = 0 \quad : \quad \text{Impossible!}
 \end{aligned}$$

So, using proof by contradiction, we proved that ZMP is "not" outside the convex hull.

Part B-2) Proof of $\mathbf{F}_{ige}^{zmp} \cdot \mathbf{j} \leq 0$:

$$\mathbf{F}_{ige}^{zmp} + \int_{Y_{Total}} \mathbf{f}_c dA = \mathbf{0} \quad , \quad \mathbf{f}_c \cdot \mathbf{j} \geq 0 \quad \Rightarrow \quad \mathbf{F}_{ige}^{zmp} \cdot \mathbf{j} \leq 0$$

The results of Part B-1 and Part B-2 prove that statement 1 holds.

Therefore, based on Theorem 4.1, ZMP constraint indicates that during any type of motion for any system, if the ZMP is located outside the convex hull of all the ZMP contact areas Y_{Total} , then that motion is impossible in the real world. That is because we will not be able to find non-adhesive contact forces for equilibrating \mathbf{F}_{ige}^{zmp} and \mathbf{M}_{ige}^{zmp} . If it is inside the convex hull and the component of \mathbf{F}_{ige}^{zmp} in the y direction is not upwards, then one can find unilateral distributed contact forces (or their equivalent concentrated forces and moments) that can equilibrate the IGE forces associated with the given motion and therefore, it is possible to generate that motion by using the given contact areas.

4.2.2. ZMP Location and the Location of Ground Reaction Forces

In this subsection, we present a less important theorem which shows that ZMP is on an edge of the convex hull, if and only if all distributed ground reaction force are on that edge.

Theorem 4.2: ZMP Location and the Location of Ground Reaction Forces

Consider a dynamic system having external contact areas in the same horizontal plane (the ground). For example, consider the problem depicted in Figures 4.1 and 4.2 with some of its features shown again in Figure 4.5. For any arbitrary \mathbf{F}_{ige}^{zmp} and \mathbf{M}_{ige}^{zmp} acting at location \mathbf{z} on this system, the following two statements are equivalent:

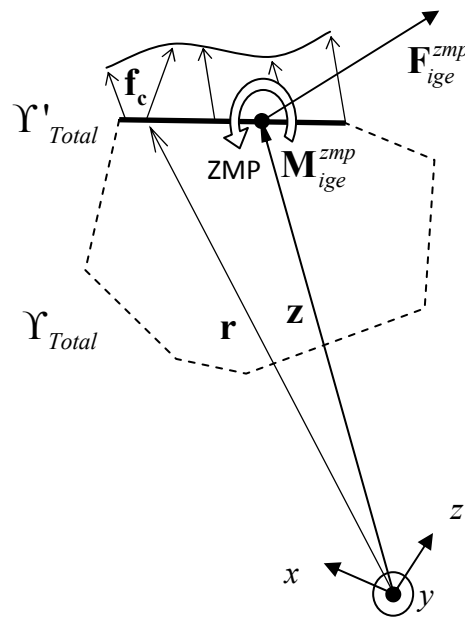


Figure 4.5. Distributed contact forces and the net force and moment of inertial, gravitational and external forces at the ZMP on an edge of the convex hull of all contact points

1- The ZMP is on the edge Υ'_{Total} of the convex hull of all the contact points and

$$\mathbf{F}_{ige}^{zmp} \cdot \mathbf{j} \leq 0 .$$

2- The unilateral distributed contact forces \mathbf{f}_c which equilibrate \mathbf{F}_{ige}^{zmp} and \mathbf{M}_{ige}^{zmp}

(according to Theorem 4.1), are only on the edge Υ'_{Total} of the convex hull (no \mathbf{f}_c can

exist outside Υ'_{Total}), for all $\mathbf{f}_c \cdot \mathbf{j} \neq 0$. (the trivial condition $\mathbf{f}_c \cdot \mathbf{j} \neq 0$ is equivalent to $\mathbf{f}_c \neq 0$, due to coulomb friction law, and can be ignored).

Proof:

Part A)

Assume statement 1 holds, we prove statement 2:

Part A-1) Proving that: \mathbf{f}_c "can be found on" Υ'_{Total} to equilibrate \mathbf{F}_{ige}^{zmp} and \mathbf{M}_{ige}^{zmp} :

The proof is exactly the same as Part A of Theorem 4.1, if we consider edge Υ'_{Total} instead of area Υ_{Total} in that part.

Part A-2) Proving that: \mathbf{f}_c are "only" on the edge Υ'_{Total} :

In this part, we need to prove that no non-adhesive \mathbf{f}_c can exist outside edge Υ'_{Total} .

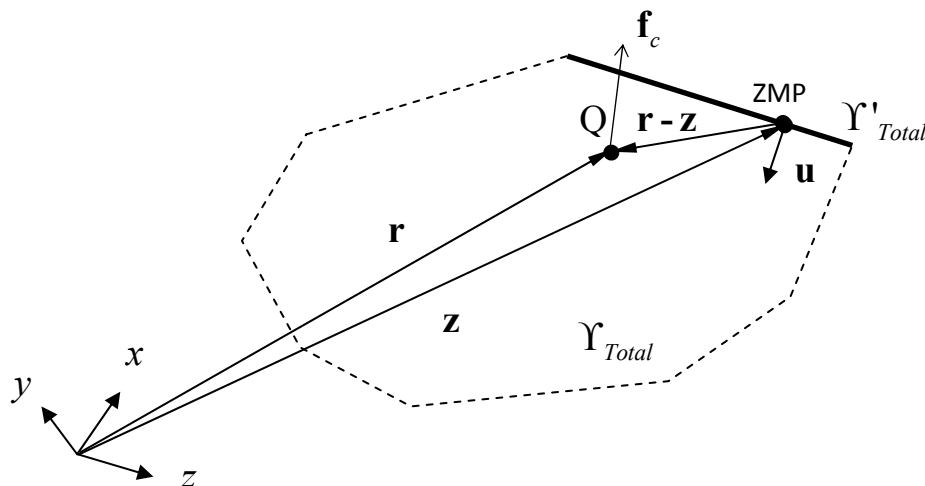


Figure 4.6. Part (A-2) of the proof: proving that if ZMP is on an edge of the convex hull of contact points, then no contact force can exist outside that edge

The ZMP is located at \mathbf{z} on edge Υ'_{Total} . As shown in Figure 4.6, let us define a unit vector \mathbf{u} pointing from the ZMP towards the inside of the convex hull, perpendicular to edge Υ'_{Total} . Due to the definition of the convex hull, for any point Q inside the convex hull located at \mathbf{r} :

$$\begin{aligned}
 \mathbf{M}_{ige}^{zmp} + \int_{\Upsilon'_{Total}} (\mathbf{r} - \mathbf{z}) \times \mathbf{f}_c dA &= \mathbf{0} \quad , \quad \mathbf{M}_{ige}^{zmp} \times \mathbf{j} = \mathbf{0} \\
 \Rightarrow \int_{\Upsilon'_{Total}} (\mathbf{r} - \mathbf{z}) \times \mathbf{f}_c dA \times \mathbf{j} &= \mathbf{0} \\
 \Rightarrow \int_{\Upsilon'_{Total}} \left[\underbrace{(\mathbf{j} \cdot (\mathbf{r} - \mathbf{z}))}_0 \mathbf{f}_c - (\mathbf{j} \cdot \mathbf{f}_c)(\mathbf{r} - \mathbf{z}) \right] dA &= \mathbf{0} \\
 \Rightarrow \int_{\Upsilon'_{Total}} (\mathbf{f}_c \cdot \mathbf{j})(\mathbf{r} - \mathbf{z}) dA &= \mathbf{0} \quad (4.2.16)
 \end{aligned}$$

$$\begin{aligned}
 \Rightarrow \int_{\Upsilon'_{Total}} (\mathbf{f}_c \cdot \mathbf{j})(\mathbf{r} - \mathbf{z}) \cdot \mathbf{u} dA &= 0 \\
 \text{For any point } Q, \text{ we have: } & \left. \begin{aligned} (\mathbf{r} - \mathbf{z}) \cdot \mathbf{u} \geq 0 \quad \text{and} \quad \mathbf{f}_c \cdot \mathbf{j} > 0 \end{aligned} \right\}
 \end{aligned}$$

$$\Rightarrow \text{For any point } Q, \text{ we should have: } \quad (\mathbf{r} - \mathbf{z}) \cdot \mathbf{u} = 0$$

$$\Rightarrow \text{No } \mathbf{f}_c \text{ exists outside edge } \Upsilon'_{Total}$$

The results of Part A-1 and Part A-2 prove that statement 2 holds.

Part B) Assume statement 2 holds, we prove statement 1:

Part B-1) Proving that ZMP is on the edge of the convex hull (proof by contradiction):

As shown in Figure 4.7, if ZMP is not on edge Υ'_{Total} , define a unit vector \mathbf{u} pointing from the ZMP towards the edge Υ'_{Total} , perpendicular to edge Υ'_{Total} and on the ground. Then it is obvious that for any point Q on edge Υ'_{Total} , located at \mathbf{r} :

$$(\mathbf{r} - \mathbf{z}) \cdot \mathbf{u} > 0 \quad \text{And} \quad \mathbf{u} \cdot \mathbf{j} = 0 \quad (4.2.17)$$

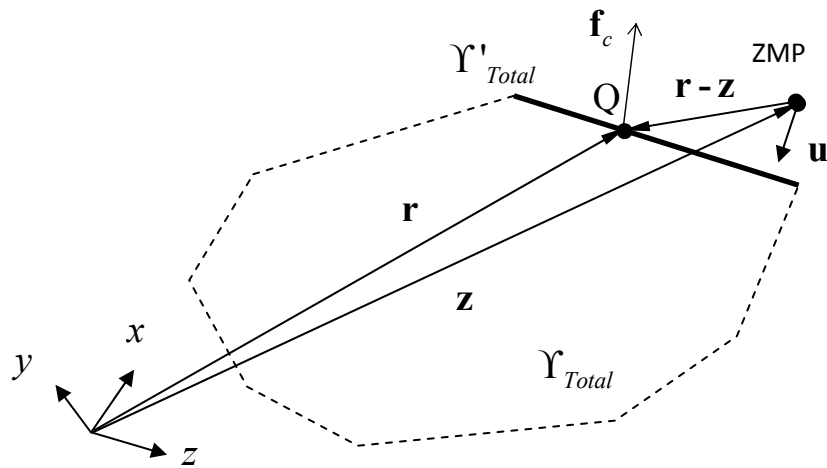


Figure 4.7. Part (B-1) of the proof: proving that if all contact forces are on an edge then ZMP is on that edge

$$\begin{aligned} \mathbf{M}_{ige}^{zmp} + \int_{\Upsilon'_{Total}} (\mathbf{r} - \mathbf{z}) \times \mathbf{f}_c dA = \mathbf{0} \quad , \quad \mathbf{M}_{ige}^{zmp} \times \mathbf{j} = \mathbf{0} \\ \Rightarrow \int_{\Upsilon'_{Total}} (\mathbf{r} - \mathbf{z}) \times \mathbf{f}_c dA \times \mathbf{j} = \mathbf{0} \quad \Rightarrow \quad \int_{\Upsilon'_{Total}} \left[\underbrace{(\mathbf{j} \cdot (\mathbf{r} - \mathbf{z}))}_0 \mathbf{f}_c - (\mathbf{j} \cdot \mathbf{f}_c)(\mathbf{r} - \mathbf{z}) \right] dA = \mathbf{0} \end{aligned}$$

$$\Rightarrow \int_{\Upsilon'_{Total}} (\mathbf{f}_c \cdot \mathbf{j})(\mathbf{r} - \mathbf{z}) dA = \mathbf{0} \quad (4.2.18)$$

$$\Rightarrow \int_{\Upsilon'_{Total}} (\mathbf{f}_c \cdot \mathbf{j})((\mathbf{r} - \mathbf{z}) \cdot \mathbf{u}) dA = 0 \quad (4.2.19)$$

For any point on Υ'_{Total} we have :

$$\left. \begin{array}{l} \text{Statement 2} \Rightarrow \mathbf{f}_c \cdot \mathbf{j} > 0 \\ (4.2.17) \Rightarrow (\mathbf{r} - \mathbf{z}) \cdot \mathbf{u} > 0 \quad (\text{If ZMP is not on the edge}) \end{array} \right\}$$

$$\Rightarrow \int_{\Upsilon'_{Total}} (+)(+) dA = 0 \quad : \quad \text{Impossible!}$$

Thus, ZMP is on the edge of the convex hull.

Part B-2) Proof of $\mathbf{F}_{ige}^{zmp} \cdot \mathbf{j} \leq 0$:

$$\mathbf{F}_{ige}^{zmp} + \int_{\Upsilon'_{Total}} \mathbf{f}_c dA = \mathbf{0} \quad , \quad \mathbf{f}_c \cdot \mathbf{j} \geq 0 \quad \Rightarrow \quad \mathbf{F}_{ige}^{zmp} \cdot \mathbf{j} \leq 0$$

The results of Part B-1 and Part B-2 prove that statement 1 holds.

4.3 Application and the Significance of the ZMP Constraint in Predictive Dynamics

In predictive dynamics, the constraints in the optimization problem represent three type of limitations. These three are the limitations of the environment, the digital human model and the task being modeled. Design variables are the joint angle profiles. Based on the value of design variables, the kinematic analysis of the model is carried out using the Denavit-Hartenberg method. Let us assume that a set of design variables produces an arbitrary motion of the digital human denoted by Θ .

In the ZMP method, it is assumed that the digital human has several non-adhesive contact areas with the horizontal ground. All the forces except the ground reaction forces are known, which are the IGE forces. The possibility of generation of the arbitrary motion Θ by using the given ground contact areas is ensured by using the ZMP constraint. According to Theorem 4.1, when ZMP constraint is satisfied, we are sure that it is possible to find unilateral distributed contact forces on those contact areas to cancel (equilibrate) \mathbf{F}_{ige}^{zmp} and \mathbf{M}_{ige}^{zmp} . In other words, neglecting the limitations of the digital human and the motion task, when ZMP constraint is satisfied, we are sure that it is possible to generate the arbitrary motion Θ using the given contact areas if enough friction exists on them.

A force vector and a moment vector equivalent to the distributed contact forces are considered to act on the digital human from each contact area. After the ZMP constraint ensures that it is possible to find unilateral distributed contact forces to generate the arbitrary motion Θ , the equivalent contact reaction force and moment

vectors at each contact area can be calculated. In general, if we have more than one contact area, these equivalent contact reaction force and moment vectors will be indeterminate and may be considered as unknown values (design variables). They just need to satisfy the six global force and moment equilibrium equations. But in the ZMP method, the normal practice has been to assume that the global equivalent contact forces and moments (which should equilibrate IGE forces and moments to ensure dynamic equilibrium) are partitioned on contact areas based on the distances of the contact areas from the ZMP. This method and the justification for such assumptions are explained in details in Section 4.6. Using these equivalent ground reaction forces and moments, the required torques at all joints are calculated by the recursive Lagrangian formulation.

4.4 Ground Contact Modeling in the ZMP Method

For any dynamic system such as the digital human, the possibility of motion and the dynamic stability of motion depend on the contact areas of the system with the environment. Also, the values of the ground reaction forces and moments exerted on the digital human by each individual contact area will be used in the calculation of actuation torques at the joints of the digital human. Based on the ZMP concepts used in predictive dynamics, generalized programming structures and modules have been developed by the author for the definition and calculation of reaction forces and moments exerted from individual ground contact areas on the digital human. The ZMP constraint and the ZMP stability margin are also defined and implemented in the predictive dynamics code. The

ground reaction forces and moments are not considered as design variables in this formulation. The components of ground reaction forces and moments are assumed to be partitioned uniformly between the contact areas based on the distance of those contact areas to the ZMP location as will be shown in Section 4.6.

4.5 General Algorithms for Ground Contact Modeling in ZMP Method

Based on the ZMP method explained in Section 4.3, general algorithms are developed to check the ZMP constraint and stability margins and calculate the ground reaction forces and moments on each separate contact area.

The contact areas of the avatar with the ground in predictive dynamics are assumed to be flat, rigid and non-adhesive. These ground contact areas affect the dynamics of the system in two different ways:

- 1- For the digital human, the possibility of motion (ZMP constraint) and the dynamic stability of motion (ZMP stability margin) depend on these contact areas. The ZMP constraint and the ZMP stability margins depend on the convex hull of the ground contact areas. The shape and size of this convex hull is variable during the motion and depends on the contact areas of the digital human with the ground at each moment during the motion.
- 2- The values of the ground reaction forces and moments exerted on the digital human by each individual contact area will be used in the calculation of

actuation torques at the joints of the digital human. The distributed ground reaction forces acting on each individual contact area are replaced by an equivalent concentrated force and moment acting at a point on that contact area. We call them the GRF (Ground Reaction Force) points. They are the points on the digital human which can take the equivalent concentrated ground reaction forces and moments during the motion whenever those contact areas come in contact with the ground.

These algorithms allow the definition of transient GRF points, transient contact points and transient ZMP areas that vary during the motion. Therefore, the changes of GRF points, contact points and ZMP areas can be modeled very precisely during the motion. Data arrays are used in these algorithms to define the changes of GRF points, contact points, and ZMP areas during the motion. These data arrays can be filled differently based on different motion tasks that need to be modeled in the predictive dynamics environment.

For example, Tables 4.1-4.3 and Figures 4.8-4.10 show the changes of GRF points, ZMP areas for the "Kneeling", "Going Prone" and "Aiming While Prone" tasks. In these tables, "LeftMiddle" and "RightMiddle" refer to the middle points of the feet. "Outer" postfix refers to the points on the right side of right foot and on the left side of left foot:

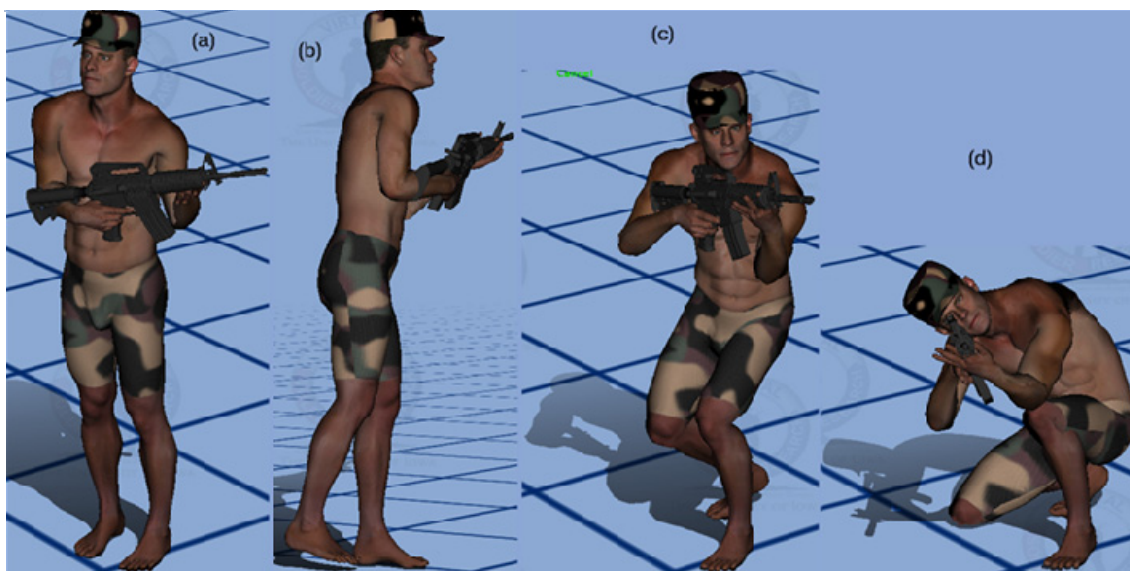


Figure 4.8. Frames of motion for the "Kneeling" task (considering the removal of feet from the ground)

Figure Part	GRF Points (Points that can take GRF)		Points defining the ZMP convex hull		
(a)	LeftMiddle	RightMiddle	RightHeelOuter LeftHeelOuter	RightToeOuter	LeftToeOuter
(b)	LeftMiddle		LeftHeelOuter LeftToeOuter	LeftHeelInner	LeftToeInner
(c)	LeftMiddle	RightToe	LeftToeOuter RightMiddleOuter	LeftHeelOuter RightToeOuter	RightMiddleInner RightToeInner
(d)	LeftMiddle RightKnee	RightToe	LeftToeOuter RightMiddleOuter	LeftHeelOuter RightToeOuter	RightMiddleInner RightKnee

Table. 4.1. Changes of ground contact conditions for the "Kneeling" task

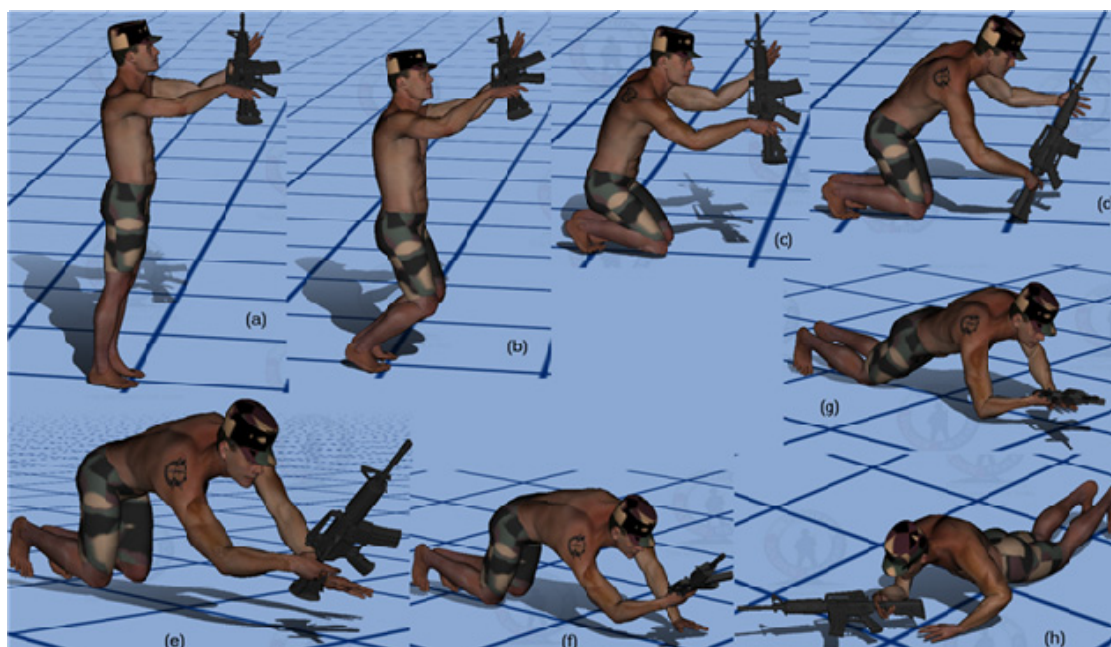


Figure 4.9. Frames of motion for the "Going Prone" task

Figure Part	GRF Points (Points that can take ground reaction forces)		Points defining the ZMP convex hull	
(a)	LeftMiddle	RightMiddle	RightHeelOuter LeftToeOuter	RightToeOuter LeftHeelOuter
(b)	LeftMiddle	RightMiddle	RightMiddleOuter LeftToeOuter	RightToeOuter LeftMiddleOuter
(c)	LeftMiddle LeftKnee	RightMiddle RightKnee	RightMiddleOuter RightKnee LeftToeOuter	RightToeOuter LeftKnee LeftMiddleOuter
(d)	LeftToe LeftKnee GunButt	RightToe RightKnee	RightToeOuter GunButt LeftToeOuter	RightKnee LeftKnee
(e), (f)	LeftKnee	RightKnee	LeftKnee	RightKnee
(g)	LeftKnee LeftWrist	RightKnee	LeftKnee LeftWrist	RightKnee
(h)	LeftKnee LeftWrist	RightKnee RightElbow	LeftKnee RightElbow	RightKnee LeftWrist

Table. 4.2. Changes of ground contact conditions for the "Going Prone" task

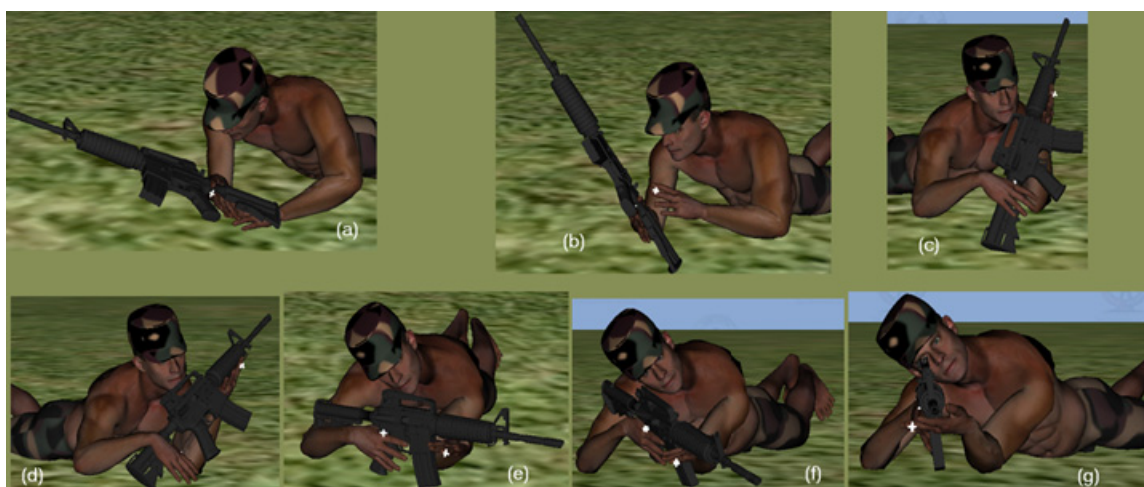


Figure 4.10. Frames of motion for the "Aim While Prone" task

Figure Part	GRF Points (Points that can take ground reaction forces)		Points defining the ZMP convex hull	
(a),(b)	RightHip	RightElbow	RightHip	RightElbow
	LeftHip	LeftKnee	LeftHip	LeftKnee
	RightKnee		RightKnee	
(d),(e)	RightHip	LeftElbow	RightHip	LeftElbow
	LeftHip	LeftKnee	LeftHip	LeftKnee
	RightKnee		RightKnee	
(c),(f),(g)	RightHip	RightElbow	RightHip	RightElbow
	LeftElbow	LeftHip	LeftElbow	LeftHip
	LeftKnee	RightKnee	LeftKnee	RightKnee

Table. 4.3. Changes of ground contact conditions for the "Aim While Prone" task

In this algorithm for implementation of the ZMP method, the above data are stored in arrays. A generalized algorithm for calculations of the "Equations of Motion" is also developed based on these data arrays. This "Equations of Motion" algorithm which calculates the ground reaction forces and torques, operates differently for each motion task based on the these data arrays.

4.6 Calculation of Ground Reaction Forces and Moments

Consider a digital human having n rigid and non-adhesive external contact areas Υ_α ($\alpha=1\cdots n$) with the environment which are all located on the ground (or same plane) as shown in Figure 4.11. Also, let \mathbf{F}_α and \mathbf{M}_α acting at \mathbf{p}_α denote the concentrated contact forces and moments equivalent to the distributed contact forces on contact area Υ_α acting from the ground on the digital human. Let \mathbf{F}_{ige}^{zmp} and \mathbf{M}_{ige}^{zmp} be the net force and moment of inertial, gravitational and external forces at the ZMP located at \mathbf{z} .

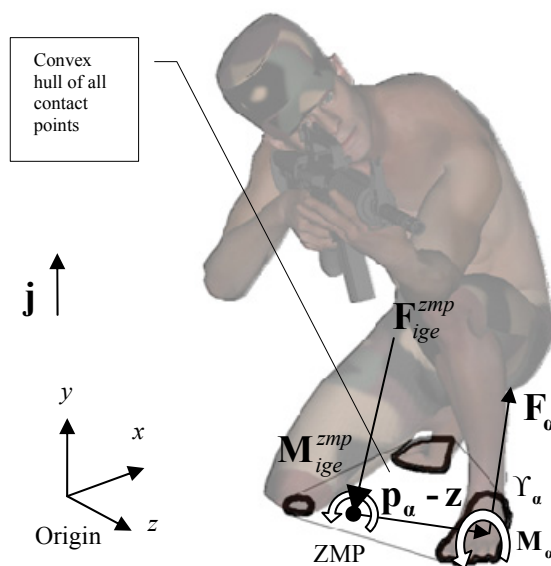


Figure 4.11. Calculation of ground reaction forces and moments based on the ZMP location in a sample motion frame in an "Aiming While Kneeling" task

As it was explained in Section 4.3, for any motion Θ , all the forces (IGE) except the ground reaction forces are known. The possibility of the generation of the arbitrary

motion Θ by using the given ground contact areas is ensured by using the well known ZMP constraint.

According to Theorem 4.1, when ZMP constraint is satisfied, we are sure that it is possible to find unilateral distributed contact forces on those contact areas to equilibrate \mathbf{F}_{ige}^{zmp} and \mathbf{M}_{ige}^{zmp} .

Let $\mathbf{F}_a^{ZMP} = \mathbf{F}_a$, $\mathbf{M}_a^{ZMP} = \mathbf{M}_a + (\mathbf{p}_a - \mathbf{z}) \times \mathbf{F}_a$ denote the force and moment system equal to \mathbf{F}_a and \mathbf{M}_a acting at the ZMP. The dynamic equilibrium equations for the digital human require that:

$$\begin{aligned} \sum \mathbf{F}_{ZMP} = \mathbf{0} &\Rightarrow \mathbf{F}_{ige}^{ZMP} + \sum \mathbf{F}_a = \mathbf{0} \\ &\Rightarrow \sum \mathbf{F}_a = -\mathbf{F}_{ige}^{ZMP} \end{aligned} \quad (4.6.1)$$

$$\begin{aligned} \sum \mathbf{M}_{ZMP} = \mathbf{0} &\Rightarrow \mathbf{M}_{ige}^{ZMP} + \sum \mathbf{M}_a^{ZMP} = \mathbf{0} \\ &\Rightarrow \sum \mathbf{M}_a + \sum (\mathbf{p}_a - \mathbf{z}) \times \mathbf{F}_a = -\mathbf{M}_{ige}^{ZMP} \end{aligned} \quad (4.6.2)$$

In general, if we have more than one contact area, these equivalent contact reaction force and moment vectors \mathbf{F}_a and \mathbf{M}_a are indeterminate because there are more than 6 unknowns for the 6 equilibrium equations. This is an underdetermined system that has infinite number of solutions.

There has been some work to resolve this indeterminacy in the ZMP method in predictive dynamics. For example, one design variable per contact area to represent the ratio of the six components of the equivalent forces and moment vector on that contact

area to the IGE forces and moments has been considered. It is also possible to consider each of these six ratios separately as design variables (six design variables per contact area). But, in the ZMP method, the normal practice (which has shown to be more successful) has been to assume that the global equivalent contact forces and moments (which should cancel IGE forces and moments to ensure dynamic equilibrium) are partitioned to the contact areas based on the distances of the contact areas from the ZMP. This assumption is based on several experimental data which suggest that the ratio of the vertical component of the ground reaction force (one component out of the six components of the ground reaction forces and moments) tolerated by each foot in walking motion seems to be inversely proportional to the distance of that foot from the ZMP location (see Ren, Jones, Howard, 2005, 2007; Winter, 1990, 2009).

For example, we consider the data measured in the walking experiment published in Winter (2009) in Figure 4.12. In this figure, we plot the ratio of ZMP distances from the left and right feet versus the inverse of the ratio of the vertical forces on them during the double support phase. Of course, these data are measured in two dimensions and the lateral dimension is ignored in these measurements. In the figure, z_R and z_L respectively denote the distances of the ZMP to the right and left foot in the forward-backward direction. Also, F_{yR} and F_{yL} respectively denote the vertical ground reaction force on the right and left foot.

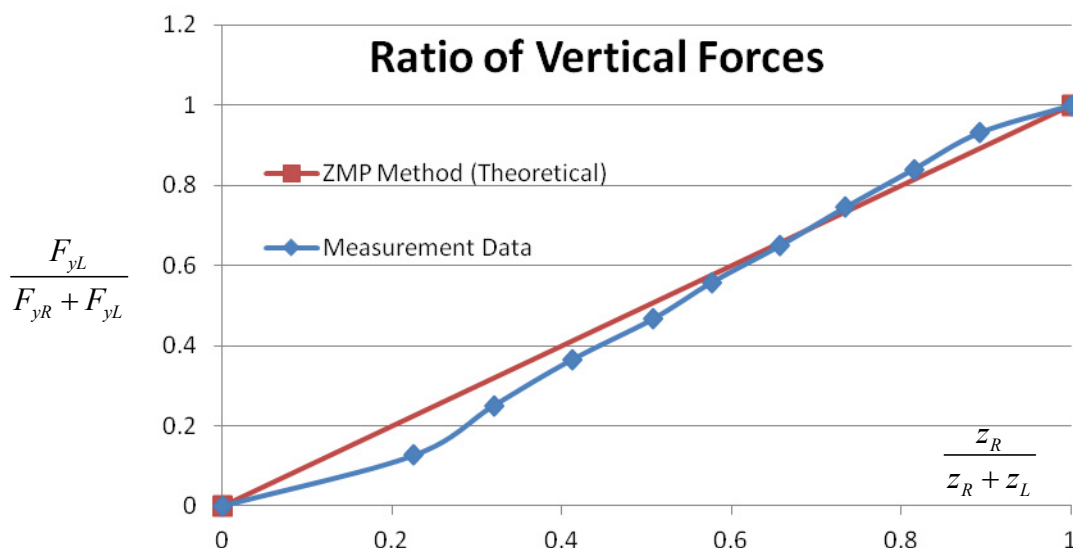


Figure 4.12. Walking measurement data from Winter (2009), approximately matching the proportionality of the vertical ground reaction forces (F_y) on the feet to the inverse of the ZMP distances from them (subscripts L and R refer to left foot and right foot)

The measurement data shown in Figure 4.12 approve this approximation only for the vertical component of the ground reaction force. However, in the ZMP method, for simplicity, we assume that all the other five components of the ground reaction forces and moments are also partitioned on the contact areas by the same ratios. In other words:

- 1- We assume that for each of the contact areas Υ_{β} , the ratio of all the six components of equivalent concentrated contact forces and moments to the IGE force and moment at the ZMP are the same which we denote by r_{β} . We call this “the uniform partitioning of the components of the concentrated contact forces and moments by the ratios r_{β} between the contact areas Υ_{β} ”.

This means that we approximate each \mathbf{F}_{β} and \mathbf{M}_{β} by the below equations:

$$\begin{cases} \mathbf{F}_\beta^{ZMP} = -r_\beta \mathbf{F}_{ige}^{ZMP} & \Rightarrow \mathbf{F}_\beta = -r_\beta \mathbf{F}_{ige}^{ZMP} & (4.6.3) \\ \mathbf{M}_\beta^{ZMP} = -r_\beta \mathbf{M}_{ige}^{ZMP} & \Rightarrow \mathbf{M}_\beta + (\mathbf{p}_\beta - \mathbf{z}) \times \mathbf{F}_\beta = -r_\beta \mathbf{M}_{ige}^{ZMP} & (4.6.4) \end{cases}$$

2- We assume that the ratio r_β for each contact area is inversely linearly proportional to the distance of that contact area from the ZMP location. Therefore, contact areas near the ZMP are supposed to have larger values of r_β . Let's denote the distance of the point of action of equivalent forces and moments \mathbf{F}_β and \mathbf{M}_β (denoted by "GRF points" in Section 4.5) from the ZMP by $d_\beta = \|\mathbf{p}_\beta - \mathbf{z}\|$. Therefore, we need to have:

$$\frac{r_\alpha}{r_\beta} = \frac{d_\beta}{d_\alpha} \quad (4.6.5)$$

3- To satisfy the dynamic equilibrium equations (4.6.1) and (4.6.2), the sum of the ratios r_β has to be equal to 1. Therefore:

$$\sum r_\alpha = 1 \quad (4.6.6)$$

Predictive dynamics is based on optimization. Therefore, we need to provide the gradient (sensitivity) of the ground reaction forces and moments for the optimization algorithm. They are calculated as shown below:

$$\left\{ \begin{array}{l} r_1 + r_2 + \dots + r_n = 1 \\ \frac{r_2}{r_1} = \frac{d_1}{d_2} \\ \vdots \\ \frac{r_n}{r_1} = \frac{d_1}{d_n} \end{array} \right. \Rightarrow \left\{ \begin{array}{l} r_1 = (k \times d_1)^{-1} \\ r_2 = (k \times d_2)^{-1} \\ \vdots \\ r_n = (k \times d_n)^{-1} \end{array} \right. \quad (4.6.7) \text{ and} \quad \left\{ \begin{array}{l} \frac{\partial r_1}{\partial q_i} = r_1^2 \left(L \times d_1 - k \frac{\partial d_1}{\partial q_i} \right) \\ \frac{\partial r_2}{\partial q_i} = r_2^2 \left(L \times d_2 - k \frac{\partial d_2}{\partial q_i} \right) \\ \vdots \\ \frac{\partial r_n}{\partial q_i} = r_n^2 \left(L \times d_n - k \frac{\partial d_n}{\partial q_i} \right) \end{array} \right. \quad (4.6.8)$$

$$\text{where:} \quad k = \frac{1}{d_1} + \frac{1}{d_2} + \dots + \frac{1}{d_n} \quad \text{and} \quad L = \frac{1}{d_1^2} \frac{\partial d_1}{\partial q_i} + \frac{1}{d_2^2} \frac{\partial d_2}{\partial q_i} + \dots + \frac{1}{d_n^2} \frac{\partial d_n}{\partial q_i}$$

It is good to note that several plots similar to Figure 4.12 can be seen in Ren, Jones, Howard (2005, 2007) where they use the experimental data in Winter (1990) as their references. They also assume a linear approximation for the distribution of the ground reaction forces in predicting a walking motion. They use such plots as their justification for linear partitioning of ground contact forces.

4.7 Summary and Conclusion

This chapter presented an important theorem (Theorem 4.1) which showed the relation between the ZMP constraint and the unilaterality of ground reaction forces. It was shown that an additional constraint (net of the vertical component of the IGE forces being downwards) is required besides the ZMP constraint to ensure the unilaterality of

ground reaction forces in the ZMP method. The ZMP method was defined as a method in predictive dynamics which uses the ZMP constraint along with this additional constraint to ensure the possibility of arbitrary motions. Theorem 4.1 shows that the ZMP method used in predictive dynamics (Sections 4.3 to 4.5) is a legitimate method for producing motions that are possible in the real world. However, as shown in Section 4.6, an assumption is used for the calculation (partitioning) of ground reaction forces in the ZMP method which is not mathematically proved to be correct and is based on observations from the experimental data. The assumption is that the ratio of the net contact forces and moments to the equivalent ground reaction forces and moments acting on each contact area, evaluated at the ZMP, are the same for all the six components of forces and moments (uniform partitioning). By the way it is assumed that this ratio is equal to the ratio of distances of those contact areas to the ZMP. This assumption was partially evaluated in Section 4.6 to show its backgrounds and will be further evaluated in Section 8.4 to show its deficiencies.

CHAPTER 5

DYNAMIC SIMULATION OF A SOLDIERS' MOTION USING THE ZMP METHOD: KNEELING AND AIMING TASKS

5.1 Introduction

The objective of this chapter is to formulate and solve problems of the "aiming while kneeling" and "aiming while standing" motion tasks for a soldier (human) using the Santos™ digital human model. The ZMP method introduced in Chapters 3 and 4 is used to ensure the possibility of the motion in nature and calculate ground reaction forces. As explained in Sections 4.2 – 4.5, the ZMP method along with an assumption for the partitioning of net global (IGE) forces and moments can be used to ensure that a given motion can be generated by using the given environment (ground) contact areas and calculate the environment (ground) contact forces on those contact areas. In Chapter 8, the NCM method along with the assumption of forces as design variables will be used to ensure the possibility of the motion in the real world and calculate ground reaction forces.

Using the ZMP method in predictive dynamics as explained in Section 4.2, we can predict realistic motions for the "aiming while standing" and "aiming while kneeling" tasks. The optimization is able to very well predict the "Natural Point of Aim" which is a well known concept for soldiers. In other words, the optimization is able to predict the most comfortable final orientation of the feet on the ground for engaging a specific target. We also simulate cases where the orientation of the soldier's feet are enforced (for example engaging several targets without moving the feet on the ground) and not choosable by optimization.

The effect of changing the target location in the 3D space, changing the anthropometry of the soldier, adding armor to different joints, changing the rifle stock length, adding backpack and using different weapons have also been studied using this approach.

In this chapter, we first try to address the general problems encountered in modeling the four military tasks introduced in this chapter and the next chapter. These general problems are discussed in Sections 5.3 - 5.11. Considering the timeline of developing these four tasks, "aiming while kneeling" was studied first. Therefore, it is used more often as reference when these general problems and their solutions are discussed.

5.2 A Literature Review of Modeling Military Tasks

The need for representing simulated soldiers has been primarily driven by military requirements. These requirements appeared very early in the beginning stages of the digital human modeling field. Some examples are Wysocki and Fowlkes(1994) and Pratt *et al* (1994).

Despite this need, there have been very few samples of aiming or kneeling tasks simulated by simplified or whole body digital human models. This has been due to the complexity of these tasks. This complexity arises from the complex combination of joint angle variables that are required to achieve these motions or postures. As a result, most of these efforts have been actually focused on the playback of a recorded motion on a digital human model rather than the simulation of these motions. Such efforts have appeared in

the literature as early as 1995. Granieri, Crabtree and Badler (1995) from the University of Pennsylvania use postures and motions of a human and maps them on a digital human called "Jack" with a lower number of degrees of freedom. These motions include: standing, kneeling, firing, crawling, going prone, running, walking. They store them for later playback in digital environments.

Even at the time being, the most relevant works use motion captured data for modeling aiming and kneeling motions of digital humans. Alexander, and Conradi (2011) have recently tested the existing digital human models for performing more complex motions. This complex motion is a stand to kneeling motion (without aiming part). In that work, several digital human models are used. The report indicates that: "Modeling of complex motions with the digital human models was complex and intensive. None of them allowed a realistic simulation of specific movements. Although modeling was possible, it was very complex to model the movement and it required manual actions".

There is also other less relevant work, using over-simplified models to calculate some specific parameters in question. For example, Macko, Balaz, and Racek (2009) try to determine the significant points on a shooter's body to compare the computed and measured shooter movements in standing, kneeling and prone firing positions.

5.3 Marksmanship

Marksmanship refers to the art or skill of using a firearm, such as a rifle or a pistol. In this research we use the "Rifle Marksmanship" instructions from the latest

available versions of "U.S. Army Field Manual" (U.S. Army, 2011) and "U.S. Marine Corps Reference Publication (MCRP)" (U.S. Marine Corps., 2001) as the major reference for definition of terms and procedures.

5.3.1. Principles of Aiming

There are several principles that are common and remain the same for all aiming positions (U.S. Army, 2011 and U.S. Marine Corps., 2001), such as:

- 1- Left hand under the barrel
- 2- Rifle stock in shoulder pocket
- 3- Grip of the right hand
- 4- Cheek to stock welding
- 5- Sight alignment
- 6- Sight picture

In this research, all of these principles have been taken into consideration for the modeling of aiming and kneeling tasks.

5.3.2. Natural point of Aim (NPOA)

The most suitable body position/orientation for any aiming task is when NPOA is achieved. To define the NPOA concept, two important elements need to be defined first (U.S. Army, 2011 and U.S. Marine Corps., 2001):

- **Bone Support**

Muscular support is insufficient to provide a stable platform for shooting, especially more than one shot. Instead, the shooter must rely on non-muscular (bone) support to provide the shooting platform. This eliminates changes in aiming due to muscle fatigue and also minimizes the shaking associated with muscle tension.

- **Muscular Relaxation**

Muscular relaxation helps to hold the rifle steady and increase the accuracy of the aim. During the shooting process, the muscles of the body must be relaxed as much as possible. Muscles that are tense will cause excessive movement of the rifle, disturbing the aim.

In U.S. Marine Corps. (2001), the term "Natural Point of Aim" is defined as "*the location at which the rifle's sights settle if bone support and muscular relaxation are achieved*".

5.4 Kneeling Task

To perform this task, the soldier should (U.S. Army, 2011 and U.S. Marine Corps., 2001):

- 1- Position the body at a 45-degree angle to the target.

- 2- Keep the left foot in place.
- 3- Step back with the right foot.
- 4- Drop to the right knee.
- 5- Place upper arm triceps on left knee for support.
- 6- Rest the ball of the right foot firmly on the ground
- 7- Rest the buttock on the heel.
- 8- Aim.

The first item in the above list mentions a 45 degree angle. This angle is an initial guess for achieving NPOA and may actually be variable for different soldiers or rifles or target locations. Therefore, instead of enforcing this angle in simulations, we predict the best value for it to maximize comfort (achieve NPOA). As will be seen in next sections, the digital human avatar (SantosTM) is exact enough to predict this angle well.

5.5 Environment Contact Modeling for Kneeling

As indicated previously in Section 4.4, the new modules and code structures for modeling environmental contact make it possible to define the changes of GRF points, contact points, ZMP areas more exactly and easily during each motion segment for any dynamic task. Figure 5.1 and Table 5.1 show the changes of GRF points, ZMP areas for the "kneeling" task.

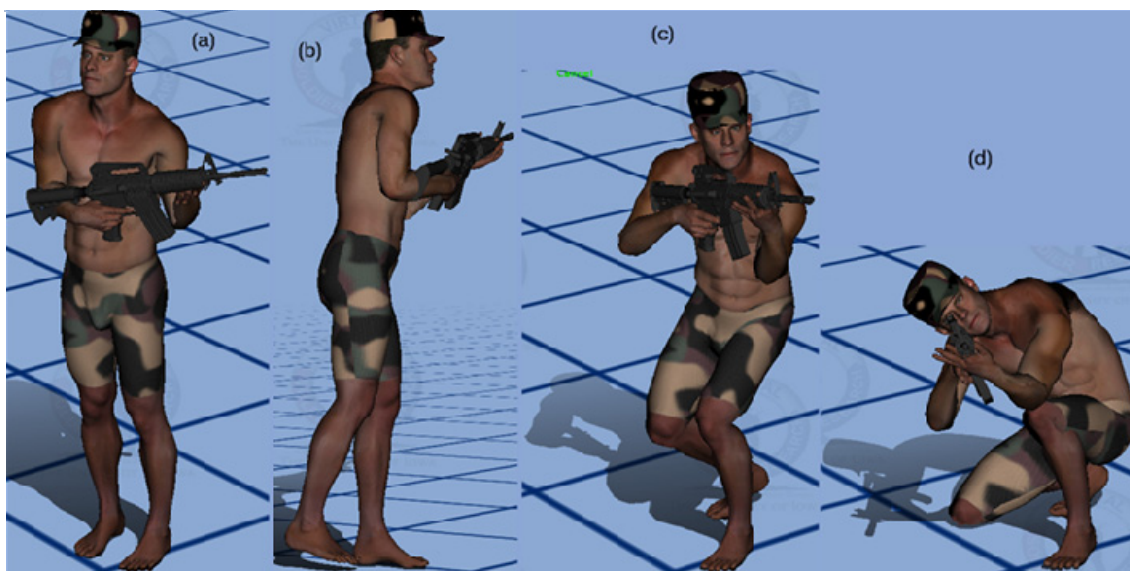


Figure 5.1. Frames of motion for the "Kneeling" task (considering the removal of feet from the ground)

Figure Part	GRF Points (Points that can take GRF)		Points defining the ZMP convex hull		
(a)	LeftMiddle	RightMiddle	RightHeelOuter LeftHeelOuter	RightToeOuter	LeftToeOuter
(b)	LeftMiddle		LeftHeelOuter LeftToeOuter	LeftHeelInner	LeftToeInner
(c)	LeftMiddle	RightToe	LeftToeOuter RightMiddleOuter	LeftHeelOuter RightToeOuter	RightMiddleInner RightToeInner
(d)	LeftMiddle RightKnee	RightToe	LeftToeOuter RightMiddleOuter	LeftHeelOuter RightToeOuter	RightMiddleInner RightKnee

Table 5.1. Changes of ground contact conditions for the "Kneeling" task

In Table 5.1, "LeftMiddle" and "RightMiddle" refer to the middle points of the feet. "Outer" postfix refers to the points on the right side of right foot and on the left side of left foot.

5.6 Initial Efforts: Lower Body Motion Prediction for Kneeling

In this section, we review the initial efforts in modeling "aiming while kneeling" in order to show a problem that we encountered in modeling it. That problem and its solution are discussed in Section 5.7.

Design Variables:	<i>Joint Angle Profiles $q(t)$</i>
Objective Function:	<i>Minimize $f(q) = \int_{t=0}^T \sum_{i=1}^{ndof} \tau_i^2 dt$</i>
Environment Contact Modeling:	<i>ZMP Method + Linear Partitioning of Contact Forces</i>
Torque Calculation Method:	<i>Recursive Lagrangian Formulation</i>
Constraints Imposed Throughout the motion:	<ul style="list-style-type: none"> • <i>Joint Angle Limits</i> $q^L \leq q(t) \leq q^U$, $0 \leq t \leq T$ • <i>Torque Limits</i> $\tau^L \leq \tau(t) \leq \tau^U$, $0 \leq t \leq T$ • <i>Left Foot Position Fixed on the Ground</i> $(x_i(t), z_i(t)) = \text{Fixed}$ i: corresponds to several points on left foot • <i>Look Forward</i>
Initial Motion Frame Constraints:	<ul style="list-style-type: none"> • <i>Right Foot Initial Position</i> • <i>Initial Static Condition</i>
Final Motion Frame Constraints:	<ul style="list-style-type: none"> • <i>Right Knee Touches Ground</i> • <i>Final Static Condition</i>

Table 5.2. Problem formulation for lower body motion prediction of "Kneeling"

In order to get initial results, we initially assign a fixed posture for SantosTM upper body and only predicted the lower body motion under this constraint. After obtaining results and improving the formulation and constraints for lower body motion, we will let the optimization predict the whole body motion of SantosTM in following sections. The problem formulation for this motion prediction is shown in Table 5.2.

5.7 Passive Joint Angle Limits (Expanded Ranges of Motion)

It was observed that although SantosTM upper body motion in Section 5.6 was assigned (not predicted), optimization is unable to find a suitable motion for just lower body. The reason was that the default joint angle limits used for previous tasks were also initially used for kneeling but they were too restrictive at some joints for the kneeling motion. Examples are the right knee bending degree of freedom and the right midfoot (toe) bending degree of freedom which exceed their default joint angle limits in the final kneeling position. The reason is that in the final kneeling position, they are under "pressure" i.e., for right knee bending, a large lateral force (about half of the body weight) is acting on the right upper leg and right lower leg which squeeze the knee bending degree of freedom beyond its normal range of motion. So, new upper or lower joint limits called "passive joint limits" were defined for these degrees of freedom such that the kneeling motion becomes predictable under the new, less restricted degrees of freedom. Some of the Passive Joint Angle Limits (Expanded Ranges of Motion) are listed in Table 5.3:

Right Knee, Bending:		<i>Q39 (39th Joint, 45th DOF)</i>
Value Required During Kneeling Motion:		<i>155°</i>
Joint Limits Modification	<i>Lower Limit (Degrees)</i>	<i>Upper Limit (Degrees)</i>
<i>Default Joint Angle Limits</i>	<i>7.0</i>	<i>138.0</i>
<i>Modified Joint Angle Limits</i>	<i>7.0</i>	<i>160.0</i>
Right Midfoot (toe) Bending:		<i>Q42 (42nd Joint, 48th DOF)</i>
Value Required During Kneeling Motion:		<i>-85°</i>
Joint Limits Modification	<i>Lower Limit (Degrees)</i>	<i>Upper Limit (Degrees)</i>
<i>Default Joint Angle Limits</i>	<i>-71.0</i>	<i>-9.0</i>
<i>Modified Joint Angle Limits</i>	<i>-90.0</i>	<i>-9.0</i>
Left Hip Fore-and-Back:		<i>Q37 (37th Joint, 43rd DOF)</i>
Value Required During Kneeling Motion:		<i>-130°</i>
Joint Limits Modification	<i>Lower Limit (Degrees)</i>	<i>Upper Limit (Degrees)</i>
<i>Default Joint Angle Limits</i>	<i>-102.0</i>	<i>41.0</i>
<i>Modified Joint Angle Limits</i>	<i>-150.0</i>	<i>41.0</i>

Table 5.3. Passive joint angle limits (expanded ranges of motion)

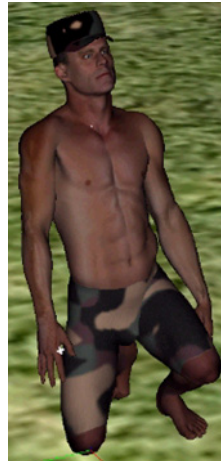


Figure 5.2. Lower body motion prediction for "Kneeling" (frozen upper body)

It may be good to note that unlike simpler tasks where only some of the joint angles (design variables) are changing during the motion such as "Walking" or "Running", in order to model the "aiming while kneeling" task precisely enough, all of the 55 DOF of the digital human need to be used as will be seen in Section 5.12. It means that no degree of freedom can be frozen by limiting its range of motion in order to simplify the problem. For example, in "aiming while kneeling", all upper body joints such as neck as well as all lower body joints need to be predicted to exactly model the motion.

Using the formulation given in Section 5.6 and the passive joint angle limits given in this section, an initial result was obtained. The final motion frame for kneeling looked as shown in Figure 5.2.

5.8 The Natural Point of Aim (NPOA) in Details

There are different definitions given for the NPOA (Anderson, 2002) in aiming trainings which all refer to the same concept. We collect some of these definitions here:

- NPOA is the body posture that allows the gun to remain on target with minimal muscle input. Once you are in your natural point of aim you can hold the rifle for a long time without getting tired because you are holding the rifle in place with your skeleton and not your muscles.
- NPOA is a shooting skill where the shooter minimizes the effects of body movement on the firearm's impact point. Along with proper stance, sight picture and trigger control, it forms the basis of rifle marksmanship.
- NPOA is the one factor which separates the Riflemen from the 'wannabees'. A Rifleman takes his shooting position so that his rifle, with his body relaxed, is pointing at the target. He does not have to fight muscle strain and he makes his job of firing the shot a lot easier. Best of all, his shots will be on target, accurately and consistently, because he is not fighting his body's natural position.

An NPOA (natural point of aim) can and should be achieved in any aiming task.

To achieve NPOA in aiming tasks, the shooter must:

- Get in to the firing position.
- Aim at the target.

- Keeping the weapon pointed at the target, close his eyes, relax - should not hold any tension on weapon, take 3-4 breathes. Open eyes. Wherever the sight rests is his natural point of aim.
- Move his feet on the ground to rotate about the rifle's back sight and repeat until the sight is on target (aiming with feet instead of hands).
- Note: After opening eyes the shooter should not attempt to adjust the weapon.

Natural point of aim is not achieved if the shooter must apply pressure to the firearm so the sight picture is on target. One of the main advantages of natural point of aim is that it minimizes fatigue when shooting a long course of fire. Over time, the shooter learns to assume the correct position quickly, allowing for accurate fire immediately.

The main purpose of identifying and potentially correcting natural point of aim is to make shots with both accuracy and precision, where accuracy is the ability to place rounds on the desired target, and precision is the ability to put multiple rounds in the same location. Good shooters are always precise, and this skill is more fundamental than accuracy, which can be adjusted. Typically, precision is based on natural point of aim. If for example, the shooter fires 10 rounds down range and they all land in a similar area on the target, then he can assume that this is the natural point of aim. If the strike zone is not in the middle of the target, adjustments are made to the shooter's positioning and/or the firearm's sights so that the shots accurately strike the center of the target.

Natural point of aim marksmanship is based on the idea that muscular control is insufficient to provide a stable platform for shooting, especially more than one shot. Instead, the shooter relies on non-muscular (skeleton/ligaments/tissue) support to provide the shooting platform. This eliminates changes in aim due to muscle fatigue and also minimizes the shaking associated with muscle tension. In predictive dynamics method, all calculations are performed based on the skeleton of the digital human and muscle deformation is ignored. Therefore, predictive dynamics provides a suitable environment to predict NPOA correctly.

Natural point of aim is a concept that can be used in relation to any type of shooting position but is most often discussed in relation to prone, sitting, or kneeling positions, and less frequently with offhand/standing positions.

The most comfortable global orientation of the body as the most important aspect of NPOA, is different for each individual, each target elevation and each aiming task. But there are some average values common in shooting trainings for specific aiming tasks. For example, in "aiming while kneeling", to achieve NPOA, the common training given to shooters is as follows: The most comfortable orientation of the left foot to engage a specific target is to align the left foot on the ground at an angle of about 45 degrees to the right of the target line based on the army instructions in Section 5.4. As we will see in next sections, the digital human avatar (SantosTM) is exact enough to predict this angle for a real soldier.

5.9 The Target Engagement Constraint in Aiming Tasks

In this section, we first review the input parameters given to the target engagement constraint in aiming tasks (such as "aiming while kneeling"). Then based on those input parameters, we show how the target engagement constraint manages to engage the desired target point in aiming tasks.

5.9.1. Input Parameters for the Target Engagement Constraint

The input parameters in aiming tasks are designed to address the NPOA concept. The input parameters for the target engagement constraint are:

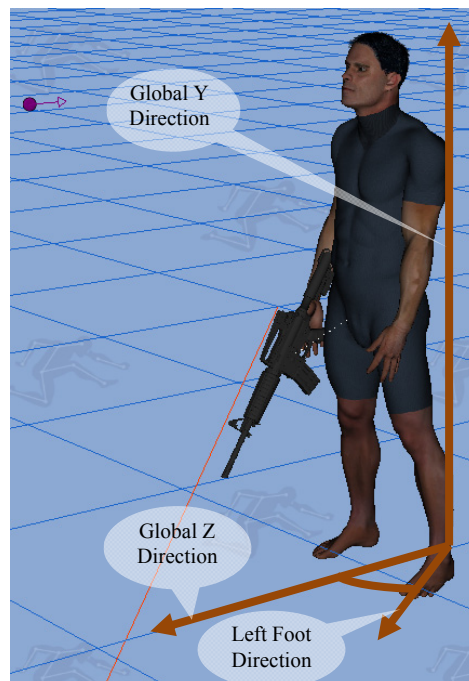


Figure 5.3. Definition of input parameters for an arbitrary posture

1) Target Position (X, Y, Z):

The line connecting the back sight and the foresight of the rifle need to pass through this position and the soldier's eyeball.

2) Body/Left Foot Azimuth Angle Flag (Azimuth Flag):

Determines whether the user assigns the value of "Body/Left Foot Azimuth Angle" or the optimization decides the best value for it. It can have two values:

- False (0) : Indicates that the optimization decides the best body rotation to engage a target
- True (1) : Indicates that the "Body/Left Foot Azimuth Angle" is assigned by the user

3) Body/Left Foot Azimuth Angle:

It is defined as the angle of the rotation about "positive global Y" from the "global positive Z direction" to the direction of left foot on the ground (for "aiming" and "kneeling" tasks) or to the direction of body line on the ground (for "aiming while prone" task) in the final aiming posture. If "Azimuth Flag" is set to zero, this input value is ignored and it is predicted by optimization in order to engage the target. If "Azimuth Flag" is set to 1, this input value will be implemented and will be observed in the results.

To understand these inputs better, several figures are presented in this section. Figure 5.3 shows the familiar neutral posture to illustrate the global y and z axes. Figure 5.4 illustrates all the input parameters for two sample "kneeling" tasks. Figure 5.5 illustrates all the input parameters for a sample "aiming while prone" task.

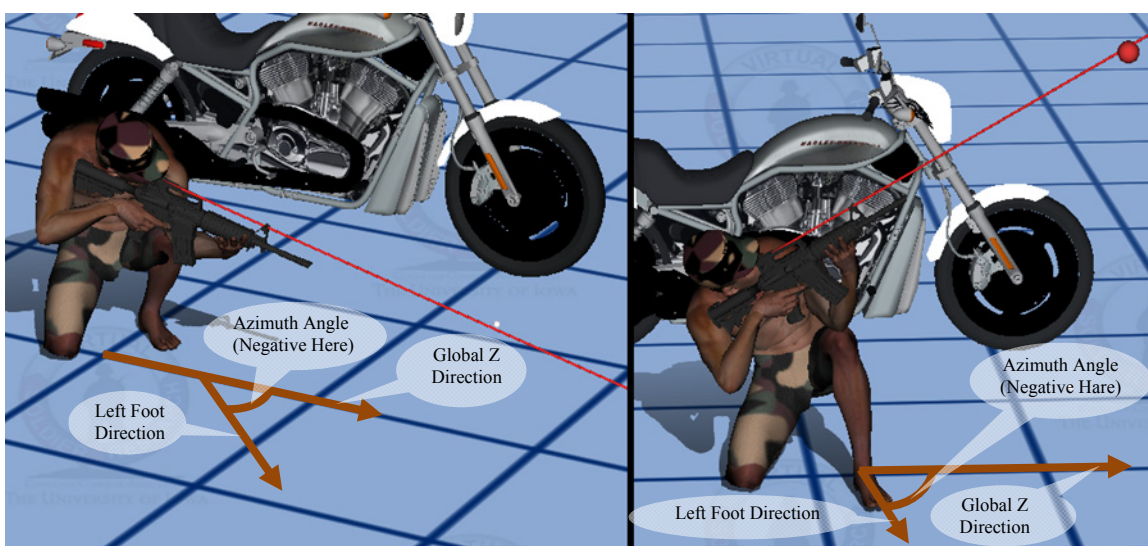


Figure 5.4. Examples of two "Kneeling" tasks with predicted "Left Foot Azimuth Angle" values

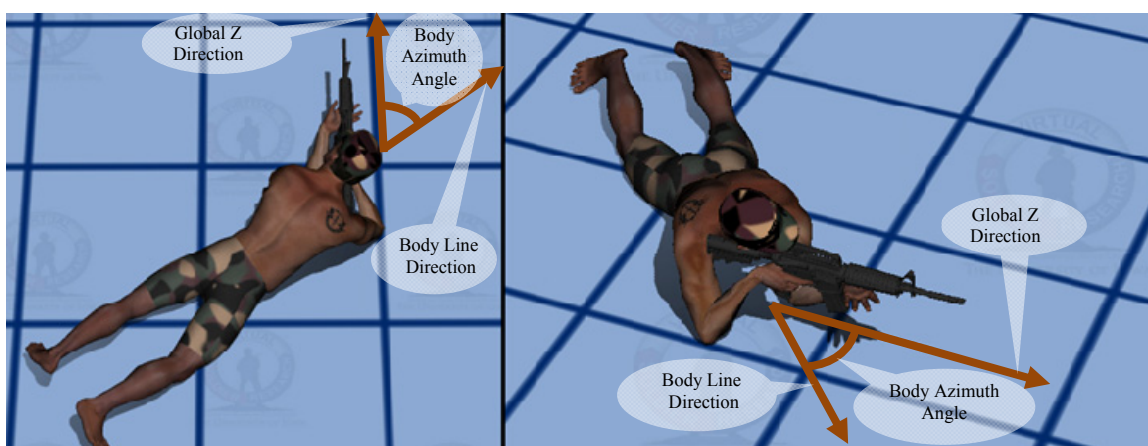


Figure 5.5. Example of an "Aiming While Prone" task with predicted "Body Azimuth Angle" values

5.9.2. The Target Engagement Constraint

Based on the input parameters introduced in Section 5.9.1, we show how the target engagement constraint manages to engage the desired target point in aiming tasks.

The method for target engagement is illustrated in Figure 5.6:

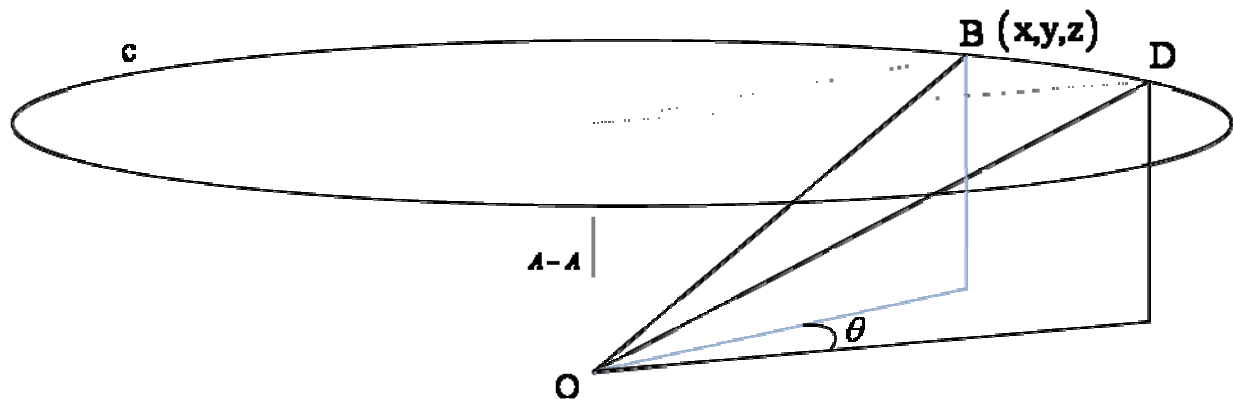


Figure 5.6. Points of interest in Target engagement

The points, lines and curves shown in Figure 5.6 correspond to the following geometrical positions in aiming:

- Point B: Target Point
- Point O : Rifle Back Sights
- Axis A-A : Perpendicular to the Ground at Point O
- Circle c: The Circle About Axis A-A Passing Through Point B

Based on the input value given for "Azimuth Flag" (0 or 1) as explained in Section 5.9.1, two different methods are used:

I. Azimuth Flag=0

In this case, optimization determines the most suitable "Body/Left Foot Azimuth Angle". The predictive dynamics code constrains the rifle to aim at the most comfortable point (D) on a circle "c" in Figure 5.6. Circle "c" is the circle drawn about axis A-A and passing through point B. Axis A-A is the axis passing through the final location of rifle's back sights (Point O) and perpendicular to the ground. After the optimization solves the problem, avatar will be aiming at point D. Angle θ should be determined and a secondary optimization procedure rotates the avatar as a rigid body by $-\theta$ to aim at point B. This is very similar to the procedure that soldiers perform in order to find their NPOA (see Section 5.8).

II. Azimuth Flag=1

In this case, "Body/Left Foot Azimuth Angle" angle is assigned by the user (input value as explained in Section 5.9.1. The code fixes the "Body/Left Foot" of the avatar along Z axis in an assigned position. Then it rotates the target from point B on circle "c" by an angle equal to $-(\text{Body/Left Foot Azimuth Angle})$ and calls this point: "D". Then the main optimization procedure tries to enforce SantosTM to aim at exactly point "D". After the main optimization solves the problem, SantosTM will be aiming at point D. Now, a secondary optimization rotates the avatar by $+(\text{Body/Left Foot Azimuth Angle})$ to aim at point B.

5.10 NPOA and the Target Engagement Constraints

One may think that the procedure given in Section 5.9 for target engagement is unnecessarily complicated and for example, to engage a specific target in kneeling, the most comfortable way is to set the left foot direction parallel to the target line and perform "aiming while kneeling". This is not true. The shooting trainings do not advice such a method (see Section 5.8). However, the user is able to enforce the left foot of the avatar to be parallel to the target line by manipulating the input parameters. For such a purpose, the user should set "Azimuth Flag" equal to 1 and selecting a suitable value for "Left Foot Azimuth Angle". The result of such an effort is shown below:

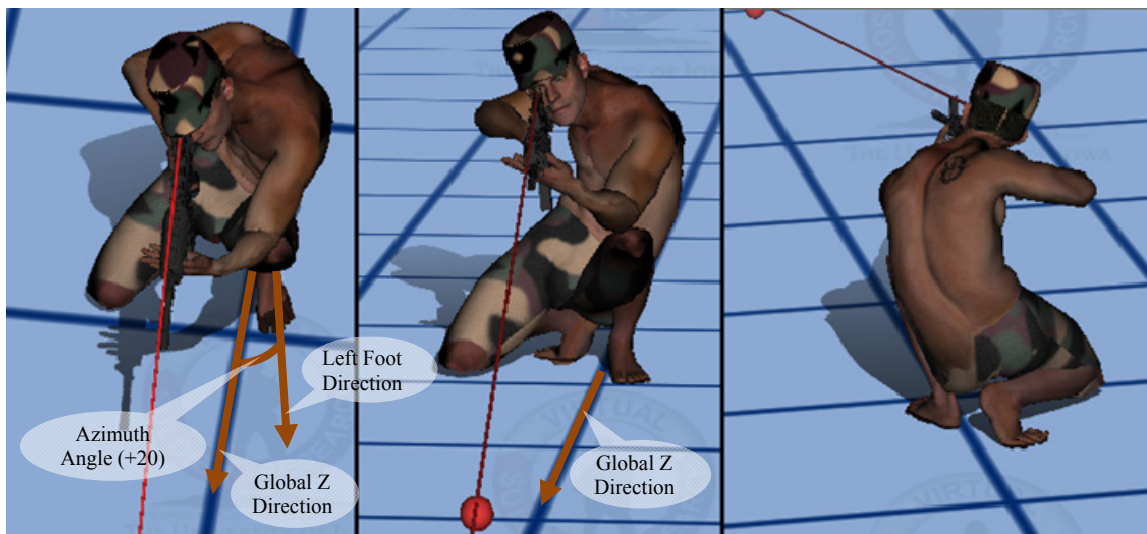


Figure 5.7. Unsuitable kneeling position caused by enforcing unsuitable "Left Foot Azimuth Angle". Target located at (0, 0.2, 3), "Azimuth Flag =1" and "Left Foot Azimuth Angle =20"

In the picture on the left in Figure 5.7, you can see that the left foot is almost parallel to the target line. The resulting kneeling position of the avatar looks very uncomfortable with extreme bending in the spine.

The most comfortable orientation of the left foot to engage a specific target is to align the left foot on the ground at an angle of about 45 degrees to the right of the target line based on the army instructions in Section 5.4. Our avatar (Santos™) is exact enough to predict this angle for a real soldier. To find this angle in any "aiming while kneeling" task, the "Azimuth Flag" can be set to zero. In that case, the optimization decides the best angle for left foot on the ground and outputs this angle to the user. This angle changes a little bit depending on the target elevation, and is about 42 degrees to the right of the target line which agrees very well with shooting trainings (Also see Section 5.16).

For example, for the same "Target Position" that was used in Figure 5.7, if you let optimization decide the left foot orientation (set "Azimuth Flag" equal to 0), the result shown in Figure 5.8 is achieved:

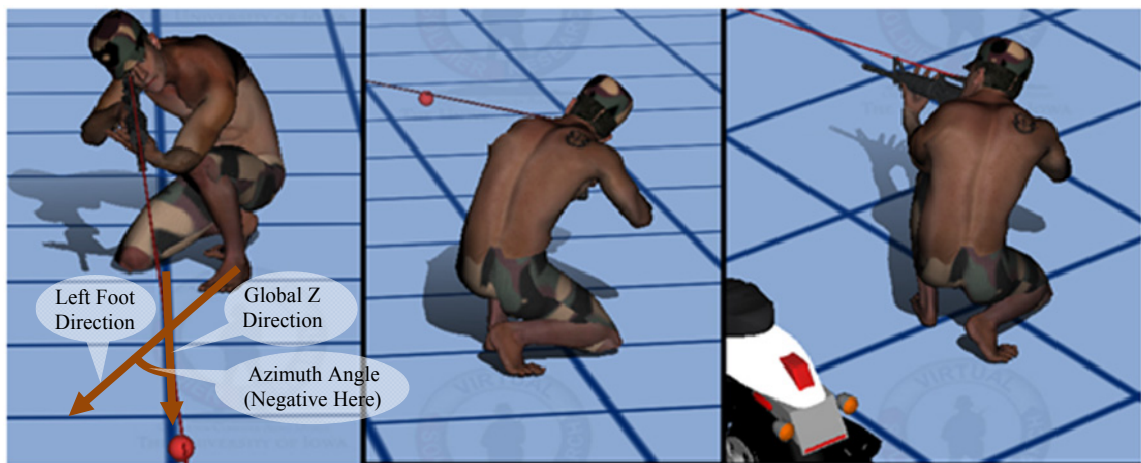


Figure 5.8. Suitable kneeling position when optimization predicts the "Left Foot Azimuth Angle". Target located at (0,.2,3) and "Azimuth Flag =0"

In the picture on the left in Figure 5.8, you can see that the left foot is located at an angle of about 42 degrees to the right of the target line. The resulting kneeling position of the avatar looks much more comfortable than Figure 5.7.

To show the variety of motions made possible by varying "Left Foot Azimuth Angle", we show an extremely uncomfortable case in Figure 5.9 where the soldier is required to engage a specific target having a specific "Left Foot Azimuth Angle".

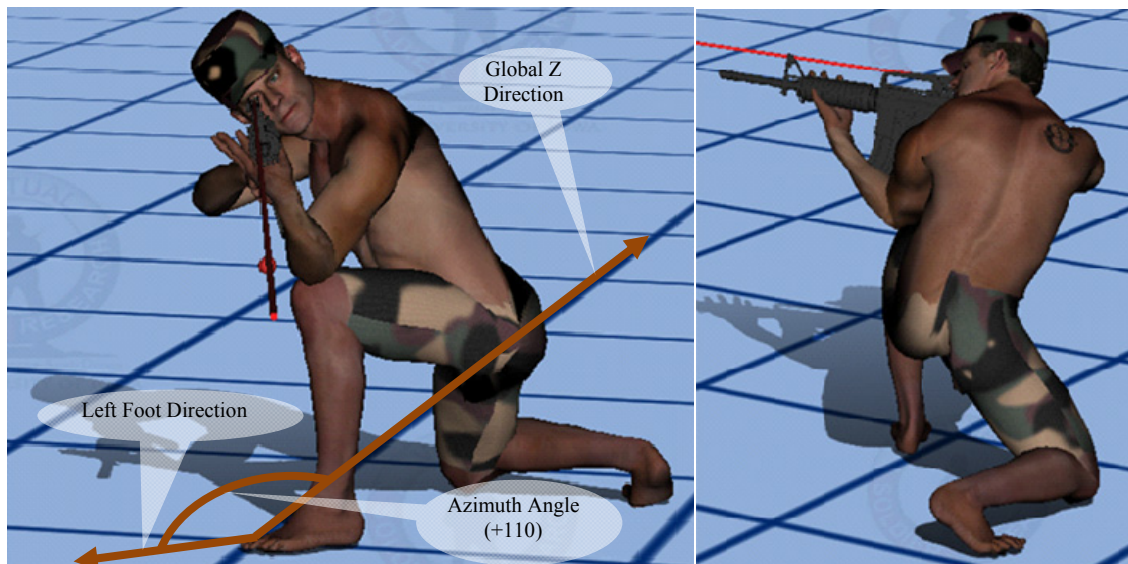


Figure 5.9. An extreme case: Target located at $(-1,1,-3)$, "Azimuth Flag =1" and "Azimuth Angle =110"

5.11 Joint Discomfort Objective Function

When a soldier is performing a military task such as "aiming while kneeling", many of his joints reach their limits. When a joint reaches its limits, normally the two adjacent limbs which are connected by that joint are pressed against each other. The reaction force of this pressing on the internal forces and torques is not present in any of the calculations. To consider these resultant internal forces and torques caused by joints

reaching their limits, a "Joint Discomfort Objective Function" is introduced in this section. The formula for calculating this objective function is proposed as below:

$$f = \int_{t=0}^T \sum_{i=1}^{ndof} \left(\frac{4q_i - 2(ul_i + ll_i)}{ul_i - ll_i} \right)^{2k} dt * scale \quad (5.11.1)$$

$$\text{Where: } \begin{cases} k = 1, 2, 3, \dots \\ q_i \triangleq \text{The value of Joint Angle } i \\ ul_i \triangleq \text{Upper Limit of Joint Angle } i \\ ll_i \triangleq \text{Lower Limit of Joint Angle } i \\ f \triangleq \text{Joint Discomfort Objective Function} \end{cases} \quad (5.11.2)$$

For example, assume that the lower and the upper limits for joint number "i" are respectively equal to: $ll_i = 45$ and $ul_i = 230$. Let $scale = 1$ and $k = 5, 10$. In Figure 5.10, we show the plots of $f_i = \left(\frac{4q_i - 2(ul_i + ll_i)}{ul_i - ll_i} \right)^{10}$ and $f_i = \left(\frac{4q_i - 2(ul_i + ll_i)}{ul_i - ll_i} \right)^{20}$, if we change q_i from $ll_i = 45$ to $ul_i = 230$.

We use this objective function along with the dynamic effort $\left(\int_{t=0}^T \sum_{i=1}^{ndof} \tau_i^2 dt \right)$ objective function to form a multi-objective optimization problem in predictive dynamics. This "Joint Discomfort Objective Function" prevents the joint angles from getting very near to their limits, if it is not necessary for performing the task. It does so by increasing the cost function of the optimization (objective function) by large amounts when joint angles get very near to their limits. The value of k can be modified to change the behavior of the function as shown in the above graphs.

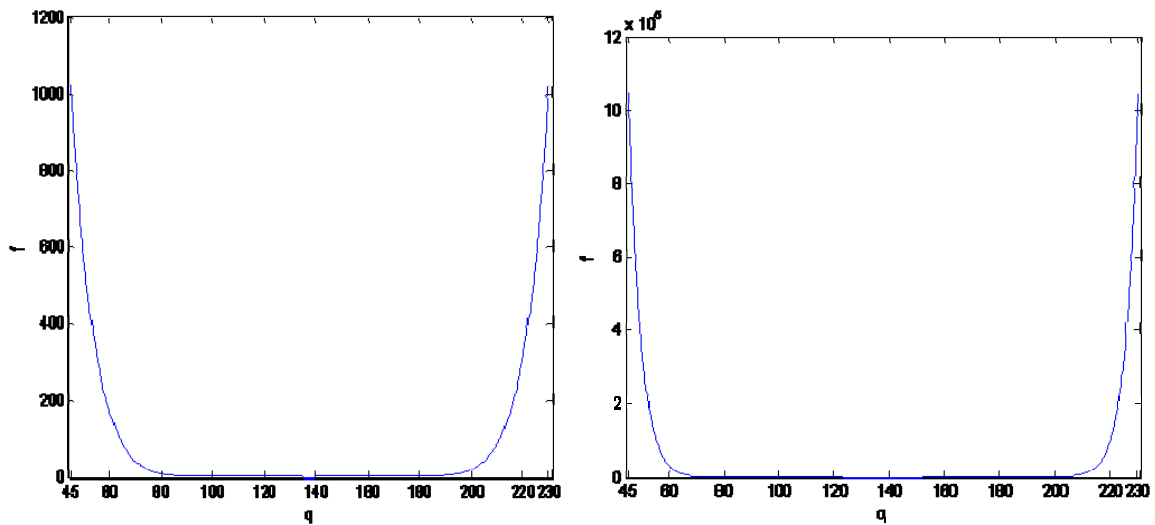


Figure 5.10. Plots of the joint discomfort objective function for $k=5$ (left) and $k=10$ (right)

Without this penalty function, the avatar acts just like a robot in the sense that the avatar "feels that he can use the range of motion of any of its joints fully without worrying whether one of the joints is at its limit while the next joint is in the middle of its range of motion". The effect of this "Joint Discomfort Objective Function" on the final frame of the "aiming while kneeling" task is shown in Figures 5.11, 5.12.



Figure 5.11. Final kneeling position with "Dynamic Effort" as the only objective function (without the "Joint Discomfort Objective Function")



Figure 5.12. Final kneeling position using the "Joint Discomfort Objective Function" along with the "Dynamic Effort Objective Function"

Comparing Figures 5.11 and 5.12, it seems that the results look more natural using the "Joint Discomfort Objective Function" along with the "Dynamic Effort Objective Function". This additional objective function prevents the joint angles to get near their limits as much as possible.

5.12 Problem Formulation for Kneeling

To predict the whole body motion for kneeling, we release the fixed posture assigned for SantosTM upper body in Section 5.6 and use the conclusions of Sections 5.7 to 5.11 and let optimization predict the motion for the whole body. The formulation for kneeling is shown in Table 5.4.

Design Variables:	<i>Joint Angle Profiles $q(t)$</i>
Objective Function:	$f(\mathbf{q}) = \int_{t=0}^T \sum_{i=1}^{ndof} \left(\tau_i^2 + \left((4q_i - 2(u_i + l_i)) / (u_i - l_i) \right)^{2k} * scale \right) dt$
Environment Contact Modeling:	<i>ZMP Method + Linear Partitioning of Contact Forces</i>
Torque Calculation Method:	<i>Recursive Lagrangian Formulation</i>
Constraints Imposed Throughout the motion:	<ul style="list-style-type: none"> • <i>Joint Angle Limits</i> • <i>Torque Limits</i> • <i>Left Foot Position Fixed on the Ground</i> • <i>Left Hand Face Almost Upward and be Perpendicular to Rifle</i> • <i>Look Forward</i> • <i>Collision Avoidance</i>
Initial Motion Frame Constraints:	<ul style="list-style-type: none"> • <i>Right Foot Initial Position</i> • <i>Initial Static Condition</i>
Final Motion Frame Constraints:	<ul style="list-style-type: none"> • <i>Right Knee Touches Ground</i> • <i>Left Elbow Touches Left Knee</i> • <i>Final Static Condition</i>
Additional Final Constraints For Aiming:	<ul style="list-style-type: none"> • <i>Right Shoulder Touches Rifle Butt</i> • <i>Eye Line Parallel to Rifle Line</i> • <i>Right Eye Behind the Sight of the Rifle</i> • <i>The Target Engagement Constraints</i>

Table 5.4. Problem formulation for prediction of "Kneeling"

5.12.1. Kneeling Then Aiming Task

This task consists of two separate stages. They are:

1. Kneeling from Standing Position (Stage 1)

For this motion, the "Additional Final Constraints For Aiming" in the Table 5.4 are ignored. The optimization finds the most comfortable type of kneeling without taking into consideration the aiming requirement that may follow this motion. Figure 5.13 shows different views of the final motion frame of the kneeling task.



Figure 5.13. "Kneeling Then Aiming" task (Stage 1: Kneeling from Standing)

2. Aiming from Kneeling Position (Stage 2)

This motion is assumed to follow the kneeling motion. Therefore, continuity constraints (position, velocity and acceleration) are imposed between this motion and the previous motion. For the final frame of this motion, the "Additional Final Constraints For Aiming" in Table 5.4 are also enforced.

Figure 5.14 shows different views of the final motion frame of the "aiming from kneeling" task.

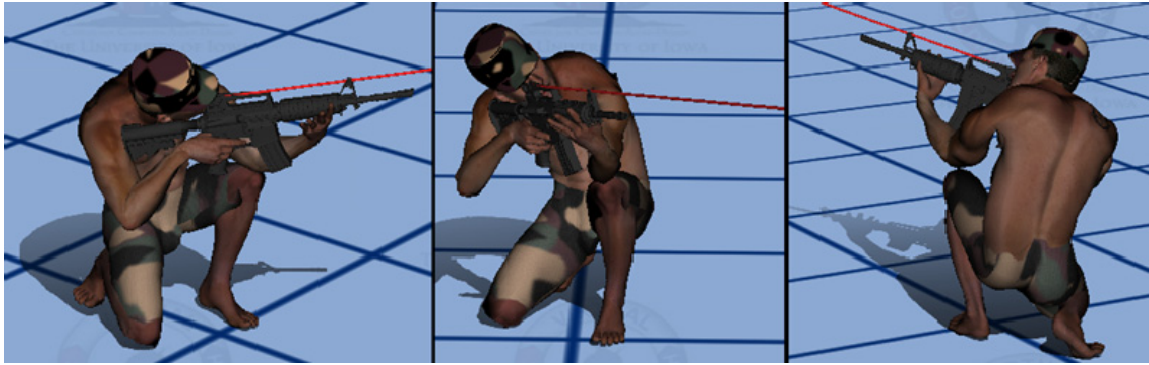


Figure 5.14. "Kneeling Then Aiming" task (Stage 2: Aiming from Kneeling)

5.12.2. Aiming While Kneeling Task

The two subtasks included in the "kneeling then aiming" task in Section 5.12.1 (two separate optimizations) can be replaced by one single task (one single optimization) in which the avatar starts from standing posture and ends in the final posture where he is both kneeling and aiming. In military, this final position is normally referred to as the "kneeling unsupported firing position" where the soldier is not using any obstacle or object as a supporting base for increasing the stability of firing. It means that the intermediate stage where SantosTM gets into the kneeling position without aiming is removed and instead of two separate optimization procedures we have one single optimization procedure. This is a preferred method compared to two separate optimizations, because both aiming and kneeling constraints affect the whole motion,

while the aiming constraints do not affect the motion in stage 1 for the other method. The downside of this method is that we do not see a kneeling position without aiming.

5.13 Motion Prediction Results for Kneeling

Many results of the kneeling motion prediction were shown in previous parts where the formulation was being described. For example, Figures 5.1, 5.4, 5.7, 5.8, 5.9, 5.11, 5.12, 5.13, 5.14 all show the results of the kneeling motion. In this part we show some additional results with different input parameters.

5.13.1. Results for Engaging Targets at Different Positions

In this section, we show the different results obtained by changing the target location. A fixed motorcycle is shown in Figures 5.15 and 5.16 to assist in recognizing the target movement.

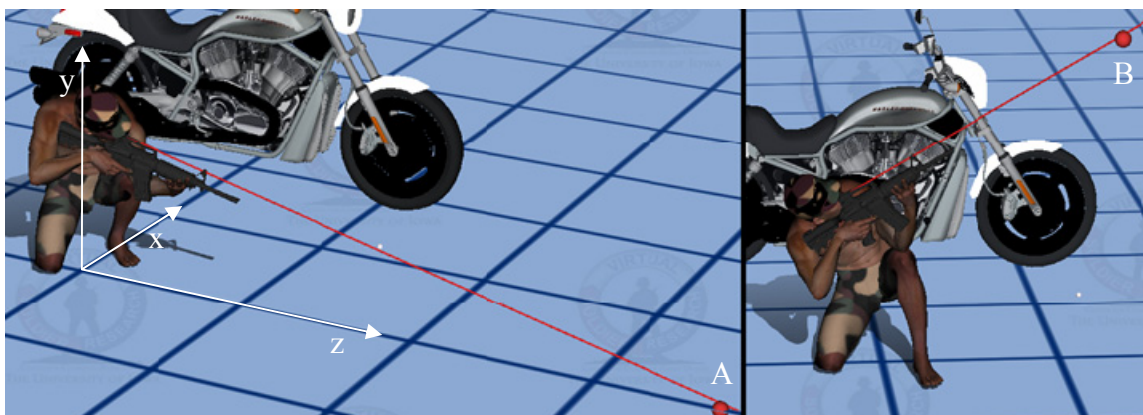


Figure 5.15. Results of kneeling for "Azimuth Flag = 0" and target located at A(0,-1,3) and B(-1,1.5,1)

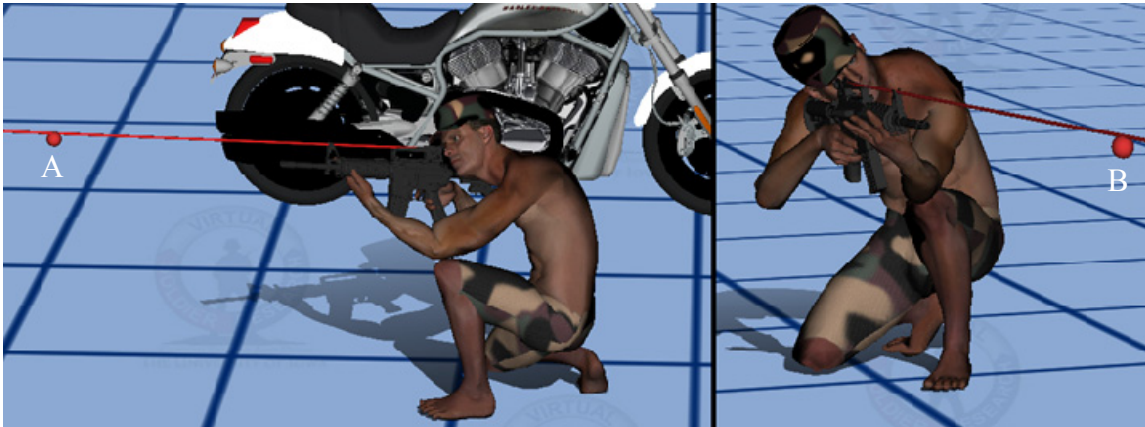


Figure 5.16. Results of kneeling for "Azimuth Flag = 0" and target located at A(-1,1,-1) and B(-1,.7,2)

5.13.2. Cause and Effect Study for Adding Armor

In this section, we study the effect of adding armor plates to different limbs of the avatar on the kneeling task. The major effect of adding armor to two limbs is to reduce the range of motion of the joint connecting them. In other words we are modifying the lower and upper bounds for the "joint angle limits constraint" as mentioned in Table 5.4 and observing the results.

Here, we show the result of adding armor to the back of "Right Upper Leg" and "Right Lower Leg" in two experiments:

- Experiment 1 :

We add two armor chiclets one near right hip and one near right ankle. It reduces the upper limit of the range of motion of the "Right Knee" from 160 degrees (it is a passive joint limit as was shown in Table 5.3) to 126 degrees and run the kneeling prediction code. The results achieved are shown in Figure 5.17. In order

to visually confirm the accuracy of the results, it should be noted that the chiclets are not allowed to interfere with each other in the 3D space. If they do, the results can be visually rejected.

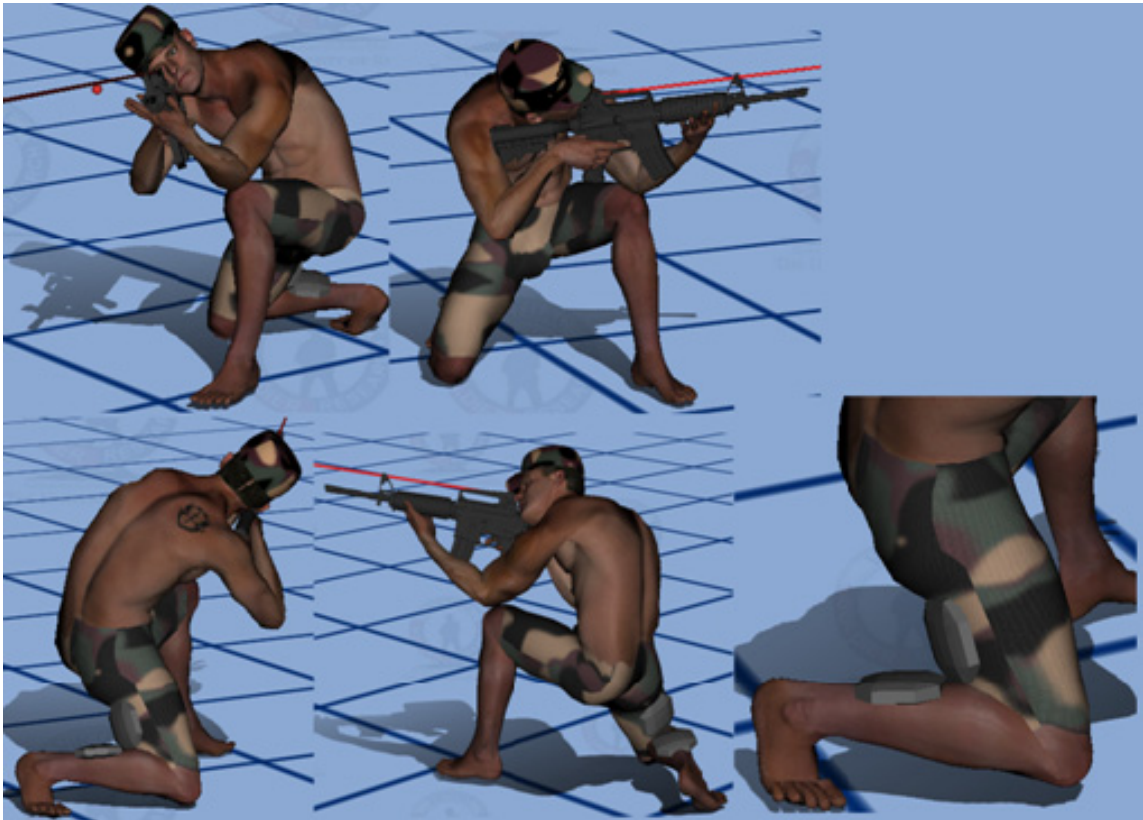


Figure 5.17. Kneeling prediction with two armor chiclets reducing right knee's range of motion

- Experiment 2:

We move the two armor chiclets closer to each other near the Right Knee. It further reduces the upper limit of the range of motion of Right Knee down to 75 degrees. The results achieved are shown in Figure 5.18.

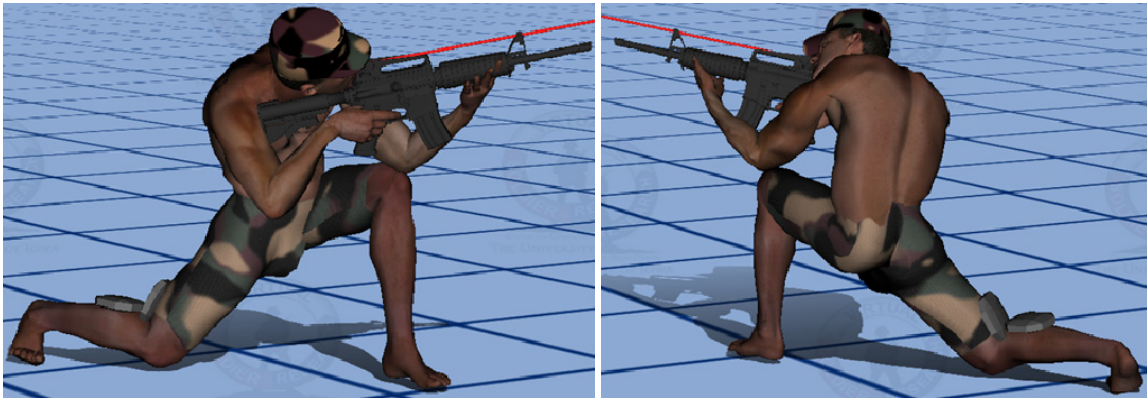


Figure 5.18. Kneeling prediction with armor chiclets reducing right knee's range of motion considerably

5.13.3. Effect of Changing Avatars

Every avatar has a specific set of "Link Lengths". Therefore, different solutions for design variables (joint angle profiles) are required for different avatars if all other inputs remain the same. We predict the kneeling motion for a same target location for different avatars. Target is located at (1,1,1) and "Azimuth Flag" is set to zero so that the optimization predicts the optimal position for engaging the target for different avatars. The results are shown in Figures 5.19 , 5.20. The avatars used in these figures are:

- Santos™ : Male, Average
- Santos A: Male, Tall, Heavy, H-Shaped Torso
- Santos C: Male, Short, Lean, V-Shaped Torso
- Sophia: Female, Tall, Lean

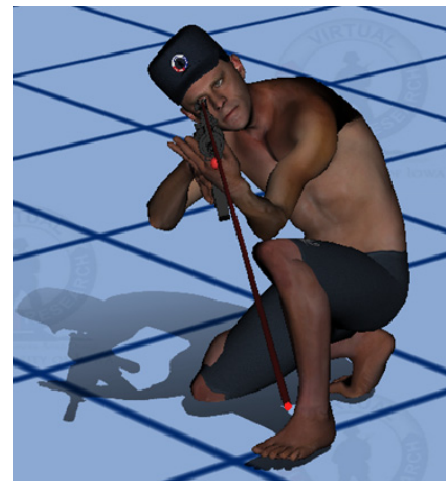


(a)



(b)

Figure 5.19. Slides of the results of "Kneeling then Aiming" motion prediction for different avatars
 (a) "Sophia" avatar (b) "Santos A" avatar



(a)



(b)

Figure 5.20. Results of "Aiming While Kneeling" motion prediction for different avatars:
 (a) "Santos C" avatar
 (b) " Santos A" avatar

It should be noted that if you predict a motion task using a specific avatar, then that result is only valid for that specific avatar. If the solution of a motion task for one avatar is shown on another avatar, very abnormal and visually unacceptable results may be observed. This shows that each avatar requires a different solution.

Aiming tasks are delicate tasks and are very sensitive to an avatar's link lengths, for example, the solution of one avatar will look very bad if it is played on another avatar. In order to demonstrate this issue, some of those results are shown in Figure 5.21.



Figure 5.21. Solution of an avatar played on a different avatar intentionally to show the sensitivity of "Kneeling" task to input parameters
 (a) Solution of "Sophia" incorrectly played on "Santos A"
 (b) Solution of "Santos A" incorrectly played on "Sophia"

5.14 Problem Formulation for Aiming While Standing

As indicated in Section 5.1, considering the timeline of developing dynamic tasks, "kneeling" was the first dynamic task to be studied by the author. The development of kneeling task was slowed down and this task (aiming while standing) was started by the same developer to provide more insight of the "aiming" that was required to be done as the last part of the "kneeling" motion. So, they share most of the concepts which were discussed in previous sections.

Design Variables:	<i>Joint Angle Profiles $q(t)$</i>
Objective Function:	$f(\mathbf{q}) = \int_{t=0}^T \sum_{i=1}^{ndof} \left(\tau_i^2 + \left((4q_i - 2(u_i + l_i)) / (u_i - l_i) \right)^{2k} * scale \right) dt$
Environment Contact Modeling:	<i>ZMP Method + Linear Partitioning of Contact Forces</i>
Torque Calculation Method:	<i>Recursive Lagrangian Formulation</i>
Constraints Imposed Throughout the motion:	<ul style="list-style-type: none"> • <i>Joint Angle Limits</i> • <i>Torque Limits</i> • <i>Feet Position Fixed on the Ground</i> • <i>Left Hand Perpendicular to Rifle</i> • <i>Left Hand Face Almost Upward</i> • <i>Look Forward</i> • <i>Collision Avoidance</i>
Initial Motion Frame Constraints:	<ul style="list-style-type: none"> • <i>Initial Static Condition</i>
Final Motion Frame Constraints:	<ul style="list-style-type: none"> • <i>Final Static Condition</i> • <i>Right Shoulder Touches Rifle Butt</i> • <i>Eye Line Parallel to Rifle Line</i> • <i>Right Eye Behind the Sight of the Rifle</i> • <i>The Target Engagement Constraints</i>

Table 5.5. Problem formulation for prediction of "Aiming"

Same as kneeling, this task uses the "Joint Discomfort Objective Function" discussed in Section 5.11. It also uses the same "Target Engagement Constraints" discussed in Section 5.9. Similar to kneeling, the NPOA concept that is implicitly embedded in Section 5.11 is essential in obtaining comfortable aiming postures. Also, it follows the insight from Section 5.7 to consider expanded ranges of motion for a few joints under pressure. Also, the input and output parameters of this task almost exactly match those of kneeling. The formulation for aiming task is shown in Table 5.5.

5.15 Motion Prediction Results for Aiming While Standing

5.15.1. Results for Engaging Targets at Different Positions

In this section, we show the different results obtained by changing the target location. A fixed motorcycle is shown in Figures 5.22 and 5.23 to assist in recognizing the target movement.

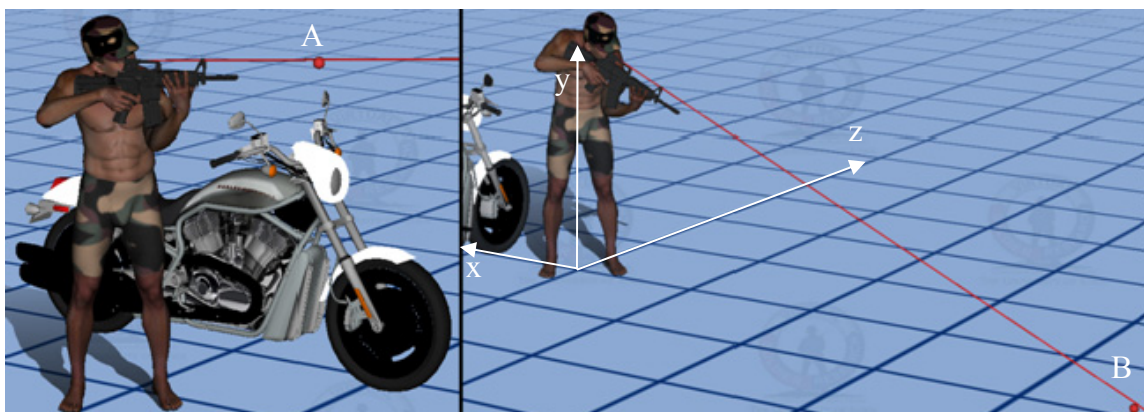


Figure 5.22. Results of aiming for "Azimuth Flag = 0" and target located at $A(0,1.5,1.5)$ and $B(-3,0,0)$

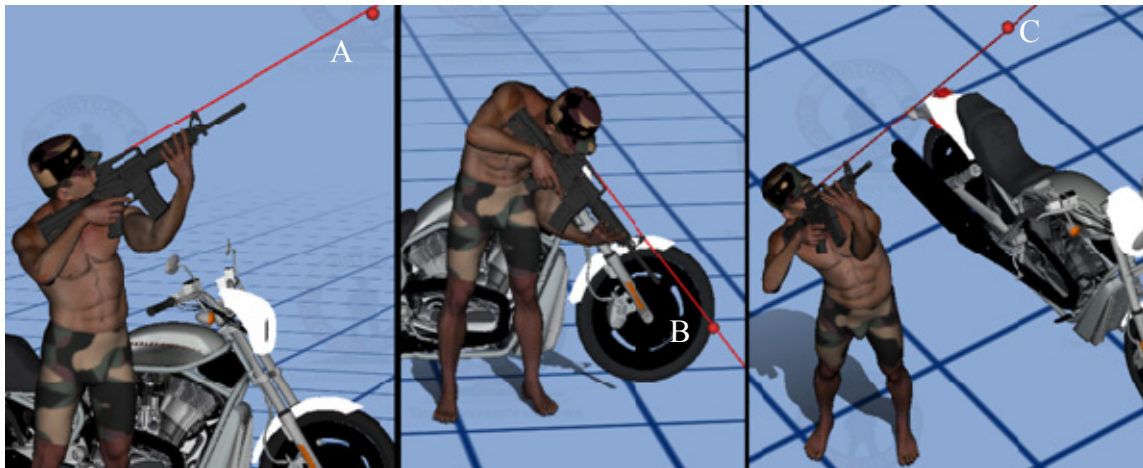


Figure 5.23. Aiming with "Azimuth Flag = 0" and target located at A(0,2,1.5), B(0,.5,1), C(0,3,1.5)

5.15.2. Effect of Changing Avatars

Every avatar has a specific set of "Link Lengths". Therefore, different solutions for design variables (joint angle profiles) are required for different avatars if all other inputs remain the same. We predict the kneeling motion for a same target location for different avatars. Target is located at (1,1,1) and "Azimuth Flag" is set to zero so that optimization predicts the optimal position for engaging the target for different avatars.

The results are shown in Figure 5.24. The avatars shown in these figures are:

- Santos™ : Male, Average
- Santos A: Male, Tall, Heavy, H-Shaped Torso
- Santos D: Male, Short, Heavy, V-Shaped Torso
- Sophia: Female, Tall, Lean



Figure 5.24. Results of "Aiming" for different avatars. Left to right: "Santos D", "Santos A", "Sophia"

It should be noted that if you predict a motion task using a specific avatar, then that result is only valid for that specific avatar. If the solution of a motion task for one avatar is shown on another avatar, very abnormal and visually unacceptable results may be observed. This shows that each avatar requires a different solution.



Figure 5.25. Solution of an avatar played on a different avatar intentionally to show the sensitivity of "Aiming" task to input parameters (a) Solution of "Sophia" incorrectly played on "Santos D" (b) Solution of "Santos D" incorrectly played on "Sophia"

Aiming tasks are delicate tasks and are very sensitive to an avatar's link lengths, for example, the solution of one avatar will look very bad if it is played on another avatar. In order to demonstrate this issue, some of those results are shown in Figure 5.25.

5.16 Validation of the Predicted NPOA in Kneeling and Aiming Tasks

The Natural Point of Aim (NPOA) was predicted for aiming and kneeling tasks in this research. As explained previously, this is accomplished by optimizing the value for the angle between the left foot of the avatar and the target line on the ground. A sample of such predicted values for this angle are shown in Figure 5.26 for aiming and kneeling.

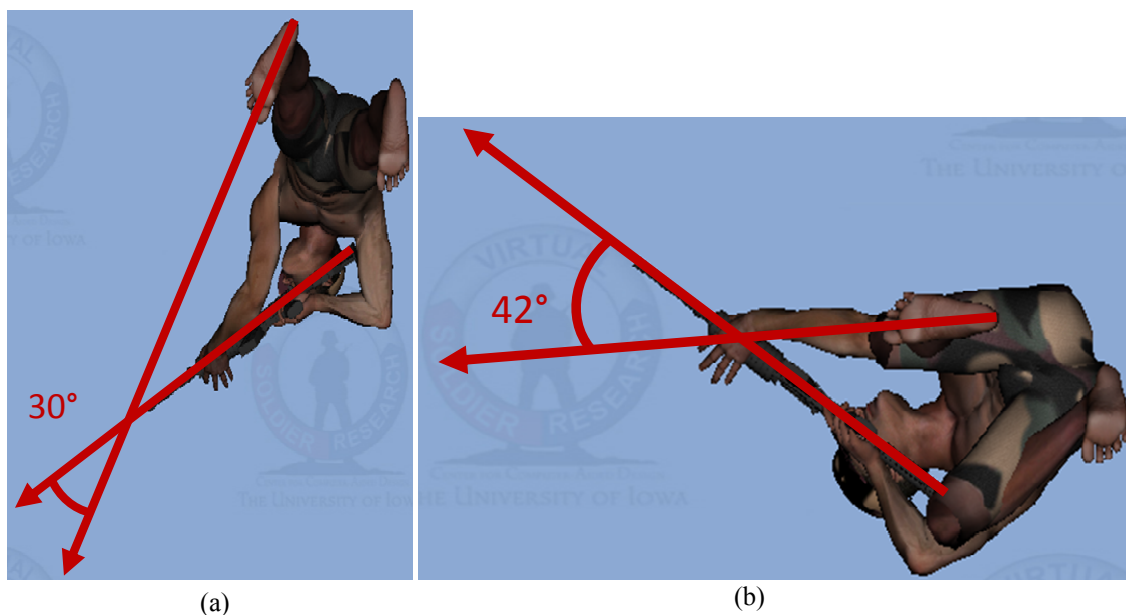


Figure 5.26. Predicted angle between the left foot of avatar and the target line in predictive dynamics for motion tasks: (a) Aiming and (b) Aiming While Kneeling

The NPOA predicted by the predictive dynamics method for aiming and kneeling are validated at the VSR Lab at the University of Iowa. The angle between the left foot of the avatar and the target line on the ground was measured for several subjects performing aiming and kneeling tasks. The results are as follows:

- **Comparison in Aiming While Kneeling**

Four experiments were performed and the below values were observed for the angle:

49 50 53 54

They all seem higher but not very far from the value of 42 degrees that was predicted.

- **Comparison in Aiming While Standing**

Four experiments were performed and the below values were observed for the angle:

34 43 43 51

They all seem higher but not very far from the value of 30 that was predicted.

CHAPTER 6
DYNAMIC SIMULATION OF A SOLDIERS' MOTION USING THE ZMP METHOD:
STAND-PRONE-AIM TASK

6.1 Introduction

The objective of this chapter is to simulate the "stand-to-prone-to-aim" task for a soldier using the Santos™ digital human model. In this chapter, the ZMP method introduced in Chapters 3 and 4 is used to ensure the motion possibility and calculate ground reaction forces. As explained in Sections 4.2-4.5, the ZMP method along with an assumption for the partitioning of ground reaction forces can be used to ensure the possibility of the generation of any arbitrary motion using the given environmental contact areas and calculate the environment contact forces on those contact areas. In Chapter 9, the NCM method along with the assumption of forces as design variables will be used to ensure the motion feasibility and calculate ground reaction forces.

During the Stand-to-Prone-to-Aim motion task, different parts of the body come in contact and lose contact with the ground which is very finely modeled and considered using the general approach introduced in Section 4.4. Using the ZMP method in predictive dynamics as explained in Section 4.2, we can predict a realistic motion for the "Stand-to-Prone-to-Aim" task which consists of two motion subtasks: "going prone" and "aim while prone". The optimization is able to very well predict the "Natural Point of Aim" for the "aim while prone" subtask. In other words, the optimization is able to predict the most comfortable final orientation of the body line for engaging a specific

target. We also simulate cases where the orientation of the soldier's body line is enforced (by the environment or due to the requirements of the task) and not predicted.

Instead of the pistol grip, the rifle stock is held in the right hand and the end of the rifle stock touches the ground as an extra support point in the "Going Prone" subtask. Therefore, the rifle is held by two completely different styles in the "Going Prone" and "aim while prone" subtasks and there will be inevitable transfers of weapon as an external object between the two hands. Collision avoidance of the rifle with the hands and body during these rifle transfers is a very challenging constraint that has been implemented using the collision avoidance of compound primitives such as finite cylinders and finite planes whose edges are smoothed out in order to have continuous gradients for the collision avoidance constraint.

The effect of changing the target location in the 3D space, changing the anthropometry of the soldier, adding backpack, adding armor plates on the shoulder and changing the rifle stock length have also been studied using this approach.

6.2 The Stand-to-Prone-to-Aim Task

In this research, we use the "Rifle Marksmanship" instructions from the "U.S. Army Field Manual" and "U.S. Marine Corps Reference Publication (MCRP)" as the major references for definition of terms and procedures. The "Stand-to-Prone-to-Aim" task can be performed in several ways with or without using the rifle butt as support. In this research we model the classic method presented in U.S. Army (1974) (using the rifle butt). According to U.S. Army (1974) , the stages for this task are:

- 1- The firer stands facing his target, turn 30 degrees to his right.
- 2- Spreads his feet a comfortable distance apart, and drops to his knees.
- 3- With his right hand at the heel of the stock, he places the rifle butt well out to his front on a line connecting the target and his right knee.
- 4- Using the rifle butt as a pivot, the firer rolls down on his left side, placing his left elbow as nearly under the rifle as possible.
- 5- Grasp the pistol grip with the firing hand.
- 6- Place both elbows on the ground to support the upper body.
- 7- Rest the rifle in the "V" formed by the non-firing hand.
- 8- Engage the target (Aim).

The first item in the above list mentions a 30 degree angle. This angle is an initial guess for achieving NPOA and may actually be variable for different soldiers or rifles or target locations. Therefore, instead of enforcing this angle in simulations, we predict the best value for it to maximize comfort (achieve NPOA). However, increasing this angle will increase the exposure of the body of the shooter to the enemy. So, comfort is sometimes sacrificed and the 30 degree value for this angle is less than the value that maximizes comfort. As will be seen in Section 6.11, the digital human avatar (SantosTM) predicts the angle for maximizing comfort which is larger than 30 digress, but matches very well with experimental data that also maximize comfort.

6.3 The Going Prone Subtask






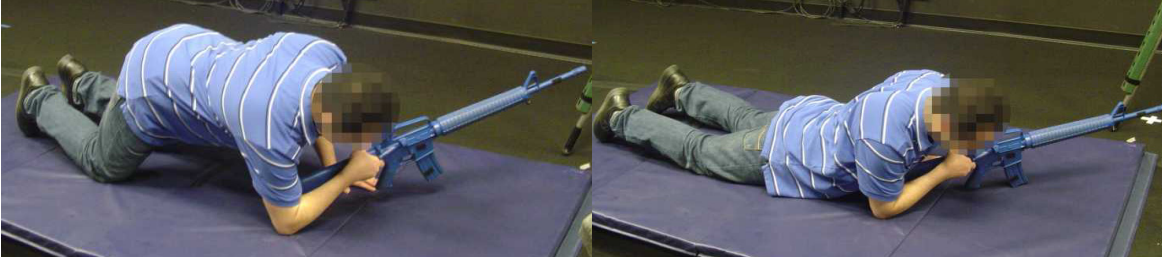
<p>Stage 1: Standing Position. The narrow part of the rifle stock is held in right hand.</p> 	<p>Stage 2: Both Knees touch the ground. Ball of right and left feet are fixed on the ground between stages 1,2.</p> 	<p>Stage 3: Additional to all constraints in Stage 2, rifle stock also touches the ground.</p> 
<p>Stage 4: Constraint for left hand to grip the barrel is removed.</p> 	<p>Stage 5: Left hand fully touches the ground.</p> 	
<p>Stage 6: Right elbow touches the ground. Left hand keeps touching the ground. Hip is lowered.</p> 		

Table 6.1. The stages defined for modeling the going prone subtask

As indicated in Section 6.1, the "Stand-to-Prone-to-Aim" task consists of two motion subtasks: "going prone" and "aim while prone". These two subtasks are connected together by continuity constraints on the position, velocity and acceleration of the design variables (joint angle profiles). We first study the "Going Prone" subtask. This subtask requires several stages. Based on the instructions given to soldiers for performing this subtask, the stages and constraints listed in Table 6.1 have been considered for developing the "going prone" subtask.

6.4 Problem Formulation for Going Prone

This subtask uses the "Joint Discomfort Objective Function" discussed in Section 6.9. Also, it follows the insight from Section 5.7 to consider expanded ranges of motion for some joints under pressure. The formulation for the going prone subtask consists of two optimization problems connected by continuity constraints on the position, velocity and acceleration of the design variables (joint angle profiles).

- Optimization Problem #1

The first optimization problem consists of stages 1, 2, 3 in Table 6.1. The formulation for this optimization problem is shown in Table 6.2.

- Optimization Problem #2

The second optimization problem consists of stages 4, 5, 6 in Table 6.1. The formulation for this optimization problem is shown in Table 6.3.

Design Variables:	<i>Joint Angle Profiles $q(t)$</i>
Objective Function:	$f(\mathbf{q}) = \int_{t=0}^T \sum_{i=1}^{ndof} \left(\tau_i^2 + \left((4q_i - 2(u_i + l_i)) / (u_i - l_i) \right)^{2k} * scale \right) dt$
Environment Contact Modeling:	<i>ZMP Method + Linear Partitioning of Contact Forces</i>
Torque Calculation Method:	<i>Recursive Lagrangian Formulation</i>
Constraints Imposed Throughout the motion:	<ul style="list-style-type: none"> • <i>Joint Angle Limits</i> • <i>Torque Limits</i> • <i>Ground Penetration</i> • <i>Left and Right Foot Balls Fixed</i> • <i>Local z Axis of Right Hand Opposite Direction to the Local z Axis of Left Hand</i> • <i>Look Forward</i> • <i>Left Hand under the Barrel</i> • <i>Collision Avoidance</i>
Initial Motion Frame Constraints:	<ul style="list-style-type: none"> • <i>Initial Static Condition</i>
Constraints Imposed at Stage 2:	<ul style="list-style-type: none"> • <i>Right Knee touches ground.</i> • <i>Left knee touches ground.</i> • <i>Right hip touches right heel.</i> • <i>Left hip touches left heel.</i>
Final Motion Frame Constraints:	<ul style="list-style-type: none"> • <i>Final Static Condition</i> • <i>Rifle stock touches ground.</i>

Table 6.2. Formulation for the first optimization problem of going prone

Design Variables:	<i>Joint Angle Profiles $q(t)$</i>
Objective Function:	$f(\mathbf{q}) = \int_{t=0}^T \sum_{i=1}^{ndof} \left(\tau_i^2 + \left((4q_i - 2(u_i + l_i)) / (u_i - l_i) \right)^{2k} * scale \right) dt$
Environment Contact Modeling:	<i>ZMP Method + Linear Partitioning of Contact Forces</i>
Torque Calculation Method:	<i>Recursive Lagrangian Formulation</i>
Constraints Imposed Throughout the motion:	<ul style="list-style-type: none"> • <i>Joint Angle Limits</i> • <i>Torque Limits</i> • <i>Ground Penetration</i> • <i>Left and Right Knees Fixed</i> • <i>Look Forward</i> • <i>Collision Avoidance</i>
Initial Motion Frame Constraints:	<ul style="list-style-type: none"> • <i>Continuity conditions to the last motion frame of optimization problem #1.</i>
Constraints Imposed at Stage 5:	<ul style="list-style-type: none"> • <i>Left hand palm touches the ground.</i>
Constraints Imposed at Stage 6:	<ul style="list-style-type: none"> • <i>Left Hand Palm Static on Ground</i> • <i>Right elbow touches ground.</i>
Final Motion Frame Constraints:	<ul style="list-style-type: none"> • <i>Final Static Condition</i> • <i>Left Hand Palm Static on Ground</i> • <i>Right Elbow Static on Ground</i>

Table 6.3. Formulation for the second optimization problem of going prone

6.5 Motion Prediction Results for Going Prone

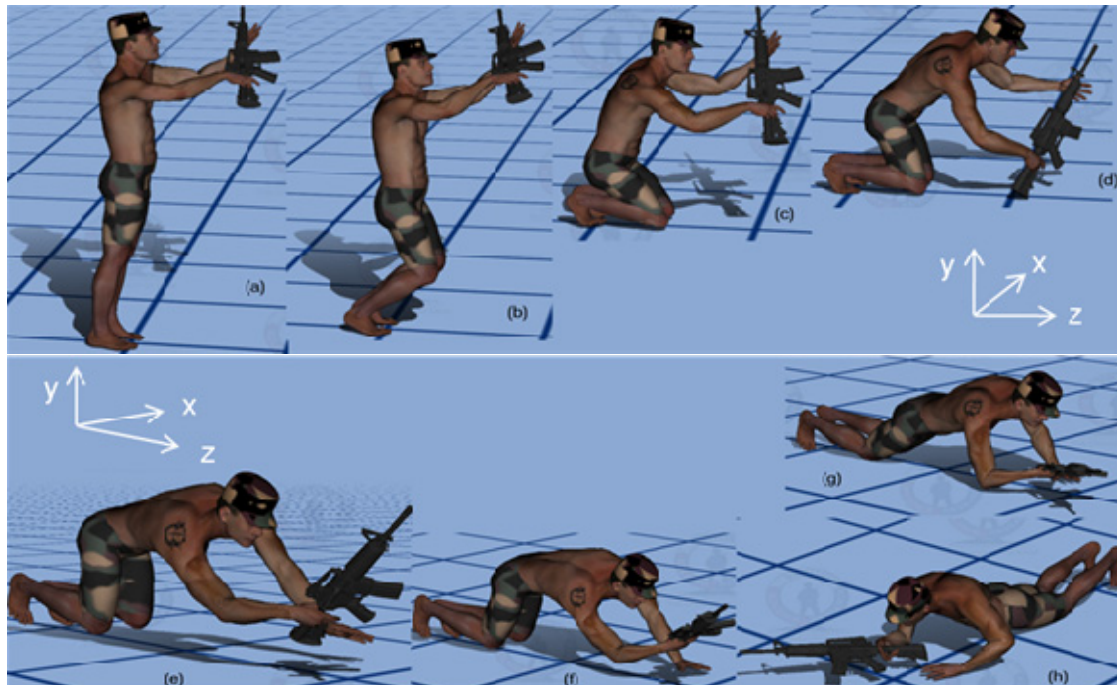


Figure Part	GRF Points (Points that can take ground reaction forces)		Points defining the ZMP convex hull	
(a)	LeftMiddle	RightMiddle	RightHeelOuter LeftToeOuter	RightToeOuter LeftHeelOuter
(b)	LeftMiddle	RightMiddle	RightMiddleOuter LeftToeOuter	RightToeOuter LeftMiddleOuter
(c)	LeftMiddle LeftKnee	RightMiddle RightKnee	RightMiddleOuter RightKnee LeftToeOuter	RightToeOuter LeftKnee LeftMiddleOuter
(d)	LeftToe LeftKnee GunButt	RightToe RightKnee	RightToeOuter GunButt LeftToeOuter	RightKnee LeftKnee
(e), (f)	LeftKnee	RightKnee	LeftKnee	RightKnee
(g)	LeftKnee LeftWrist	RightKnee	LeftKnee LeftWrist	RightKnee
(h)	LeftKnee LeftWrist	RightKnee RightElbow	LeftKnee RightElbow	RightKnee LeftWrist

Figure 6.1. Motion prediction results for the "Going Prone" subtask

The motion prediction frames for the "going prone" subtask are shown in Figure 6.1 with the ground contact modeling for each stage. In this figure, "LeftMiddle" and "RightMiddle" refer to the middle points of the feet. "Outer" postfix refers to the points on the right side of right foot and on the left side of left foot. As it will be discussed, the kinematic results are validated and match well with the experimental data. However, abnormal and unacceptable values were encountered for some components of ground reaction forces and moments.

The ground contact modeling specifies the GRF points and the ZMP boundary points for each motion stage (a,b,c,...,h) as shown in Figure 6.1. The values for ground reaction forces and moments in each direction which are F_x , F_y , F_z , M_x , M_y , M_z , are calculated at each of the GRF points specified for that motion stage.

Going Prone Task	Motion Stage	Time Grid Points
Subtask 1	a	1
	b	2, 3, 4
	c	5, 6
	d	7
Subtask 2	d	1
	e	2, 3, 4
	f	5
	g	6
	h	7

Table 6.4. List of time grid points corresponding to each motion stage of going prone task

Based on the time discretization strategy for the task, each motion stage consists of one or several time grid points. Predictive dynamic calculations including the GRF calculations are performed at each time grid point. In the two subtasks of “going prone”, the time grid points corresponding to each motion stage are as shown in Table 6.4.

The list of GRF points at each motion stage for the going prone task was shown in Figure 6.1. The ground reaction forces and moments at each of those GRF point are calculated at each time grid point (shown in Table 6.4) for the two subtasks. The values of GRF at some of the GRF points are shown in Tables 6.5 and 6.6, for the two subtasks (GRF at Left Knee, Right Knee, Rifle Stock).

Point of Effect of the Ground Reaction Force System	Force, Moment Components	Value at Time Grid #1	Value at Time Grid #2	Value at Time Grid #3	Value at Time Grid #4	Value at Time Grid #5	Value at Time Grid #6	Value at Time Grid #7
Left Knee	Fx	< NA >	< NA >	< NA >	< NA >	-2.046	-1.682	6.274
	Fy	< NA >	< NA >	< NA >	< NA >	140.086	183.641	36.488
	Fz	< NA >	< NA >	< NA >	< NA >	12.211	27.339	-0.266
	Mx	< NA >	< NA >	< NA >	< NA >	38.812	35.496	0.057
	My	< NA >	< NA >	< NA >	< NA >	1.468	3.344	0.398
	Mz	< NA >	< NA >	< NA >	< NA >	-11.361	-16.528	-6.672
Right Knee	Fx	< NA >	< NA >	< NA >	< NA >	-2.030	-1.771	67.737
	Fy	< NA >	< NA >	< NA >	< NA >	138.964	193.443	393.953
	Fz	< NA >	< NA >	< NA >	< NA >	12.113	28.798	-2.871
	Mx	< NA >	< NA >	< NA >	< NA >	38.668	34.685	-5.374
	My	< NA >	< NA >	< NA >	< NA >	-0.553	-1.805	5.863
	Mz	< NA >	< NA >	< NA >	< NA >	11.806	18.208	1.565

Table 6.5. The value of ground reaction forces and moments for the first subtask of going prone

Point of Effect of the Ground Reaction Force System	Force, Moment Components	Value at Time Grid #1	Value at Time Grid #2	Value at Time Grid #3	Value at Time Grid #4	Value at Time Grid #5	Value at Time Grid #6	Value at Time Grid #7
Left Knee	Fx	-43.966	32.046	-44.821	-38.814	0.081	6.517	17.952
	Fy	436.724	306.507	640.312	515.490	320.994	141.418	54.399
	Fz	-39.337	34.896	105.391	167.142	-19.711	-50.271	-61.958
	Mx	-32.505	3.036	-0.500	-0.190	-87.489	-71.605	-40.594
	My	-44.636	2.151	-12.428	35.330	2.320	-8.280	0.882
	Mz	-14.141	-34.781	-19.651	-27.305	-29.518	-14.877	-9.693
Right Knee	Fx	-21.839	64.443	-10.303	-14.961	0.075	6.405	18.443
	Fy	216.937	616.365	147.188	198.694	296.358	138.994	55.886
	Fz	-19.540	70.173	24.226	64.424	-18.198	-49.409	-63.653
	Mx	-16.473	-3.223	-2.413	-3.891	-86.709	-72.657	-41.736
	My	-18.705	-6.646	-7.429	1.048	5.766	0.956	12.314
	Mz	31.833	34.987	22.287	27.356	31.737	10.667	0.048
Rifle Stock	Fx	-8.246	< NA >	< NA >	< NA >	< NA >	< NA >	< NA >
	Fy	81.908	< NA >	< NA >	< NA >	< NA >	< NA >	< NA >
	Fz	-7.378	< NA >	< NA >	< NA >	< NA >	< NA >	< NA >
	Mx	33.901	< NA >	< NA >	< NA >	< NA >	< NA >	< NA >
	My	-2.876	< NA >	< NA >	< NA >	< NA >	< NA >	< NA >
	Mz	13.653	< NA >	< NA >	< NA >	< NA >	< NA >	< NA >

Table 6.6. The value of ground reaction forces and moments for the second subtask of going prone

The kinematic results for the "Going Prone" subtask are validated and match well with the experimental data which is motion captured in the VSR Lab at the University of Iowa. However, abnormal and unacceptable values were encountered for some components of ground reaction forces and moments.

As it is highlighted in Tables 6.5 and 6.6, large and unacceptable values of ground reaction moments are predicted to be exerted from the ground to the avatar at Left Knee, Right Knee, Rifle Stock. These three contact areas have very small contact areas with the ground and therefore they should actually only be able to exert force but no moment

(about the GRF points) to the avatar. Therefore, the highlighted values in Tables 6.5 and 6.6 are completely unacceptable. In Chapter 9 we will discuss this issue in more details and present methods to correct these values.

6.6 The Aim While Prone Subtask





<p>Stage 1: Left Hand is touching the ground.</p>	
<p>Stage 2: Left Hand Leaves the ground and holds the barrel</p>	
<p>Stage 3: Right hand Leaves the stock and holds the handle</p>	
<p>Stage 4: Aiming While in Prone position.</p>	

Table 6.7. The stages defined for modeling the “Aim While Prone” subtask

As indicated in Section 6.1, the "Stand-to-Prone-to-Aim" task consists of two motion subtasks: "going prone" and "aim while prone". These two subtasks are connected together by continuity constraints on the position, velocity and acceleration of the design variables (joint angle profiles). In this section, we study the "aim while prone" (aiming while in prone position) subtask. This subtask requires several stages. Based on the instructions given in Section 6.2, the following stages and constraints listed in Table 6.7 have been considered for developing the "aim while prone" subtask.

6.7 Attachment of Rifle to the Avatar

In general, the rifle may be assumed to be attached rigidly to one of the body segments of the avatar. Therefore, it is possible to define many different types of rifle attachment to the avatar. In the dynamic tasks studied so far (in Chapter 5 and 6), we have encountered 3 different types of rifle attachment which are explained in Table 6.8.

In the Aim-While-Prone task, the type of rifle attachment changes during the motion contrary to previous tasks (aiming, kneeling, going prone) where the type of rifle attachment was constant during the motion. Calculations in each of the motion stages are performed considering the correct type of rifle attachment.


<p>Type 1: The right hand holds the handle of the rifle firmly. This type is used in aiming, kneeling, aim while prone tasks.</p>  <p>Right Hand</p>	
<p>Type 2: The right hand holds the narrow part of the rifle stock firmly. This type is used in going prone, aim while prone tasks.</p>  <p>Right Hand</p>	
<p>Type 3: The left hand holds the barrel of the rifle firmly. This type is only used in aim while prone task.</p>  <p>Left Hand</p>	

Table 6.8. Different types of rifle attachment in aiming, kneeling, going prone, aim while prone tasks

6.8 Problem Formulation for Aim While Prone

As indicated in Section 6.1, the "Stand-to-Prone-to-Aim" task consists of two motion subtasks: "going prone" and "aim while prone". Aim while prone subtask follows the going prone subtask. So, it is connected to the going prone subtask by continuity constraints on the position, velocity and acceleration of the design variables (joint angle profiles). The aim while prone subtask uses the "Joint Discomfort Objective Function" discussed in Section 5.11. Also, it follows the insight from Section 5.7 to consider expanded ranges of motion for some joints under pressure. The formulation for the aim while prone subtask consists of one optimization problem divided into 3 parts.

- Part 1:

The first part of the problem consists of the motion between stages 1 and 2 in Table 6.7. All Calculations in this part should be performed considering "Rifle Attachment Type 2" in Table 6.8. The formulation for this part is shown in Table 6.9:

- Part 2:

The second part of the problem consists of the motion between stages 2,3 in Table 6.7. All Calculations in this part should be performed considering "Rifle Attachment Type 3" in Table 6.8. The formulation for this part is shown in Table 6.10.

- Part 3:

The third part of the problem consists of the motion between stages 3 and 4 in Table 6.7. All Calculations in this part should be performed considering "Rifle Attachment Type 1" in Table 6.8. The formulation for this part is shown in Table 6.11.

Design Variables:	<i>Joint Angle Profiles $q(t)$</i>
Objective Function:	$f(\mathbf{q}) = \int_{t=0}^T \sum_{i=1}^{ndof} \left(\tau_i^2 + \left((4q_i - 2(u_i + l_i)) / (u_i - l_i) \right)^{2k} * scale \right) dt$
Environment Contact Modeling:	<i>ZMP Method + Linear Partitioning of Contact Forces</i>
Torque Calculation Method:	<i>Recursive Lagrangian Formulation</i>
Constraints Imposed Throughout the motion:	<ul style="list-style-type: none"> • <i>Joint Angle Limits</i> • <i>Torque Limits</i> • <i>Ground Penetration</i> • <i>Look Forward</i> • <i>Collision Avoidance</i> • <i>Right Elbow Static</i>
Initial Motion Frame Constraints:	<ul style="list-style-type: none"> • <i>Initial Static Condition</i> • <i>Continuity Constraints (From Going Prone)</i>
Final Motion Frame Constraints:	<ul style="list-style-type: none"> • <i>Left Hand Under the Barrel</i> • <i>Left elbow touches ground.</i> • <i>Continuity of Rifle Motion (Without this constraint, the rifle would jump from one location to another location, when type of rifle attachment changes.)</i>

Table 6.9. Formulation for the first part of "Aim While Prone"

Design Variables:	<i>Joint Angle Profiles $q(t)$</i>
Objective Function:	$f(\mathbf{q}) = \int_{t=0}^T \sum_{i=1}^{ndof} \left(\tau_i^2 + \left((4q_i - 2(u_i + l_i)) / (u_i - l_i) \right)^{2k} * scale \right) dt$
Environment Contact Modeling:	<i>ZMP Method + Linear Partitioning of Contact Forces</i>
Torque Calculation Method:	<i>Recursive Lagrangian Formulation</i>
Constraints Imposed Throughout the motion:	<ul style="list-style-type: none"> • <i>Joint Angle Limits</i> • <i>Torque Limits</i> • <i>Ground Penetration</i> • <i>Look Forward</i> • <i>Collision Avoidance</i> • <i>Left Elbow Static</i>
Final Motion Frame Constraints:	<ul style="list-style-type: none"> • <i>Right hand gets hold of the handle.</i> • <i>Right elbow touches ground.</i> • <i>Continuity of Rifle Motion (Without this constraint, the rifle would jump from one location to another location, when type of rifle attachment changes.)</i>

Table 6.10. Formulation for the second part of "Aim While Prone"

Design Variables:	<i>Joint Angle Profiles $q(t)$</i>
Objective Function:	$f(\mathbf{q}) = \int_{t=0}^T \sum_{i=1}^{ndof} \left(\tau_i^2 + \left((4q_i - 2(u_i + l_i)) / (u_i - l_i) \right)^{2k} * scale \right) dt$
Environment Contact Modeling:	<i>ZMP Method + Linear Partitioning of Contact Forces</i>
Torque Calculation Method:	<i>Recursive Lagrangian Formulation</i>
Constraints Imposed Throughout the motion:	<ul style="list-style-type: none"> • <i>Joint Angle Limits</i> • <i>Torque Limits</i> • <i>Ground Penetration</i> • <i>Look Forward</i> • <i>Collision Avoidance</i> • <i>Right and Left Elbows Static</i>
Final Motion Frame Constraints:	<ul style="list-style-type: none"> • <i>Right Shoulder Touches Rifle Butt</i> • <i>Eye Line Parallel to Rifle Line</i> • <i>Right Eye Behind the Sight of the Rifle</i> • <i>Target Engagement Constraints</i> • <i>Left Palm under the Barrel</i> • <i>Final Static Condition</i>

Table 6.11. Formulation for the third part of "Aim While Prone"

6.9 Rifle Motion in the Aim While Prone Task

As described previously in Section 6.7, the rifle is assumed to be attached rigidly to either the left hand or right hand at a specific orientation and rotation denoted in Table 6.8 by Type 1, Type 2 or Type 3 rifle attachment.

"Continuity of Rifle Motion" constraint which is seen twice in Section 6.8 (in Tables 6.9 and 6.10) ensures that the orientation and the global position of the rifle remains the same when the rifle is transferred in Stage 2 in Table 6.7 (type of rifle attachment changes from Type 2 to Type 3) and Stage 3 (type of rifle attachment changes from Type 3 to Type 1). In the real world the transfer of the rifle from a primary attachment to a secondary attachment is usually accomplished by loosening (making less rigid) the primary attachment and making the secondary attachment more rigid such that at the instant of the transfer (see position 2 and position 3 pictures), both the primary and the secondary attachments are loose (non-rigid). But in predictive dynamics, we only calculate and visualize a rigid attachment of the rifle. Therefore in Stage 2 and Stage 3 in our code, the rifle is rigidly attached to the left and right hand, which is not the same as the experiment pictures in Table 6.7 where rifle attachment is loose in both hands.

For more clarification, we compare Stage 2 in the real world with Stage 2 in our simulations. In Table 6.12, this comparison is performed for 2 different cases of rifle continuity constraints in the predictive dynamics code. In one case, the constraint is "loosely" (increased tolerance for the constraint function) and in the other case, the constraint is imposed "strictly" (decreased tolerance for the constraint function).




<p>Stage 2 in the Experiment:</p>	<p>Left Hand Leaves the ground and holds the barrel</p> 
<p>Stage 2 in the predictive dynamics code with continuity constraint imposed loosely (Rifle motion is not continuous and it jumps during the transfer from Type 2 to Type 3 attachments):</p> 	<p>Stage 2 in the predictive dynamics code with continuity constraint imposed strictly (Rifle motion is continuous and it transfers from a rigid attachment Type 2 to another rigid attachment Type 3 without any jump):</p> 

Table 6.12. Comparison of the stage 2 of "Aim While Prone" in the real world with our simulations

We also compare Stage 3 in the real world with Stage 3 in our simulations. Similar to Table 6.12, in Table 6.13, this comparison is performed for 2 different cases of "loose" and "strict" rifle continuity constraints.




<p>Stage 3 in the Experiment: Right hand Leaves the stock and holds the handle.</p> 	
<p>Stage 3 in the predictive dynamics code with continuity constraint imposed loosely (Rifle motion is not continuous and it jumps during the transfer from Type 3 to Type 1 attachment):</p> 	<p>Stage 3 in the predictive dynamics code with continuity constraint imposed strictly (Rifle motion is continuous and it transfers from a rigid attachment Type 2 to another rigid attachment Type 3 without any jump):</p> 

Table 6.13. Comparison of the stage 3 of "Aim While Prone" in the real world with our simulations

Rigid attachments of the rifle to hands in our simulation in the pictures in Tables 6.9 and 6.10 are highlighted by white circles. The jumps in the rifle motion mentioned in Tables 6.9 and 6.10 at stages 2 and 3 (if continuity constraints are loose) do not model the loose attachment of weapon well enough because collisions may occur between these

jumps which cannot be calculated or avoided. We have assumed that these jumps are unacceptable although this assumption reduces the feasible solution space size in optimization.

6.10 Collision Avoidance Implementation in Aim While Prone

When the rifle motion continuity constraint was imposed strictly as mentioned in Section 6.9, it was observed that the rifle penetrates the head of the avatar very obviously and the result is by no means acceptable and is far from the reality. The snapshots of the motion when the rifle penetrates the avatar's head are shown in Figure 6.2.



Figure 6.2. Penetration of rifle into the avatar without collision avoidance constraints

Therefore, it is necessary to use the collision avoidance modules explained in Appendix A to avoid the collision between the rifle and the head of the avatar. All the spheres that fill (model) different segments of the avatar are previously defined in an

input file ("segment_structure.txt") for all predictive dynamics tasks. To implement collision avoidance for any object in the environment, we need to fill it by using spheres, infinite cylinders, infinite planes, finite cylinders or finite planes as explained in Appendix A. In order to model the rifle in collision avoidance, we can use a model as shown below which consists of 4 finite cylinders and 2 finite planes. For simplicity, initially we only consider one finite cylinder for modeling the rifle. The considered finite cylinder is highlighted in Figure 6.3.



Figure 6.3. Modeling of rifle for collision avoidance with one finite cylinder

Change in the results after the implementation of collision avoidance is shown in Figure 6.4. The only change in the code is the addition of the collision avoidance of head (one moving sphere which is defined in the input file "segment_structure.txt") with rifle (one finite cylinder moving as a function of design variables in space).



Figure 6.4. Preventing the interference of rifle with the avatar using collision avoidance constraints



Figure 6.5. Comparison of the results with and without collision avoidance: Collision avoidance constraints change the avatar's motion to prevent the penetration of the rifle with the avatar.

We compare the snapshots between Figures 6.2 and 6.4 in Figure 6.5. Comparing the two snapshots in Figure 6.5, one can see that the avatar has moved its head back,

changed the orientation of the rifle by bending its wrist and has moved its right elbow closer to the body to elevate the upper body (all decided by optimization) to avoid the collision of the rifle with its head.

However, the modeling of the rifle shown in Figure 6.3 was not enough to completely avoid any collision of the whole rifle with all body segments of the avatar. Still, the left and right hands of the avatar occasionally penetrated other parts of the rifle that were not modeled in Figure 6.3. For a more detailed modeling of the rifle in collision avoidance, we use 5 finite cylinders and 2 finite planes. The considered finite cylinders and finite planes are highlighted in Figure 6.6.



Figure 6.6. Modeling of rifle for collision avoidance with 5 finite cylinders and 2 finite planes

The modeling shown in Figure 6.6 improves the collision avoidance to more completely avoid the collision of the whole rifle with the avatar. However, no matter how much detail is considered in modeling the rifle in collision avoidance, still minor collisions may occur. Because the constraints in predictive dynamics are imposed at a finite number of stages during the motion and minor collision still may occur and remain undetected in the intervals between constraint checks. The solution would be to increase the number of constraint checks. However, doubling the number of constraint checks is always equal to doubling the number of constraints in the optimization algorithm and slows down the speed of computation. To overcome this drawback, unlike other tasks, in aim while prone task, we check the constraints with different frequency during the motion. In the intervals where collisions are more likely to occur, the frequency of constraint checks during the motion is set to be much higher than the intervals where collisions are less likely to occur. With this strategy, suitable results are achieved for the aim while prone task.

6.11 Motion Prediction Result for Aim While Prone

The motion prediction frames for the "aim while prone" subtask are shown in Figure 6.7 along with the ground contact modeling for each stage.

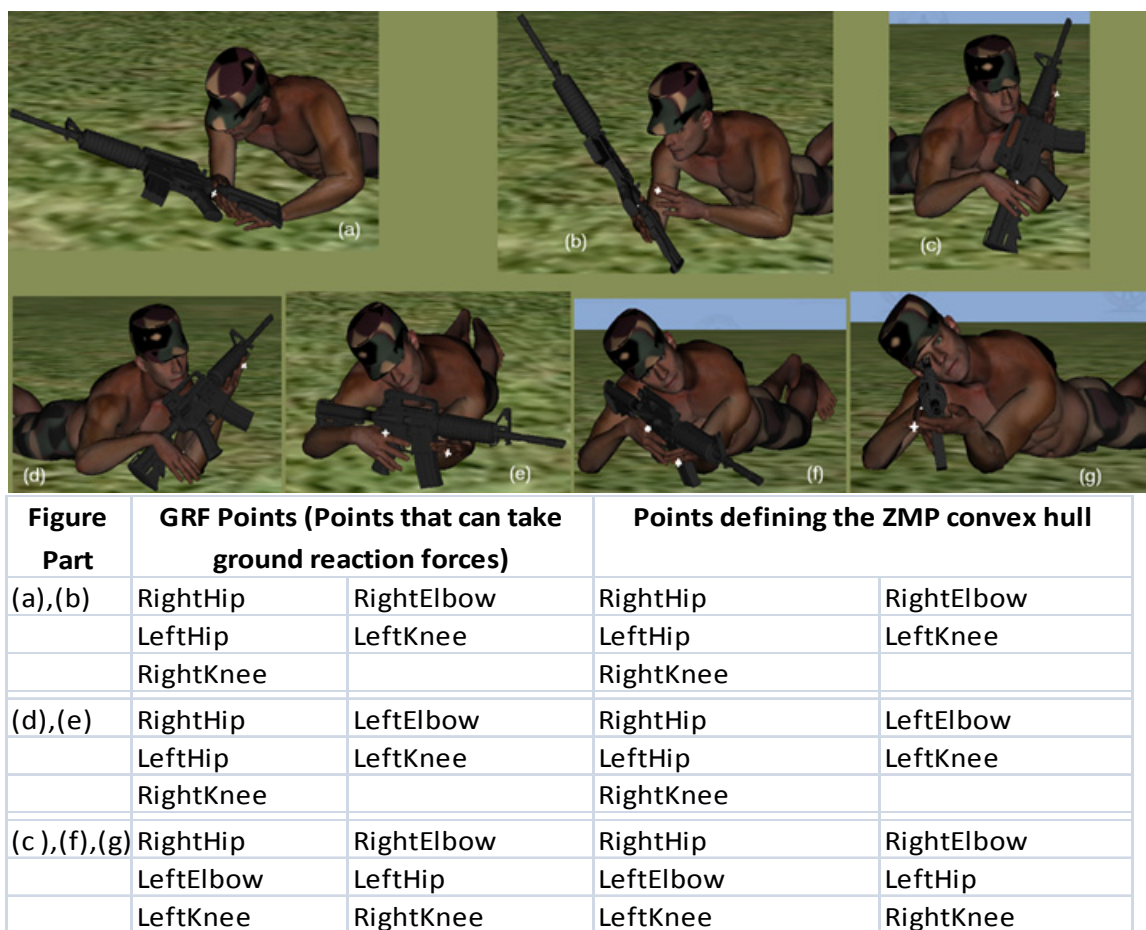


Figure 6.7. Motion prediction results for the "Aim While Prone" subtask

6.11.1. Results for Changing Target Engagement Inputs

In this section, first we compare the results for the case when the "Body Azimuth Angle" explained in Section 6.6.1 is enforced (Azimuth Flag=1) versus the case where it is predicted (Azimuth Flag =0). Figure 6.8 shows the last motion frame for the case where body azimuth angle is predicted. Figure 6.9 shows the last motion frame for the case where body azimuth angle is enforced to have a value of "-10" degrees. The target is located at (0,1,100) in both cases. Visually, the predicted case looks more comfortable.

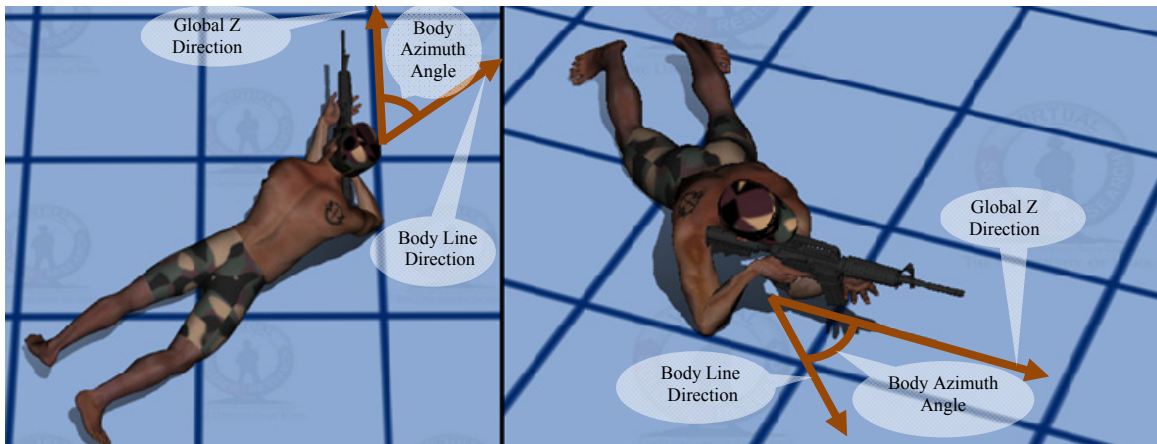


Figure 6.8. Comfortable "Aim While Prone" motion with predicted "Body Azimuth Angle"

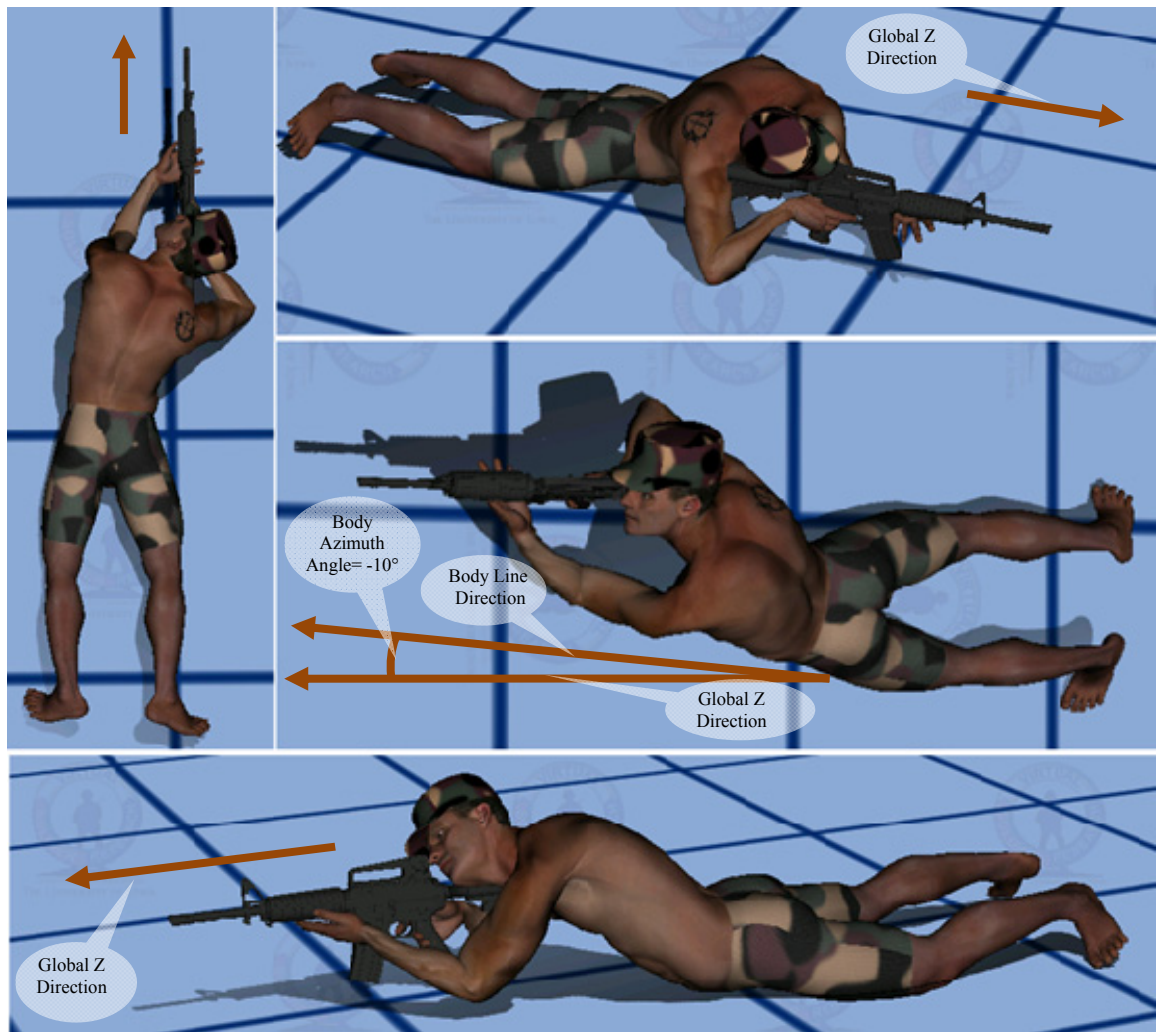


Figure 6.9. Uncomfortable "Aim While Prone" motion with enforced "Body Azimuth Angle=-10°"

As another example for changing target engagement inputs, we change the target location and observe the change in results. Figure 6.10 shows the results for two target locations at (0,1,100) and (0,20,100). “Body Azimuth Angle Flag” as described in Section 6.6 is set to zero for both cases. Therefore, the optimization predicts the best body orientation to engage these targets.



Figure 6.10. Results of "Aim While Prone" for target located at Left: (0,20,100), Right: (0,1,100)

6.11.2. Results for Changing the Rifle Stock Length

Due to its importance, the effect of "changing the rifle stock length" or "adding armor plate to the shoulder" needs to be studied closely in all aiming tasks. Therefore, this value is directly given to all the aiming tasks by an input number. This input number specifies the difference between the modified "Rifle Stock Length" (or the thickness of armor) and its default value. This input number can be either positive or negative. For example a value of zero indicates the default rifle stock length (or no Armor plate on shoulder). The effect of changing this number is shown in Table 6.14 for the aim while prone task.





<p>Rifle Stock Length Retracted by 2 cm</p>	
<p>No Armor Plate or Default Rifle Stock Length</p>	
<p>Armor Plate Thickness or Rifle Stock Length Increased by 5 cm</p>	
<p>Armor Plate Thickness or Rifle Stock Length Increased by 8 cm</p>	

Table 6.14. Results of "Aim While Prone" for variable rifle stock length (shoulder armor plate thickness)

6.12 Validation of the Predicted NPOA and the Motion

To validate the predicted NPOA in the "Aim While Prone" subtask, the angle between the body line and the target line on the ground was measured for several subjects. The average angle observed was 52.47 degrees. The predicted angle shown in Figure 6.11 is normally about 54 degrees which matches very closely with the experiment.



Figure 6.11. Predicted angle between the body line and target line to minimize joint discomfort

The results for the "Going Prone" subtask are also independently validated and match well with the experimental data which is motion captured in the VSR Lab at the University of Iowa.

CHAPTER 7

NORMAL CONTACT MOMENT (NCM) CONCEPTS

7.1 Introduction

The goal of this chapter is to present a general set of constraints on the equivalent contact force systems of individual non-adhesive contact areas which model the non-adhesiveness of the contact areas. These constraints can be used to model dynamic systems with several non-adhesive contact areas with the environment. These contact areas can be oriented arbitrarily with respect to each other and do not have to be coplanar (unlike what was required for the ZMP concepts). In order to do so, a new concept of Normal Contact Moment (NCM) point is introduced and used to model the non-adhesiveness property.

Based on the general constraints, we will also define margins of tipping and slipping stabilities in Chapter 10 which are also applicable for the most general cases of contact areas.

7.2 Motivation for NCM Constraints

As was described in Chapter 4 and implemented in Chapters 5 and 6, the effect of distributed forces acting on a system from a contact area are modeled by equivalent contact force systems (forces and moments) in the predictive dynamics method. It was observed in the simulation results of the “going prone” task in Chapter 6, that some of the components of these contact force systems calculated by the ZMP method seemed to be

unacceptable, considering the ground contact areas to be non-adhesive. Therefore, it is investigated to determine if there are any realistic bounds on the contact forces and moments.

Non-adhesiveness of an environmental contact area of a dynamic system imposes two distinct types of limitations on the distributed contact forces that can be applied from that contact area on the system. They need to be unilaterally compressive and also obey coulomb friction laws.

In this chapter we model the effect of distributed contact forces on a contact area by an equivalent concentrated reaction force systems (a force vector and a moment vector). The limitations imposed on the distributed contact forces result in some constraints on the equivalent force systems. The effect of the unilaterality of distributed contact forces on equivalent contact force systems is addressed by defining a point called Normal Contact Moment (NCM) point and the corresponding NCM constraints. The coulomb friction constraints presented in this chapter also use the definition of the NCM point.

7.3 Definitions for Environment Contact Modeling

Consider a digital human model Φ having rigid, flat, non-adhesive contact areas with other bodies in the environment (such as the ground), as shown in Figure 7.1. Consider one of its contact areas with another solid body Ψ . Although not necessary for the derivations in this research, let us assume that Ψ is fixed and non-movable. Consider this contact area Γ (the contact area of the hand of the avatar with the environment) and

the convex hull of this contact area denoted by Υ to be on an arbitrary plane σ and a right-handed local reference coordinate frame $\mathbf{e}_1, \mathbf{e}_2, \mathbf{e}_3$ attached to the plane with \mathbf{e}_3 normal to the plane pointing from Ψ towards Φ . Let \mathbf{f}_c denote the distributed contact force on Γ applied from Ψ on Φ at location \mathbf{r} (in the $\mathbf{e}_1, \mathbf{e}_2, \mathbf{e}_3$ reference frame).

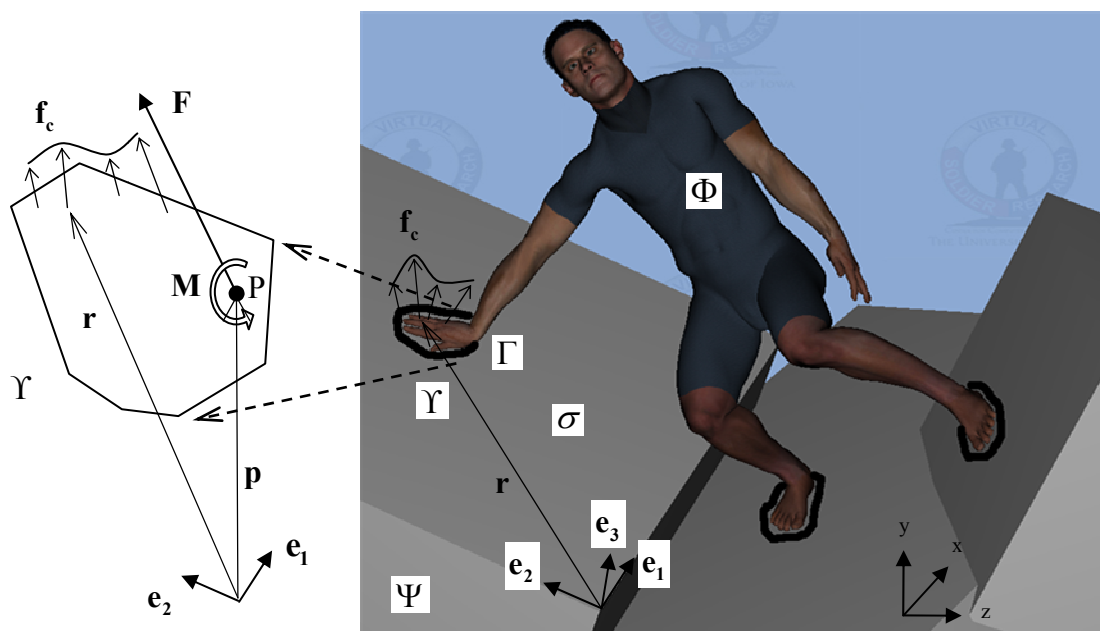


Figure 7.1. A schematic of the general environmental contact problem

7.4 Replacing Distributed Contact Forces by Concentrated Equivalent

This section explains that it is a valid assumption to consider one concentrated force and one concentrated moment to represent the effect of reaction distributed forces exerted from any contact area, such as Γ , on body Φ . Because the contact area Γ is

rigid, it is always possible to replace the distributed contact forces \mathbf{f}_c by a resultant force \mathbf{F} and a resultant concentrated moment \mathbf{M} at any desired point acting from body Ψ to body Φ . The effect of the resultant is the same as distributed forces in our calculations, because we do not consider the deformation of Γ . Let us define \mathbf{F} and \mathbf{M} to act at a point P located at \mathbf{p} on plane σ (inside or outside the contact area) as shown in Figure 7.1. Therefore we have:

$$\mathbf{F} = \int_{\Gamma} \mathbf{f}_c dA \quad , \quad \mathbf{M} = \int_{\Gamma} (\mathbf{r} - \mathbf{p}) \times \mathbf{f}_c dA \quad (7.4.1)$$

Also, let us define the components of vectors \mathbf{F} , \mathbf{M} , \mathbf{f}_c and \mathbf{p} in the coordinate frame $\mathbf{e}_1, \mathbf{e}_2, \mathbf{e}_3$ such that:

$$\left\{ \begin{array}{l} \mathbf{M} = M_1 \mathbf{e}_1 + M_2 \mathbf{e}_2 + M_3 \mathbf{e}_3 \\ \mathbf{p} = p_1 \mathbf{e}_1 + p_2 \mathbf{e}_2 + p_3 \mathbf{e}_3 \end{array} \quad , \quad \left\{ \begin{array}{l} \mathbf{F} = F_1 \mathbf{e}_1 + F_2 \mathbf{e}_2 + F_3 \mathbf{e}_3 \\ \mathbf{f}_c = f_1 \mathbf{e}_1 + f_2 \mathbf{e}_2 + f_3 \mathbf{e}_3 \end{array} \right. \right\} \quad (7.4.2)$$

7.5 Replacing Concentrated Contact Forces by Distributed Equivalents

This section explains that a non-adhesive contact surface is not able to exert every arbitrary \mathbf{F} and \mathbf{M} on body Φ . It is obvious that the contact area Γ can exert any arbitrary \mathbf{F} and \mathbf{M} on body Φ if and only if it is possible to find non-adhesive distributed contact forces on Γ to replace \mathbf{F} and \mathbf{M} . Therefore, we consider the inverse problem of replacing a concentrated force and a moment at any point P located at \mathbf{p} on

plane σ by distributed contact forces \mathbf{f}_c acting from body Ψ on body Φ through the contact area Γ as shown in Figure 7.1. Unlike the problem discussed in Section 7.4, this inverse problem may not always have a solution, because the contact area Γ is assumed to be non-adhesive. Non-adhesiveness of contact area Γ limits its ability to produce all desired arbitrary resultant contact forces and moments \mathbf{F} and \mathbf{M} . In other words it is not always possible to replace any desired \mathbf{F} and \mathbf{M} by distributed contact forces \mathbf{f}_c acting on contact area Γ . Non-adhesiveness limits the choices for \mathbf{F} and \mathbf{M} in the following ways:

➤ Limitation 7.1:

\mathbf{f}_c can only have positive components along \mathbf{e}_3 axis

➤ Limitation 7.2:

Coulomb friction law limits the possible values for planar (frictional) components of the distributed forces and therefore the concentrated force and moment (F_1, F_2, M_3).

7.6 Definitions of NCM Point and NCM Force System

To study the possibility of replacing a desired \mathbf{F} and \mathbf{M} acting at \mathbf{p} under Limitation 7.1, we define a point and a force system called NCM (Normal Contact Moment) point and NCM force system corresponding to \mathbf{F} , \mathbf{M} and \mathbf{p} which only depend on the components of these three vectors.

Definition 7.1: NCM Point and NCM Force System

NCM point is defined as that point on plane σ at which the moment of the force system equivalent to \mathbf{F} and \mathbf{M} will be only about the normal axis to the plane σ . We call that equivalent force system the NCM force system (the contact force system in which the contact moment is normal to the contact area) and denote it by \mathbf{F} and \mathbf{M}' as shown in Figure 7.2.

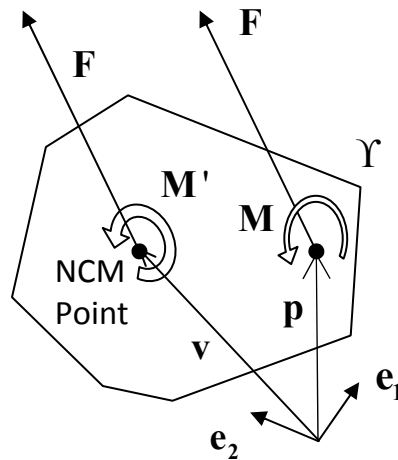


Figure 7.2. The NCM force system equivalent to \mathbf{F} , \mathbf{M}

The convex hull Y of the contact area from Figure 7.1 along with the NCM point and the NCM force system corresponding to \mathbf{F} and \mathbf{M} are shown in Figure 7.2. Therefore \mathbf{M}' should have no component along \mathbf{e}_1 and \mathbf{e}_2 . The location of the NCM point, denoted by \mathbf{v} can be calculated as shown below:

$$\begin{aligned}
\mathbf{M}' &= \mathbf{M} + (\mathbf{p} - \mathbf{v}) \times \mathbf{F} \quad \Rightarrow \quad \underbrace{\mathbf{M}' \times \mathbf{e}_3}_0 = \mathbf{M} \times \mathbf{e}_3 + (\mathbf{p} - \mathbf{v}) \times \mathbf{F} \times \mathbf{e}_3 \\
\Rightarrow \mathbf{0} &= [-M_1 \mathbf{e}_2 + M_2 \mathbf{e}_1] + \left[\underbrace{(\mathbf{e}_3 \cdot (\mathbf{p} - \mathbf{v})) \mathbf{F}}_0 - (\mathbf{e}_3 \cdot \mathbf{F})(\mathbf{p} - \mathbf{v}) \right] \\
\Rightarrow \mathbf{0} &= [-M_1 \mathbf{e}_2 + M_2 \mathbf{e}_1] + [-(F_3)(\mathbf{p} - \mathbf{v})] \tag{7.6.1}
\end{aligned}$$

$$\Rightarrow \begin{cases} F_3 \neq 0 : (v_1, v_2, v_3) = \left(p_1 - \frac{M_2}{F_3}, p_2 + \frac{M_1}{F_3}, 0 \right) \\ F_3 = 0 : M_1 = M_2 = 0 \end{cases} \tag{7.6.2}$$

As seen in Equation (7.6.2), if $F_3 \neq 0$ then the location of NCM point is unique. If we have $F_3 = 0$ and $M_1 = M_2 = 0$, then any point will be an NCM point because Equation (7.6.1) will hold true for any value of \mathbf{p} and \mathbf{v} . If we have $F_3 = 0$ but $M_1 \neq 0$ or $M_2 \neq 0$, then no point will be an NCM point because Equation (7.6.1) will hold true for no value of \mathbf{p} and \mathbf{v} . Therefore, if we have $F_3 = 0$, it is obvious that the constraints on the equivalent forces and moments to model the non-adhesiveness of a contact area are: $\mathbf{F} = \mathbf{M} = \mathbf{0}$ (other components of \mathbf{F} and \mathbf{M} will also be zero due to coulomb friction law as will be shown later). So, in order to avoid further confusion, we only define NCM point for the cases when $F_3 \neq 0$.

7.7 Unilaterality Constraints via NCM Concepts

To simplify the problem presented in Section 7.5, we initially ignore Limitation 7.2 and only consider the constraints on \mathbf{F} and \mathbf{M} imposed by Limitation 7.1. Later in Section 7.8, we will consider the additional constraints on \mathbf{F} and \mathbf{M} imposed by Limitation 7.2.

7.7.1 NCM Constraint and the Unilaterality of Distributed Contact Forces

To study the possibility of replacing a desired \mathbf{F} and \mathbf{M} acting at \mathbf{p} under Limitation 7.1, we use the NCM point and NCM force system concepts introduced in Section 7.6. This possibility will be studied using Theorem 7.1 given later in this subsection. Using results from Theorem 7.1, we will establish constraints on \mathbf{F} and \mathbf{M} that ensure this possibility and denote them as “NCM Constraints” later in this section.

Theorem 7.1: *NCM Constraint and the Unilaterality of Distributed Contact Forces*

Consider an arbitrary dynamic system having several contact area with the environment such as Γ shown in Figure 7.1. Consider its convex hull Υ repeated again in Figure 7.3 for convenience. For any arbitrary contact force system \mathbf{F} and \mathbf{M} acting on the contact area at location \mathbf{p} , the following two statements are equivalent (they are necessary and sufficient conditions for each other, or one can conclude statement 1 from 2 and vice versa.):

- 1- The NCM point corresponding to the force system \mathbf{F} and \mathbf{M} , located at \mathbf{v} is inside the convex hull of Γ , denoted by Υ and $\mathbf{F} \cdot \mathbf{e}_3 > 0$
- 2- It is possible to find unilateral distributed contact forces \mathbf{f}_c inside the contact area Γ with $\mathbf{f}_c \cdot \mathbf{e}_3 \geq 0$ that are equivalent to \mathbf{F} and \mathbf{M} .

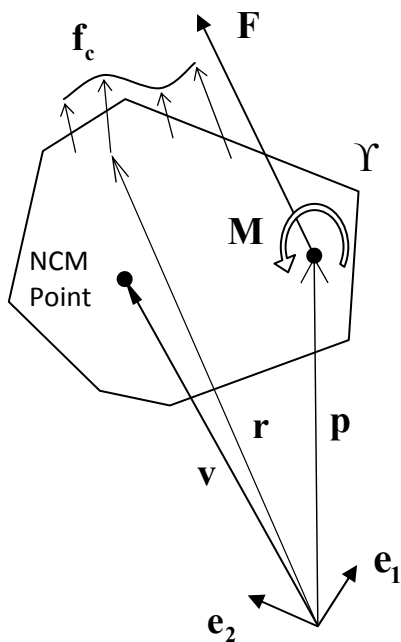


Figure 7.3. Distributed forces on a contact area and their equivalent concentrated force and moment and NCM point

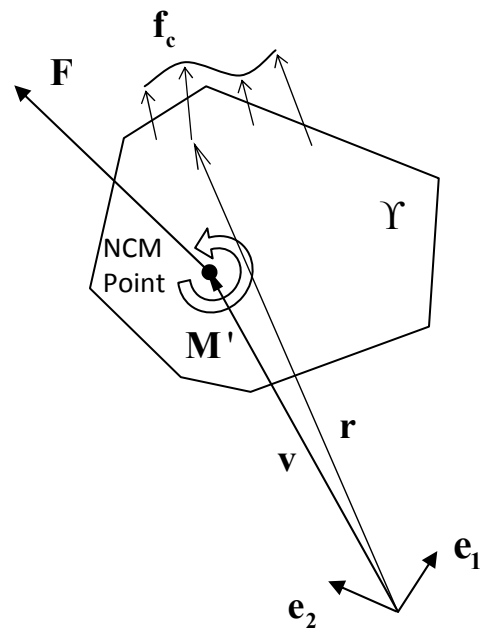


Figure 7.4. Distributed forces on a contact area and their equivalent NCM force system

Proof:

Part A) Assume statement 1 holds, we prove statement 2:

The proof method we use in this part is a constructive proof, i.e. we provide a method for creating the distributed forces \mathbf{f}_c that can replace \mathbf{F} and \mathbf{M} . Consider the NCM force

system \mathbf{F} and \mathbf{M}' acting at the NCM point inside the convex hull. We construct 3 different subsets of \mathbf{f}_c called $\mathbf{w}_a, \mathbf{w}_b, \mathbf{w}_c$, one (\mathbf{w}_a) for replacing \mathbf{F} without any contribution to \mathbf{M}' and the 2 others ($\mathbf{w}_b, \mathbf{w}_c$) for replacing \mathbf{M}' without any contribution to \mathbf{F} . These three subsets satisfy the following conditions:

$$\begin{cases} \{\mathbf{w}_a\} \cap \{\mathbf{w}_b\} = \{\mathbf{w}_a\} \cap \{\mathbf{w}_c\} = \{\mathbf{w}_b\} \cap \{\mathbf{w}_c\} = \phi \\ \{\mathbf{w}_a\} \cup \{\mathbf{w}_b\} \cup \{\mathbf{w}_c\} = \{\mathbf{f}_c\} \end{cases} \quad (7.7.1)$$

Constructing \mathbf{w}_a :

The first subset of \mathbf{f}_c called \mathbf{w}_a can be constructed as follows:

Case 1:

When NCM point is a contact point (it is inside Γ):

Assume all distributed forces \mathbf{w}_a to be concentrated at the NCM point and all have same directions as \mathbf{F} . Although there is a constraint ($\mathbf{f}_c \cdot \mathbf{e}_3 \geq 0 \Rightarrow \mathbf{w}_a \cdot \mathbf{e}_3 \geq 0$), it is always possible to do so because $\mathbf{F} \cdot \mathbf{e}_3 \geq 0$.

It is also obvious that it is possible to select the magnitudes of \mathbf{w}_a such that:

$$\mathbf{F} = \int_{\Gamma} \mathbf{w}_a dA \quad (7.7.2)$$

Also because \mathbf{w}_a is located at the NCM point, \mathbf{w}_a will have no contribution to \mathbf{M}' .

Case 2:

When NCM is not a contact point (it is inside Υ , but not inside Γ):

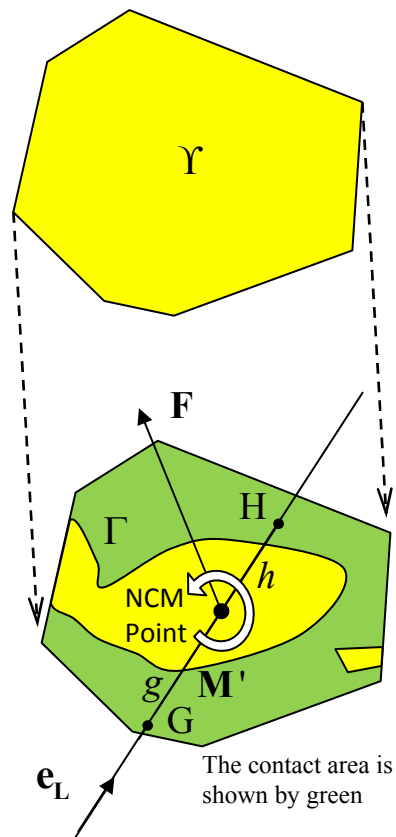


Figure 7.5. Proving statement 2 when NCM point is inside the convex hull, but not a contact point

The convex hull of the contact area Υ which was previously shown in Figure 7.4 is repeated in Figure 7.5 and identified in yellow. The contact area Γ (which is a subset of Υ) is shown by another color (green), overlaid on the yellow colored areas. Therefore, the green areas in this figure denote points that belong to both Υ and Γ , while the yellow areas only belong to Υ but not Γ . It is possible to find a line that passes through the NCM point and contains two arbitrary contact points G and H in Γ . Let us denote the unit vector along that line by \mathbf{e}_L . In this case, NCM point would be located between

G and H. Let us denote the distance from the NCM point to G and H by g and h . We assume \mathbf{w}_a to be composed of two subsets \mathbf{w}_{a_G} and \mathbf{w}_{a_H} such that:

$$\{\mathbf{w}_{a_G}\} \cap \{\mathbf{w}_{a_H}\} = \phi, \{\mathbf{w}_{a_G}\} \cup \{\mathbf{w}_{a_H}\} = \{\mathbf{w}_a\} \quad (7.7.3)$$

Assume all distributed forces \mathbf{w}_{a_G} to be concentrated at the point G and all have same directions as \mathbf{F} . It is obvious that it is possible to select the magnitudes of \mathbf{w}_{a_G} such that:

$$\mathbf{F} \frac{g}{g+h} = \int_{\Gamma} \mathbf{w}_{a_G} dA \quad (7.7.4)$$

Assume all distributed forces \mathbf{w}_{a_H} to be concentrated at the point H and all have same directions as \mathbf{F} . It is obvious that it is possible to select the magnitudes of \mathbf{w}_{a_H} such that:

$$\mathbf{F} \frac{h}{g+h} = \int_{\Gamma} \mathbf{w}_{a_H} dA \quad (7.7.5)$$

So, the total contribution of \mathbf{w}_a to forces and moments about NCM point is:

$$\mathbf{F}_{\mathbf{w}_a, \text{VCM}} = \int_{\Gamma} \mathbf{w}_a dA = \int_{\Gamma} \mathbf{w}_{a_G} dA + \int_{\Gamma} \mathbf{w}_{a_H} dA = \mathbf{F} \frac{h}{g+h} + \mathbf{F} \frac{g}{g+h} = \mathbf{F} \quad (7.7.6)$$

$$\mathbf{M}_{\mathbf{w}_a, \text{VCM}} = -g\mathbf{e}_L \times \int_{\Gamma} \mathbf{w}_{a_G} dA + h\mathbf{e}_L \times \int_{\Gamma} \mathbf{w}_{a_H} dA = -g\mathbf{e}_L \times \mathbf{F} \frac{h}{g+h} + h\mathbf{e}_L \times \mathbf{F} \frac{g}{g+h} = \mathbf{0} \quad (7.7.7)$$

Constructing $\mathbf{w}_b, \mathbf{w}_c$:

The second and third subsets of \mathbf{f}_c respectively called $\mathbf{w}_b, \mathbf{w}_c$ can be considered to be concentrated at two locations $\mathbf{r}_b, \mathbf{r}_c$ inside Υ and acting along $\mathbf{e}_3 \times (\mathbf{r}_b - \mathbf{r}_c), -\mathbf{e}_3 \times (\mathbf{r}_b - \mathbf{r}_c)$ (in the $\mathbf{e}_1\mathbf{e}_2$ plane, normal to $\mathbf{r}_b, \mathbf{r}_c$). So, they are all planar (frictional) distributed forces ($\mathbf{w}_b \cdot \mathbf{e}_3 = \mathbf{0}, \mathbf{w}_c \cdot \mathbf{e}_3 = \mathbf{0}$). It is possible to select the magnitudes of $\mathbf{w}_b, \mathbf{w}_c$ such that:

$$\int_{\Gamma} \|\mathbf{w}_b\| dA = \int_{\Gamma} \|\mathbf{w}_c\| dA = \frac{\|\mathbf{M}'\|}{\|\mathbf{r}_b - \mathbf{r}_c\|} \quad (7.7.8)$$

Therefore, the distributed forces $\mathbf{w}_b, \mathbf{w}_c$ are equivalent to a couple (same magnitude and opposite directions) that has no contribution to \mathbf{F} and produces a same moment about any point equal to \mathbf{M}' as shown below:

$$\mathbf{w}_b = \|\mathbf{w}_b\| \left(\frac{\mathbf{e}_3 \times (\mathbf{r}_b - \mathbf{r}_c)}{\|\mathbf{r}_b - \mathbf{r}_c\|} \right), \quad \mathbf{w}_c = \|\mathbf{w}_c\| \left(\frac{-\mathbf{e}_3 \times (\mathbf{r}_b - \mathbf{r}_c)}{\|\mathbf{r}_b - \mathbf{r}_c\|} \right) \quad (7.7.9)$$

$$\mathbf{M}_{w_b} + \mathbf{M}_{w_c} = \mathbf{r}_b \times \int_{\Gamma} \mathbf{w}_b dA + \mathbf{r}_c \times \int_{\Gamma} \mathbf{w}_c dA \quad (7.7.10)$$

$$\Rightarrow \mathbf{M}_{w_b} + \mathbf{M}_{w_c} = \mathbf{r}_b \times \left(\int_{\Gamma} \|\mathbf{w}_b\| \frac{\mathbf{e}_3 \times (\mathbf{r}_b - \mathbf{r}_c)}{\|\mathbf{r}_b - \mathbf{r}_c\|} dA \right) + \mathbf{r}_c \times \left(\int_{\Gamma} \|\mathbf{w}_c\| \frac{-\mathbf{e}_3 \times (\mathbf{r}_b - \mathbf{r}_c)}{\|\mathbf{r}_b - \mathbf{r}_c\|} dA \right) \quad (7.7.11)$$

$$\Rightarrow \mathbf{M}_{w_b} + \mathbf{M}_{w_c} = \left(\left(\int_{\Gamma} \|\mathbf{w}_b\| dA \right) \mathbf{r}_b - \left(\int_{\Gamma} \|\mathbf{w}_c\| dA \right) \mathbf{r}_c \right) \times \left(\frac{\mathbf{e}_3 \times (\mathbf{r}_b - \mathbf{r}_c)}{\|\mathbf{r}_b - \mathbf{r}_c\|} \right)$$

$$\Rightarrow \mathbf{M}_{w_b} + \mathbf{M}_{w_c} = \frac{\|\mathbf{M}'\|}{\|\mathbf{r}_b - \mathbf{r}_c\|} (\mathbf{r}_b - \mathbf{r}_c) \times \left(\frac{\mathbf{e}_3 \times (\mathbf{r}_b - \mathbf{r}_c)}{\|\mathbf{r}_b - \mathbf{r}_c\|} \right)$$

$$\Rightarrow \mathbf{M}_{w_b} + \mathbf{M}_{w_c} = \frac{\|\mathbf{M}'\|}{\|\mathbf{r}_b - \mathbf{r}_c\|} \frac{(\mathbf{r}_b - \mathbf{r}_c) \times \mathbf{e}_3 \times (\mathbf{r}_b - \mathbf{r}_c)}{\|\mathbf{r}_b - \mathbf{r}_c\|}$$

$$\Rightarrow \mathbf{M}_{w_b} + \mathbf{M}_{w_c} = \frac{\|\mathbf{M}'\|}{\|\mathbf{r}_b - \mathbf{r}_c\|} \frac{\overbrace{((\mathbf{r}_b - \mathbf{r}_c) \cdot (\mathbf{r}_b - \mathbf{r}_c))}^{\|\mathbf{r}_b - \mathbf{r}_c\|^2} \mathbf{e}_3 - \overbrace{((\mathbf{r}_b - \mathbf{r}_c) \cdot \mathbf{e}_3)}^0 (\mathbf{r}_b - \mathbf{r}_c)}{\|\mathbf{r}_b - \mathbf{r}_c\|}$$

$$\Rightarrow \mathbf{M}_{w_b} + \mathbf{M}_{w_c} = \frac{\|\mathbf{M}'\|}{\|\mathbf{r}_b - \mathbf{r}_c\|} \|\mathbf{r}_b - \mathbf{r}_c\| \mathbf{e}_3 = \|\mathbf{M}'\| \mathbf{e}_3$$

$$\Rightarrow \mathbf{M}_{w_b} + \mathbf{M}_{w_c} = \frac{\|\mathbf{M}'\|}{\|\mathbf{r}_b - \mathbf{r}_c\|} \|\mathbf{r}_b - \mathbf{r}_c\| \mathbf{e}_3 = \|\mathbf{M}'\| \mathbf{e}_3$$

$$\text{Definition of NCM Point} \Rightarrow \mathbf{M}' \text{ is along } \mathbf{e}_3 \Rightarrow \|\mathbf{M}'\| \mathbf{e}_3 = \mathbf{M}'$$

$$\Rightarrow \mathbf{M}_{w_b} + \mathbf{M}_{w_c} = \mathbf{M}' \quad (7.7.12)$$

Also,

$$\begin{aligned}
\mathbf{F}_{\mathbf{w}_b} + \mathbf{F}_{\mathbf{w}_c} &= \int_{\Upsilon} \mathbf{w}_b dA + \int_{\Upsilon} \mathbf{w}_c dA \\
\Rightarrow \mathbf{F}_{\mathbf{w}_b} + \mathbf{F}_{\mathbf{w}_c} &= \int_{\Upsilon} \|\mathbf{w}_b\| \frac{\mathbf{e}_3 \times (\mathbf{r}_b - \mathbf{r}_c)}{\|\mathbf{r}_b - \mathbf{r}_c\|} dA + \int_{\Upsilon} \|\mathbf{w}_c\| \frac{-\mathbf{e}_3 \times (\mathbf{r}_b - \mathbf{r}_c)}{\|\mathbf{r}_b - \mathbf{r}_c\|} dA \\
\Rightarrow \mathbf{F}_{\mathbf{w}_b} + \mathbf{F}_{\mathbf{w}_c} &= \left(\int_{\Upsilon} \|\mathbf{w}_b\| dA - \int_{\Upsilon} \|\mathbf{w}_c\| dA \right) \left(\frac{\mathbf{e}_3 \times (\mathbf{r}_b - \mathbf{r}_c)}{\|\mathbf{r}_b - \mathbf{r}_c\|} \right) \\
\Rightarrow \mathbf{F}_{\mathbf{w}_b} + \mathbf{F}_{\mathbf{w}_c} &= \left(\frac{\|\mathbf{M}'\|}{\|\mathbf{r}_b - \mathbf{r}_c\|} - \frac{\|\mathbf{M}'\|}{\|\mathbf{r}_b - \mathbf{r}_c\|} \right) \left(\frac{\mathbf{e}_3 \times (\mathbf{r}_b - \mathbf{r}_c)}{\|\mathbf{r}_b - \mathbf{r}_c\|} \right) \\
\Rightarrow \mathbf{F}_{\mathbf{w}_b} + \mathbf{F}_{\mathbf{w}_c} &= \mathbf{0} \tag{7.7.13}
\end{aligned}$$

Therefore, the set of distributed forces \mathbf{f}_c that we constructed by the subsets $\mathbf{w}_a, \mathbf{w}_b, \mathbf{w}_c$ are equivalent to \mathbf{F} and \mathbf{M}' and therefore are equivalent to \mathbf{F} and \mathbf{M} .

Part B) Assume statement 2 holds, we prove statement 1:

Part B-1) Proving that NCM point is “not” outside the convex hull (Proof by contradiction):

As shown in Figure 7.6, if NCM point is outside the convex hull of the contact area Υ , consider the nearest edge of the convex hull to the NCM point. Due to the definition of the convex hull, if you draw a line parallel to that edge, the line will not intersect the convex hull and the convex hull will lie on one side of the line. Now, define a unit vector \mathbf{u} perpendicular to this line and pointing from the NCM point to the convex hull. Then it is obvious that for any point Q in the convex hull, located at \mathbf{r} :

$$(\mathbf{r} - \mathbf{v}) \cdot \mathbf{u} > 0 \quad \text{and} \quad \mathbf{u} \cdot \mathbf{e}_3 = 0 \tag{7.7.14}$$

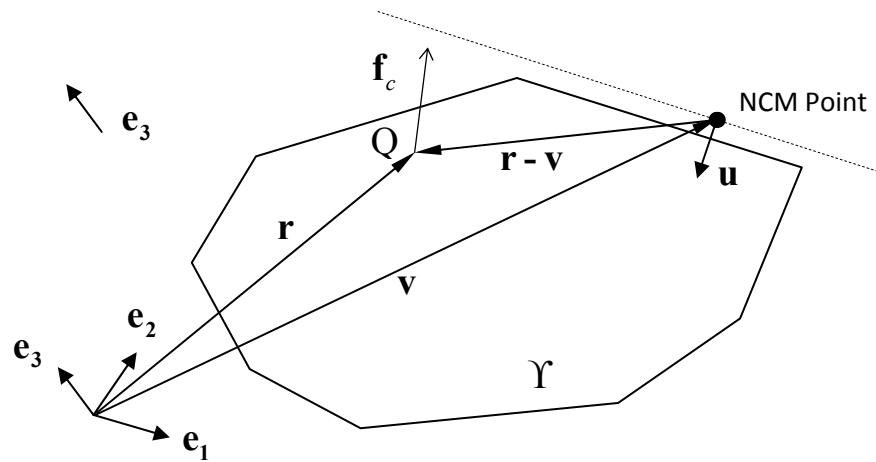


Figure 7.6. Part (B-1) of the proof: proving that it is impossible for NCM point to be outside the convex hull if the contact area is non-adhesive

$$\begin{aligned}
 \mathbf{M}' &= \int_{\Upsilon} (\mathbf{r} - \mathbf{v}) \times \mathbf{f}_c \, dA \quad , \quad \mathbf{M}' \times \mathbf{e}_3 = \mathbf{0} \quad \Rightarrow \quad \int_{\Upsilon} (\mathbf{r} - \mathbf{v}) \times \mathbf{f}_c \, dA \times \mathbf{e}_3 = \mathbf{0} \\
 &\Rightarrow \int_{\Upsilon} \left[\underbrace{(\mathbf{e}_3 \cdot (\mathbf{r} - \mathbf{v}))}_0 \mathbf{f}_c - (\mathbf{e}_3 \cdot \mathbf{f}_c)(\mathbf{r} - \mathbf{v}) \right] dA = \mathbf{0} \Rightarrow \int_{\Upsilon} (\mathbf{f}_c \cdot \mathbf{e}_3)(\mathbf{r} - \mathbf{v}) \, dA = \mathbf{0} \\
 &\stackrel{\mathbf{u}}{\Rightarrow} \int_{\Upsilon} (\mathbf{f}_c \cdot \mathbf{e}_3)((\mathbf{r} - \mathbf{v}) \cdot \mathbf{u}) \, dA = 0 \quad (7.7.15)
 \end{aligned}$$

For any point on Υ we have :

$$\begin{aligned}
 \left\{ \begin{array}{l} \text{Statement 2} \Rightarrow \mathbf{f}_c \cdot \mathbf{e}_3 \geq 0 \\ (7.7.14) \Rightarrow (\mathbf{r} - \mathbf{v}) \cdot \mathbf{u} > 0 \quad (\text{If NCM point is outside the convex hull}) \end{array} \right. \\
 \Rightarrow \int_{\Upsilon} (+)(+) \, dA = 0 \quad : \quad \text{Impossible!}
 \end{aligned}$$

So, we have proved that NCM point is inside the convex hull.

Part B-2) Proof of $\mathbf{F} \cdot \mathbf{e}_3 \geq 0$:

$$\mathbf{F} = \int_{\Upsilon} \mathbf{f}_c \, dA \quad , \quad \mathbf{f}_c \cdot \mathbf{e}_3 \geq 0 \quad \Rightarrow \quad \mathbf{F} \cdot \mathbf{e}_3 \geq 0$$

The results of Part B-1 and Part B-2 prove that statement 1 holds.

It is obvious that if we can find non-adhesive distributed contact forces in the contact area Γ , to replace \mathbf{F} and \mathbf{M} , we are sure that exerting \mathbf{F} and \mathbf{M} on body Φ is possible for that contact area in the real world. Based on the results from Theorem 7.1, “NCM Constraints” are defined as follows:

Definition 7.2: NCM Constraints

The NCM constraints for a force system \mathbf{F} and \mathbf{M} acting on a non-adhesive contact area Γ indicate that the NCM point corresponding to \mathbf{F} and \mathbf{M} should be inside the convex hull Υ of the contact area and $\mathbf{F} \cdot \mathbf{e}_3 > 0$ in order for \mathbf{F} and \mathbf{M} to be exerable from contact area Γ onto the body Φ .

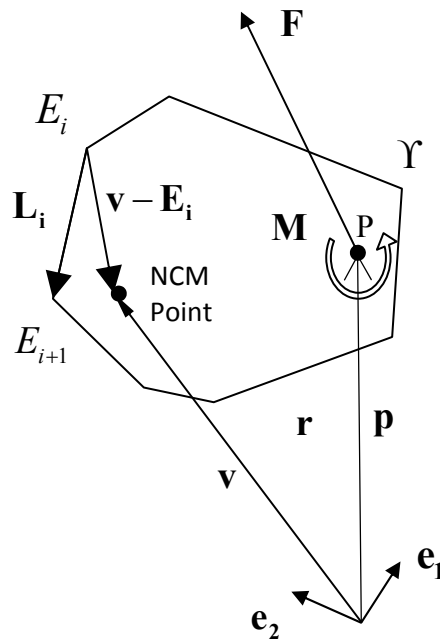


Figure 7.7. Method for checking the NCM constraints

For computational purposes, if the convex hull Υ of the contact area is a polygon with corners $E_i (i=1\dots m)$, as shown in Figure 7.7, we can use a general formula to check whether the NCM point is inside the convex hull. To do that, let us assume that E_i move counter-clockwise around the convex hull about \mathbf{e}_3 as we increase i . Denote the position of each corner E_i by the vector \mathbf{E}_i . Also define $\mathbf{L}_i = \mathbf{E}_{i+1} - \mathbf{E}_i$ as the vector connecting the two adjacent corners E_i and E_{i+1} and define $d_i \triangleq (\mathbf{L}_i \times (\mathbf{v} - \mathbf{E}_i)) \cdot \mathbf{e}_3$ where \mathbf{v} is the location of the NCM point. Then, in order for the NCM point to be inside the convex hull Υ , we should have:

$$(7.4.1) \quad \left. \begin{aligned} \forall i=1\dots m: \quad d_i = (\mathbf{L}_i \times (\mathbf{v} - \mathbf{E}_i)) \cdot \mathbf{e}_3 \geq 0 \\ \Rightarrow (v_1, v_2, v_3) = \left(p_1 - \frac{M_2}{F_3}, p_2 + \frac{M_1}{F_3}, 0 \right) \end{aligned} \right\} \Rightarrow d_i = \left(\mathbf{L}_i \times \begin{pmatrix} p_1 - \frac{M_2}{F_3} - E_{i1} \\ p_2 + \frac{M_1}{F_3} - E_{i2} \\ 0 \end{pmatrix} \right) \cdot \mathbf{e}_3 \geq 0$$

$$\Rightarrow d_i = (L_i)_1 \left(p_2 + \frac{M_1}{F_3} - E_{i2} \right) - (L_i)_2 \left(p_1 - \frac{M_2}{F_3} - E_{i1} \right) \geq 0$$

$$\stackrel{F_3 > 0}{\Rightarrow} d_i F_3 = (L_i)_1 (p_2 F_3 + M_1 - E_{i2} F_3) - (L_i)_2 (p_1 F_3 - M_2 - E_{i1} F_3) \geq 0$$

Therefore the NCM constraints in the case where the convex hull Υ of the contact area is a polygon with corners $E_i (i=1\dots m)$ will be:

$$\begin{cases} F_3 = \mathbf{F} \cdot \mathbf{e}_3 > 0 \\ \forall i=1\dots m: \quad d_i F_3 = (L_i)_1 (p_2 F_3 + M_1 - E_{i2} F_3) - (L_i)_2 (p_1 F_3 - M_2 - E_{i1} F_3) \geq 0 \end{cases} \quad (7.7.16)$$

As it is seen in Equation (7.7.16), besides a constraint on the NCM point location, the NCM constraints also include a constraint on the equivalent force system to be compressive. Also it is noted that NCM constraints are composed of constraints on some components of the equivalent contact forces and moments (M_1, M_2, F_3) . As it will be seen later, the other three components of the equivalent forces and moments (F_1, F_2, M_3) will be constrained by the coulomb friction constraints.

7.7.2 NCM Point Location and the Location of Distributed Contact Forces

In this subsection, we present another theorem which shows that the NCM point is on an edge of the convex hull, if and only if all distributed contact forces are on that edge.

Theorem 7.2: *NCM Point Location and the Location of Contact Forces*

Consider an arbitrary dynamic system having several contact area with the environment. For example, consider the problem depicted in Figures 7.1 and 7.3 with some of its features shown again in Figure 7.8. For any arbitrary contact force system \mathbf{F} and \mathbf{M} acting on the contact area at location \mathbf{p} , then:

- 1- if the corresponding NCM point is on the edge Υ' of the convex hull Υ of the contact area and $\mathbf{F} \cdot \mathbf{e}_3 \geq 0$, then
- 2- the distributed contact forces \mathbf{f}_c to replace \mathbf{F} and \mathbf{M} , are only on the edge Υ' of the convex hull of the non-adhesive contact area (no \mathbf{f}_c can exist outside Υ'), and vice versa.

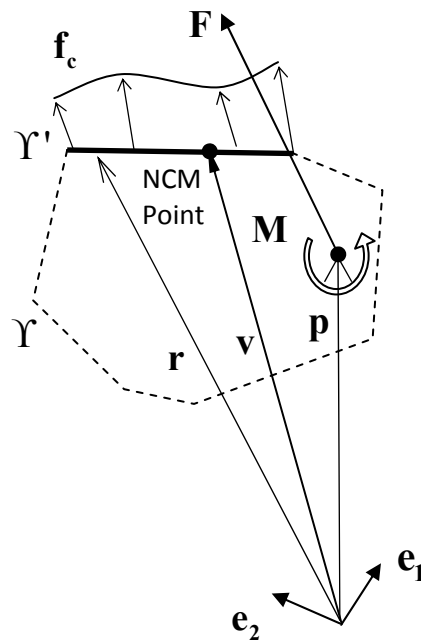


Figure 7.8. Distributed forces and the NCM point being on an edge of a contact area

Proof:

First, it should be noted that unilaterality requires $\mathbf{f}_c \cdot \mathbf{e}_3 \geq 0$ and due to coulomb friction law we also have: $\mathbf{f}_c \cdot \mathbf{e}_3 \neq 0$ (because $\mathbf{f}_c \cdot \mathbf{e}_3 = 0$ will result in $\mathbf{f}_c = 0$ due to friction constraints). Therefore, for a non-adhesive contact area we will always have: $\mathbf{f}_c \cdot \mathbf{e}_3 > 0$.

Part A) Assume statement 1 holds, we prove statement 2:

Part A-1) Proving that: \mathbf{f}_c "can be found on" Υ' to replace \mathbf{F} and \mathbf{M} :

The proof is exactly the same as Part A of Theorem 7.1, if we consider edge Υ' instead of area Υ in that part.

Part A-2) Proving that: \mathbf{f}_c are "only" on the edge Υ' :

In this part, we need to prove that no non-adhesive \mathbf{f}_c can exist outside edge Υ' .

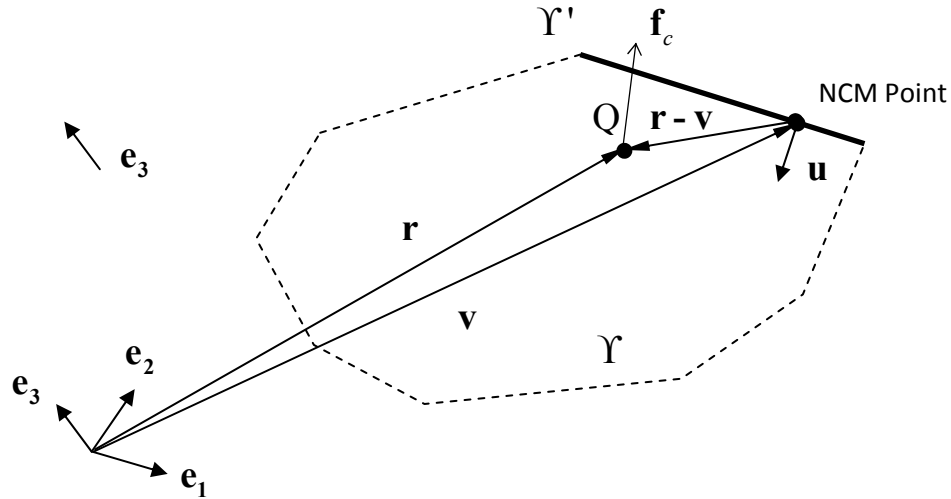


Figure 7.9. Part (A-2) of the proof: proving that contact forces are only on an edge of the contact area if NCM point is on that edge

The NCM point is located at \mathbf{v} on edge Υ' . As shown in Figure 7.9, let's define a unit vector \mathbf{u} pointing from the NCM point towards the inside of the convex hull, perpendicular to edge Υ' . Due to the definition of the convex hull, for any point Q inside the convex hull located at \mathbf{r} :

$$\begin{aligned} \mathbf{M}' &= \int_{\Upsilon'} (\mathbf{r} - \mathbf{v}) \times \mathbf{f}_c \, dA \quad , \quad \mathbf{M}' \times \mathbf{e}_3 = \mathbf{0} \\ \Rightarrow \int_{\Upsilon'} (\mathbf{r} - \mathbf{v}) \times \mathbf{f}_c \, dA \times \mathbf{e}_3 &= \mathbf{0} \quad \Rightarrow \int_{\Upsilon'} \left[\underbrace{(\mathbf{e}_3 \cdot (\mathbf{r} - \mathbf{v}))}_{0} \mathbf{f}_c - (\mathbf{e}_3 \cdot \mathbf{f}_c)(\mathbf{r} - \mathbf{v}) \right] dA = \mathbf{0} \\ \Rightarrow \int_{\Upsilon'} (\mathbf{f}_c \cdot \mathbf{e}_3)(\mathbf{r} - \mathbf{v}) \, dA &= \mathbf{0} \quad (7.7.17) \end{aligned}$$

$$\Rightarrow \left. \begin{aligned} \int_{\gamma} (\mathbf{f}_c \cdot \mathbf{e}_3) ((\mathbf{r} - \mathbf{v}) \cdot \mathbf{u}) dA &= 0 \\ \text{For any point } Q, \text{ we have: } & (\mathbf{r} - \mathbf{v}) \cdot \mathbf{u} \geq 0 \quad \text{and} \quad \mathbf{f}_c \cdot \mathbf{e}_3 > 0 \end{aligned} \right\}$$

\Rightarrow For any point Q , we should have: $(\mathbf{r} - \mathbf{v}) \cdot \mathbf{u} = 0$

\Rightarrow No \mathbf{f}_c exists outside edge γ'

The results of Part A-1 and Part A-2 prove that statement 2 holds.

Part B) Assume statement 2 holds, we prove statement 1:

Part B-1) Proving that NCM point is on γ' (proof by contradiction):

As shown in Figure 7.10, if NCM point is not on edge γ' , define a unit vector \mathbf{u} pointing from the NCM point towards the edge γ' , perpendicular to edge γ' and on the plane σ (defined in Figure 7.1). Then it is obvious that for any point Q on edge γ' , located at \mathbf{r} : $(\mathbf{r} - \mathbf{v}) \cdot \mathbf{u} > 0$ And $\mathbf{u} \cdot \mathbf{e}_3 = 0$ (7.7.18)

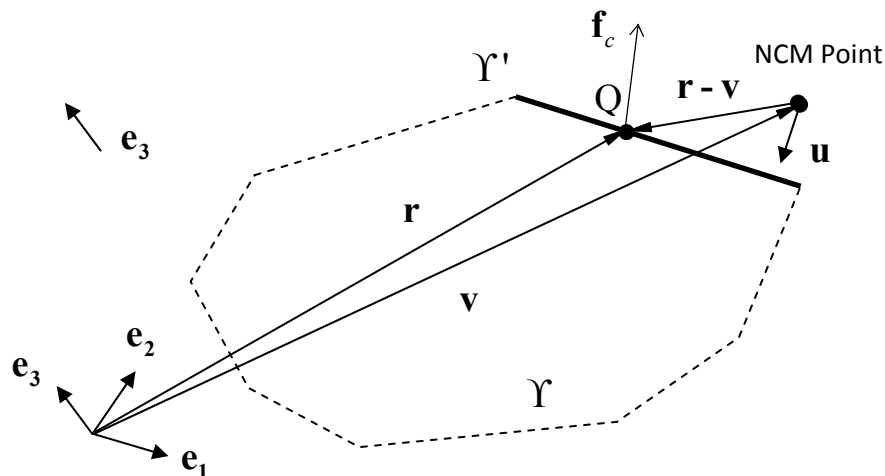


Figure 7.10. Part (B-1) of the proof: proving that that if all contact forces are on an edge then NCM point is on that edge

$$\mathbf{M}' = \int_{\Upsilon'} (\mathbf{r} - \mathbf{v}) \times \mathbf{f}_c dA \quad , \quad \mathbf{M}' \times \mathbf{e}_3 = \mathbf{0}$$

$$\begin{aligned} \Rightarrow \int_{\Upsilon'} (\mathbf{r} - \mathbf{v}) \times \mathbf{f}_c dA \times \mathbf{e}_3 = \mathbf{0} & \Rightarrow \int_{\Upsilon'} \left[\underbrace{(\mathbf{e}_3 \cdot (\mathbf{r} - \mathbf{v}))}_0 \mathbf{f}_c - (\mathbf{e}_3 \cdot \mathbf{f}_c)(\mathbf{r} - \mathbf{v}) \right] dA = \mathbf{0} \\ \Rightarrow \int_{\Upsilon'} (\mathbf{f}_c \cdot \mathbf{e}_3)(\mathbf{r} - \mathbf{v}) dA = \mathbf{0} & \quad (7.7.19) \\ \Rightarrow \int_{\Upsilon'} (\mathbf{f}_c \cdot \mathbf{e}_3)((\mathbf{r} - \mathbf{v}) \cdot \mathbf{u}) dA = 0 & \quad (7.7.20) \end{aligned}$$

For any point on Υ' we have :

$$\begin{cases} \text{Statement 2} & \Rightarrow \mathbf{f}_c \cdot \mathbf{e}_3 \geq 0 \\ (7.7.18) & \Rightarrow (\mathbf{r} - \mathbf{v}) \cdot \mathbf{u} > 0 \quad (\text{If NCM Point is not on the edge}) \end{cases}$$

$$\Rightarrow \int_{\Upsilon'} (+)(+) dA = 0 \quad : \quad \text{Impossible!}$$

So, using proof by contradiction, we have proved that NCM point is on the edge of the convex hull.

Part B-2) Proof of $\mathbf{F} \cdot \mathbf{e}_3 \geq 0$:

$$\mathbf{F} = \int_{\Upsilon'} \mathbf{f}_c dA \quad , \quad \mathbf{f}_c \cdot \mathbf{e}_3 \geq 0 \quad \Rightarrow \quad \mathbf{F} \cdot \mathbf{e}_3 \geq 0$$

The results of Part B-1 and Part B-2 prove that statement 1 holds.

7.8 Coulomb Friction Constraints via NCM Concepts

As expressed in Section 7.6, non-adhesiveness of contact area Γ limits its ability to produce all desired arbitrary resultant contact forces and moments \mathbf{F} and \mathbf{M} . Non-adhesiveness imposes 2 different types of limitations on the choices for \mathbf{F} and \mathbf{M} as discussed in Section 7.6. In the theorems expressed in previous sections, we have only considered Limitation 7.1 and neglected Limitation 7.2 (NCM constraints allow the existence of unlimited frictional forces and apply no constraint on them).

In this section, we consider the additional constraints on \mathbf{F} and \mathbf{M}' (equivalent force and moment at the NCM point) caused by Limitation 7.2 in Section 7.6. Coulomb friction law limits the possible values for planar (frictional) components of the distributed forces and therefore the concentrated force and moment at the NCM point (F_1, F_2, M'_3) .

A simplified formula usually used to account for sliding friction is:

$$\begin{aligned} \|\mathbf{F}_f\| &\leq \mu \|F_3\| & \mathbf{F} &= F_1\mathbf{e}_1 + F_2\mathbf{e}_2 + F_3\mathbf{e}_3 = \mathbf{F}_f + F_3\mathbf{e}_3 \\ \mathbf{F}_f &= F_1\mathbf{e}_1 + F_2\mathbf{e}_2 \Rightarrow \|\mathbf{F}_f\| = \sqrt{F_1^2 + F_2^2} & \Rightarrow & F_1^2 + F_2^2 \leq \mu^2 F_3^2 \end{aligned} \quad (7.8.1)$$

Friction law also imposes a constraint on the value of M'_3 :

$$\begin{aligned} \mathbf{M}' &= \int_{\Gamma} (\mathbf{r} - \mathbf{v}) \times \mathbf{f}_c \, dA \xrightarrow{\mathbf{e}_3} \\ M'_3 &= \mathbf{M}' \cdot \mathbf{e}_3 = \int_{\Gamma} (\mathbf{r} - \mathbf{v}) \times \mathbf{f}_c \cdot \mathbf{e}_3 \, dA = \int_{\Gamma} (\mathbf{r} - \mathbf{v}) \cdot \mathbf{f}_c \times \mathbf{e}_3 \, dA \end{aligned} \quad (7.8.2)$$

$$\begin{aligned} -\|(\mathbf{r} - \mathbf{v})\| \|\mathbf{f}_c \times \mathbf{e}_3\| &\leq (\mathbf{r} - \mathbf{v}) \cdot \mathbf{f}_c \times \mathbf{e}_3 \leq \|(\mathbf{r} - \mathbf{v})\| \|\mathbf{f}_c \times \mathbf{e}_3\| \\ \Rightarrow -\int_{\Gamma} \|(\mathbf{r} - \mathbf{v})\| \|\mathbf{f}_c \times \mathbf{e}_3\| \, dA &\leq M'_3 \leq \int_{\Gamma} \|(\mathbf{r} - \mathbf{v})\| \|\mathbf{f}_c \times \mathbf{e}_3\| \, dA \end{aligned} \quad (7.8.3)$$

Considering that $\|\mathbf{f}_c \times \mathbf{e}_3\| > 0$, the maximum and minimum possible values for M'_3 are achieved when $\|\mathbf{r} - \mathbf{v}\|$ are maximum. Therefore, a loose constraint for M'_3 is :

$$\Rightarrow -\|\mathbf{r} - \mathbf{v}\|_{Max} \int_{\Upsilon} \|\mathbf{f}_c \times \mathbf{e}_3\| dA \leq M'_3 \leq \|\mathbf{r} - \mathbf{v}\|_{Max} \int_{\Upsilon} \|\mathbf{f}_c \times \mathbf{e}_3\| dA \quad (7.8.4)$$

Coulomb friction law, considered for distributed forces, can be written as:

$$\mathbf{f}_c = f_1 \mathbf{e}_1 + f_2 \mathbf{e}_2 + f_3 \mathbf{e}_3 = \mathbf{f}_f + f_3 \mathbf{e}_3$$

$$\|\mathbf{f}_f\| \leq \mu f_3$$

$$\mathbf{f}_f = f_1 \mathbf{e}_1 + f_2 \mathbf{e}_2 \Rightarrow \|\mathbf{f}_f\| = \sqrt{f_1^2 + f_2^2}$$

$$\mathbf{f}_c \times \mathbf{e}_3 = -f_1 \mathbf{e}_2 + f_2 \mathbf{e}_1 \Rightarrow \|\mathbf{f}_c \times \mathbf{e}_3\| = \sqrt{f_1^2 + f_2^2}$$

$$\left. \begin{array}{l} \|\mathbf{f}_f\| \leq \mu f_3 \\ \mathbf{f}_f = f_1 \mathbf{e}_1 + f_2 \mathbf{e}_2 \Rightarrow \|\mathbf{f}_f\| = \sqrt{f_1^2 + f_2^2} \\ \mathbf{f}_c \times \mathbf{e}_3 = -f_1 \mathbf{e}_2 + f_2 \mathbf{e}_1 \Rightarrow \|\mathbf{f}_c \times \mathbf{e}_3\| = \sqrt{f_1^2 + f_2^2} \end{array} \right\} \Rightarrow \|\mathbf{f}_c \times \mathbf{e}_3\| \leq \mu f_3$$

$$\Rightarrow -\|\mathbf{r} - \mathbf{v}\|_{Max} \int_{\Upsilon} \mu f_3 dA \leq M'_3 \leq \|\mathbf{r} - \mathbf{v}\|_{Max} \int_{\Upsilon} \mu f_3 dA$$

$$\Rightarrow -\mu \|\mathbf{r} - \mathbf{v}\|_{Max} F_3 \leq M'_3 \leq \mu \|\mathbf{r} - \mathbf{v}\|_{Max} F_3 \quad (7.8.5)$$

To find an approximation for $\|\mathbf{r} - \mathbf{v}\|_{Max}$, consider a circle with its center at the NCM point as shown in Figure 7.11. We find the maximum radius R for this circle such that there exist at least two points inside the convex hull Υ and on the circumference of the circle on exactly opposite sides of the NCM point (or find the largest line segment inside the convex hull with NCM point as its midpoint). To maximize M'_3 , we assume that the distributed contact forces are only concentrated at these two points with each point tolerating a concentrated force equal to $\frac{\mathbf{F}}{2}$. The ranges for the frictional moment

M'_3 at the NCM point that can be produced by these two concentrated forces will be:

$$\Rightarrow -\mu R F_3 \leq M'_3 \leq \mu R F_3 \quad (7.8.6)$$

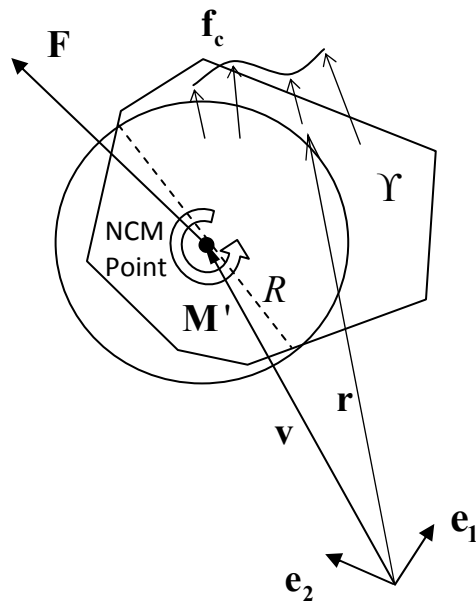


Figure 7.11. Finding the largest line segment in the convex hull with NCM point as its midpoint

As an approximation we assume without a mathematical proof that it is impossible to consider a case in which M'_3 can exceed the limits in constraint (7.8.6).

The explanation for assuming two opposite points taking exactly $\frac{F}{2}$ is that the distributed forces should not produce any net moment about planar axes about NCM point according to the definition of the NCM point. Plots of the values of R versus the location of NCM point are calculated for different contact areas and shown in Figures 7.12-7.16.

It is observed from these figures that when NCM point is at any of the corners of Υ , we will have $R = 0$ and the contact area can take no frictional moment according to constraint (7.8.6) and $M'_3 = 0$. If the NCM point is located on one of the sides of Υ , the maximum allowable range for frictional moment (maximum R) occurs when NCM is the midpoint of that side. It is also observed from these figures that the maximum

possible range for frictional moment (maximum R) occurs when the NCM point is somewhere near the geometrical center of Υ . These figures seem to match the reality very well and can be an evidence for the validity of constraint (7.8.6).

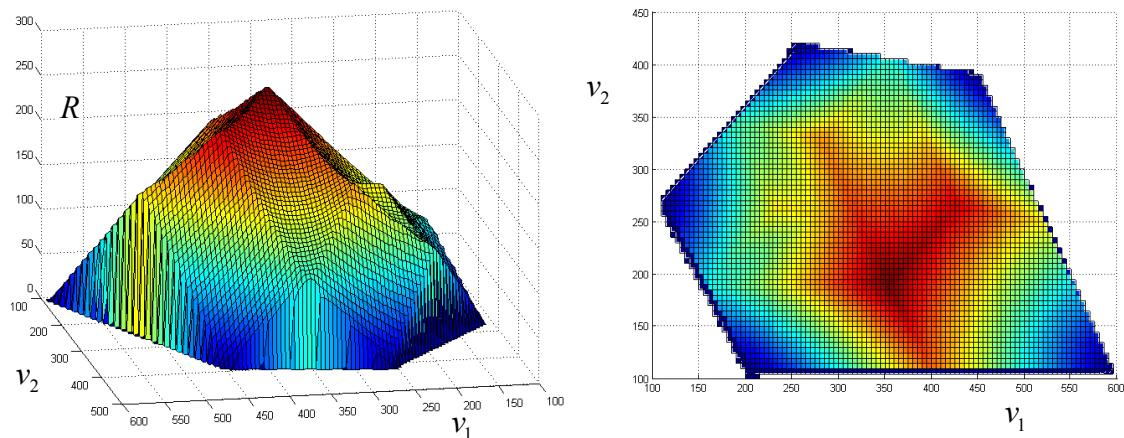


Figure 7.12. The value of R for an irregular pentagon - Left: Perspective view, Right: Top View

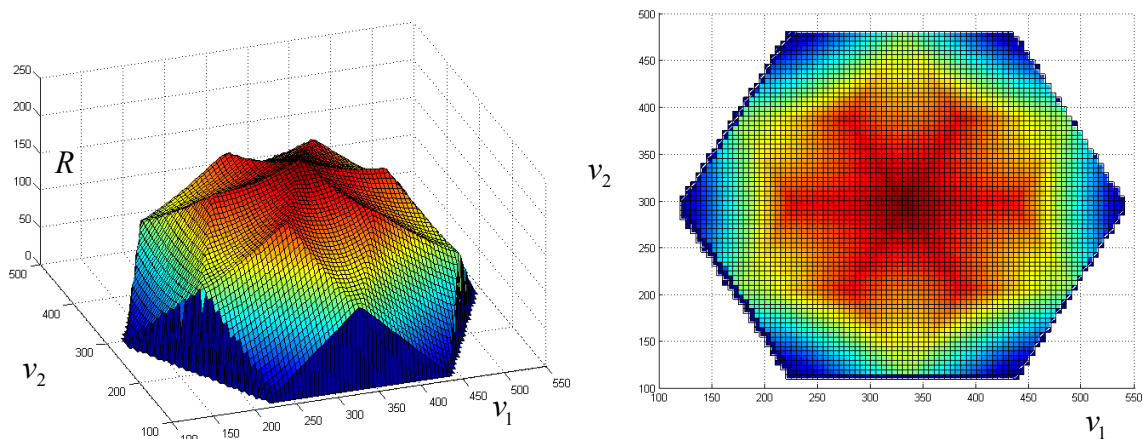


Figure 7.13. The value of R for a regular hexagon - Left: Perspective view, Right: Top View

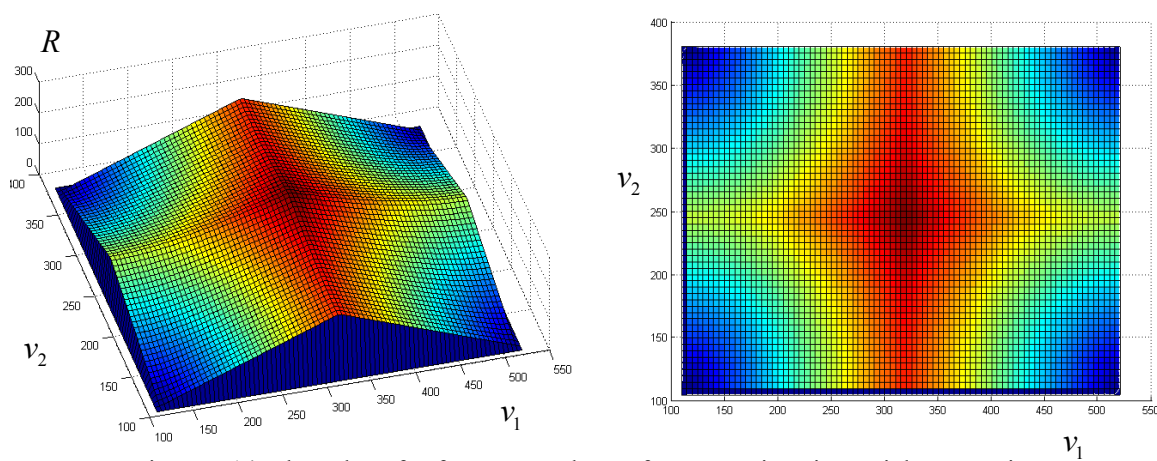


Figure 7.14. The value of R for a rectangle - Left: Perspective view, Right: Top View

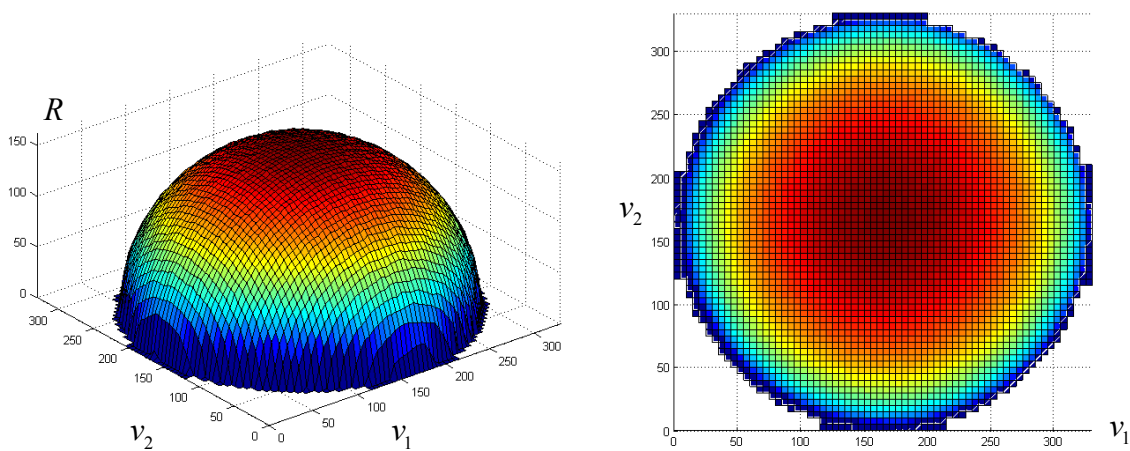


Figure 7.15. The value of R for a disk - Left: Perspective view, Right: Top View

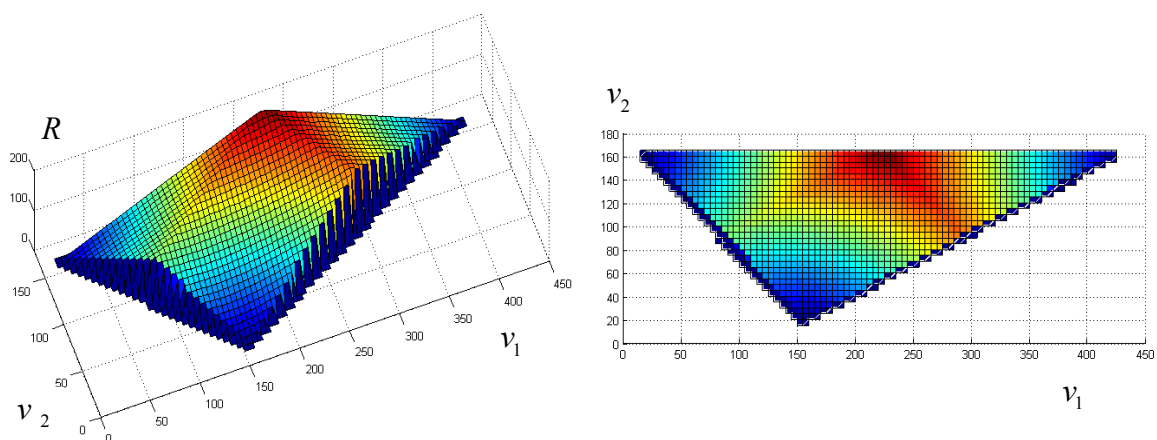


Figure 7.16. The value of R for a triangle - Left: Perspective view, Right: Top View

Anyway, constraint (7.8.6) may still not be a perfect constraint and will be a topic of future research. Due to this imperfectness, the satisfaction/violation of this constraint does not completely and mathematically ensure that the given solution is possible/impossible in the real world. So, one may want to consider larger values for R to have a more loose constraint and to be sure of including all solutions which are possible in the real world and this constraint might omit. On the other hand, one may want to consider smaller values to ensure that the solution obtained is completely possible in the real world.

Nevertheless, the role of M'_3 on the total net moment in the global coordinate frame is normally small compared to the moments produced by the components of \mathbf{F} . This is because the distance of the global origin from \mathbf{F} is normally larger than the value of R . Therefore, the possible inexactness of constraint (7.8.6) will not cause a major problem in the final results. Constraints (7.8.1) and (7.8.6) along with the NCM constraints are our proposed constraints on the resultant contact forces and moments \mathbf{F}_α and \mathbf{M}_α acting on each contact area Υ_α .

In Chapter 10, we shall see that in order to find the margins of stability, we have to solve an optimization problem. There, we shall see that inequality (7.8.6) is the only constraint that makes that optimization problem nonlinear. Therefore, we also propose here a linear constraint that can be used instead of the nonlinear constraint (7.8.6). We can derive the following inequality in a way similar to (7.8.5):

$$-\mu \|\mathbf{r} - \mathbf{p}\|_{Max} F_3 \leq M_3 \leq \mu \|\mathbf{r} - \mathbf{p}\|_{Max} F_3 \quad (7.8.7)$$

Because the distributed forces are in a convex hull, the maximum imaginable value for $\|\mathbf{r} - \mathbf{p}\|_{Max}$ can be achieved at one of the corners of the convex hull as shown in Figure 7.17. Assume that it is achieved at corner E_i of the convex hull Υ of the contact area located at \mathbf{E}_i . Then, we can consider the following linear constraint instead of constraint (7.8.6):

$$-\mu \|\mathbf{E}_i - \mathbf{p}\|_{F_3} \leq M_3 \leq \mu \|\mathbf{E}_i - \mathbf{p}\|_{F_3} \quad (7.8.8)$$

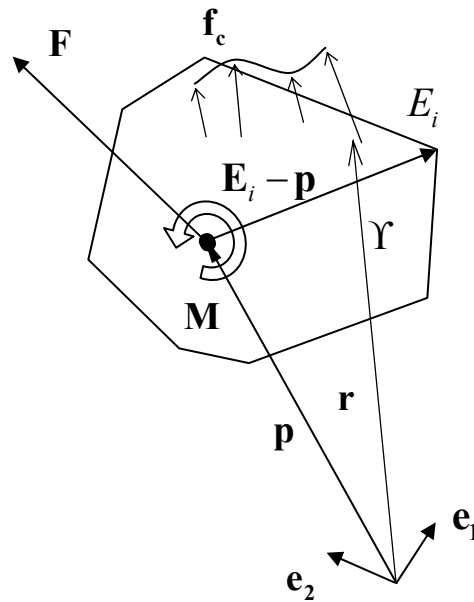


Figure 7.17. A loose constraint on the frictional moment which is linear

7.9 Summary and Conclusion

This chapter presented a general set of constraints on the equivalent reaction force systems (forces and moments) of non-adhesive contact areas by defining a point called NCM point. The NCM (Normal Contact Moment) point is defined as that point on the contact area at which the moment of the equivalent reaction force system is normal to the contact area. The general set of constraints is composed of NCM constraints and some suggested constraints on frictional forces and moments which use the NCM point definition. Major conclusions from the present study are:

- 1- A given contact force system \mathbf{F} and \mathbf{M} for a contact area is the resultant (equivalent) of unilaterally compressive distributed forces on that contact area, if and only if the NCM point corresponding to that force system is inside the convex hull of that contact area and \mathbf{F} is compressive, i.e., $\mathbf{F} \cdot \mathbf{e}_3 > 0$ (Theorem 7.1).
- 2- The NCM point corresponding to a contact force system \mathbf{F} and \mathbf{M} is on an edge of the convex hull of the contact area, if and only if all the distributed contact forces on that contact area are acting on that edge (Theorem 7.2).

According to the item 1 above, the NCM constraints (7.7.16) are necessary and sufficient for modeling the unilaterality of distributed contact forces. Therefore, the unilaterality of distributed contact forces can be modeled completely by the NCM constraints. Based on the NCM point location, we presented new constraints on the frictional contact moment of a contact area. NCM constraints along with these proposed

coulomb friction constraints ((7.8.1) and (7.8.6)) should be used in any problem where we want to model the equivalent concentrated forces and moments exerted on a body by an external contact area which is rigid, flat and non-adhesive. As no assumption was made in this chapter for the orientation of the contact areas, the presented NCM and friction constraints are applicable for systems with any number of contact areas with the environment, oriented arbitrarily with respect to each other.

CHAPTER 8

ZMP VERSUS NCM CONSTRAINTS

8.1 Introduction

It is noted that if there is only one contact area between the dynamic system and the environment, then the ZMP and the NCM point coincide. When there are multiple contact areas, then each contact area has its own NCM point and the ZMP is somewhere inside the convex hull of all the contact points. In this chapter, we study the relationship between the ZMP and NCM point locations and compare the ZMP and NCM constraints. It is shown that ZMP constraint can be derived from the NCM constraints. It is also shown that ZMP constraint is a weaker constraint that can lead to unacceptable solutions for GRF. In a separate effort, we present a theorem which proves that the ZMP method in Chapter 4 produces incorrect solutions for GRF due to an assumption used in the ZMP method. The ZMP constraint also does not prevent this undesirable GRF to be produced due to its forementioned weakness. The pitfall in the logical reasoning that supported the ZMP method is also pointed out. The experimental data that supported the ZMP method are also analyzed to complete this study. Applicability of the ZMP constraint and its drawbacks are also compared with the NCM constraints.

8.2. NCM as the Physical Reason for the ZMP Constraint

In this chapter, it is mathematically proved that the NCM constraints are the real physical reason for the ZMP constraint (due to the dynamic equilibrium equations that

relates the GRF to IGE forces). As previously mentioned in Sections 3.3 and 3.6, the ZMP constraint is an inequality constraint which can be considered as a conversion of the two equations of the general dynamic equilibrium (out of the 6 force and moment equilibrium equations for the whole system) into inequalities by removing the contact forces acting on the system from the equations. These two are the equations of dynamic equilibrium of the moments of all the forces exerted on the whole system about the two horizontal axes. In fact, it is because of the constraints enforced by nature on the contact forces exerted by the ZMP contact areas that the ZMP constraint should hold true. Nature enforces these constraints due to the non-adhesiveness of the ZMP contact areas. For example consider a case where one of the contact areas (one foot) of a walking robot is strongly glued to the ground and the robot is bending forward extensively in a static posture. Then the ZMP constraint does not hold and is invalid because the contact forces are no longer unilateral. The ZMP can move out of the convex hull of the contact points and the robot will not fall.

In Chapter 7, we replaced the effect of distributed contact forces exerted on the system from a particular contact area by the equivalent concentrated force and moment vectors. Due to non-adhesiveness, it was shown that each contact area can naturally exert only a specific range of possible contact forces and moments on the system based on the shape and the size of that contact area. In other words, each contact area is naturally unable to provide any arbitrary value for the six components of the equivalent forces and moments due to the non-adhesiveness of the contact area (which was modeled by the NCM and friction constraints). Dynamic equilibrium equations require that the sum of

contact forces and moments for all the contact areas cancel the net force and moment of all other (IGE) forces. Therefore, it is in fact because of the natural constraints on the equivalent contact forces and moments of non-adhesive contact areas (NCM and friction constraints) that ZMP constraint should hold true. In the next section, we identify the exact relationship between ZMP and NCM (or friction) constraints.

8.3. Mathematical Relationship Between ZMP and NCM Constraints

Figure 8.1 shows a sample frame of motion of the digital human. Assume that the digital human having n rigid and non-adhesive external contact areas Γ_α ($\alpha = 1 \dots n$) with the environment which are all located on the ground (or same plane). As shown in this figure, let us define the global coordinate frame zxy attached to the ground with the unit vector along the y axis perpendicular to the ground ($\mathbf{j} = \mathbf{k} \times \mathbf{i}$). Let us denote the ZMP location by the vector \mathbf{z} . Let \mathbf{F}_{ige}^{zmp} and \mathbf{M}_{ige}^{zmp} be the net equivalent force and moment of inertial, gravitational and external forces acting at the ZMP.

Also, let \mathbf{F}_α and \mathbf{M}_α acting at \mathbf{p}_α denote the concentrated contact force and moment equivalent to the distributed contact forces on contact area Γ_α acting from the ground on the digital human. Denote the convex hull of Γ_α by Υ_α . The dynamic equilibrium equation about ZMP is :

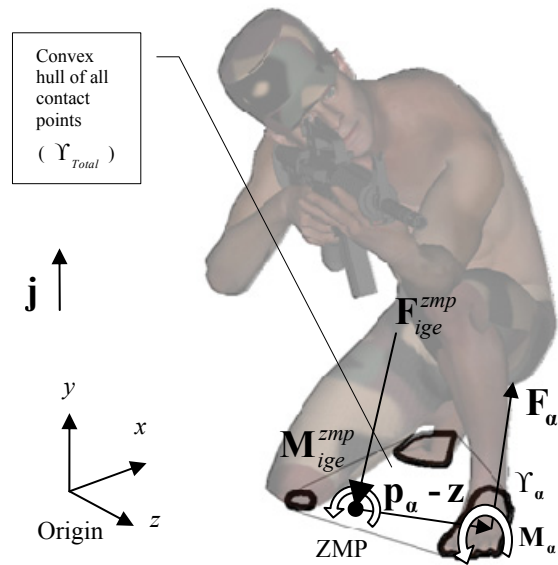


Figure 8.1. Relation of NCM points to the ZMP in a sample motion frame in the "Aiming While Kneeling" task

$$\begin{aligned}
 \sum \mathbf{F}_{ZMP} &= \mathbf{0} \\
 \Rightarrow \mathbf{F}_{ige}^{zmp} + \sum \mathbf{F}_\alpha &= \mathbf{0} \\
 \Rightarrow -\mathbf{F}_{ige}^{zmp} &= \sum \mathbf{F}_\alpha \quad (8.3.1)
 \end{aligned}$$

$$\begin{aligned}
 \sum \mathbf{M}_{ZMP} &= \mathbf{0} \\
 \Rightarrow \mathbf{M}_{ige}^{zmp} + \sum \mathbf{M}_\alpha + \sum (\mathbf{p}_\alpha - \mathbf{z}) \times \mathbf{F}_\alpha &= \mathbf{0} \\
 \Rightarrow \underbrace{\mathbf{M}_{ige}^{zmp} \times \mathbf{j}}_0 + \sum \mathbf{M}_\alpha \times \mathbf{j} + \sum (\mathbf{p}_\alpha - \mathbf{z}) \times \mathbf{F}_\alpha \times \mathbf{j} &= \mathbf{0} \\
 \Rightarrow \sum \mathbf{M}_\alpha \times \mathbf{j} + \sum (\mathbf{p}_\alpha - \mathbf{z}) \times \mathbf{F}_\alpha \times \mathbf{j} &= \mathbf{0} \quad (8.3.2) \\
 \Rightarrow \sum (-M_{\alpha_z} \mathbf{i} + M_{\alpha_x} \mathbf{k}) + \sum \left[\underbrace{(\mathbf{j} \cdot (\mathbf{p}_\alpha - \mathbf{z}))}_0 \mathbf{F}_\alpha - \underbrace{(\mathbf{j} \cdot \mathbf{F}_\alpha)}_{F_{\alpha_y}} (\mathbf{p}_\alpha - \mathbf{z}) \right] &= \mathbf{0} \\
 \Rightarrow \sum (M_{\alpha_z} \mathbf{i} - M_{\alpha_x} \mathbf{k}) + \sum F_{\alpha_y} \mathbf{p}_\alpha &= \mathbf{z} \sum F_{\alpha_y}
 \end{aligned}$$

$$\Rightarrow \mathbf{z} = \frac{\sum (M_{\alpha_z} \mathbf{i} - M_{\alpha_x} \mathbf{k}) + F_{\alpha_y} \mathbf{p}_a}{\sum F_{\alpha_y}} \quad (8.3.3)$$

$$\Rightarrow \mathbf{z} = (z_z, z_x, z_y) = \frac{\left(\sum (P_{\alpha_z} F_{\alpha_y} - M_{\alpha_x}), \sum (P_{\alpha_x} F_{\alpha_y} + M_{\alpha_z}), 0 \right)}{\sum F_{\alpha_y}} \quad (8.3.4)$$

$$\Rightarrow \mathbf{z} = (z_z, z_x, z_y) = \frac{\left(\sum F_{\alpha_y} \left(P_{\alpha_z} - \frac{M_{\alpha_x}}{F_{\alpha_y}} \right), \sum F_{\alpha_y} \left(P_{\alpha_x} + \frac{M_{\alpha_z}}{F_{\alpha_y}} \right), 0 \right)}{\sum F_{\alpha_y}} \quad (8.3.5)$$

Considering Equation (7.6.2) in the $zxy(k,i,j)$ instead of the (e_1, e_2, e_3) coordinate frame:

$$(7.6.2) \Rightarrow \mathbf{v} = (v_z, v_x, v_y) = \left(p_z - \frac{M_x}{F_y}, p_x + \frac{M_z}{F_y}, 0 \right)$$

$$\text{For contact Area } \Gamma_a : \quad \mathbf{v}_a = (v_{\alpha_z}, v_{\alpha_x}, v_{\alpha_y}) = \left(P_{\alpha_z} - \frac{M_{\alpha_x}}{F_{\alpha_y}}, P_{\alpha_x} + \frac{M_{\alpha_z}}{F_{\alpha_y}}, 0 \right) \quad (8.3.6)$$

$$\text{Therefore:} \quad (8.3.5) \text{ and } (8.3.6) \quad \Rightarrow \quad \mathbf{z} = \frac{\sum F_{\alpha_y} \mathbf{v}_a}{\sum F_{\alpha_y}} \quad (8.3.7)$$

Thus, the location of the ZMP \mathbf{z} , is the weighted average of the locations of \mathbf{v}_a .

\mathbf{v}_a is the NCM point for the contact force system \mathbf{F}_a and \mathbf{M}_a acting on contact area Γ_a .

Lemma 8.1:

The convex hull of n points is precisely the set of all the points which are the weighted averages of those n points.

This lemma appears with a rigorous proof as Theorem IV.8 in Buss (2003).

Lemma 8.2:

Any weighted average of n points falls within the convex hull of the n points.

This is an obvious result from Lemma 8.1. It also appears in several works such as such as in Foley (1996).

Theorem 8.1:

ZMP Constraint is Necessary but not Sufficient for NCM Constraints

Consider a system having external rigid and non-adhesive contact areas Γ_α which are all located on the ground (or same plane), such as shown in Figure 8.1. Let \mathbf{F}_α and \mathbf{M}_α acting at \mathbf{p}_α denote the concentrated contact forces and moments equivalent to the distributed contact forces on contact area Γ_α acting from the ground on the system. Then statement 2, shown below is a necessary but not sufficient condition for statement 1:

- 1- Each NCM point corresponding to a \mathbf{F}_α and \mathbf{M}_α located at \mathbf{v}_α is inside the convex hull of Γ_α denoted by Υ_α (for any value of $\alpha = 1 \dots n$).
- 2- ZMP located at \mathbf{z} is inside the convex hull of all the contact points Υ_{Total} .

Proof:

Part A) In this part, we show that statement 2 is a necessary condition for statement 1.

To do so, we assume that if statement 1 is true, then statement 2 has to be true, too:

Each Υ_{α} is a subset of Υ_{Total} . If 1 is true, then it is obvious that all \mathbf{v}_{α} are inside Υ_{Total} . So, their weighted average which is equal to the location of the ZMP, \mathbf{z} (Equation (8.3.7)) is also inside Υ_{Total} according to Lemma 8.2. Therefore, statement 2 is true.

Part B)

In this part, we show that statement 2 is not a sufficient condition for statement 1.

To do so, we show examples where statement 2 is true, but statement 1 is false:

Example 1: If some or all of \mathbf{v}_{α} are located outside Υ_{α} but inside Υ_{Total} , then statement 1 is false for those values of α . Statement 2 is true because any weighted average of the locations of \mathbf{v}_{α} (such as ZMP location according to Equation (8.3.7)) is inside their convex hull, Υ_{Total} according to Lemma 8.2. This example presented some cases where Statement 1 is definitely false and Statement 2 is definitely true.

Example 2: If some or all of the \mathbf{v}_{α} are located outside Υ_{Total} , then statement 1 is false for those values of α . But some specific weighted average of them (ZMP location for some specific values of F_{α_y} in Equation (8.3.7)) may still be inside Υ_{Total} . So, statement 2 can be true in such cases, too. This example presented some cases where Statement 1 is definitely false but Statement 2 may be true.

In other words, Theorem 8.1 states that:

- 1- For a system having external contact areas which are all on the ground (or on a same plane) , if each \mathbf{v}_a is inside Υ_a (first part of NCM constraints in Definition 7.2), then the ZMP constraint is satisfied.
- 2- The ZMP constraint cannot ensure that the reaction forces can be produced by the contact areas (whether each \mathbf{v}_a is inside Υ_a). Proof of Theorem 8.1 shows that if some or all of the NCM points are located outside Υ_a but all are inside Υ_{Total} , then the ZMP is inside Υ_{Total} . Even if some or all of the NCM points are located outside Υ_a and outside of Υ_{Total} , we may still have ZMP inside Υ_{Total} .

8.4. Inaccuracies of the ZMP Method in Chapter 4

It was observed in the modeling of the “going prone” task in Chapter 6 that some of the components of the ground contact reaction forces and moments calculated by the ZMP method seem to be unacceptable and impossible in the real world. For problems where contact reaction forces are calculated, such as in "Optimization-Based Motion Prediction", constraining contact reaction forces and moments by NCM constraints will ensure that they are possible in the real world and also ensures that the ZMP constraint is automatically satisfied according to Theorem 8.1. Therefore, NCM constraints should be used in such problems and there is no need for the ZMP constraint. According to Theorem 8.1, NCM constraints will not be necessarily satisfied if ZMP constraint is satisfied. Therefore, in such problems, ZMP constraint cannot be used instead of the

NCM constraints, because it is very weak and cannot ensure that the calculated ground reaction forces and moments are possible in the real world, such as what we observed in the modeling of the “going prone” task in Chapter 6.

8.4.1 Logical Pitfall in the ZMP method in Chapter 4

As a first step, we identify the pitfall in the procedure for the ZMP method presented in Chapter 4. So, let us take a look at the reasons we previously used in Sections 4.3 and 4.6 to defend the ZMP method:

Considering the method presented in Sections 4.3 and 4.6, we normally have more than one ground contact area and therefore, the ground reaction forces and moments are indeterminate. It means that there exist infinite sets of solutions for ground reaction forces and moments that can satisfy the dynamic equilibrium equations (can cancel \mathbf{F}_{ige}^{zmp} and \mathbf{M}_{ige}^{zmp}). In the ZMP method, we first ensured that it was possible to find a set of unilateral distributed forces on these contact areas to cancel \mathbf{F}_{ige}^{zmp} and \mathbf{M}_{ige}^{zmp} and produce an acceptable motion Θ . Then, we used an assumption to partition $-\mathbf{F}_{ige}^{zmp}$ and $-\mathbf{M}_{ige}^{zmp}$ on these contact areas to calculate the ground reaction forces. This is not an exactly logical procedure. The logical procedure is to first calculate a set of ground reaction forces on all contact areas to cancel \mathbf{F}_{ige}^{zmp} and \mathbf{M}_{ige}^{zmp} and then use the NCM constraints to check whether each separate contact area is able to produce that equivalent ground reaction force and moment.

8.4.2 Mathematical Impossibility of Uniform Partitioning

In this subsection, we first study the effect of uniform partitioning of GRF on location of the NCM point for each contact area. This is done in Theorem 8.2 which proves that any uniform partitioning of GRF will enforce all NCM points to coincide. Then, in Corollary 8.1, we discuss how this assumption produces GRF which are mathematically impossible in the real world.

Theorem 8.2:

Uniform Partitioning of GRF Enforces all the NCM Points to Coincide

Consider an arbitrary dynamic system shown in Figure 8.2, having external rigid and non-adhesive contact areas Γ_a which are all located on the ground (or a same plane). Also, let \mathbf{F}_a and \mathbf{M}_a acting at \mathbf{p}_a denote the concentrated contact forces and moments equivalent to the distributed contact forces on contact area Γ_a acting from the ground on the system. Assume all forces acting on the system except the ground reaction forces are determined. Consider an arbitrary point H located at \mathbf{h} (such as at ZMP or origin or any other arbitrary location). Let \mathbf{F}_{ige}^H and \mathbf{M}_{ige}^H be the net force and moment of inertial forces, gravity forces and external loads at H. The dynamic equilibrium equations for the system evaluated at H require that:

$$\left. \begin{aligned} \sum \mathbf{F}_H = \mathbf{0} &\Rightarrow \sum \mathbf{F}_a = -\mathbf{F}_{ige}^H \\ \sum \mathbf{M}_H = \mathbf{0} &\Rightarrow \sum \mathbf{M}_a + \sum (\mathbf{p}_a - \mathbf{h}) \times \mathbf{F}_a = -\mathbf{M}_{ige}^H \end{aligned} \right\} \quad (8.4.1)$$

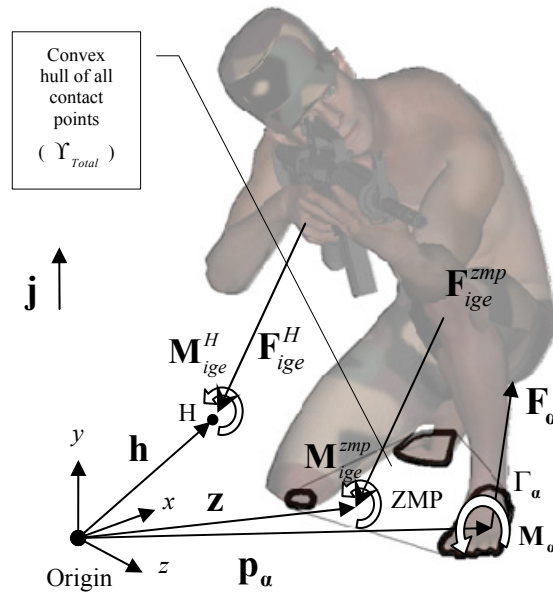


Figure 8.2. Effect of uniform partitioning of GRF at an arbitrary point H on the NCM point locations

At the point H, we assume a uniform partitioning of the components of the concentrated contact forces and moments by ratios r_β between the contact areas Γ_β , i.e., we approximate each \mathbf{F}_β and \mathbf{M}_β similar to Section 4.6, for H instead of ZMP:

$$\begin{cases} \mathbf{F}_\beta^H = -r_\beta \mathbf{F}_{ige}^H & \Rightarrow & \mathbf{F}_\beta^H = r_\beta \sum \mathbf{F}_\alpha^H \\ \mathbf{M}_\beta^H = -r_\beta \mathbf{M}_{ige}^H & \Rightarrow & \mathbf{M}_\beta^H = r_\beta \sum \mathbf{M}_\alpha^H \end{cases}$$

$$\begin{array}{l} \xrightarrow{\substack{\mathbf{F}_\beta^H = \mathbf{F}_\beta \\ \mathbf{M}_\beta^H = \mathbf{M}_\beta + (\mathbf{p}_\beta - \mathbf{h}) \times \mathbf{F}_\beta}} \\ \left\{ \begin{array}{l} \mathbf{F}_\beta = r_\beta \sum \mathbf{F}_\alpha \\ \mathbf{M}_\beta + (\mathbf{p}_\beta - \mathbf{h}) \times \mathbf{F}_\beta = r_\beta \sum (\mathbf{M}_\alpha + (\mathbf{p}_\alpha - \mathbf{h}) \times \mathbf{F}_\alpha) \end{array} \right. \quad (8.4.2) \end{array}$$

Then the uniform partitioning of GRF components enforces the NCM point corresponding to any \mathbf{F}_β and \mathbf{M}_β to coincide with the ZMP.

(i.e., regardless of where the arbitrary point H is located, such as at ZMP, origin, arbitrary joint of the avatar, etc., $\mathbf{v}_\beta = \mathbf{z}$ for any value of $\beta = 1 \dots n$, where n is the number of contact areas).

Proof:

$$\begin{aligned}
 (8.4.2) &\Rightarrow \mathbf{M}_\beta = r_\beta \sum (\mathbf{M}_\alpha + (\mathbf{p}_\alpha - \mathbf{h}) \times \mathbf{F}_\alpha) - (\mathbf{p}_\beta - \mathbf{h}) \times \mathbf{F}_\beta \\
 &\Rightarrow \mathbf{M}_\beta = r_\beta \sum (\mathbf{M}_\alpha + \mathbf{p}_\alpha \times \mathbf{F}_\alpha) - \mathbf{p}_\beta \times \mathbf{F}_\beta - r_\beta \sum (\mathbf{h} \times \mathbf{F}_\alpha) + \mathbf{h} \times \mathbf{F}_\beta \\
 &\Rightarrow \mathbf{M}_\beta = r_\beta \sum (\mathbf{M}_\alpha + \mathbf{p}_\alpha \times \mathbf{F}_\alpha) - \mathbf{p}_\beta \times \mathbf{F}_\beta + \mathbf{h} \times \underbrace{\left(-r_\beta \sum \mathbf{F}_\alpha + \mathbf{F}_\beta \right)}_0 \\
 &\Rightarrow \mathbf{M}_\beta = r_\beta \sum (\mathbf{M}_\alpha + \mathbf{p}_\alpha \times \mathbf{F}_\alpha) - \mathbf{p}_\beta \times \mathbf{F}_\beta \tag{8.4.3}
 \end{aligned}$$

$$(7.6.2) \text{ in } xzy \text{ coordinate system} \Rightarrow \mathbf{v}_\beta = (v_{\beta_z}, v_{\beta_x}, v_{\beta_y}) = \left(p_{\beta_z} - \frac{M_{\beta_x}}{F_{\beta_y}}, p_{\beta_x} + \frac{M_{\beta_z}}{F_{\beta_y}}, 0 \right)$$

$$(8.4.3) \Rightarrow \begin{cases} v_{\beta_z} = p_{\beta_z} - \frac{(r_\beta \sum (\mathbf{M}_\alpha + \mathbf{p}_\alpha \times \mathbf{F}_\alpha) - \mathbf{p}_\beta \times \mathbf{F}_\beta) \cdot \mathbf{i}}{(r_\beta \sum \mathbf{F}_\alpha) \cdot \mathbf{j}} \\ v_{\beta_x} = p_{\beta_x} + \frac{(r_\beta \sum (\mathbf{M}_\alpha + \mathbf{p}_\alpha \times \mathbf{F}_\alpha) - \mathbf{p}_\beta \times \mathbf{F}_\beta) \cdot \mathbf{k}}{(r_\beta \sum \mathbf{F}_\alpha) \cdot \mathbf{j}} \end{cases}$$

$$\Rightarrow \begin{cases} v_{\beta_z} = p_{\beta_z} - \frac{r_\beta \sum (\mathbf{M}_\alpha \cdot \mathbf{i} + (\mathbf{p}_\alpha \times \mathbf{F}_\alpha) \cdot \mathbf{i}) - (\mathbf{p}_\beta \times \mathbf{F}_\beta) \cdot \mathbf{i}}{(r_\beta \sum \mathbf{F}_\alpha \cdot \mathbf{j})} \\ v_{\beta_x} = p_{\beta_x} + \frac{r_\beta \sum (\mathbf{M}_\alpha \cdot \mathbf{k} + (\mathbf{p}_\alpha \times \mathbf{F}_\alpha) \cdot \mathbf{k}) - (\mathbf{p}_\beta \times \mathbf{F}_\beta) \cdot \mathbf{k}}{(r_\beta \sum \mathbf{F}_\alpha \cdot \mathbf{j})} \end{cases}$$

$$\Rightarrow \begin{cases} v_{\beta_z} = p_{\beta_z} - \frac{r_{\beta} \sum (M_{\alpha_x} + (\mathbf{p}_a \times \mathbf{F}_a) \cdot \mathbf{i}) - (\mathbf{p}_{\beta} \times \mathbf{F}_{\beta}) \cdot \mathbf{i}}{(r_{\beta} \sum F_{\alpha_y})} \\ v_{\beta_x} = p_{\beta_x} + \frac{r_{\beta} \sum (M_{\alpha_z} + (\mathbf{p}_a \times \mathbf{F}_a) \cdot \mathbf{k}) - (\mathbf{p}_{\beta} \times \mathbf{F}_{\beta}) \cdot \mathbf{k}}{(r_{\beta} \sum F_{\alpha_y})} \end{cases}$$

$$\begin{cases} (\mathbf{p}_a \times \mathbf{F}_a) \cdot \mathbf{i} = (\mathbf{i} \times \mathbf{p}_a) \cdot \mathbf{F}_a = (\mathbf{i} \times (p_{\alpha_z} \mathbf{k} + p_{\alpha_x} \mathbf{i})) \cdot \mathbf{F}_a = (-p_{\alpha_z} \mathbf{j}) \cdot \mathbf{F}_a = -p_{\alpha_z} F_{\alpha_y} \\ (\mathbf{p}_a \times \mathbf{F}_a) \cdot \mathbf{k} = (\mathbf{k} \times \mathbf{p}_a) \cdot \mathbf{F}_a = (\mathbf{k} \times (p_{\alpha_z} \mathbf{k} + p_{\alpha_x} \mathbf{i})) \cdot \mathbf{F}_a = (p_{\alpha_x} \mathbf{j}) \cdot \mathbf{F}_a = p_{\alpha_x} F_{\alpha_y} \end{cases}$$

$$\Rightarrow \begin{cases} v_{\beta_z} = p_{\beta_z} - \frac{r_{\beta} \sum (M_{\alpha_x} - p_{\alpha_z} F_{\alpha_y}) + p_{\beta_z} F_{\beta_y}}{(r_{\beta} \sum F_{\alpha_y})} = p_{\beta_z} - \frac{r_{\beta} \sum (M_{\alpha_x} - p_{\alpha_z} F_{\alpha_y}) + p_{\beta_z} (r_{\beta} \sum F_{\alpha_y})}{(r_{\beta} \sum F_{\alpha_y})} \\ v_{\beta_x} = p_{\beta_x} + \frac{r_{\beta} \sum (M_{\alpha_z} + p_{\alpha_x} F_{\alpha_y}) - p_{\beta_x} F_{\beta_y}}{(r_{\beta} \sum F_{\alpha_y})} = p_{\beta_x} + \frac{r_{\beta} \sum (M_{\alpha_z} + p_{\alpha_x} F_{\alpha_y}) - p_{\beta_x} (r_{\beta} \sum F_{\alpha_y})}{(r_{\beta} \sum F_{\alpha_y})} \end{cases}$$

$$\Rightarrow \begin{cases} v_{\beta_z} = -\frac{r_{\beta} \sum (M_{\alpha_x} - P_{\alpha_z} F_{\alpha_y})}{(r_{\beta} \sum F_{\alpha_y})} = \frac{\sum (P_{\alpha_z} F_{\alpha_y} - M_{\alpha_x})}{\sum F_{\alpha_y}} \\ v_{\beta_x} = \frac{r_{\beta} \sum (M_{\alpha_z} + P_{\alpha_x} F_{\alpha_y})}{(r_{\beta} \sum F_{\alpha_y})} = \frac{\sum (P_{\alpha_x} F_{\alpha_y} + M_{\alpha_z})}{\sum F_{\alpha_y}} \end{cases}$$

$$\Rightarrow \mathbf{v}_{\beta} = (v_{\beta_z}, v_{\beta_x}, v_{\beta_y}) = \frac{(\sum (P_{\alpha_z} F_{\alpha_y} - M_{\alpha_x}), \sum (P_{\alpha_x} F_{\alpha_y} + M_{\alpha_z}), 0)}{\sum F_{\alpha_y}}$$

(8.3.4)

$$\Rightarrow \mathbf{v}_{\beta} = \mathbf{z}$$

(8.4.4)

Definition 8.1:

Linearly Separable Subsets and Linearly Separable Contact Areas

According to Elizondo (2006), two subsets X and Y of \mathfrak{R}^d are said to be linearly separable (LS) if there exists a hyper plane P of \mathfrak{R}^d such that the elements of X and those of Y lie on opposite sides of it. In this chapter we define the term "Separable Contact Areas" for contact areas on a same plane (considering plane as the \mathfrak{R}^2 set). Two contact areas Γ_a and Γ_b on this plane (as the two subsets X and Y of \mathfrak{R}^2) are said to be linearly separable (LS) if there exists a line on this plane such that the two contact areas Γ_a and Γ_b lie on opposite sides of it. In other words, two contact areas are linearly separable if their convex hulls do not overlap (have no point in common).

Corollary 8.1:

Contradiction of any Uniform Partitioning of GRF with the NCM Constraints

Consider the problem presented in Theorem 8.2. Assume that all of the contact areas of the dynamic system are linearly separable (see definition 8.1). In other words, no two contact areas have convex hulls that overlap with each other. Then, for any two contact areas Γ_a and Γ_b and their convex hulls Υ_a and Υ_b , at least one of the following conditions holds true:

1- The NCM point \mathbf{v}_a corresponding to \mathbf{F}_a and \mathbf{M}_a is outside Υ_a .

(NCM constraint is violated and \mathbf{F}_a and \mathbf{M}_a are impossible in the real world).

2- The NCM point \mathbf{v}_b corresponding to \mathbf{F}_b and \mathbf{M}_b is outside Υ_b .

(NCM constraint is violated and \mathbf{F}_b and \mathbf{M}_b are impossible in the real world).

This is because \mathbf{v}_a and \mathbf{v}_b should both coincide with the ZMP which cannot exist inside both of the two non-overlapping convex hulls Υ_a and Υ_b . Therefore, in a dynamic simulation problem with contact areas that have non-overlapping convex hulls, the assumption of a uniform partitioning of the components of GRF between the contact areas will ensure that all calculated ground reaction forces and moments \mathbf{F}_a and \mathbf{M}_a on all contact areas Γ_a are in fact impossible in the real world except maybe for one of the contact areas. This is because even if ZMP constraint is satisfied, ZMP can belong to either zero or one (but not more than one) convex hull at the same time. Also, all the NCM points should coincide at the ZMP according to Theorem 8.2. Therefore, all NCM points will be at a same location which cannot be inside more than one of the non-overlapping convex hulls Υ_a (For the possibility of any \mathbf{F}_a and \mathbf{M}_a in the real world, the NCM point corresponding to them should be inside Υ_a).

Corollary 8.2:

Uniform Partitioning versus GRF as Design Variables in ZMP Method

We could have used other methods for the partitioning of GRF in the ZMP method in Chapter 4. For example, we could:

- 1- Consider the ratio of all the 6 components of GRF to the IGE forces and moments as one design variable along with using the ZMP constraint.
- 2- Consider the ratio of any of the 6 components of GRF to the IGE forces and moments as a separate design variable along with using the ZMP constraint.

In the Case 1 above, the GRF components are also uniformly partitioned on the contact areas, only their ratio to the IGE forces is not set equal to the ratio of ZMP distance from the contact areas. Therefore, they inherit all the problems of “uniform partitioning” assumption.

However, Case 2 above can be compared with the “uniform partitioning” assumption used in Chapter 4. It should be noted that using the “uniform partitioning” helps the reaction forces and moments to be not too far away from the range that is possible in the real world. Because the “uniform partitioning” will keep the NCM points inside convex hull of all the contact points Υ_{Total} , which contains points not too far away from individual contact areas (if they are not much smaller than the convex hull of all the contact points Υ_{Total}). Considering each component of the reaction forces and moments as design variables along with using the ZMP constraint (instead of NCM constraints) may produce a worse result, because although it will not enforce the reaction forces and moments to have values which are impossible in the real world, as “uniform partitioning”

does, it will allow the reaction forces and moments to be too far away from the range that is possible in the real world according to Theorem 8.1.

On the other hand, NCM constraints contradict and cannot be used along with the assumption of a uniform partitioning of concentrated contact forces and moments that was used in Chapter 4 or the uniform partitioning along with using GRF as design variables as shown in Case 1 of this corollary. Because, if two contact areas with non-overlapping convex hulls exist, then the NCM constraints cannot hold true and contradict with the “uniform partitioning” assumption and the optimization problem will render no feasible solution. Therefore, each component of the reaction forces and moments should be considered as a separate design variable when NCM constraints are used.

Due to the lack of NCM constraints, the ZMP method in Chapter 4 has been used in the literature (along with the assumption that the components of the concentrated ground reaction forces are partitioned uniformly between the contact areas as explained in Section 4.6). Some examples are: Xiang *et al* (2007, 2009), Kim *et al* (2008), Bhatt *et al* (2008) in which the environmental contact areas of the system are the contact areas of the two feet with the ground which have non-overlapping convex hulls. The dynamic tasks shown in Chapters 5 and 6 were also modeled following the same method. As it was proved by Theorem 8.2 and Corollary 8.1, the values of ground reaction forces and moments calculated in the forementioned works on all of the contact areas are impossible in the real world (according to NCM constraints) except maybe for one of the contact

areas. This inaccuracy is enforced on them by the assumption of uniform partitioning of the components of contact forces and moments (which contradicts with the NCM constraints). This inaccuracy is not prevented by the ZMP constraint (ZMP constraint is too weak for that formulation). However, if the contact areas are not too far apart, then the points on the contact areas will not be too far away from the convex hull of all contact points. In such cases, according to Corollary 8.1, the ground reaction forces and moments (which are later used for calculating torques at joints) will not be too far away from the range that is possible in the real world and therefore, the results for the joint torques will look reasonable.

By the way, the additional constraint $\mathbf{F}_{ige}^{zmp} \cdot \mathbf{j} \leq 0$, suggested in Chapter 4 has not been mentioned in the literature to complete the ZMP constraint. But this additional constraint was used in the modeling of the dynamic tasks shown in Chapters 5 and 6 to ensure the possibility of motion. Therefore, although the calculated ground reaction forces and moments are impossible in the real world, the motion is ensured to be possible according to Theorem 4.1.

8.4.3 A Re-Examination of the Basis for the Uniform Partitioning Assumption

As discussed in Section 4.6, the ZMP-based partitioning of the GRF is based on several measurement data from experiments which suggest that the ratio of the vertical component of the ground reaction force (1 component out of the 6 components) tolerated by each foot in walking motion seems to be inversely proportional to the distance of that foot from the ZMP location (see Ren, 2005, 2007; Winter, 1990, 2009).

The pitfall in this partitioning is that this approximation and these measurement data are only for the vertical component of the ground reaction force. In the ZMP method, for simplicity, we assume that all the other 5 components of the ground reaction forces and moments are also partitioned on the contact areas by the same ratios. This is impossible according to Theorem 8.2 and Corollary 8.1, as discussed before.

Therefore, to complete this study, let us go back to the original reference (Winter, 1990, 2009) for calculating GRF in the ZMP method. And this time, let us study the measurement data for all of the GRF components, not just the vertical GRF component. Similar to Section 4.6, we replot the data measured in the walking experiment published in Winter (2009) in Figures 8.3, 8.4, 8.5. In these figures, we plot the ratio of ZMP distances from the left and right feet versus the inverse of the ratio of the vertical forces on them. Of course, these data are measured in 2 dimensions and the lateral dimension is ignored in these measurements. In Figures 8.3, 8.4, 8.5, z_R and z_L respectively denote the distances of the ZMP to the right and left foot in the forward-backward direction. Also, $F_{yR}, F_{yL}, F_{zR}, F_{zL}, M_{xR}, M_{xL}$ respectively denote the vertical and frictional ground reaction forces and tipping ground reaction moments on the right and left foot.

Of course, instead of the 6 components of the GRF for 3D case, these measurement data are for 2D case (sagittal plane for walking) and only consider 3 components of the GRF (vertical and horizontal force and the moment perpendicular to plane). It is seen that the measurement data only approximately approve the linear assumption for the vertical force of the GRF. They violate the linear assumption for the frictional force and tipping moments of the GRF.

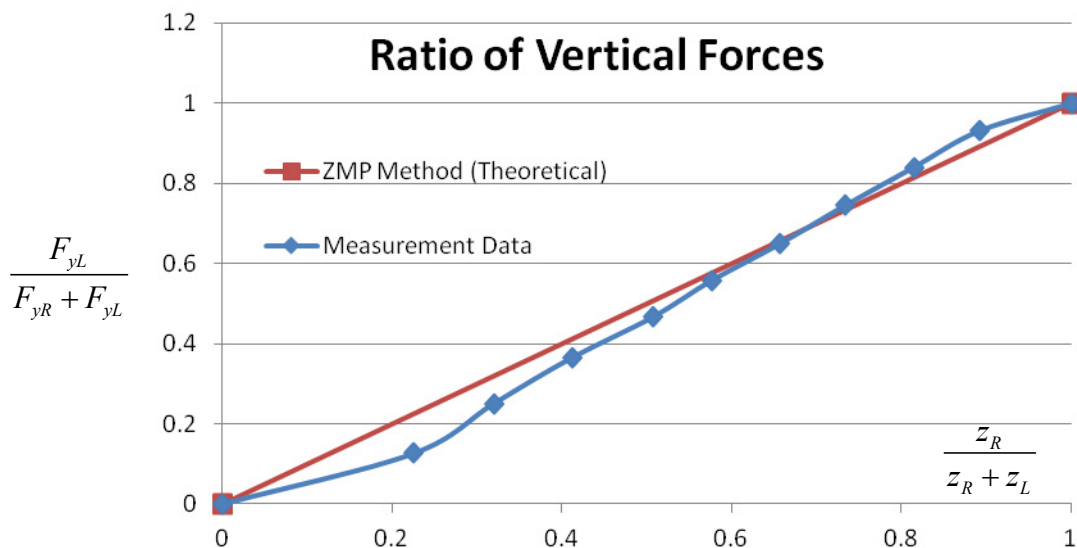


Figure 8.3. Walking measurement data from Winter (2009), approximately matching the proportionality of the vertical ground reaction forces (F_y) on the feet to the inverse of the ZMP distances from them (subscripts L and R refer to left foot and right foot)

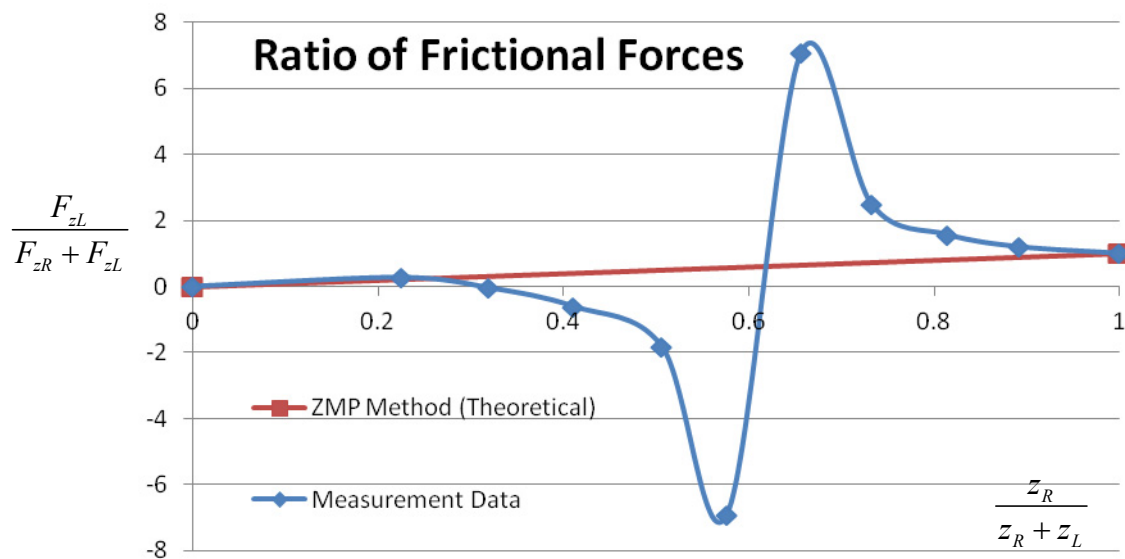


Figure 8.4. Walking measurement data from Winter (2009), showing disparity of the proportionality of the frictional ground reaction forces (F_x) on the feet to the inverse of the ZMP distances from them

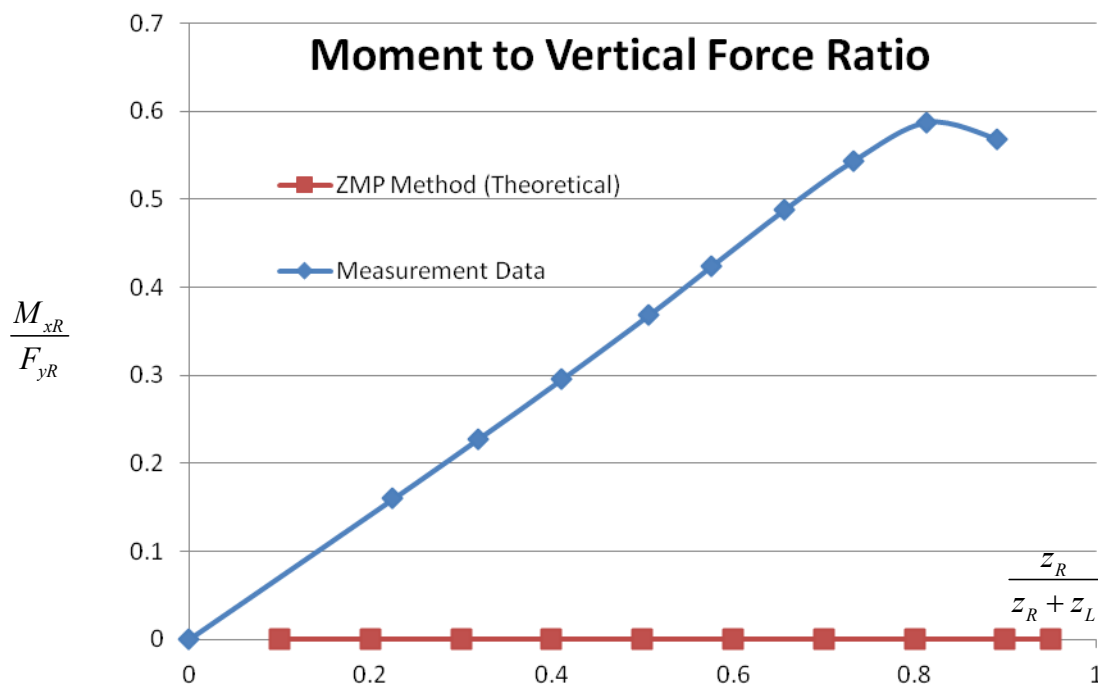


Figure 8.5. Walking measurement data from Winter (2009), showing disparity of the value of contact moment of right foot at ZMP (normalized by dividing it by the vertical force) vs. the ratio of the distances of ZMP from the feet

8.4.4 Partitioning of the Vertical Component of GRF in NCM versus ZMP Method

As a final study in this section, one may become curious that the linear assumption for the data plotted in Figure 8.3 seems to be approximately true for the vertical component of the ground reaction force. The interesting point is that this is not a coincidence. It is in fact a theoretical inequality which is implicitly embedded in the NCM constraints and will be enforced automatically when NCM constraints are used. This relation between the “vertical component of GRF for each contact area” (denoted in our 3D formulations by F_{α_y}) and the ZMP location (denoted in our formulations by z) is enforced by Equation (8.3.7) that we derived in the previous section. Equation (8.3.7)

indicated that the location of ZMP \mathbf{z} , is the weighted average of the locations of \mathbf{v}_α weighted by the values of F_{α_y} . \mathbf{v}_α is the NCM point location for contact area Γ_α and it is constrained by the NCM constraints (NCM constraints cause the approximate linear relation). Based on the definition of NCM constraints (Definition 7.2), the value for any \mathbf{v}_α is constrained to remain in the convex hull of its contact area. To plot the relation enforced by NCM constraints between \mathbf{z} and F_{α_y} ratios, we start from Equation (8.3.7):

$$(8.3.7) \quad \Rightarrow \quad \mathbf{z} = \frac{\sum F_{\alpha_y} \mathbf{v}_\alpha}{\sum F_{\alpha_y}}$$

NCM constraints enforce: \mathbf{v}_α should be inside Υ_α

Let us define $r_\alpha \triangleq \frac{F_{\alpha_y}}{\sum F_{\alpha_y}} \Rightarrow \mathbf{z} = \sum r_\alpha \mathbf{v}_\alpha \quad (8.4.5)$

Now, we try to find all the geometrical possible locations of \mathbf{z} for given values of r_α (not for all possible values of r_α). According to Lemma 8.2, Equation (8.4.5) shows that for a given value of r_α and all possible locations of \mathbf{v}_α , the locations of \mathbf{z} is some subset of the convex hull of all the contact areas Γ_α . To plot the geometrical location of \mathbf{z} for specific set of values for r_α , let us consider the simple case of having only two contact areas. For example, consider a dynamic system having two coplanar contact areas with the environment with convex hulls Υ_1 and Υ_2 . In this case, we shall have:

$$\begin{aligned} r_1 + r_2 = 1 & \Rightarrow r_1 = 1 - r_2 \\ & \stackrel{(8.4.5)}{\Rightarrow} \mathbf{z} = r_1 \mathbf{v}_1 + r_2 \mathbf{v}_2 = (1 - r_2) \mathbf{v}_1 + r_2 \mathbf{v}_2 \end{aligned} \quad (8.4.6)$$

NCM constraints enforce: $\begin{cases} \mathbf{v}_1 \text{ should be inside } \Upsilon_1 \\ \mathbf{v}_2 \text{ should be inside } \Upsilon_2 \end{cases}$

For example, consider convex hull Υ_1 to be a pentagon and convex hull Υ_2 to be a triangle located at positions shown in Figure 8.6. The convex hull Υ_{Total} of all the contact points is shown as $C_4C_5C_1D_1D_2D_3$. We are trying to find the locus (geometrical possible locations) of ZMP point (z) for a given value of r_2 (r_2 is the ratio of the vertical components of GRF tolerated by each of the two contact areas) in Υ_{Total} . Let us denote the mentioned locus by Area Λ_{r_2} for a specific value of r_2 . We will show that the Areas Λ_{r_2} will look similar to what is shown in Figure 8.6. In order to do that, let us denote one fixed arbitrary corner of convex hull Υ_1 by C_1 . Let us also denote all corners of convex hull Υ_2 by D_i .

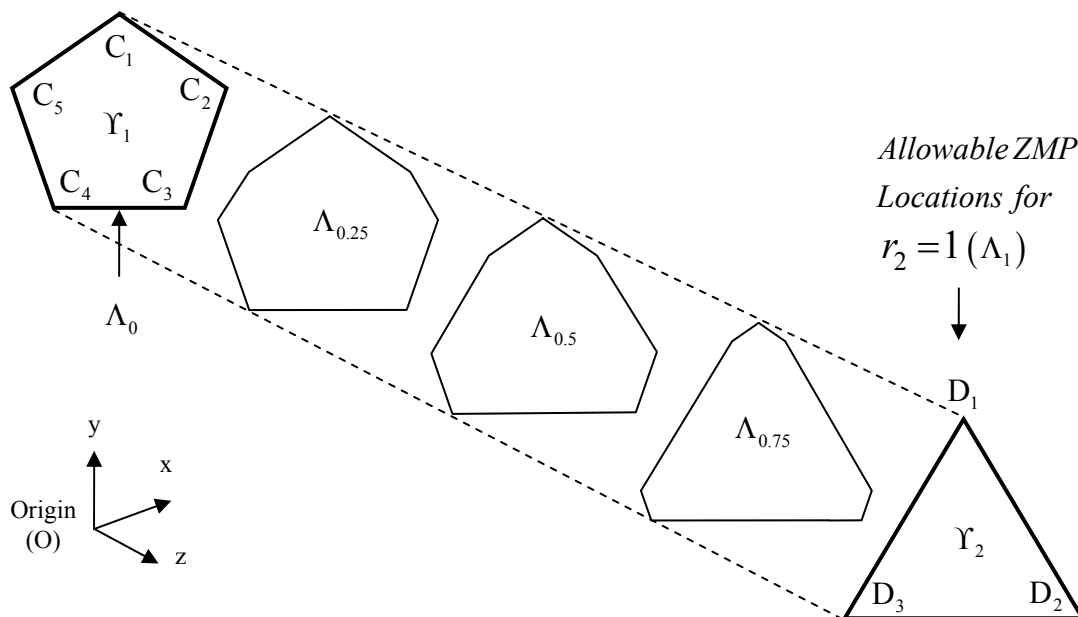


Figure 8.6. Sample problem of finding the locus of the ZMP for different values of r_2 is depicted for two convex hulls Υ_1 and Υ_2 of two contact areas. The locus denoted by Areas Λ_{r_2} is shown for several values of r_2 (0, 0.25, 0.5, 0.75, 1).

The locus of \mathbf{z} for any specific value of r_2 (Area Λ_{r_2}) can be found by the following procedure. New symbols that appear in this procedure are shown in Figure 8.7 and the procedure is depicted in that figure for $r_2 = 0.75$ (Area $\Lambda_{0.75}$). Also, let A and B denote two arbitrary points inside the convex hulls Υ_1 and Υ_2 (they will be used later):

- 1- Consider the NCM point (\mathbf{v}_1) to be fixed to corner C_1 . Vary \mathbf{v}_2 on all corners D_i and plot the locations of \mathbf{z} denoted by E_i .
- 2- Draw copies of Υ_1 scaled by $(1 - r_2)$ with corner C_1 located at all points E_i denoted by Π_i . This gives the locus of point \mathbf{z} that are obtained by all values of \mathbf{v}_1 and specific values of \mathbf{v}_2 (evaluated at the corners of the convex hull Υ_2). Therefore, the location of points inside Π_i are (O is the origin point of the reference coordinate frame):

$$\begin{cases} \text{Locus of } \Pi_i : \\ \text{for all } \mathbf{v}_1 \text{ inside } \Upsilon_1 : \end{cases} \quad \mathbf{z} = (1 - r_2)\mathbf{v}_1 + r_2(\overline{OD_i}) \quad (8.4.7)$$

- 3- Draw the convex hull of all the areas Π_i (denoted by Area Λ_{r_2}).

According to the below explanation, Area Λ_{r_2} is the exact locus of \mathbf{z} :

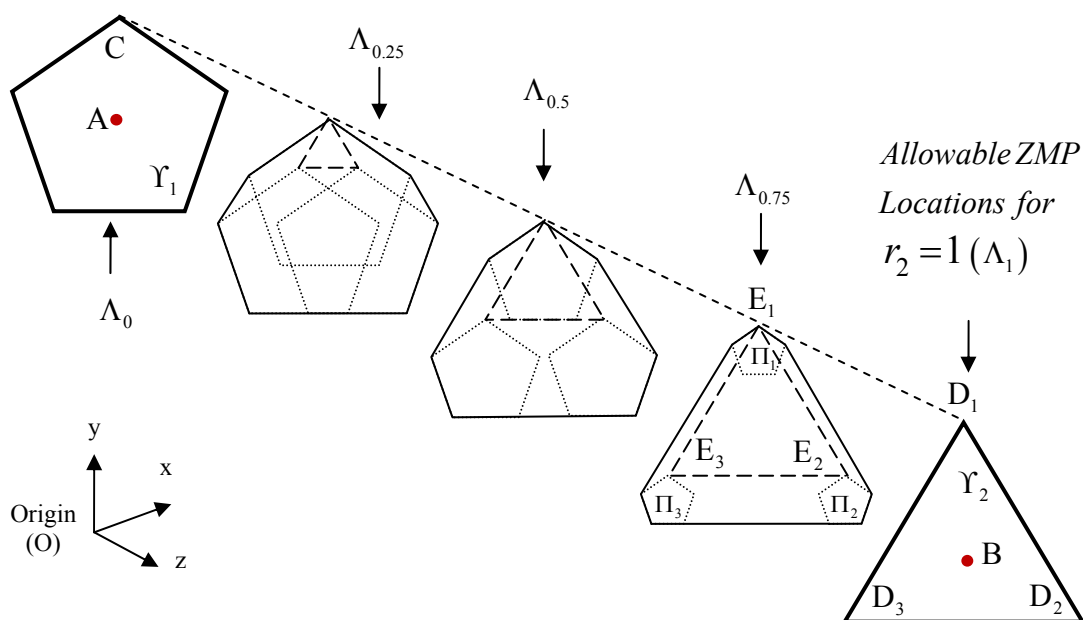


Figure 8.7. The procedure for constructing Areas Λ_{r_2} for the value of r_2 is depicted in detail for $r_2 = 0.75$ and in brief for other values of r_2 . Boundaries of Λ_{r_2} are shown by continuous lines. Boundaries of Π_i are shown by dotted lines. For each r_2 , points E_i are connected by dashed lines.

The locus of the points inside the convex hull of all the Π_i in step 2 (denoted by Area Λ_{r_2}) is equal to all weighted averages of the points in Π_i (according to Lemma 8.1). As indicated in step 2, the location of the points inside Π_i are found from Equation (8.4.7). Therefore, the locus for all the possible weighted averages of these values (the locus of the points inside Λ_{r_2}) are:

$$\left\{ \begin{array}{l} \text{Locus of } \Lambda_{r_2} : \\ \text{for all } \mathbf{v}_1 \text{ inside } \Upsilon_1 \text{ and for all } k_i > 0 : \\ \mathbf{z} = \frac{\sum_i k_i ((1-r_2)\mathbf{v}_1 + r_2(\overline{OD}_i))}{\sum_i k_i} = (1-r_2)\mathbf{v}_1 + r_2 \frac{\sum_i k_i (\overline{OD}_i)}{\sum_i k_i} \end{array} \right. \quad (8.4.8)$$

On the other hand, the location of the points inside the convex hull Υ_2 (the values of \mathbf{v}_2) is equal to all possible weighted average of the locations of the corners of that convex hull (according to Lemma 8.1). Therefore:

$$\left\{ \begin{array}{l} \text{Locus of } \Upsilon_2 : \\ \text{for all } k_i > 0 : \end{array} \right. \quad \mathbf{v}_2 = \frac{\sum_i k_i (\overline{OD}_i)}{\sum_i k_i} \quad (8.4.9)$$

$$(8.4.8) \text{ and } (8.4.9) \Rightarrow \left\{ \begin{array}{l} \text{Locus of } \Lambda_{r_2} : \\ \text{for all } \mathbf{v}_1 \text{ inside } \Upsilon_1 \text{ and all } \mathbf{v}_2 \text{ inside } \Upsilon_2 \\ \mathbf{z} = (1-r_2)\mathbf{v}_1 + r_2\mathbf{v}_2 \end{array} \right. \quad (8.4.10)$$

Therefore, Area Λ_{r_2} is the exact locus of \mathbf{z} . This means that a limitation on the location of ZMP is automatically enforced by the NCM constraints for any fixed value of r_2 . Now, we try to compare this limitation with the limitation imposed by uniform partitioning assumption. The ZMP constraint only limits the location of ZMP to remain in the convex hull of the two contact areas (Γ_1 and Γ_2). However, the assumption of uniform partitioning used along with the ZMP constraint does limit the location of ZMP for each fixed value of r_2 because the uniform partitioning assigns the value of r_2 based on the ZMP location. Therefore, for any fixed value of r_2 , ZMP location is implicitly constrained by the uniform partitioning assumption. We use the relations from Section 4.6 to derive this implicit constraint on the ZMP for each fixed value of r_2 :

$$(4.6.5) \quad \Rightarrow \quad r_1 / r_2 = d_2 / d_1$$

In (4.6.5), $d_1 = \|\mathbf{p}_1 - \mathbf{z}\|$ denotes the distance of the point of action of equivalent forces and moments \mathbf{F}_1 and \mathbf{M}_1 (acting at \mathbf{p}_1) from the ZMP and $d_2 = \|\mathbf{p}_2 - \mathbf{z}\|$ denotes the distance of the point of action of equivalent forces and moments \mathbf{F}_2 and \mathbf{M}_2 (acting at \mathbf{p}_2) from the ZMP.

Let us consider the contact areas with the convex hulls Υ_1 and Υ_2 in Figure 8.7. And let the locations of \mathbf{p}_1 and \mathbf{p}_2 be some point near the geometric centers of Υ_1 and Υ_2 denoted of by A and B in that figure (for simplicity of drawing the next figures). Therefore, (4.6.5) turns into $r_1 / r_2 = d_2 / d_1 = (1 - r_2) / r_2$. It means that for any fixed value of r_2 , only points on the ground (or plane) whose distances from points A and B have a ratio equal to $(1 - r_2) / r_2$ can be the location of the ZMP. This corresponds to the classical geometrical definition of Apollonian Circle, which we redefine here:

Definition 8.2: Apollonian Circle

Consider points A and B, and some constant k. The locus of point P satisfying the condition $\|\overline{AP}\| = k \|\overline{BP}\|$ is called an Apollonian Circle as shown in Figure 8.8. For any two points, there is an infinite number of Apollonian circles, one for each distinct value of k. When $k = 1$, The circle becomes a line, the perpendicular bisector of segment AB.

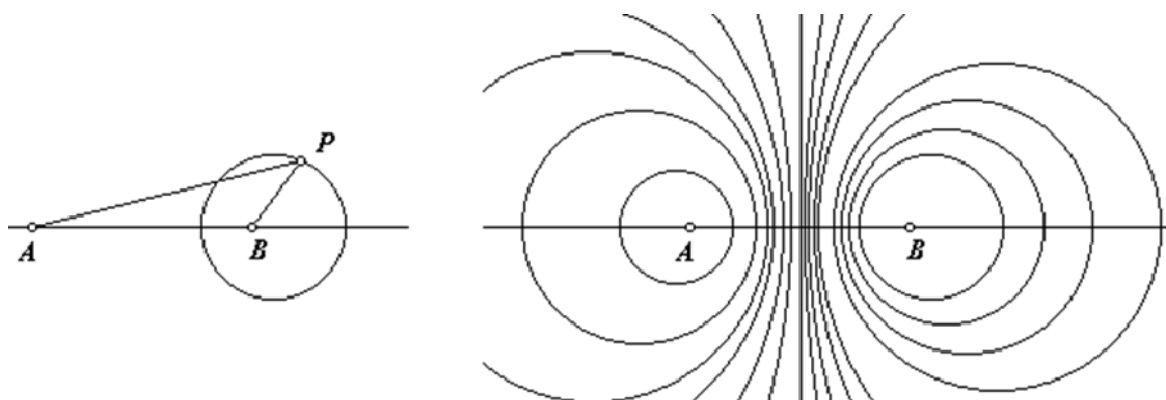


Figure 8.8. Apollonian Circles for different ratio of distances from points A,B. The picture is borrowed from Kunkel (2011).

Therefore, for any fixed value of r_2 , the allowable ZMP locations based on the assumption of linear partitioning are the apollonian circles with $k = \frac{1-r_2}{r_2}$. These locations (Apollonian Circles) are superimposed on Figure 8.7 for the example depicted in that figure to obtain Figure 8.9. Apollonian Circles in Figure 8.9 are shown by red curves. ZMP constraint furthermore constrains the ZMP to be inside the convex hulls Υ_1 and Υ_2 . Therefore, based on the ZMP method introduced in Chapter 4, for the convex hulls Υ_1 and Υ_2 , the allowable ZMP locations for any fixed value of r_2 are the parts of Apollonian Circles with $k = \frac{1-r_2}{r_2}$ that are inside the convex hulls Υ_1 and Υ_2 in Figure 8.9. For example, the red straight line drawn in the middle of this figure is the Apollonian Circle corresponding to $k=1$. The part of the line that is inside the convex hull specifies the regions at which ZMP can be located in order to have $r_1 = r_2 = 0.5$ in the ZMP

method. On the other hand, the Area $\Lambda_{0.5}$ in Figures 8.7 and 8.9 specifies the region at which ZMP can be located in order to have $r_1 = r_2 = 0.5$ in the NCM method.

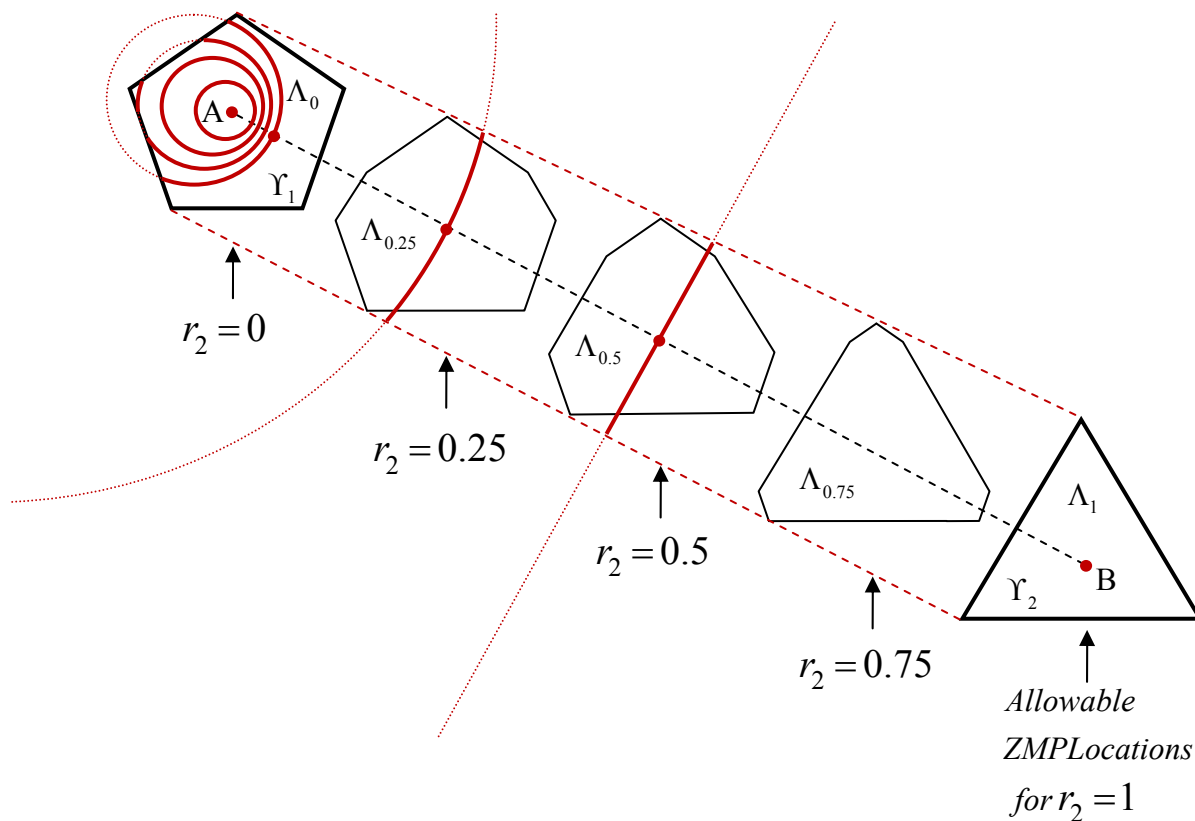


Figure 8.9. An example for the locus of the ZMP for different r_2 based on the ZMP method with linear GRF partitioning (locus are the points on the red curves - Apollonian Circles) and NCM method with GRF as design variables (locus are the points inside the Λ_{r_2} shapes).

8.5. Uniform Partitioning of GRF versus Uniform Pressure on Contact Areas

In Section 8.4.2, it was proved that uniform partitioning of GRF components is mathematically impossible in the real world. The nomenclature "uniform partitioning of GRF components" may be mistaken with the assumption of "uniform pressure" on contact areas. The assumption of "uniform pressure" on a system's contact areas is a very common assumption that can be used when the net of IGE forces and moments have specific values (cannot be used for general cases of IGE forces and moments). To further clarify the difference between these two assumptions, we present an example in this section which shows a system with a specific value of IGE forces and moments whose GRF can also be calculated using the "uniform pressure" assumption. We compare the results of "uniform pressure" with the results of "uniform partitioning of GRF components" in this example:

Example 8.1: Uniform Pressure versus Uniform Partitioning (Special Case)

Consider a dynamic system in Figure 8.10 which has two similar disc-shaped contact areas with the ground at an instant of its motion. Assume that $\mathbf{F}_{ige}^{zmp} = -2F\mathbf{j}$ and the distributed forces exerted from the ground on these contact areas is in form of a pressure uniformly distributed on these contact areas (which can equilibrate this special case of net IGE forces and moments).

This is a very common assumption for the distribution of GRF (for cases with the net of IGE forces similar to this example) and is a possible case in the real world. Is this a counter-example for Theorem 8.2 and Corollary 8.1 ?

(One of the results of Theorem 8.2 and Corollary 8.1 is that: The assumption of the uniform partitioning of the GRF components ensures that the calculated GRF are impossible values in the real world for all ground contact areas, except may be for one of the contact areas.)

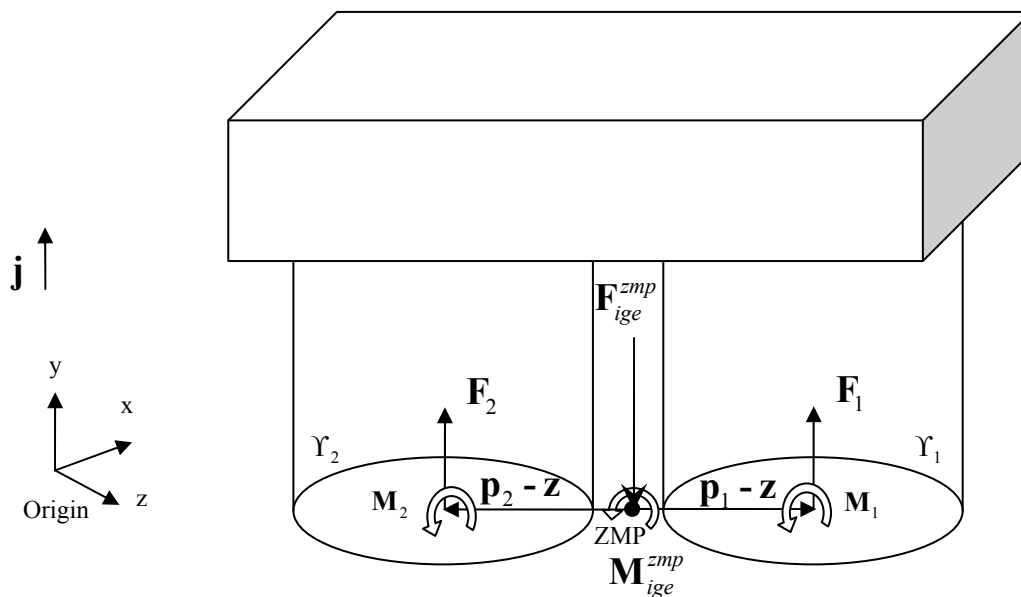


Figure 8.10. An example to show the difference between "Uniform Pressure" and "Uniform Partitioning" assumptions for GRF partitioning

Answer:

No. Because, "uniform pressure" is not a case of "uniform partitioning of GRF components" as defined in Section 4.6. This is shown below:

- Uniform pressure on Υ_1 and Υ_2 results in:

$$\begin{cases} \mathbf{F}_1 = \mathbf{F}_2 = F \mathbf{j} & (8.5.1) \\ \mathbf{M}_1 = \mathbf{M}_2 = 0 & (8.5.2) \end{cases}$$

- Uniform partitioning of GRF components on Υ_1 and Υ_2 according to Equations (4.6.3) – (4.6.6), results in:

$$\begin{cases} \mathbf{F}_\beta^{ZMP} = -r_\beta \mathbf{F}_{ige}^{ZMP} & (4.6.3) \\ \mathbf{M}_\beta^{ZMP} = -r_\beta \mathbf{M}_{ige}^{ZMP} & (4.6.4) \\ \frac{r_\alpha}{r_\beta} = \frac{d_\beta}{d_\alpha} & (4.6.5) \\ \sum r_\alpha = 1 & (4.6.6) \end{cases} \Rightarrow \begin{cases} \mathbf{F}_1^{ZMP} = -r_1 \mathbf{F}_{ige}^{ZMP}, \mathbf{F}_2^{ZMP} = -r_2 \mathbf{F}_{ige}^{ZMP} & (8.5.3) \\ \mathbf{M}_1^{ZMP} = -r_1 \mathbf{M}_{ige}^{ZMP}, \mathbf{M}_2^{ZMP} = -r_2 \mathbf{M}_{ige}^{ZMP} & (8.5.4) \\ \frac{r_1}{r_2} = 1 & (8.5.5) \\ r_1 + r_2 = 1 & (8.5.6) \end{cases}$$

$$(8.5.5), (8.5.6) \Rightarrow \left. \begin{matrix} r_1 = r_2 = 0.5 & (8.5.7) \\ (8.5.3), (8.5.4) \end{matrix} \right\} \Rightarrow \begin{cases} \mathbf{F}_1^{ZMP} = \mathbf{F}_2^{ZMP} = -\frac{\mathbf{F}_{ige}^{ZMP}}{2} = F \mathbf{j} & (8.5.8) \\ \mathbf{M}_1^{ZMP} = \mathbf{M}_2^{ZMP} = -\frac{\mathbf{M}_{ige}^{ZMP}}{2} = \mathbf{0} & (8.5.9) \end{cases}$$

This condition is shown in Figure 8.11:

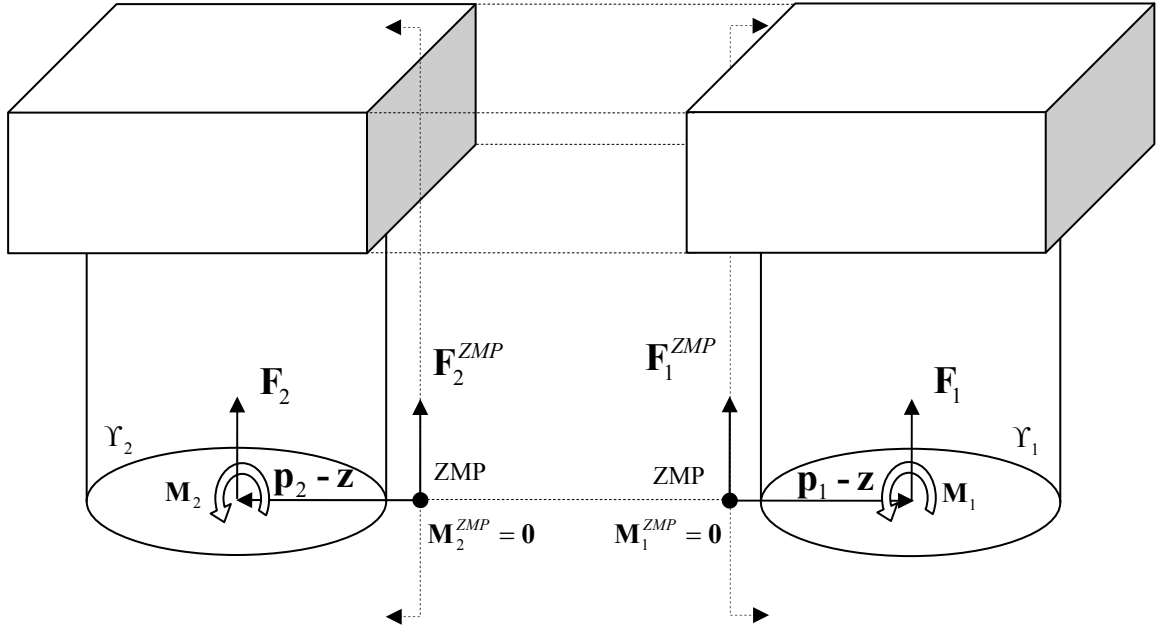


Figure 8.11. Results of GRF by using the "Uniform Partitioning" assumptions

Also, according to the definition given in Section 4.6, $\mathbf{F}_a^{ZMP} = \mathbf{F}_a$, $\mathbf{M}_a^{ZMP} = \mathbf{M}_a + (\mathbf{p}_a - \mathbf{z}) \times \mathbf{F}_a$ denote the force and moment system equal to \mathbf{F}_a and \mathbf{M}_a acting at the ZMP. Therefore, \mathbf{F}_a and \mathbf{M}_a will be equal to:

$$\begin{cases} \mathbf{F}_1 = \mathbf{F}_1^{ZMP} = \mathbf{F}_2 = \mathbf{F}_2^{ZMP} \\ \mathbf{M}_1 = \mathbf{M}_1^{ZMP} - (\mathbf{p}_1 - \mathbf{z}) \times \mathbf{F}_1 \\ \mathbf{M}_2 = \mathbf{M}_2^{ZMP} - (\mathbf{p}_2 - \mathbf{z}) \times \mathbf{F}_2 \end{cases} \Rightarrow \begin{cases} \mathbf{F}_1 = \mathbf{F}_2 = F\mathbf{j} & (8.5.10) \\ \mathbf{M}_1 = (\mathbf{z} - \mathbf{p}_1) \times \mathbf{F}_1 & (8.5.11) \\ \mathbf{M}_2 = (\mathbf{z} - \mathbf{p}_2) \times \mathbf{F}_2 & (8.5.12) \end{cases}$$

As a more special case of this problem, let $\mathbf{z} = \mathbf{0}$, $\mathbf{p}_1 = d\mathbf{i}$, $\mathbf{p}_2 = -d\mathbf{i}$ (center of the two discs on the x axis and the origin of the coordinate frame located at ZMP). Then:

$$\begin{cases} (8.5.10) & \Rightarrow & \mathbf{F}_1 = \mathbf{F}_2 = F\mathbf{j} \\ (8.5.11) & \Rightarrow & \mathbf{M}_1 = -Fd\mathbf{k} \\ (8.5.12) & \Rightarrow & \mathbf{M}_2 = Fd\mathbf{k} \end{cases}$$

It is seen that Equation (8.5.10) is the same as Equation (8.5.1), but Equation (8.5.11) and (8.5.12) are not the same as Equation (8.5.2). So, the assumption of "uniform pressure" gives similar results for the partitioning of forces as the assumption of "uniform partitioning of GRF components", but does not give similar results for the partitioning of moments.

Example 8.2: Uniform Pressure versus Uniform Partitioning (General Case)

Is there a case where the assumption of "uniform partitioning of GRF components" in a dynamic system with several arbitrary contact areas with the ground render GRF that are equal to the results rendered by the assumption of "uniform pressure"?

No. The assumption of "uniform partitioning of GRF components" can never render the results of a "uniform pressure" assumption for any system with more than one contact area with the environment.

Because the assumption of "uniform pressure" will enforce NCM points for each contact area to be at the geometrical center of that contact area. But, the assumption of

"uniform partitioning of GRF components" will enforce all the NCM points for all contact areas to coincide at a same point which is the ZMP point (according to Theorem 8.2). ZMP point cannot be at the same time the geometrical center of all the contact areas. Because the contact areas do not overlap. So, partitioning the GRF components uniformly will render GRF that are never equal to uniform pressure on the contact areas.

8.6. A Discussion of the Applicability and Drawbacks of NCM versus ZMP Constraints

8.6.1. Applicability of NCM versus ZMP Constraints

ZMP constraint is suitable in problems such as dynamic simulation or virtual reality problems (for example an offline simulation of a robot motion), in which ground reaction forces and moments on individual contact areas are not calculated. In such problems, the role of the ZMP constraint (if used along with the proposed additional constraint in Theorem 4.1 that constrains the IGE forces to be downwards) is to ensure that those simulated motions of the dynamic system can be produced by its given environmental contact areas.

But, if ground reaction forces and moments on individual contact areas are also calculated in such problems, NCM constraints are more suitable than the ZMP constraint as discussed in Section 8.4. In such cases, ZMP constraint is too weak to check whether those calculated ground reaction forces are possible in the real world according to Section 8.3 and undesirable results may be achieved as discussed in Section 8.4. Instead of ZMP

constraint, NCM constraints should be used which are stronger than the ZMP constraint and their satisfaction will ensure the satisfaction of ZMP constraint, too.

8.6.2. Drawbacks of the ZMP versus NCM Constraints

A major drawback of the ZMP constraint that it applies only to the cases in which the system's contact with the environment is in one plane only. It cannot be used when different parts of the system come into contact with the environment and the contact areas are in different planes. Unlike the ZMP constraint, NCM constraints are applicable for the most general cases of contact areas (coplanar or non-coplanar contact areas which are horizontal or inclined or parallel or non-parallel).

Also the effect of the natural limitations on the frictional forces exerted from external contact areas (such as between the ground and the foot) on the possibility or stability of the motion is not taken into account in the ZMP or NCM constraints. In Chapter 7, using the NCM point location, the effect of friction was also considered in the proposed constraints.

8.7. Summary and Conclusion

Using the NCM concepts introduced in Chapter 7, this chapter presented a relationship between the location of the ZMP and NCM points for multiple contact areas for cases where the contact areas are coplanar. This relationship let us evaluate the ZMP

concepts and compare them with the NCM concepts. From the presented study, the conclusions are:

- 1- ZMP constraint is just a results of NCM constraints and is weaker than NCM constraint. In problems where GRF are calculated, ZMP constraint cannot ensure that the calculated GRF are possible in the real world. The NCM constraints can ensure that and also ensure that ZMP constraint is satisfied, too. So, the ZMP method introduced in Chapter 4 allows unacceptable solutions which are impossible in the real world.
- 2- The linear, uniform partitioning assumption used in the ZMP method in fact causes all the calculated GRF to have values that are mathematically impossible in the real world.
- 3- The pitfall in the reasoning that supported the ZMP method is that the ZMP constraint ensures the unilaterality of the contact forces before partitioning them. This should logically be done after partitioning the GRF using the NCM constraints.
- 4- The experimental data that supported the ZMP method are only for the ratio of the vertical component of the GRF but not for the remaining 5 components of GRF. It is also shown that this experimental data that really supported the linear, uniform partitioning of vertical component of GRF is just a logical physical phenomenon that would have resulted automatically if the NCM constraints had been used (it is embedded in NCM constraints).

- 5- Unlike ZMP constraint, NCM constraints are applicable for the most general cases of contact areas (coplanar or non-coplanar contact areas which are horizontal or inclined or parallel or non-parallel).

CHAPTER 9

PREDICTIVE DYNAMICS SIMULATIONS USING THE NCM METHOD

9.1 Introduction

The theoretical aspects of the ZMP method for modeling dynamic tasks were explained in Chapters 3 and 4. ZMP method was used to model four dynamic tasks in Chapters 5 and 6. Chapter 8 discussed some limitations of the ZMP method, summarized as follows:

- 1- ZMP constraint is too weak to ensure that the ground reaction forces are possible in the real world (when there are more than one contact areas). This is a direct conclusion from Theorem 8.1 which states that the satisfaction of NCM constraints ensures that the ZMP constraint is satisfied. But the opposite is not true (i.e., the satisfaction of ZMP constraint does not ensure that the NCM constraints are satisfied).
- 2- The assumption of the uniform partitioning of the IGE forces and moments to GRF components (based on the distance of contact areas to the ZMP such as in the ZMP method or any other type of uniform partitioning of GRF components) gives GRF that are impossible in the real world (at least one component of the GRF is impossible for all ground contact areas, except may be for one contact area).

However, according to Theorem 4.1, satisfaction of ZMP constraint ensures that it is possible to find unilateral contact forces on the given contact areas to cancel the given

IGE forces for the dynamic system. Therefore, if ZMP constraint is satisfied, it will be possible to generate the given motion (equilibrate the given IGE forces) by some other GRF values (other than the ones calculated in the ZMP method) which are possible in the real world (satisfy NCM constraints).

In this chapter, we introduce algorithms that correct the GRF values obtained by the ZMP method such that the values are possible in the real world (satisfy the NCM constraints).

As an example, in this chapter, we implement these algorithms on the "Going Prone" task introduced in Chapter 6 and on a sample "Walking" task.

9.2 Initial Values of GRF in the ZMP Method

In this section, we analyze the initial ground reaction forces and moments obtained by the ZMP method for the "Going Prone" motion task introduced in Chapter 6. As explained in Section 6.3, the formulation for the going prone task consists of two optimization problems (two subtasks) connected by the continuity constraints. The first subtask consists of motion stages a, b, c, d in Figure 9.1. The second subtask consists of stages d, e, f, g, h in Figure 9.1.

The ground contact modeling specifies the GRF points and the ZMP boundary points for each motion stage (a, b, c, ..., h) as shown in Figure 9.1. The values for ground reaction forces and moments in each direction which are F_x , F_y , F_z , M_x , M_y , M_z , are calculated at each of the GRF points specified for that motion stage.

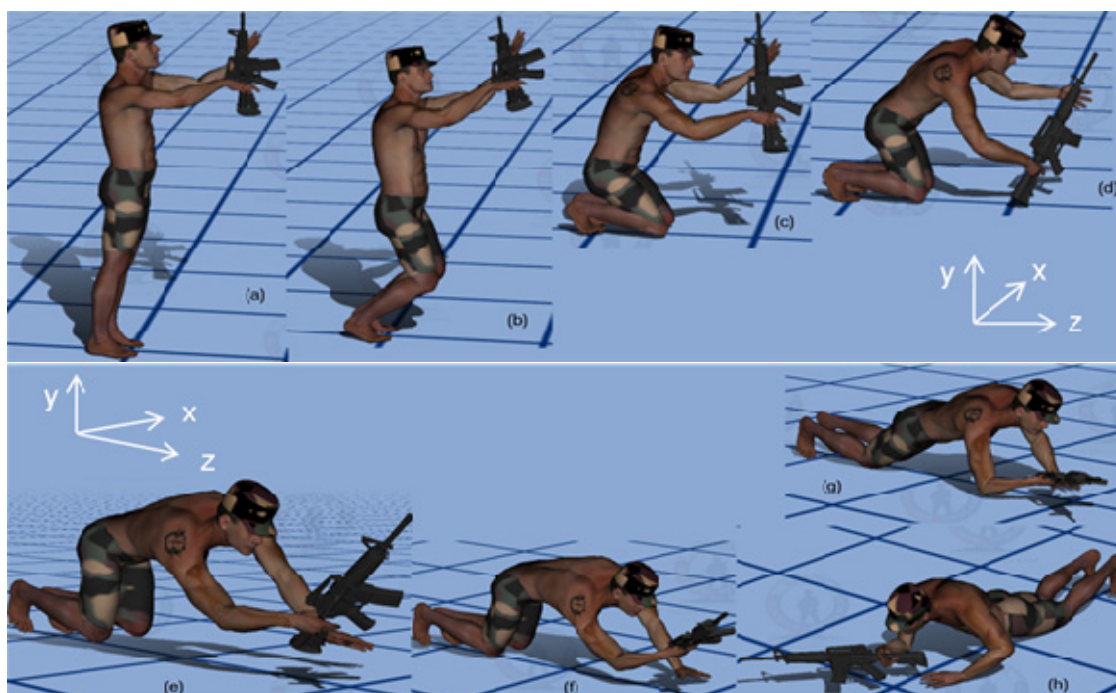


Figure Part	GRF Points (Points that can take ground reaction forces)		Points defining the ZMP convex hull	
(a)	LeftMiddle	RightMiddle	RightHeelOuter LeftToeOuter	RightToeOuter LeftHeelOuter
(b)	LeftMiddle	RightMiddle	RightMiddleOuter LeftToeOuter	RightToeOuter LeftMiddleOuter
(c)	LeftMiddle LeftKnee	RightMiddle RightKnee	RightMiddleOuter RightKnee LeftToeOuter	RightToeOuter LeftKnee LeftMiddleOuter
(d)	LeftToe LeftKnee GunButt	RightToe RightKnee	RightToeOuter GunButt LeftToeOuter	RightKnee LeftKnee
(e), (f)	LeftKnee	RightKnee	LeftKnee	RightKnee
(g)	LeftKnee LeftWrist	RightKnee	LeftKnee LeftWrist	RightKnee
(h)	LeftKnee LeftWrist	RightKnee RightElbow	LeftKnee RightElbow	RightKnee LeftWrist

Figure 9.1. Motion slides for the "Going Prone" subtask

Based on the time discretization strategy for each motion task, each motion stage consists of one or several time grid points. Predictive dynamics calculations including the GRF calculations are performed at each time grid point. In the two subtasks of the going prone motion task, the time grid points corresponding to each motion stage are as shown in Table 9.1:

Going Prone Task	Motion Stage	Time Grid Points
Subtask 1	a	1
	b	2, 3, 4
	c	5, 6
	d	7
Subtask 2	d	1
	e	2, 3, 4
	f	5
	g	6
	h	7

Table 9.1. List of time grid points corresponding to each motion stage of "Going Prone" task

The net of IGE forces and moments calculated at each time grid point for the two subtasks are shown in Tables 9.2 and 9.3, respectively. All values presented in this thesis are in SI units: Meters, Kilograms, Newtons, Newton Meters, etc.

Description of the Force System	Force, Moment Components	Value at Time Grid #1	Value at Time Grid #2	Value at Time Grid #3	Value at Time Grid #4	Value at Time Grid #5	Value at Time Grid #6	Value at Time Grid #7
Net of IGE Forces at the Hip Point	Fx	3.918	-7.173	-1.628	12.409	13.000	6.898	-83.169
	Fy	-336.024	-591.951	-798.174	-996.223	-889.904	-753.297	-483.703
	Fz	-9.873	7.960	-9.563	-21.545	-77.572	-112.144	3.525
	Mx	-5.206	4.485	1.139	6.725	16.907	41.415	27.364
	My	-3.483	-2.167	-0.922	0.105	1.178	-1.979	-10.668
	Mz	7.638	2.195	0.438	-4.793	-4.186	0.463	11.918
Net of IGE Forces at the ZMP	Fx	3.918	-7.173	-1.628	12.409	13.000	6.898	-83.169
	Fy	-336.024	-591.951	-798.174	-996.223	-889.904	-753.297	-483.703
	Fz	-9.873	7.960	-9.563	-21.545	-77.572	-112.144	3.525
	Mx	0.000	0.000	0.000	0.000	0.000	0.000	0.000
	My	-3.198	-2.143	-0.914	-0.083	0.566	-2.289	-6.050
	Mz	0.000	0.000	0.000	0.000	0.000	0.000	0.000

Table 9.2. The net value of IGE forces and moments for the first subtask of "Going Prone"

Description of the Force System	Force, Moment Components	Value at Time Grid #1	Value at Time Grid #2	Value at Time Grid #3	Value at Time Grid #4	Value at Time Grid #5	Value at Time Grid #6	Value at Time Grid #7
Net of IGE Forces at the Hip Point	Fx	93.248	-96.489	55.124	53.775	-0.194	-30.506	-172.874
	Fy	-926.257	-922.872	-787.500	-714.184	-770.510	-662.013	-523.858
	Fz	83.430	-105.069	-129.617	-231.566	47.314	235.332	596.659
	Mx	165.234	170.188	152.954	125.268	103.143	88.434	138.795
	My	99.923	-10.449	33.356	-29.041	-9.799	22.111	-18.982
	Mz	-19.304	-25.064	-20.840	5.463	1.527	-9.186	11.087
Net of IGE Forces at the ZMP	Fx	93.248	-96.489	55.124	53.775	-0.194	-30.506	-172.874
	Fy	-926.257	-922.872	-787.500	-714.184	-770.510	-662.013	-523.858
	Fz	83.430	-105.069	-129.617	-231.566	47.314	235.332	596.659
	Mx	0.000	0.000	0.000	0.000	0.000	0.000	0.000
	My	85.027	4.491	19.219	-36.702	-9.866	29.451	14.193
	Mz	0.000	0.000	0.000	0.000	0.000	0.000	0.000

Table 9.3. The net value of IGE forces and moments for the second subtask of "Going Prone"

The interesting points to note in Tables 9.2 and 9.3 are:

- 1- The vertical component of IGE forces (Fy) in Tables 9.2 and 9.3 are negative at all the times. It means that the IGE force is acting downwards (in the negative y direction). This satisfies one of the

conditions in statement 1 of Theorem 4.1. The ZMP constraint is also ensured to be satisfied at all times. Therefore, both of the conditions in statement 1 of Theorem 4.1 hold true, implying that statement 1 holds true. Therefore according to Theorem 4.1, statement 2 should hold true as well. It means that it is possible in the next calculation stages to find unilaterally upwards distributed contact forces inside the convex hull of all the contact points to generate these calculated motions.

- 2- ZMP is defined as that point at which the values for the net moment of IGE forces are zero about the two horizontal axes. In Tables 9.2 and 9.3, it is seen that the values for M_x and M_z are zero at the ZMP. This shows that the location of ZMP is calculated correctly in these subtasks.

In the next stage in predictive dynamics calculations, as discussed in Section 4.4, the ground reaction forces and moments are calculated at the defined GRF points for each motion stage by partitioning the IGE forces and moments. As explained in Chapter 4, the net force and moment vectors of ground reaction forces is set equal to the negative value of the net force and moment vectors of IGE forces. Then, the components of the net force and moment vectors of ground reaction forces are partitioned uniformly between the GRF points based on the distance of those GRF points to the ZMP (based on the formulas in Section 4.6). The list of GRF points at each motion stage for the going prone task was previously shown in Figure 9.1. The ground reaction forces and moments at each of those GRF point are calculated at each time grid point for the two subtasks. The values are shown in Tables 9.4 and 9.5, respectively.

Point of Effect of the Ground Reaction Force System	Force, Moment Components	Value at Time Grid #1	Value at Time Grid #2	Value at Time Grid #3	Value at Time Grid #4	Value at Time Grid #5	Value at Time Grid #6	Value at Time Grid #7
Left Foot Middle	Fx	-1.617	3.270	0.800	-6.403	-4.665	-1.779	< NA >
	Fy	138.648	269.890	392.194	514.020	319.334	194.225	< NA >
Support Area 0.11 x 0.25 Rectangle	Fz	4.074	-3.629	4.699	11.117	27.836	28.914	< NA >
	Mx	1.188	-17.784	-30.818	-45.455	-32.027	-35.977	< NA >
	My	1.744	0.800	0.952	0.421	1.518	2.572	< NA >
	Mz	-13.961	-29.191	-36.729	-43.691	-25.112	-15.523	< NA >
Right Foot Middle	Fx	-2.302	3.903	0.828	-6.006	-4.258	-1.667	< NA >
	Fy	197.377	322.061	405.980	482.203	291.519	181.989	< NA >
Support Area 0.11 x 0.25 Rectangle	Fz	5.800	-4.331	4.864	10.429	25.412	27.093	< NA >
	Mx	0.060	-23.647	-31.834	-40.384	-29.234	-36.204	< NA >
	My	1.469	1.784	0.100	-1.510	-3.071	-2.001	< NA >
	Mz	13.976	24.691	35.881	48.406	28.210	14.925	< NA >
Support Area 0.1 x 0.1 Rectangle	Fx	< NA >	< NA >	< NA >	< NA >	-2.046	-1.682	6.274
	Fy	< NA >	< NA >	< NA >	< NA >	140.086	183.641	36.488
	Fz	< NA >	< NA >	< NA >	< NA >	12.211	27.339	-0.266
Left Knee	Mx	< NA >	< NA >	< NA >	< NA >	38.812	35.496	0.057
	My	< NA >	< NA >	< NA >	< NA >	1.468	3.344	0.398
Right Knee	Mz	< NA >	< NA >	< NA >	< NA >	-11.361	-16.528	-6.672
	Fx	< NA >	< NA >	< NA >	< NA >	-2.030	-1.771	67.737
Support Area 0.1 x 0.1 Rectangle	Fy	< NA >	< NA >	< NA >	< NA >	138.964	193.443	393.953
	Fz	< NA >	< NA >	< NA >	< NA >	12.113	28.798	-2.871
	Mx	< NA >	< NA >	< NA >	< NA >	38.668	34.685	-5.374
	My	< NA >	< NA >	< NA >	< NA >	-0.553	-1.805	5.863
	Mz	< NA >	< NA >	< NA >	< NA >	11.806	18.208	1.565
Left Toe	Fx	< NA >	< NA >	< NA >	< NA >	< NA >	< NA >	3.362
	Fy	< NA >	< NA >	< NA >	< NA >	< NA >	< NA >	19.555
Support Area 0.1 x 0.1 Rectangle	Fz	< NA >	< NA >	< NA >	< NA >	< NA >	< NA >	-0.143
	Mx	< NA >	< NA >	< NA >	< NA >	< NA >	< NA >	-5.675
	My	< NA >	< NA >	< NA >	< NA >	< NA >	< NA >	1.194
	Mz	< NA >	< NA >	< NA >	< NA >	< NA >	< NA >	-3.676

Table 9.4. The value of ground reaction forces and moments for the first subtask of "Going Prone"
(The highlighted values violate the NCM constraints)

Right Toe Support Area 0.1 x 0.1 Rectangle	Fx	< NA >	< NA >	< NA >	< NA >	< NA >	< NA >	3.795
	Fy	< NA >	< NA >	< NA >	< NA >	< NA >	< NA >	22.068
	Fz	< NA >	< NA >	< NA >	< NA >	< NA >	< NA >	-0.161
	Mx	< NA >	< NA >	< NA >	< NA >	< NA >	< NA >	-6.743
	My	< NA >	< NA >	< NA >	< NA >	< NA >	< NA >	1.436
	Mz	< NA >	< NA >	< NA >	< NA >	< NA >	< NA >	0.039
Rifle Stock Support Area 0.05 x 0.05 Rectangle	Fx	< NA >	< NA >	< NA >	< NA >	< NA >	< NA >	2.001
	Fy	< NA >	< NA >	< NA >	< NA >	< NA >	< NA >	11.639
	Fz	< NA >	< NA >	< NA >	< NA >	< NA >	< NA >	-0.085
	Mx	< NA >	< NA >	< NA >	< NA >	< NA >	< NA >	6.632
	My	< NA >	< NA >	< NA >	< NA >	< NA >	< NA >	-0.986
	Mz	< NA >	< NA >	< NA >	< NA >	< NA >	< NA >	1.249

Table 9.4. Continued

Point of Effect of the Ground Reaction Force System	Force, Moment Components	Value at Time Grid #1	Value at Time Grid #2	Value at Time Grid #3	Value at Time Grid #4	Value at Time Grid #5	Value at Time Grid #6	Value at Time Grid #7
Left Toe Support Area 0.1 x 0.1 Rectangle	Fx	-9.943	< NA >	< NA >	< NA >	< NA >	< NA >	< NA >
	Fy	98.763	< NA >	< NA >	< NA >	< NA >	< NA >	< NA >
	Fz	-8.896	< NA >	< NA >	< NA >	< NA >	< NA >	< NA >
	Mx	-36.286	< NA >	< NA >	< NA >	< NA >	< NA >	< NA >
	My	-13.114	< NA >	< NA >	< NA >	< NA >	< NA >	< NA >
	Mz	-4.381	< NA >	< NA >	< NA >	< NA >	< NA >	< NA >
Right Toe Support Area 0.1 x 0.1 Rectangle	Fx	-9.254	< NA >	< NA >	< NA >	< NA >	< NA >	< NA >
	Fy	91.925	< NA >	< NA >	< NA >	< NA >	< NA >	< NA >
	Fz	-8.280	< NA >	< NA >	< NA >	< NA >	< NA >	< NA >
	Mx	-33.941	< NA >	< NA >	< NA >	< NA >	< NA >	< NA >
	My	-10.633	< NA >	< NA >	< NA >	< NA >	< NA >	< NA >
	Mz	13.567	< NA >	< NA >	< NA >	< NA >	< NA >	< NA >
Left Knee Support Area 0.1 x 0.1 Rectangle	Fx	-43.966	32.046	-44.821	-38.814	0.081	6.517	17.952
	Fy	436.724	306.507	640.312	515.490	320.994	141.418	54.399
	Fz	-39.337	34.896	105.391	167.142	-19.711	-50.271	-61.958
	Mx	-32.505	3.036	-0.500	-0.190	-87.489	-71.605	-40.594
	My	-44.636	2.151	-12.428	35.330	2.320	-8.280	0.882
	Mz	-14.141	-34.781	-19.651	-27.305	-29.518	-14.877	-9.693
Right Knee Support Area 0.1 x 0.1 Rectangle	Fx	-21.839	64.443	-10.303	-14.961	0.075	6.405	18.443
	Fy	216.937	616.365	147.188	198.694	296.358	138.994	55.886
	Fz	-19.540	70.173	24.226	64.424	-18.198	-49.409	-63.653
	Mx	-16.473	-3.223	-2.413	-3.891	-86.709	-72.657	-41.736
	My	-18.705	-6.646	-7.429	1.048	5.766	0.956	12.314
	Mz	31.833	34.987	22.287	27.356	31.737	10.667	0.048
Rifle Stock Support Area 0.05 x 0.05 Rectangle	Fx	-8.246	< NA >	< NA >	< NA >	< NA >	< NA >	< NA >
	Fy	81.908	< NA >	< NA >	< NA >	< NA >	< NA >	< NA >
	Fz	-7.378	< NA >	< NA >	< NA >	< NA >	< NA >	< NA >
	Mx	33.901	< NA >	< NA >	< NA >	< NA >	< NA >	< NA >
	My	-2.876	< NA >	< NA >	< NA >	< NA >	< NA >	< NA >
	Mz	13.653	< NA >	< NA >	< NA >	< NA >	< NA >	< NA >

Table 9.5. The value of ground reaction forces and moments for the second subtask of going prone
(The highlighted values violate the NCM constraints)

Left Hand	Fx	< NA >	< NA >	< NA >	< NA >	0.039	8.027	39.339
	Fy	< NA >	< NA >	< NA >	< NA >	153.158	174.205	119.207
Support Area 0.15 x 0.2 Rectangle	Fz	< NA >	< NA >	< NA >	< NA >	-9.405	-61.926	-135.774
	Mx	< NA >	< NA >	< NA >	< NA >	86.838	58.862	18.784
	My	< NA >	< NA >	< NA >	< NA >	-0.009	-26.995	-52.364
	Mz	< NA >	< NA >	< NA >	< NA >	-31.722	-46.508	-37.697
Right Elbow	Fx	< NA >	< NA >	< NA >	< NA >	9.557	97.141	
Support Area 0.1 x 0.1 Rectangle	Fy	< NA >	< NA >	< NA >	< NA >	< NA >	207.396	294.366
	Fz	< NA >	< NA >	< NA >	< NA >	< NA >	-73.725	-335.274
	Mx	< NA >	< NA >	< NA >	< NA >	< NA >	73.564	41.262
	My	< NA >	< NA >	< NA >	< NA >	< NA >	-7.588	-17.863
	Mz	< NA >	< NA >	< NA >	< NA >	< NA >	14.144	3.274

Table 9.5. Continued

As explained earlier, this section analyzes the results of the implementation of the ZMP method for the environment contact modeling. ZMP method does not consider the size and shape of each individual contact area for any of the calculations (including the calculation of ground reaction forces and moments). The ZMP method only cares about the convex hull of all the contact areas rather than each contact area individually. On the other hand, the NCM method does consider the size and shape of each individual contact area. These sizes and shapes can be used in the NCM method to check the possibility of the generation of a force system by that non-adhesive contact area (see Theorem 7.1 and Definition 7.2).

Approximate sizes and shapes for individual contact areas are shown in Tables 9.4 and 9.5 (units are meters). In these tables, the considered shapes are rectangles having specified lengths and widths with their centers located at the location of GRF points. These values are not defined or used at all in the ZMP method. They are just used after the results are obtained to check the validity of the calculated ground reaction forces and moments.

In Tables 9.4 and 9.5, the components of ground reaction forces and moments which violate the NCM constraints (are impossible in the real world) are highlighted in orange color. As explained in Section 8.4, in the ZMP method, at least one component of the calculated GRF is for sure impossible in the real world for all ground contact areas, except maybe for one contact area. The evidence for this claim can be seen in all columns of Tables 9.4 and 9.5 where some cells are highlighted. As seen there, at each time grid point, at least one component of ground reaction forces and moments is highlighted for

all contact areas (except the right knee contact area at time grid point 7 in Table 9.4 and left knee contact area at the time grid point 3 in Table 9.5) in these tables, indicating violation of reality.

To clarify the meaning of the phrase "Impossible in the real world, we study one of the items highlighted in Table 9.4 in Example 9.1.

Example 9.1: Analysis of a Sample GRF

In this example, we analyze the ground reaction forces and moments at the "Left Foot Middle" point in Table 9.4 at time grid #1. The values are repeated in Table 9.6 for convenience:

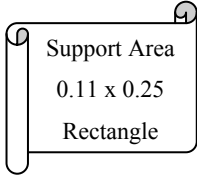
Point of Effect of the Ground Reaction Force System	Force, Moment Components	Value at Time Grid #1
Left Foot Middle 	Fx	-1.617
	Fy	138.648
	Fz	4.074
	Mx	1.188
	My	1.744
	Mz	-13.961

Table 9.6. A sample ground reaction force system for the first subtask of going prone

According to Table 9.1, time grid #1 corresponds to motion stage (a) in Figure 9.1.a. For convenience, we also repeat that picture in Figure 9.2.

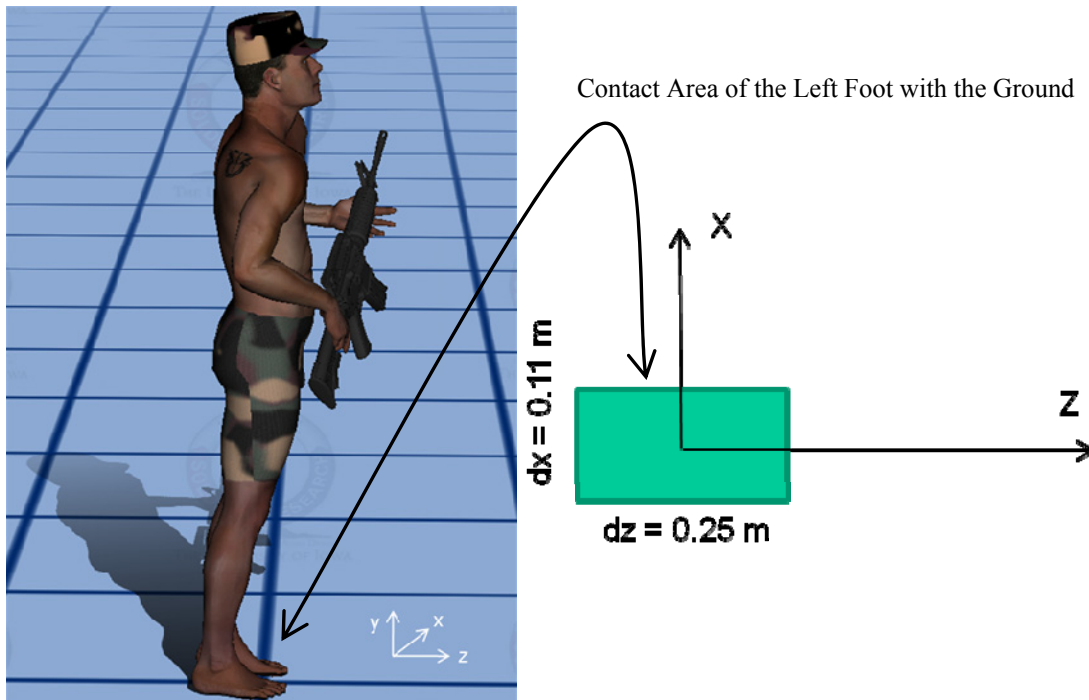


Figure 9.2. A simplified ground contact area to check NCM constraints for a sample motion frame

It is obvious that the range of M_z that can be exerted on the digital human from this contact area is equal to:

NCM Point Location (7.6.2) in zxy Reference Frame :

$$(v_1, v_2, v_3) = \left(p_1 - \frac{M_2}{F_3}, p_2 + \frac{M_1}{F_3}, 0 \right) \Rightarrow (v_z, v_x) = \left(p_z - \frac{M_x}{F_y}, p_x + \frac{M_z}{F_y} \right)$$

$$\text{NCM Constraint (Definition 7.2)} \Rightarrow \begin{cases} F_y > 0 \\ -\frac{dz}{2} \leq v_z \leq \frac{dz}{2} \text{ and } -\frac{dx}{2} \leq v_x \leq \frac{dx}{2} \end{cases}$$

$$\text{One of the NCM Constraints} \Rightarrow -\frac{dx}{2} \leq v_x \leq \frac{dx}{2} \Rightarrow -\frac{dx}{2} \leq p_x + \frac{M_z}{F_y} \leq \frac{dx}{2}$$

$$\begin{aligned} \Rightarrow \quad & -\frac{dx}{2} \leq \frac{M_z}{F_y} \leq \frac{dx}{2} \quad ((p_z, p_x) \text{ is the location of force point in the local frame}) \end{aligned}$$

$$\Rightarrow \quad -\frac{F_y dx}{2} \leq M_z \leq \frac{F_y dx}{2} \quad (9.2.1)$$

$$\begin{aligned} \Rightarrow \quad & \frac{(138.648 \text{ N})(0.11 \text{ m})}{2} \leq M_z \leq \frac{(138.648 \text{ N})(0.11 \text{ m})}{2} \\ \Rightarrow \quad & -7.62564 \text{ (N.m)} \leq M_z \leq 7.62564 \text{ (N.m)} \quad (9.2.2) \end{aligned}$$

Therefore, the value of "Mz = -13.961 N.m" violates the constraint in Equation (9.2.2). So, it is impossible that a ground reaction moment of "Mz = -13.961 N.m", as indicated in Table 9.6, is exerted on the digital human from this contact area.

9.3 GRF Re-Partitioning Based on the NCM method

According to Theorem 4.1, satisfaction of ZMP constraint ensures that it is possible to find unilateral contact forces on the given contact areas to cancel the given IGE forces for the dynamic system. Therefore, if ZMP constraint is satisfied, it will be possible to generate the given motion (equilibrate the given IGE forces) by some other GRF values (other than the ones calculated in the ZMP method) which are possible in the real world (satisfy NCM constraints).

Therefore, although the motion generated by the ZMP method and the calculated net IGE forces (and therefore the calculated net ground contact forces) are possible in the real world, the distribution of contact forces calculated by the ZMP method is impossible in the real world.

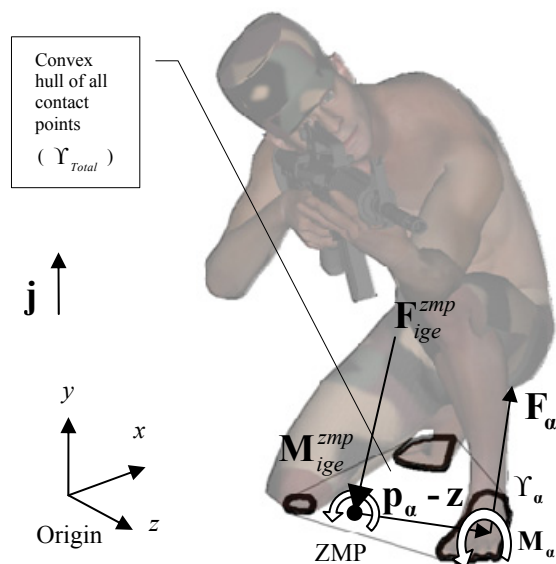


Figure 9.3. Calculation of ground reaction forces and moments based on the ZMP method and its correction by the NCM method

To overcome this problem, we introduce an algorithm that corrects the simulation results obtained by the ZMP method by finding different GRF for the same motion that was obtained by the ZMP method. This method is theoretically correct because, according to Theorem 4.1, satisfaction of the ZMP constraint in the original simulation has already ensured that it is possible to find unilateral contact forces on the given contact areas to generate the given motion. The additional algorithm in this section finds those possible contact forces on the given contact areas.

We normally have more than one ground contact area and therefore, the ground reaction forces and moments are dynamically indeterminate. It means that there exist infinite sets of solutions for ground reaction forces and moments that can satisfy the dynamic equilibrium equations (can cancel \mathbf{F}_{ige}^{zmp} and \mathbf{M}_{ige}^{zmp}). In the ZMP method for

predictive dynamics explained in Sections 4.3 and 4.6, we have first ensured by the ZMP constraint that it is possible to find a set of unilateral distributed forces on these contact areas to cancel \mathbf{F}_{ige}^{zmp} and \mathbf{M}_{ige}^{zmp} and produce the arbitrary motion Θ . Then, we have used an assumption to partition $-\mathbf{F}_{ige}^{zmp}$ and $-\mathbf{M}_{ige}^{zmp}$ on these contact areas to calculate the ground reaction forces. This is not an exactly logical procedure. The logical procedure (done in the NCM method) is to first calculate a set of ground reaction forces on all contact areas to cancel \mathbf{F}_{ige}^{zmp} and \mathbf{M}_{ige}^{zmp} and then use the NCM constraints to check whether each separate contact area is able to produce the equivalent ground reaction force and moment calculated for it.

Therefore the algorithm for the correction of ground reaction forces and moments based on the NCM method is as follows:

- 1- For each contact area, six additional design variables are considered to account for the indeterminacy of ground reaction forces and moments. These design variables are the ratios of the components of ground reaction forces and moments at each contact area to the components of the net IGE forces and moments (at any point, for example at the hip point of the avatar denoted by

$$\mathbf{F}_{ige}^{Hip} \text{ and } \mathbf{M}_{ige}^{Hip}):$$

$$\begin{cases} r_{F_{\alpha z}} = -\frac{F_{\alpha z}}{(F_{ige}^{Hip})_z}, & r_{F_{\alpha x}} = -\frac{F_{\alpha x}}{(F_{ige}^{Hip})_x}, & r_{F_{\alpha y}} = -\frac{F_{\alpha y}}{(F_{ige}^{Hip})_y} \\ r_{M_{\alpha z}} = -\frac{M_{\alpha z}^{Hip}}{(M_{ige}^{Hip})_z}, & r_{M_{\alpha x}} = -\frac{M_{\alpha x}^{Hip}}{(M_{ige}^{Hip})_x}, & r_{M_{\alpha y}} = -\frac{M_{\alpha y}^{Hip}}{(M_{ige}^{Hip})_y} \end{cases} \quad (9.3.1)$$

2- The sum of these ratios are constrained such that they satisfy the global dynamic equilibrium equations:

$$\begin{aligned} \sum \mathbf{F}_{Hip} = \mathbf{0} &\Rightarrow \mathbf{F}_{ige}^{Hip} + \sum \mathbf{F}_a = \mathbf{0} \Rightarrow \sum \mathbf{F}_a = -\mathbf{F}_{ige}^{Hip} \\ \sum \mathbf{M}_{Hip} = \mathbf{0} &\Rightarrow \mathbf{M}_{ige}^{Hip} + \sum \mathbf{M}_a^{Hip} = \mathbf{0} \Rightarrow \sum \mathbf{M}_a + \sum (\mathbf{p}_a - \mathbf{z}) \times \mathbf{F}_a = -\mathbf{M}_{ige}^{Hip} \\ \text{Or:} & \\ \sum r_{F_{\alpha z}} = \sum r_{F_{\alpha x}} = \sum r_{F_{\alpha y}} = \sum r_{M_{\alpha z}} = \sum r_{M_{\alpha x}} = \sum r_{M_{\alpha y}} = 1 & \quad (9.3.2) \end{aligned}$$

3- The reaction forces and moments on each contact area are constrained by NCM constraints as explained in Definition 7.2. For convenience, we rewrite Equation (7.7.16) for the simplified case, where the contact area is on the ground (local reference coordinate frame $(\mathbf{e}_1, \mathbf{e}_2, \mathbf{e}_3)$ for all contact areas simplifies to the global coordinate frame $(\mathbf{z}, \mathbf{x}, \mathbf{y})$). According to (7.7.16) the NCM constraints in the case where the convex hull of contact area Υ is a polygon with corners $E_i (i=1 \dots m)$ will be:

$$\begin{cases} F_y = \mathbf{F} \cdot \mathbf{j} \geq 0 \\ \forall i=1 \dots m: \quad d_i F_y = (L_i)_z (p_x F_y + M_z - E_{iz} F_y) - (L_i)_x (p_z F_y - M_x - E_{ix} F_y) \geq 0 \end{cases} \quad (9.3.3)$$

4- It may be impossible to partition the global forces and moments such that sliding and rotational friction constraints on individual contact areas hold for a given coefficient of friction. This is due to Theorem 4.1, that satisfaction of ZMP constraint only ensures the possibility of finding unilateral contact forces on the given contact areas to cancel the given IGE forces for the dynamic system. Unilaterality of GRF does not necessarily mean that the GRF also satisfy the Coulomb friction laws (See Sections 7.6, 7.8). Therefore, for the current algorithm, the coulomb friction constraints are ignored (similar to the ZMP method). However, because ground reaction forces are considered as design variables in the NCM method, they may acquire excessively large values that were not observed in the ZMP method due to the fact that in the ZMP method, they were not design variables. So, we apply a weak form of coulomb friction constraints in this algorithm to keep the friction forces in the limits similar to the ZMP constraint. However, as noted before, it may be impossible to partition the global forces and moments from the ZMP method such that sliding and rotational friction constraints on individual contact areas hold for a given coefficient of friction. The required values for the coefficient of friction such that they can hold are:

$$\left\{ \begin{array}{l} \mu \geq \mu_{slide} = \frac{\sqrt{\left((F_{ige}^{Hip})_z\right)^2 + \left((F_{ige}^{Hip})_x\right)^2}}{\left(F_{ige}^{Hip}\right)_y} \quad (7.8.1) \Rightarrow F_{\alpha z}^2 + F_{\alpha x}^2 \leq \mu^2 F_{\alpha y}^2 \quad (9.3.4) \\ \mu \geq \mu_{rotate} = \frac{\left| \left(M_{ige}^{Hip}\right)_y \right|}{\left((R_{\alpha})_{max} + (p_{\alpha})_{max} \right) \left(F_{ige}^{Hip}\right)_y} \quad (7.8.6) \Rightarrow -\mu R_{\alpha} F_{\alpha y} \leq M_{\alpha y} \leq \mu R_{\alpha} F_{\alpha y} \quad (9.3.5) \end{array} \right.$$

The justification for using the above coefficients of friction can be easily understood by considering the following question:

Question 9.1:

What is the (minimum) required coefficient of friction such that a given motion can satisfy sliding friction constraints after GRF re-partitioning?

Answer:

We want to find the solutions which need the minimum coefficient of friction to perform the motion. In other words, we want to find the case of GRF re-partitioning in which minimum coefficient of friction is needed to prevent sliding for a given motion. This should be same as the case where the vector sum of the frictional forces on all contact areas is maximum for a given coefficient of friction. In this case, frictional forces on all contact areas should act at a same direction to have a maximum sum. Therefore:

$$\left\{ \begin{array}{l} \forall \alpha: F_{ax} = kF_{az} \Rightarrow k = \frac{F_{ax}}{F_{az}} \end{array} \right. \quad (9.3.6)$$

$$\left\{ \begin{array}{l} \sum \mathbf{F}_a = -\mathbf{F}_{ige}^{Hip} \Rightarrow (F_{ige}^{Hip})_x = k(F_{ige}^{Hip})_z \Rightarrow k = \frac{(F_{ige}^{Hip})_x}{(F_{ige}^{Hip})_z} \end{array} \right. \quad (9.3.7)$$

Sliding Friction Constraint :

$$\begin{aligned} \forall \alpha: F_{az}^2 + F_{ax}^2 &\leq \mu^2 F_{ay}^2 \Leftrightarrow \sqrt{F_{az}^2 + F_{ax}^2} \leq \mu F_{ay} \stackrel{(9.3.6)}{\Leftrightarrow} |F_{az}| \sqrt{1+k^2} \leq \mu F_{ay} \\ \Leftrightarrow \sum |F_{az}| \sqrt{1+k^2} &\leq \sum \mu F_{ay} \Leftrightarrow \left| (F_{ige}^{Hip})_z \right| \sqrt{1+k^2} \leq \mu (F_{ige}^{Hip})_y \end{aligned}$$

$$\stackrel{(9.3.7)}{\Leftrightarrow} \mu \geq \frac{\sqrt{\left((F_{ige}^{Hip})_z \right)^2 + \left((F_{ige}^{Hip})_x \right)^2}}{(F_{ige}^{Hip})_y} = \mu_{slide} \quad (\text{same as (9.3.4)})$$

Using a similar procedure as in Question 9.1, we can show that the (minimum) required coefficient of friction such that a given motion can satisfy frictional moment constraints after GRF re-partitioning can be approximated by Equation (9.3.5).

9.4 Values of GRF after Re-Partitioning

Similar to what was done in Section 4.5 for the ZMP method, general algorithms are developed to check the NCM constraints and calculate the ground reaction forces and moments on each separate contact area. In these algorithms, individual contact areas can either be defined by their boundary points or by fixed shapes (rectangles, circles) on the ground (these algorithms can be later generalized to define them on non-horizontal and non-coplanar contact planes). Some of the individual contact areas for the going prone task are defined in this algorithm by fixed size rectangles with specified lengths and widths with their centers located at the GRF points (similar sizes to what was shown in Tables 9.4 and 9.5).

Some of the other individual contact areas for the going prone task are defined independently by their boundary points (such as the contact areas of the two feet with the ground at motion stages a, b, c in Figure 9.1). Although some of the contact areas are defined by boundary points in the algorithm, after obtaining the final results, we check the accuracy of the results by approximating all contact areas with rectangles. After re-partitioning, the net of IGE forces and moments calculated at each time grid point for the two subtasks are shown in Tables 9.7 and 9.8.

As expected, the IGE values have stayed the same after GRF re-partitioning. However, the ground reaction forces and moments at each contact area are different. The new values for GRF are shown in Tables 9.9 and 9.10.

Description of the Force System	Force, Moment Components	Value at Time Grid #1	Value at Time Grid #2	Value at Time Grid #3	Value at Time Grid #4	Value at Time Grid #5	Value at Time Grid #6	Value at Time Grid #7
Net of IGE Forces at the Hip Point	Fx	3.918	-7.173	-1.628	12.409	13.000	6.898	-83.169
	Fy	-336.024	-591.951	-798.174	-996.223	-889.904	-753.297	-483.703
	Fz	-9.873	7.960	-9.563	-21.545	-77.572	-112.144	3.525
	Mx	-5.206	4.485	1.139	6.725	16.907	41.415	27.364
	My	-3.483	-2.167	-0.922	0.105	1.178	-1.979	-10.668
	Mz	7.638	2.195	0.438	-4.793	-4.186	0.463	11.918
Net of IGE Forces at the ZMP	Fx	3.918	-7.173	-1.628	12.409	13.000	6.898	-83.169
	Fy	-336.024	-591.951	-798.174	-996.223	-889.904	-753.297	-483.703
	Fz	-9.873	7.960	-9.563	-21.545	-77.572	-112.144	3.525
	Mx	0.000	0.000	0.000	0.000	0.000	0.000	0.000
	My	-3.198	-2.143	-0.914	-0.083	0.566	-2.289	-6.050
	Mz	0.000	0.000	0.000	0.000	0.000	0.000	0.000

Table 9.7. IGE Forces and Moments for the first Subtask of Going Prone after GRF Re-Partitioning

Description of the Force System	Force, Moment Components	Value at Time Grid #1	Value at Time Grid #2	Value at Time Grid #3	Value at Time Grid #4	Value at Time Grid #5	Value at Time Grid #6	Value at Time Grid #7
Net of IGE Forces at the Hip Point	Fx	93.248	-96.489	55.124	53.775	-0.194	-30.506	-172.874
	Fy	-926.257	-922.872	-787.500	-714.184	-770.510	-662.013	-523.858
	Fz	83.430	-105.069	-129.617	-231.566	47.314	235.332	596.659
	Mx	165.234	170.188	152.954	125.268	103.143	88.434	138.795
	My	99.923	-10.449	33.356	-29.041	-9.799	22.111	-18.982
	Mz	-19.304	-25.064	-20.840	5.463	1.527	-9.186	11.087
Net of IGE Forces at the ZMP	Fx	93.248	-96.489	55.124	53.775	-0.194	-30.506	-172.874
	Fy	-926.257	-922.872	-787.500	-714.184	-770.510	-662.013	-523.858
	Fz	83.430	-105.069	-129.617	-231.566	47.314	235.332	596.659
	Mx	0.000	0.000	0.000	0.000	0.000	0.000	0.000
	My	85.027	4.491	19.219	-36.702	-9.866	29.451	14.193
	Mz	0.000	0.000	0.000	0.000	0.000	0.000	0.000

Table 9.8. IGE forces and moments for the second subtask of "Going Prone" after GRF Re-Partitioning

Point of Effect of the Ground Reaction Force System	Force, Moment Components	Value at Time Grid #1	Value at Time Grid #2	Value at Time Grid #3	Value at Time Grid #4	Value at Time Grid #5	Value at Time Grid #6	Value at Time Grid #7
Left Foot Middle Support Area 0.11 x 0.25 Rectangle	Fx	-7.061	2.151	-16.232	40.550	-15.938	-30.079	< NA >
	Fy	157.932	289.999	406.297	505.212	303.618	163.531	< NA >
	Fz	6.002	-1.997	17.258	15.121	-71.544	-69.694	< NA >
	Mx	0.967	-19.373	-29.599	-42.635	2.416	-0.362	< NA >
	My	1.696	0.711	0.195	4.580	10.776	6.915	< NA >
	Mz	-2.438	-5.047	-6.443	-17.952	14.690	8.493	< NA >
Right Foot Middle Support Area 0.11 x 0.25 Rectangle	Fx	3.143	5.022	17.861	-52.959	-10.092	61.479	< NA >
	Fy	178.092	301.952	391.877	491.011	307.006	149.804	< NA >
	Fz	3.871	-5.964	-7.695	6.424	-5.296	31.528	< NA >
	Mx	0.441	-21.906	-33.035	-43.150	-0.067	0.725	< NA >
	My	1.893	2.183	3.140	-4.703	2.126	2.869	< NA >
	Mz	-0.854	-3.170	3.056	24.149	6.698	-7.442	< NA >
Left Knee Support Area 0.1 x 0.1 Rectangle	Fx	< NA >	< NA >	< NA >	< NA >	-16.479	-8.593	29.040
	Fy	< NA >	< NA >	< NA >	< NA >	123.244	133.736	82.874
	Fz	< NA >	< NA >	< NA >	< NA >	128.266	160.483	7.077
	Mx	< NA >	< NA >	< NA >	< NA >	6.162	6.687	-4.144
	My	< NA >	< NA >	< NA >	< NA >	-10.633	-15.630	1.833
	Mz	< NA >	< NA >	< NA >	< NA >	-4.490	0.678	-4.144
Right Knee Support Area 0.1 x 0.1 Rectangle	Fx	< NA >	< NA >	< NA >	< NA >	29.510	-29.705	53.105
	Fy	< NA >	< NA >	< NA >	< NA >	156.035	306.226	284.019
	Fz	< NA >	< NA >	< NA >	< NA >	26.147	-10.174	15.203
	Mx	< NA >	< NA >	< NA >	< NA >	7.802	15.311	9.037
	My	< NA >	< NA >	< NA >	< NA >	-6.024	28.940	1.684
	Mz	< NA >	< NA >	< NA >	< NA >	-7.802	14.959	-9.144
Left Toe Support Area 0.1 x 0.1 Rectangle	Fx	< NA >	< NA >	< NA >	< NA >	< NA >	< NA >	-5.248
	Fy	< NA >	< NA >	< NA >	< NA >	< NA >	< NA >	29.985
	Fz	< NA >	< NA >	< NA >	< NA >	< NA >	< NA >	2.701
	Mx	< NA >	< NA >	< NA >	< NA >	< NA >	< NA >	1.499
	My	< NA >	< NA >	< NA >	< NA >	< NA >	< NA >	0.806
	Mz	< NA >	< NA >	< NA >	< NA >	< NA >	< NA >	0.376

Table 9.9. GRF for the first subtask of "Going Prone" after GRF Re-Partitioning

Right Toe Support Area 0.1 x 0.1 Rectangle	Fx	< NA >	< NA >	< NA >	< NA >	< NA >	< NA >	-3.904
	Fy	< NA >	< NA >	< NA >	< NA >	< NA >	< NA >	33.650
	Fz	< NA >	< NA >	< NA >	< NA >	< NA >	< NA >	10.154
	Mx	< NA >	< NA >	< NA >	< NA >	< NA >	< NA >	1.682
	My	< NA >	< NA >	< NA >	< NA >	< NA >	< NA >	-0.479
	Mz	< NA >	< NA >	< NA >	< NA >	< NA >	< NA >	0.746
Rifle Stock Support Area 0.05 x 0.05 Rectangle	Fx	< NA >	< NA >	< NA >	< NA >	< NA >	< NA >	10.177
	Fy	< NA >	< NA >	< NA >	< NA >	< NA >	< NA >	53.175
	Fz	< NA >	< NA >	< NA >	< NA >	< NA >	< NA >	-38.659
	Mx	< NA >	< NA >	< NA >	< NA >	< NA >	< NA >	-0.236
	My	< NA >	< NA >	< NA >	< NA >	< NA >	< NA >	0.200
	Mz	< NA >	< NA >	< NA >	< NA >	< NA >	< NA >	-1.329

Table 9.9. Continued

Point of Effect of the Ground Reaction Force System	Force, Moment Components	Value at Time Grid #1	Value at Time Grid #2	Value at Time Grid #3	Value at Time Grid #4	Value at Time Grid #5	Value at Time Grid #6	Value at Time Grid #7
Left Toe Support Area 0.1 x 0.1 Rectangle	Fx	71.718	< NA >	< NA >	< NA >	< NA >	< NA >	< NA >
	Fy	96.136	< NA >	< NA >	< NA >	< NA >	< NA >	< NA >
	Fz	-28.283	< NA >	< NA >	< NA >	< NA >	< NA >	< NA >
	Mx	4.807	< NA >	< NA >	< NA >	< NA >	< NA >	< NA >
	My	-6.201	< NA >	< NA >	< NA >	< NA >	< NA >	< NA >
	Mz	1.790	< NA >	< NA >	< NA >	< NA >	< NA >	< NA >
Right Toe Support Area 0.1 x 0.1 Rectangle	Fx	34.887	< NA >	< NA >	< NA >	< NA >	< NA >	< NA >
	Fy	29.073	< NA >	< NA >	< NA >	< NA >	< NA >	< NA >
	Fz	-15.989	< NA >	< NA >	< NA >	< NA >	< NA >	< NA >
	Mx	1.454	< NA >	< NA >	< NA >	< NA >	< NA >	< NA >
	My	-6.167	< NA >	< NA >	< NA >	< NA >	< NA >	< NA >
	Mz	0.054	< NA >	< NA >	< NA >	< NA >	< NA >	< NA >
Left Knee Support Area 0.1 x 0.1 Rectangle	Fx	-141.412	64.288	177.574	235.366	0.616	36.947	40.861
	Fy	494.376	209.853	438.572	473.233	256.560	127.095	43.144
	Fz	20.914	186.185	86.360	3.164	12.326	-17.639	-51.773
	Mx	24.719	10.493	11.384	-17.518	-12.828	-6.355	-2.157
	My	8.713	11.822	1.719	18.230	-2.041	4.880	4.409
	Mz	22.506	10.493	21.929	7.883	-9.506	-6.355	-2.157
Right Knee Support Area 0.1 x 0.1 Rectangle	Fx	-40.523	32.201	-232.699	-289.141	0.952	41.507	27.153
	Fy	33.769	713.019	348.928	240.951	283.586	169.243	67.422
	Fz	40.523	-81.116	43.257	228.402	36.470	36.396	-80.906
	Mx	1.688	-12.999	-17.446	12.048	-14.179	-8.462	-3.371
	My	-7.164	9.014	-28.514	-18.089	-1.121	14.160	14.302
	Mz	0.914	6.391	17.446	-0.816	-14.179	-7.009	-3.371
Rifle Stock Support Area 0.05 x 0.05 Rectangle	Fx	-17.917	< NA >	< NA >	< NA >	< NA >	< NA >	< NA >
	Fy	272.903	< NA >	< NA >	< NA >	< NA >	< NA >	< NA >
	Fz	-100.595	< NA >	< NA >	< NA >	< NA >	< NA >	< NA >
	Mx	-6.823	< NA >	< NA >	< NA >	< NA >	< NA >	< NA >
	My	-28.946	< NA >	< NA >	< NA >	< NA >	< NA >	< NA >
	Mz	6.823	< NA >	< NA >	< NA >	< NA >	< NA >	< NA >

Table 9.10. GRF for the second subtask of "Going Prone" after GRF Re-Partitioning

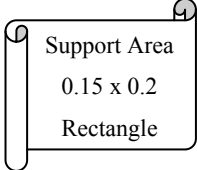
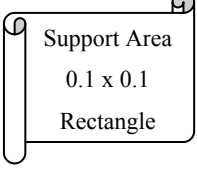
Left Hand  Support Area 0.15 x 0.2 Rectangle	Fx	< NA >	< NA >	< NA >	< NA >	-1.374	-42.837	46.727
	Fy	< NA >	< NA >	< NA >	< NA >	230.364	77.598	78.499
	Fz	< NA >	< NA >	< NA >	< NA >	-96.110	-74.394	-84.230
	Mx	< NA >	< NA >	< NA >	< NA >	6.184	4.531	-1.109
	My	< NA >	< NA >	< NA >	< NA >	-8.427	0.178	-8.300
	Mz	< NA >	< NA >	< NA >	< NA >	-17.277	1.174	-5.887
Right Elbow  Support Area 0.1 x 0.1 Rectangle	Fx	< NA >	< NA >	< NA >	< NA >	< NA >	-5.110	58.134
	Fy	< NA >	< NA >	< NA >	< NA >	< NA >	288.077	334.793
	Fz	< NA >	< NA >	< NA >	< NA >	< NA >	-179.695	-379.749
	Mx	< NA >	< NA >	< NA >	< NA >	< NA >	-14.404	-16.740
	My	< NA >	< NA >	< NA >	< NA >	< NA >	-4.228	-20.216
	Mz	< NA >	< NA >	< NA >	< NA >	< NA >	10.716	-16.740

Table 9.10. Continued

As seen in Tables 9.9 and 9.10, approximate sizes and shapes for individual contact areas are noted. Some of these sizes were used directly for ensuring NCM constraints in the algorithm. But, some of the contact areas were modeled differently in the NCM method by specifying their boundary points. However, all the approximate rectangles shown in Tables 9.9 and 9.10 are used after the results are obtained to check the validity of the calculated ground reaction forces and moments in the NCM method.

In Tables 9.9 and 9.10, the components of ground reaction forces and moments are checked to see if they violate the NCM constraints (are impossible in the real world) or not and are highlighted, if they do. However, as seen, no component of ground reaction forces and moments is highlighted in these tables or violates NCM constraints.

9.5 Comparison of GRF and Joint Torques Before and After Re-Partitioning

As a simpler reference, values for some of the components of the ground reaction forces and moments are plotted in this section before and after re-partitioning.

The term "Possible Range" for $\frac{M_x}{F_y}$ or $\frac{M_z}{F_y}$ in Figures 9.4, 9.5 and 9.6 specifies

the limitation imposed by the NCM constraints on $\frac{M_x}{F_y}$ or $\frac{M_z}{F_y}$. For a fixed size

rectangular contact area on the ground, NCM constraint is simplified to two independent

inequality constraints on the values of $\frac{M_x}{F_y}$ or $\frac{M_z}{F_y}$ with fixed upper and lower limits.

This fact can be observed from Equation (9.2.1), for example. Also, as seen in Figures 9.4, 9.5 and 9.6, the possible ranges for $\frac{M_x}{F_y}$ or $\frac{M_z}{F_y}$ are inequalities with fixed values of upper and lower limits during the motion. The horizontal axis in these graphs indicates the change of time and refers to the number of grid points after the contact area comes into contact with the ground.

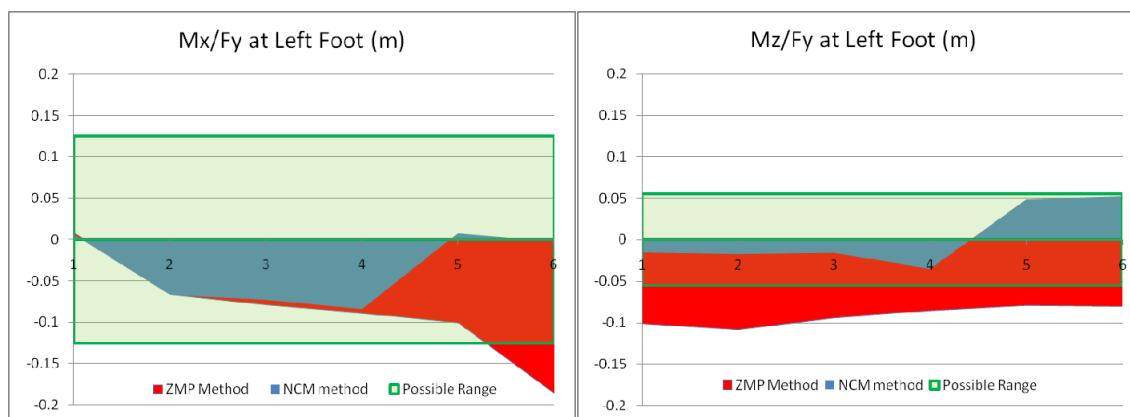


Figure 9.4. The values obtained for M_x/F_y and M_z/F_y at the Left Foot by ZMP versus NCM Methods

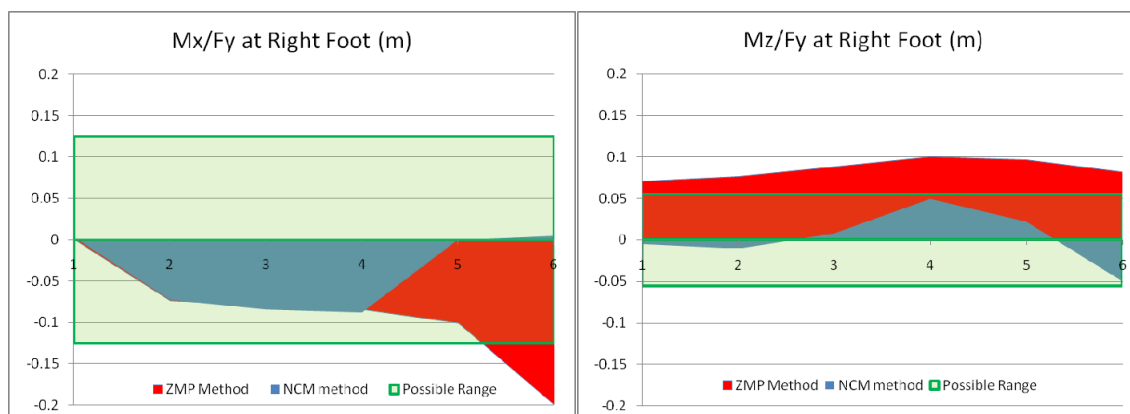


Figure 9.5. The values obtained for M_x/F_y and M_z/F_y at the Right Foot by ZMP versus NCM Methods

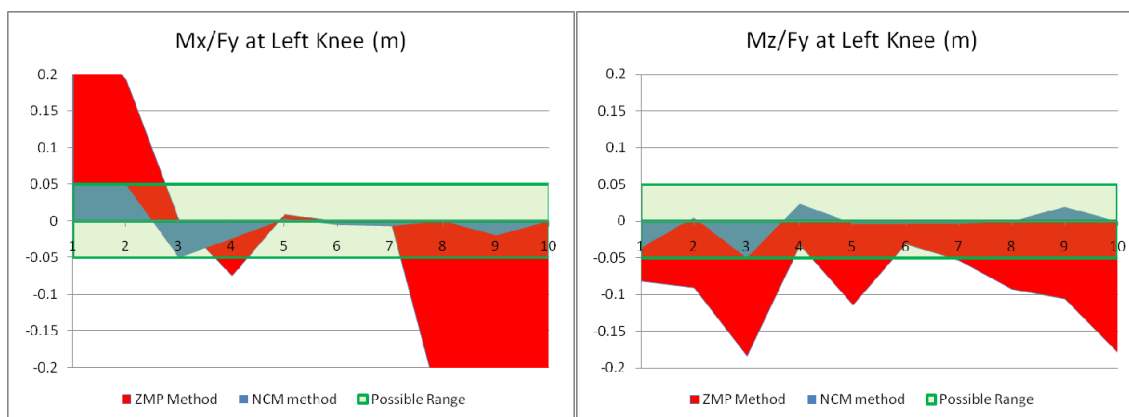


Figure 9.6. The values obtained for M_x/F_y and M_z/F_y at the Left Knee by ZMP versus NCM Methods

The term "Possible Range" for M_x or M_z in Figures 9.7 - 9.12 specifies the limitation imposed by the NCM constraints on M_x or M_z based on the value of F_y at any instant of motion. This possible range changes during the motion, because the value of F_y changes during the motion.

As previously seen in Tables 9.4 and 9.5, M_x or M_z values with the ZMP method exceed the possible ranges at several instants of time during the motion. This fact can also be observed in Figures 9.7 - 9.12.

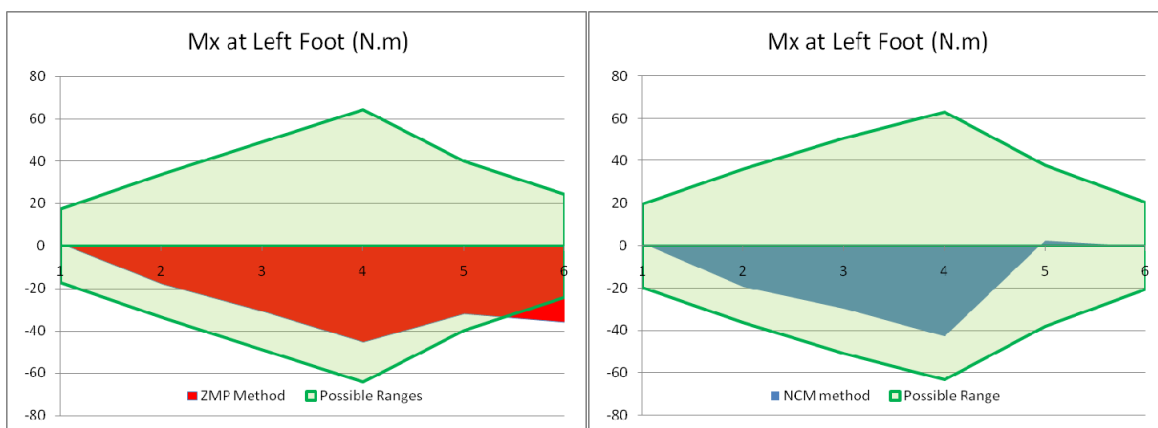


Figure 9.7. The values obtained for Mx at the Left Foot by ZMP versus NCM Methods

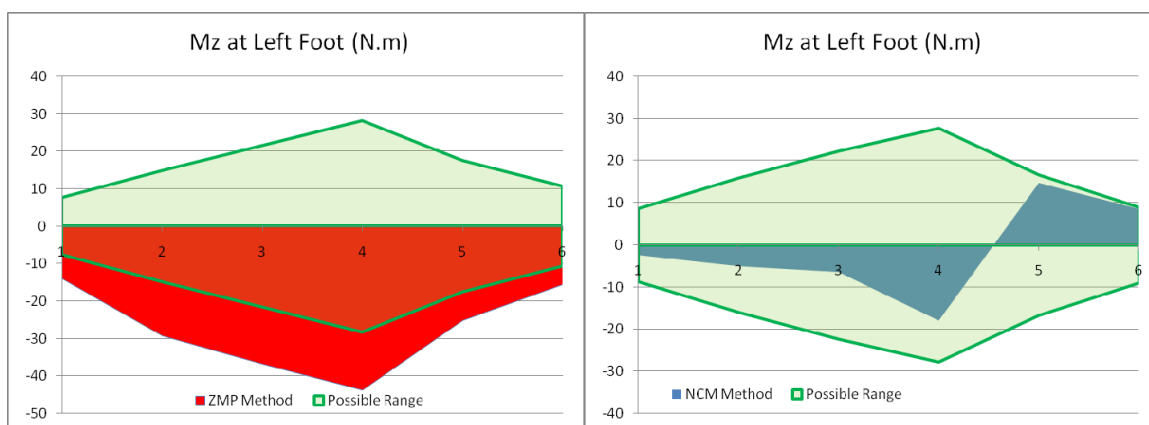


Figure 9.8. The values obtained for Mz at the Left Foot by ZMP versus NCM Methods

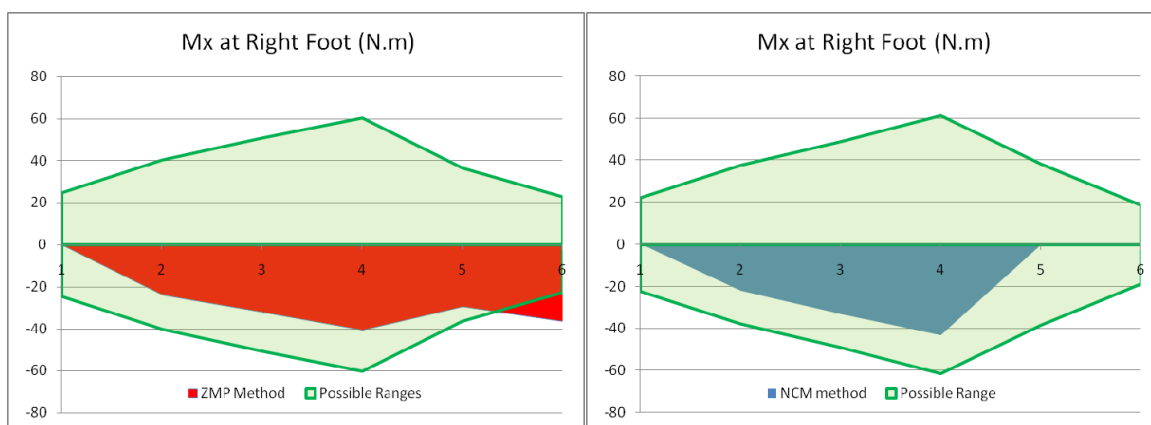


Figure 9.9. The values obtained for Mx at the Right Foot by ZMP versus NCM Methods

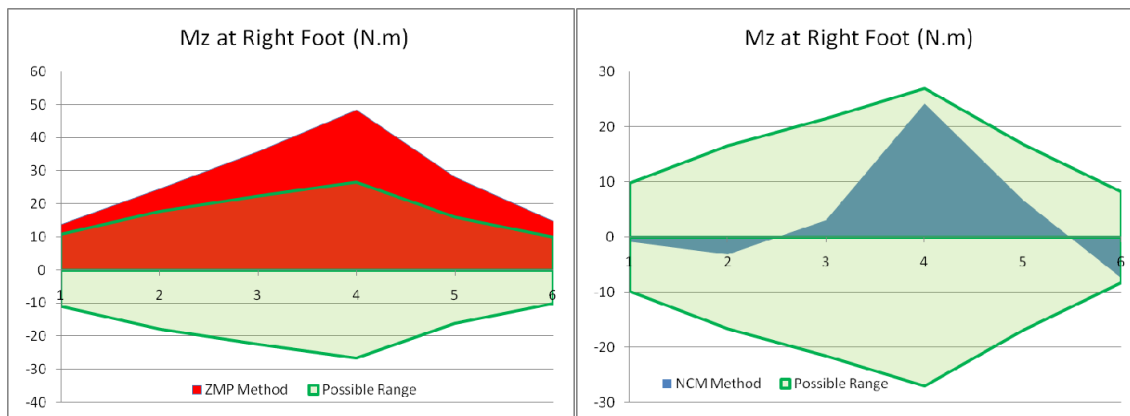


Figure 9.10. The values obtained for Mz at the Right Foot by ZMP versus NCM Methods

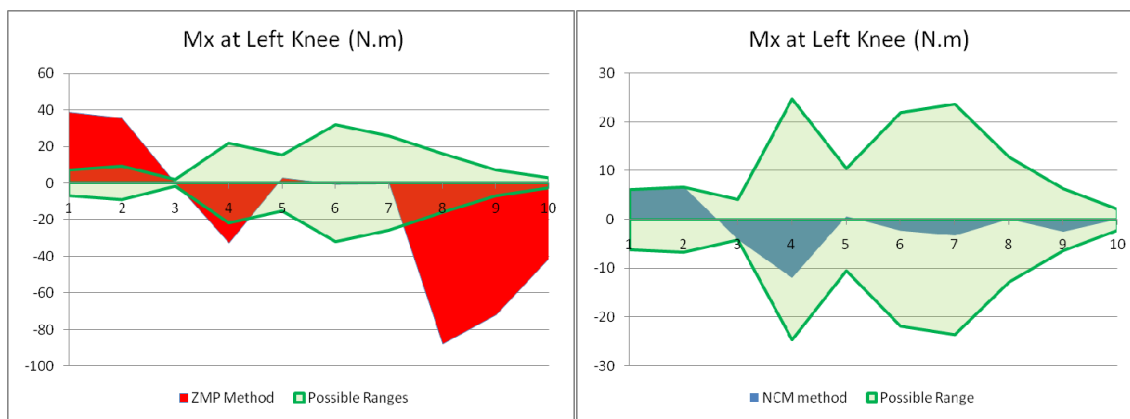


Figure 9.11. The values obtained for Mx at the Left Knee by ZMP versus NCM Methods

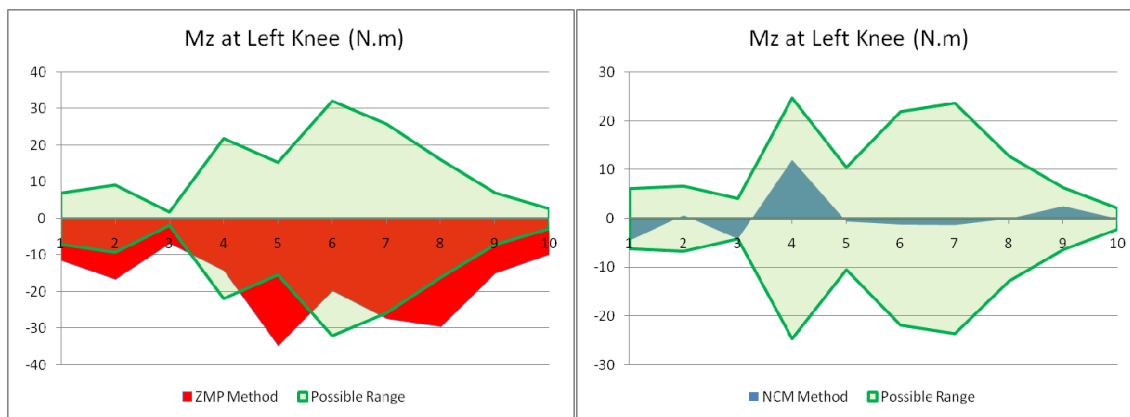


Figure 9.12. The values obtained for Mz at the Left Knee by ZMP versus NCM Methods

As described in previous chapters, GRF values are used to calculate torques at joints using the Recursive Lagrangian Formulation. Therefore, re-partitioning of GRF also affects the values of joint torques during the motion. The re-partitioning does not necessarily have to reduce the torques at joints. But, it seems to slightly reduce the joint torques at most of the joints. The values of joint torques before and after re-partitioning are compared in Appendix B. It was calculated that the sum of the squared torque values for this sample going prone task was reduced by a factor of 1.8 after the GRF re-partitioning.

An interesting point to note is that at any instant of the motion, if the end of a kinematic branch of the digital human is not connected to the ground, the values of torques remain unchanged before and after re-partitioning. The reason is that the motion and the IGE forces and moments are not affected by the re-partitioning of GRF. This fact can be seen for example in the joint torques at the neck throughout the motion and the joint torques at the spine, left arm, right arm at the start of the motion.

9.6 Effect of Re-Partitioning on the Optimality of the Kinematics of the Motion Prediction Results

As it was noted in Section 9.5, GRF values are used to calculate torques at joints using the Recursive Lagrangian Formulation. Therefore, re-partitioning of GRF also affects the values of joint torques during the motion. This change in torque may result in a previously considered optimal motion not to be kinematically optimal anymore (although the re-partitioning procedure also optimizes the GRF partitioning based on the

value of torques, it cannot affect or optimize the kinematics of the original motion that is borrowed from the ZMP method).

In order to check whether the kinematics of the "Going Prone" task is still optimal after the change in the partitioning ratios of GRF, we feed the optimal ratios of GRF partitioning from the NCM method back to the ZMP method (the original motion task simulation environment) and consider them as fixed ratios. Based on these fixed ratios for each of the 6 components of GRF at each contact area, the motion is optimized again. However, it is observed that the kinematics of the "Going Prone" task is almost unaffected and the kinematics results that are played back seem completely identical to the eye. The original joint angles of the going prone task in the ZMP method are compared in Appendix C with their values after feeding ratios. As it is seen, the changes in the kinematics are negligible. Therefore both the dynamics and the kinematics results of the re-partitioning (by NCM method) can be considered optimal as well as feasible.

9.7 Improvement of GRF for a Walking Simulation in Predictive Dynamics Using NCM Method

As it was noted in Section 8.4.2, the assumption of the uniform partitioning of the GRF components causes the calculated GRF for all contact areas (except maybe for one contact area) to have values which are impossible in the real world. This impossibility is a mathematical fact and affects any dynamic task that is modeled using this assumption. As noted in Section 8.4.2, besides the tasks modeled in Chapters 5 and 6 or the sample publications noted there (Xiang, et al (2007, 2009), Kim, et al (2008), Bhatt, et al (2008)),

any other type of uniform partitioning (partitioning about any arbitrary point other than the ZMP or consider the uniform ratios of GRF as design variables) will cause the same problem.

In this section, we try to improve the results of GRF for a sample walking simulation similar to what was noted in Xiang, *et al* (2007) by using the NCM method. This improvement only consists of finding values for GRF which are possible in the real world. The NCM method does not ensure that the calculated GRF are optimal or match the experimental data. These issues also depend on the original simulation and the constraints used in the original simulation to predict a walking task. However, because the experimental data for the GRF of walking are available in the literature, one may also be curious to know how much the NCM method improves the GRF results of a sample walking simulation. Therefore, we also perform a comparison of the GRF calculated by ZMP versus NCM methods with the experimental data at the end.

9.7.1 Original Values of GRF for the Walking Simulation (Using ZMP Method)

In this section, we analyze the initial ground reaction forces and moments obtained by the ZMP method for a "walking" motion task. The formulation for this task consists of motion stages a, b, c in Figure 9.13.

The ground contact modeling specifies the GRF points and the ZMP boundary points for each motion stage (a,b,c) as shown in Figure 9.13. The values for ground reaction forces and moments in each direction which are F_x , F_y , F_z , M_x , M_y , M_z , are calculated at each of the GRF points specified for that motion stage.

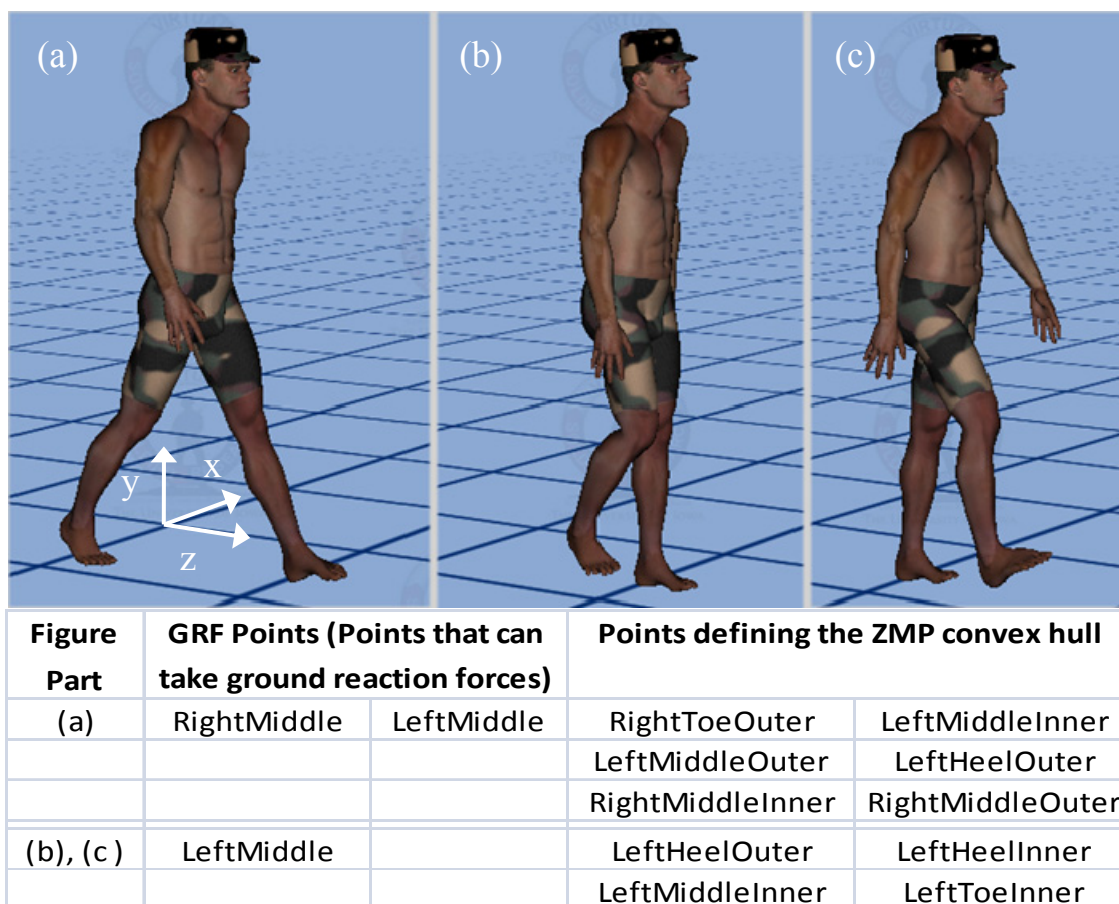


Figure 9.13. Motion stages (motion segments) for the "Walking" task

Based on the time discretization strategy for the walking task, each motion stage consists of one or several time grid points. Predictive dynamic calculations including the GRF calculations are performed at each time grid point. In the walking task, the time grid points corresponding to each motion stage are as shown in Table 9.11.

Motion Stage	Time Grid Points
a (Double Support)	1-7
b (Single Support)	7-13
c (Single Support)	13-19

Table 9.11. List of time grid points corresponding to each motion stage of the "Walking" task

The NCM method can only improve the results of GRF partitioning. It will not affect the original simulation at all if the dynamic system has only one contact area with the ground (single support such as in stages b, c in Table 9.11). Therefore, in the rest of this section, we only consider the GRF results for motion stage (a) (double support). Therefore, we will only have to deal with time grid points corresponding to double support (time grid points 1-7 in Table 9.11). The net of IGE forces and moments calculated at each of these time grid points are shown in Table 9.12.

Description of the Force System	Force, Moment Components	Value at Time Grid #1	Value at Time Grid #2	Value at Time Grid #3	Value at Time Grid #4	Value at Time Grid #5	Value at Time Grid #6	Value at Time Grid #7
Net of IGE Forces at the Hip Point	Fx	57.170	7.519	4.166	3.974	8.718	19.501	36.689
	Fy	-945.564	-316.211	-433.768	-549.115	-661.301	-769.863	-874.757
	Fz	-263.335	-68.094	-23.271	21.564	66.572	111.818	157.252
	Mx	-19.015	46.082	71.701	94.146	113.224	128.971	141.621
	My	6.508	2.358	-0.601	-2.842	-4.127	-4.403	-3.788
	Mz	-17.163	-9.104	-25.137	-37.575	-45.898	-50.001	-50.192
Net of IGE Forces at the ZMP Point	Fx	57.170	7.519	4.166	3.974	8.718	19.501	36.689
	Fy	-945.564	-316.211	-433.768	-549.115	-661.301	-769.863	-874.757
	Fz	-263.335	-68.094	-23.271	21.564	66.572	111.818	157.252
	Mx	0.000	0.000	0.000	0.000	0.000	0.000	0.000
	My	2.878	-0.698	-2.638	-2.048	-0.999	-0.407	-0.705
	Mz	0.000	0.000	0.000	0.000	0.000	0.000	0.000

Table 9.12. The net value of IGE forces and moments for the "Walking" task in ZMP method

In the next stage in the ZMP method, as discussed in Section 4.4, the ground reaction forces and moments are partitioned at the defined GRF points for that motion stage. As explained in Chapter 4, the net force and moment vectors of ground reaction forces is set equal to the negative value of the net force and moment vectors of IGE forces. Then, the components of the net force and moment vectors of ground reaction

forces are partitioned uniformly between the GRF points based on the distance of those GRF points to the ZMP (based on the formulas in Section 4.6).

The list of GRF points at each motion stage for the going prone task was previously shown in Figure 9.13. The ground reaction forces and moments at each of those GRF point are calculated at each time grid point at the GRF points indicated in Figure 9.13. The values are shown in Table 9.13.

Point of Effect of the Ground Reaction Force System	Force, Moment Components	Value at Time Grid #1	Value at Time Grid #2	Value at Time Grid #3	Value at Time Grid #4	Value at Time Grid #5	Value at Time Grid #6	Value at Time Grid #7
Right Foot Middle	Fx	-51.134	-4.414	-1.541	-0.971	-1.421	-2.106	-2.763
	Fy	845.719	185.623	160.443	134.161	107.752	83.130	65.870
Support Area 0.12 x 0.25 Rectangle	Fz	235.528	39.973	8.608	-5.269	-10.847	-12.074	-11.841
	Mx	-60.838	-53.237	-70.909	-71.125	-63.179	-51.891	-42.820
	My	-4.272	-5.657	-0.909	0.775	1.026	0.681	0.231
	Mz	-7.111	22.296	22.445	20.104	16.846	13.439	10.981
Left Foot Middle	Fx	-6.037	-3.105	-2.625	-3.003	-7.298	-17.395	-33.927
	Fy	99.846	130.588	273.324	414.954	553.549	686.733	808.886
Support Area 0.12 x 0.25 Rectangle	Fz	27.806	28.121	14.663	-16.296	-55.725	-99.744	-145.410
	Mx	62.347	53.694	71.155	71.291	62.007	46.495	26.479
	My	-0.516	2.513	2.543	2.014	1.884	2.582	4.223
	Mz	14.296	-4.400	-3.673	-1.255	2.280	7.170	13.687

Table 9.13. Ground reaction forces and moments for the "Walking" task in ZMP method

As explained earlier, this section analyzes the results of the original walking simulation (using the ZMP method). ZMP method does not consider the size and shape of each individual contact area for any of the calculations (including the calculation of ground reaction forces and moments). The ZMP method only cares about the convex hull of all the contact areas rather than each contact area individually.

Approximate sizes and shapes for individual contact areas are noted in Table 9.13. In this table, the considered shapes are rectangles having specified lengths and widths with their centers located at the location of GRF points. These values are not defined or used at all in the ZMP method. Their sizes are chosen to be larger than or equal to the actual contact areas. They are just used after the results are obtained to check the validity of the calculated ground reaction forces and moments by using NCM constraints (a sample of checking the NCM constraints for a rectangular contact area was shown in Example 9.1). Therefore, if the NCM constraints are violated for these larger contact areas, we can be sure that the NCM constraints are violated for the actual contact areas in the simulation, too.

In Table 9.13, the components of ground reaction forces and moments which violate the NCM constraints (are impossible in the real world) are highlighted in orange color. As explained in Section 8.4, in the ZMP method, at least one component of the calculated GRF is for sure impossible in the real world for all ground contact areas, except maybe for one contact area. The evidence for this claim can be seen in all columns of Table 9.13 where some cells are highlighted. As seen there, at each time grid point, at least one component of ground reaction forces and moments is highlighted for at least one of the two contact areas, indicating violation of reality.

9.7.2 Values of GRF after Re-Partitioning for Walking

As it was previously discussed in Section 9.4, general algorithms are developed to check the NCM constraints and calculate the ground reaction forces and moments on

each separate contact area. In these algorithms, individual contact areas can either be defined by their boundary points or by fixed shapes (rectangles, circles) on the ground (these algorithms can be later generalized to define them on non-horizontal and non-coplanar contact planes). The two individual contact areas (the two feet) for the walking task are defined independently in this algorithm by their boundary points (similar to the contact areas of the two feet with the ground in Figure 9.13).

Although the contact areas are defined by boundary points in the algorithm, after obtaining the final results, we check the accuracy of the results by approximating all contact areas with rectangles. After re-partitioning, the net of IGE forces and moments calculated at each time grid point for the two subtasks are shown in Table 9.14.

Description of the Force System	Force, Moment Components	Value at Time Grid #1	Value at Time Grid #2	Value at Time Grid #3	Value at Time Grid #4	Value at Time Grid #5	Value at Time Grid #6	Value at Time Grid #7
Net of IGE Forces at the Hip Point	Fx	57.170	7.519	4.166	3.974	8.718	19.501	36.689
	Fy	-945.564	-316.211	-433.768	-549.115	-661.301	-769.863	-874.757
	Fz	-263.335	-68.094	-23.271	21.564	66.572	111.818	157.252
	Mx	-19.015	46.082	71.701	94.146	113.224	128.971	141.621
	My	6.508	2.358	-0.601	-2.842	-4.127	-4.403	-3.788
	Mz	-17.163	-9.104	-25.137	-37.575	-45.898	-50.001	-50.192
Net of IGE Forces at the ZMP Point	Fx	57.170	7.519	4.166	3.974	8.718	19.501	36.689
	Fy	-945.564	-316.211	-433.768	-549.115	-661.301	-769.863	-874.757
	Fz	-263.335	-68.094	-23.271	21.564	66.572	111.818	157.252
	Mx	0.000	0.000	0.000	0.000	0.000	0.000	0.000
	My	2.878	-0.698	-2.638	-2.048	-0.999	-0.407	-0.705
	Mz	0.000	0.000	0.000	0.000	0.000	0.000	0.000

Table 9.14. The net value of IGE forces and moments for the "Walking" task in NCM method

As expected, the IGE values have stayed the same after GRF re-partitioning. However, the ground reaction forces and moments at each contact area will be different. The new values are shown in Table 9.15.

Point of Effect of the Ground Reaction Force System	Force, Moment Components	Value at Time Grid #1	Value at Time Grid #2	Value at Time Grid #3	Value at Time Grid #4	Value at Time Grid #5	Value at Time Grid #6	Value at Time Grid #7
Right Foot Middle	Fx	-48.148	30.083	-39.065	3.309	12.099	17.145	13.130
	Fy	834.730	167.981	122.917	80.247	65.779	76.128	43.668
Support Area 0.12 x 0.25 Rectangle	Fz	362.561	98.070	107.724	101.531	98.669	114.192	65.502
	Mx	0.403	-0.492	-0.472	-0.300	-5.592	-6.381	-3.526
	My	1.915	0.111	-20.467	-5.577	-3.810	2.015	7.826
	Mz	5.257	6.186	6.128	4.001	1.500	3.358	1.939
Left Foot Middle	Fx	-9.023	-37.602	34.899	-7.283	-20.818	-36.645	-49.819
	Fy	110.834	148.229	310.851	468.869	595.522	693.734	831.089
Support Area 0.12 x 0.25 Rectangle	Fz	-99.226	-29.976	-84.453	-123.095	-165.240	-226.010	-222.754
	Mx	11.416	14.447	27.800	37.757	31.828	1.972	-0.811
	My	14.807	12.055	-19.458	-4.960	-0.512	-4.537	-4.123
	Mz	3.547	8.345	7.163	6.626	11.471	16.779	20.048

Table 9.15. Ground reaction forces and moments for the "Walking" task in NCM Method

As seen in Tables 9.15, approximate sizes and shapes for individual contact areas are noted. These contact areas were modeled differently in the NCM method (by specifying their boundary points). However, the approximate rectangles shown in Table 9.15 are used after the results are obtained to check the validity of the calculated ground reaction forces and moments in the NCM method.

In Table 9.15, the components of ground reaction forces and moments are checked to see if they violate the NCM constraints (are impossible in the real world) or not and are highlighted, if they do. The checking is done based on the indicated

approximate sizes and shapes (in the repartitioning procedure, the NCM constraints were based on boundary point locations, not these fixed shapes). However, as seen, no component of ground reaction forces and moments is highlighted in these tables or violates the NCM constraints.

9.7.3 Comparison of GRF Before and After Re-Partitioning

As a simpler reference, similar to what was done in Section 9.5, values for some of the components of the ground reaction forces and moments are plotted in this section before and after re-partitioning.

The term "Possible Range" for $\frac{M_x}{F_y}$ or $\frac{M_z}{F_y}$ in Figures 9.14 and 9.15 specifies the limitation imposed by the NCM constraints (such as 9.2.1) on $\frac{M_x}{F_y}$ or $\frac{M_z}{F_y}$. For a fixed size rectangular contact area on the ground, NCM constraint is simplified to two independent inequality constraints on the values of $\frac{M_x}{F_y}$ or $\frac{M_z}{F_y}$ with fixed upper and lower limits. This fact can be observed from Equation (9.2.1), for example. Also, as seen in Figures 9.14 and 9.15, the possible ranges for $\frac{M_x}{F_y}$ or $\frac{M_z}{F_y}$ are inequalities with fixed values of upper and lower limits during the motion. The horizontal axis in these graphs indicates the change of time and refers to the number of grid points after the contact area comes into contact with the ground.

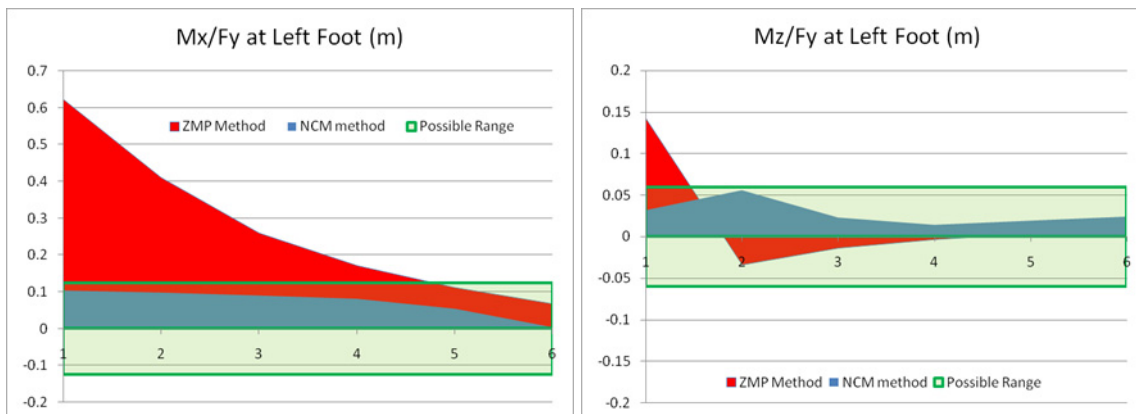


Figure 9.14. The values obtained for M_x/F_y and M_z/F_y at the Left Foot by ZMP versus NCM Methods

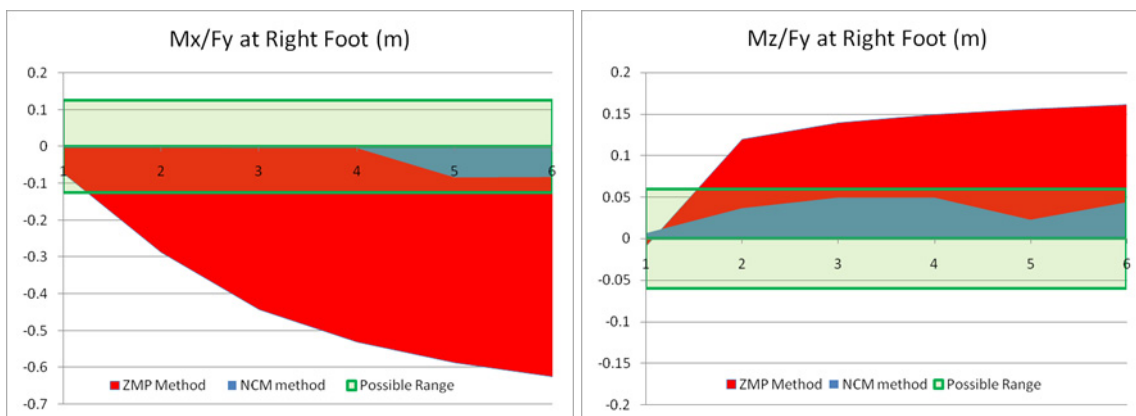


Figure 9.15. The values obtained for M_x/F_y and M_z/F_y at the Right Foot by ZMP versus NCM Methods

The term "Possible Range" for M_x or M_z in Figures 9.16 - 9.19 specifies the limitation imposed by the NCM constraints on M_x or M_z based on the value of F_y at any instant of motion. This possible range changes during the motion, because the value of F_y changes during the motion.

As previously seen in Table 9.15, M_x or M_z values with the ZMP method exceed the possible ranges at several instants of time during the motion. This fact can also be observed in Figures 9.16 - 9.19.

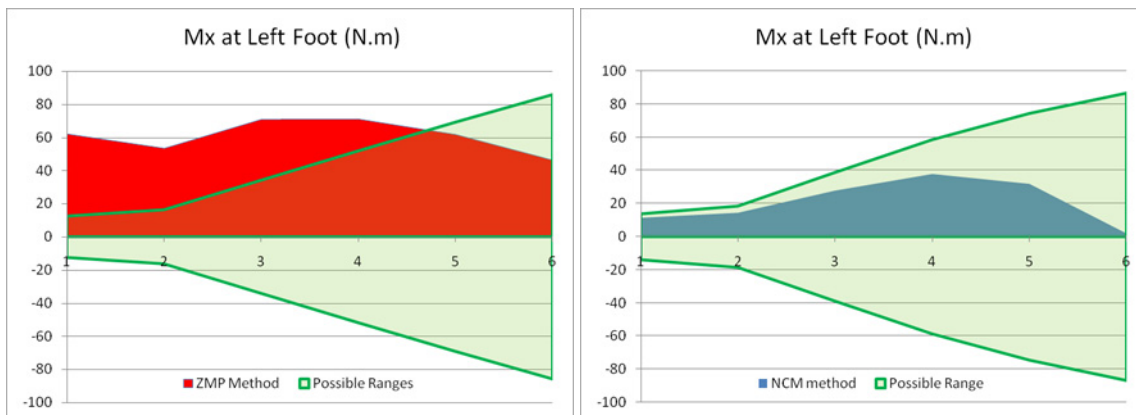


Figure 9.16. The values obtained for M_x at the Left Foot by ZMP versus NCM Methods

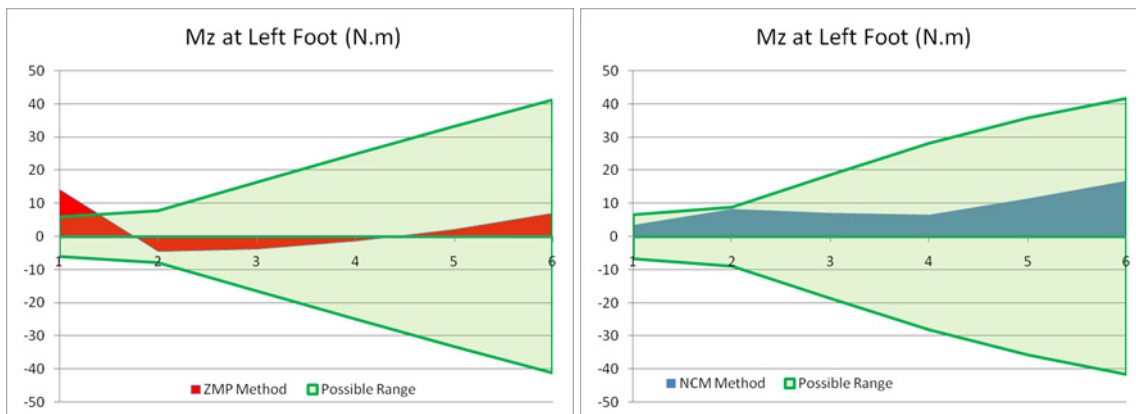


Figure 9.17. The values obtained for M_z at the Left Foot by ZMP versus NCM Methods

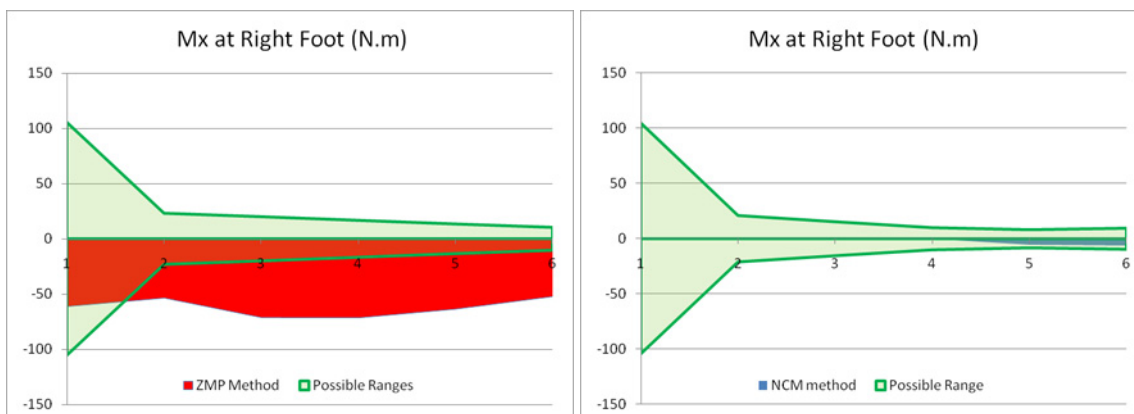


Figure 9.18. The values obtained for Mx at the Right Foot by ZMP versus NCM Methods

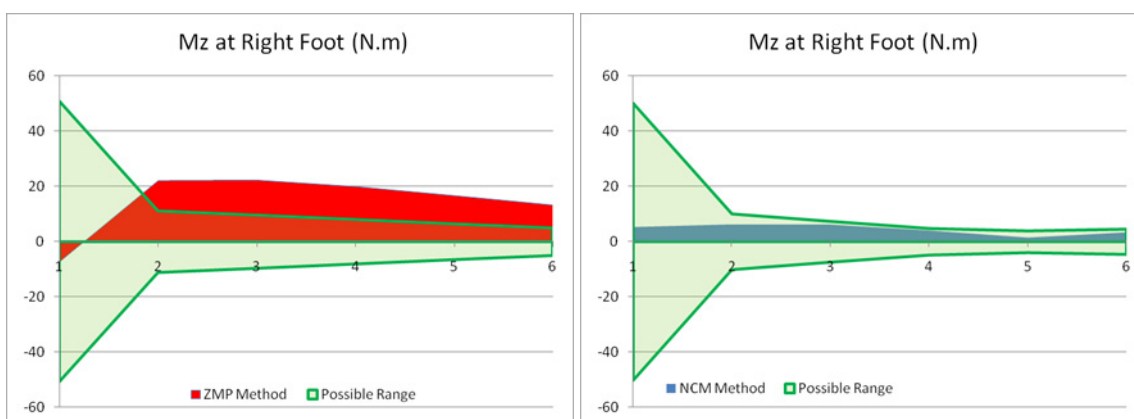


Figure 9.19. The values obtained for Mz at the Right Foot by ZMP versus NCM Methods

9.7.4 GRF Before and After Re-Partitioning versus Experimental Data

In this research, we try to improve the results of GRF for a sample walking simulation by using the NCM method. This improvement only consists of finding values for GRF which are possible in the real world. The NCM method does not ensure that the calculated GRF are optimal or match the experimental data. These issues also depend on the original simulation and the constraints used in the original simulation to predict a

walking task. However, because the experimental data for the GRF of walking are available in the literature, one may also be curious to know how much the NCM method improves the GRF results of a sample walking simulation. Therefore, we also perform a comparison of the GRF calculated by ZMP versus NCM methods with the experimental data in this section.

However, surprisingly, the result of the comparisons indicates that the Re-Partitioning results match pretty well with the experimental data. The graphs which were used to support (in Section 4.6) or criticize the support (in Section 8.4.3) for the uniform partitioning assumption are again repeated in this section. The results of NCM method surprisingly match better with these experimental data (data that were originally used as the only support for the uniform partitioning assumption in the ZMP method).

Similar to Section 8.4.3, we replot the data measured in the walking experiment published in Winter (2009) in Figures 9.20, 9.21, 9.22. In these figures, we plot the ratio of ZMP distances from the left and right feet versus the ratio of the several components of the forces and moments on them. In these figures, z_R and z_L respectively denote the distances of the ZMP to the right and left foot in the forward-backward direction. Also, $F_{yR}, F_{yL}, F_{zR}, F_{zL}, M_{xR}, M_{xL}$ respectively denote the vertical and frictional ground reaction forces and tipping ground reaction moments on the right and the left foot. The details and the numbers used in plotting these graphs are explained in Appendix D.

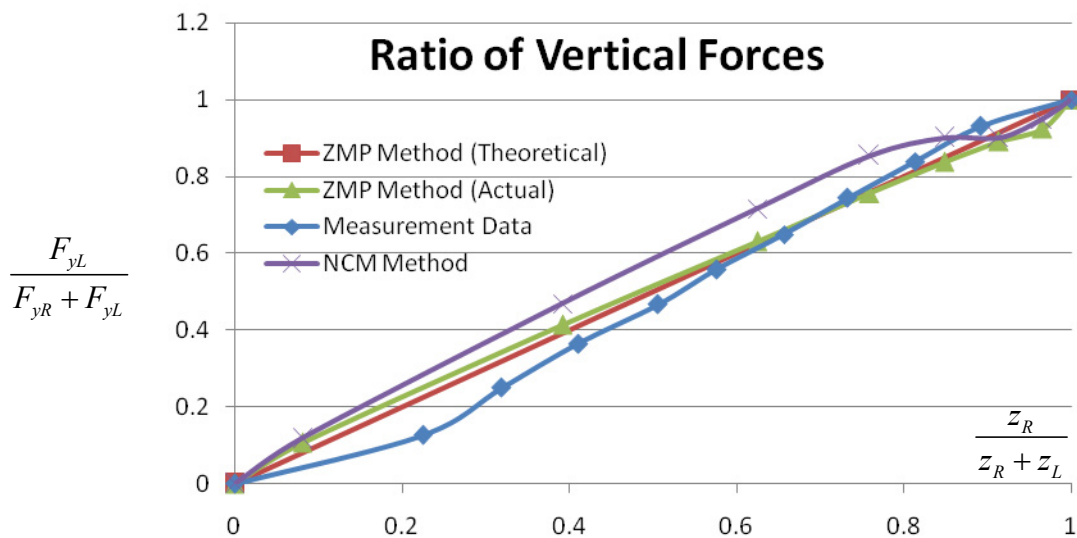


Figure 9.20. Ratio of the vertical forces acting on Left and Right feet versus the ratio of their distances from ZMP for walking task. Measurement data is compared to the results of the NCM and ZMP methods.

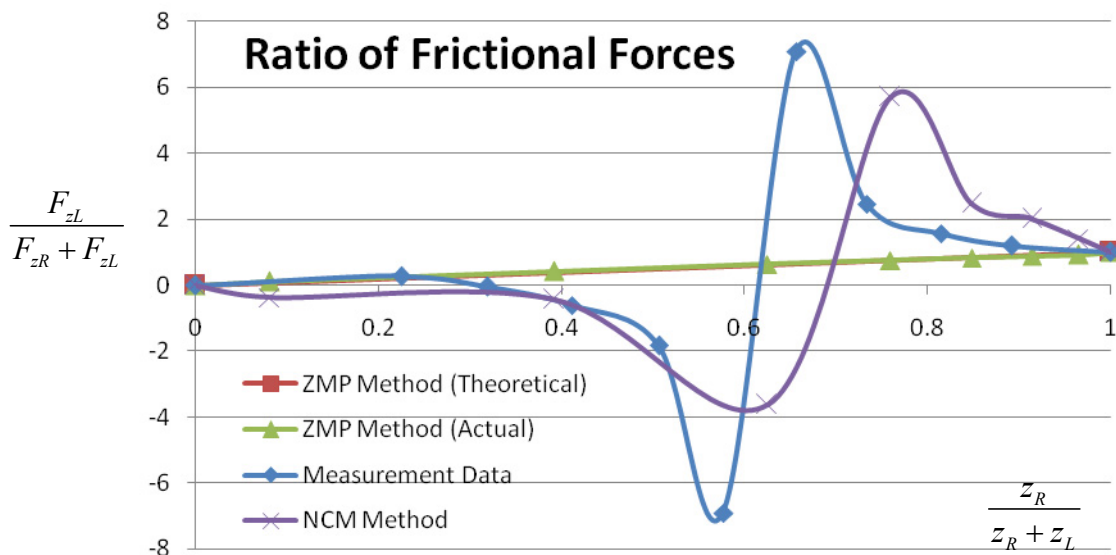


Figure 9.21. Ratio of the frictional forces acting on Left and Right feet versus the ratio of their distances from ZMP for walking task. Measurement data is compared to the results of the NCM and ZMP methods.

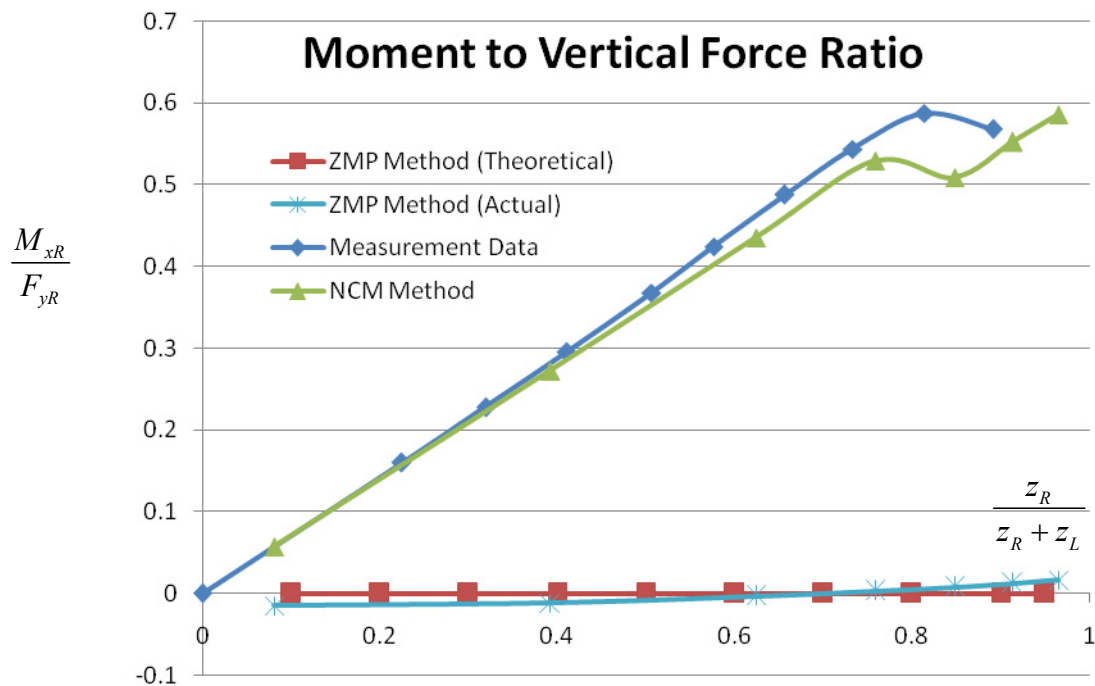


Figure 9.22. Contact moment of right foot at ZMP (normalized by dividing it by the vertical force) versus the ratio of the distances of ZMP from the feet for walking task. Measurement data is compared to the results of the NCM and ZMP methods.

9.8. Summary and Conclusion

Several dynamic tasks had been modeled in Chapters 5 and 6 using the ZMP method. However, some impossible values for GRF had been encountered in those simulations. Chapter 8 theoretically proved that those impossible values for GRF will always happen due to an imperfect assumption in the ZMP method. But it was also indicated that the satisfaction of ZMP constraint ensures that one can find values of GRF that are possible in the real world and also equilibrate the given IGE forces for those predicted motions (the motion calculated using the ZMP method is always possible, while the calculated GRF values are always impossible.). Therefore, in this chapter, we

introduced algorithms that correct the GRF values obtained by the ZMP method such that the values are possible in the real world (satisfy the NCM constraints). As an example, in this chapter, we implemented this algorithm on the "Going Prone" task introduced in Chapter 6. We also implemented it on a previously simulated "Walking" task. Conclusions from this study are as follows:

- 1- Corollary 8.1 is validated in this chapter by observing the results for the "Going Prone" and "Walking" task. In other words, at least one component of the calculated GRF is impossible in the real world for all ground contact areas, except may be for one contact area in the ZMP method.
- 2- Theorem 4.1 is validated in this chapter. In other words, satisfaction of ZMP constraint ensures that it is possible to find unilateral contact forces on the given contact areas to cancel the given IGE forces for the dynamic system. This is because we could find GRF that are possible in the real world by re-partitioning them.
- 3- The torques obtained after re-partitioning seem to be lower than the original torques. However, the optimality of the initial motion from the ZMP method seem to stay almost unaffected after re-partitioning. Therefore, although the motion obtained in the ZMP method is possible and almost optimal, the GRF need to be re-partitioned in order to obtain realistic values.
- 4- The re-partitioning (NCM method) does not ensure that the calculated GRF are optimal or match the experimental data. These issues also depend on the original simulation and the constraints used to predict a motion task.

However, it seems that the results of the re-partitioning for the walking task considerably improved similarity of the GRF ratios with the experimental data.

CHAPTER 10

NCM MARGINS OF DYNAMIC STABILITY

10.1 Introduction

In this theoretical chapter, we first define the terms “Contact Stability” and “Margins of Contact Stability” for an arbitrary dynamic system during its motion. The general NCM and friction constraints introduced in Chapter 7 are used to derive these definitions. The margins of tipping and slipping stabilities presented in this chapter are applicable for the most general cases of contact areas and are usable for both real systems such as in robot control or simulated systems or offline calculations. We show that the problem of finding the margins of tipping or slipping stability for the most general cases of contact areas turns into solving a linear optimization problem.

10.2 Motivation for NCM Stability Concepts

A major drawback of the ZMP stability concepts is that they apply only to the cases in which the system’s contact with the environment is in one plane only. They cannot be used when different parts of the system come into contact with the environment and the contact areas are in different planes. Unlike the ZMP, NCM stability concepts that we will define are applicable for the most general cases of contact areas (coplanar or non-coplanar contact areas which are horizontal, inclined, parallel, or non-parallel).

10.3 Possibility versus the Stability of Motion

Chapters 4, 7 and 8 dealt with the possibility of a motion problem. It is impossible that NCM constraints or the ZMP constraint is violated for a system in the real world. Even during the falling motion of a dynamic system, both the NCM constraints and the ZMP constraint will need to be satisfied (they will require the system to have enough acceleration under the effect of gravity during falling motion so that these constraints are not violated). But, ZMP can also be used to analyze the stability of a motion. If we define instability as a situation when the contact area of the robot with the ground reduces to a line (all contact forces are concentrated on one edge of the convex hull), then Theorem 7.2 indicates that instability occurs when the ZMP is on one edge of the convex hull. Also, the location of ZMP helps us determine the margins of dynamic stability for the motion. Conventionally, the distance of the ZMP from the edges of the convex hull in any of the horizontal axes determines the stability of motion about those axes. For the cases of contact areas on non-coplanar surfaces, ZMP is not defined and we define the margins of stability in the general case of non-coplanar contact areas (either horizontal or inclined or parallel or non-parallel) using the NCM point definition.

10.4. Contact Stability of a Dynamic System

In this section, we offer the general criteria for the contact stability of a system having several coplanar or non-coplanar contact areas with the environment. Examples of

such systems are depicted in Figures 10.1 and 10.2. In Figure 10.1 the elephant avatar shown is considered as a system with multiple coplanar contact areas with the ground.

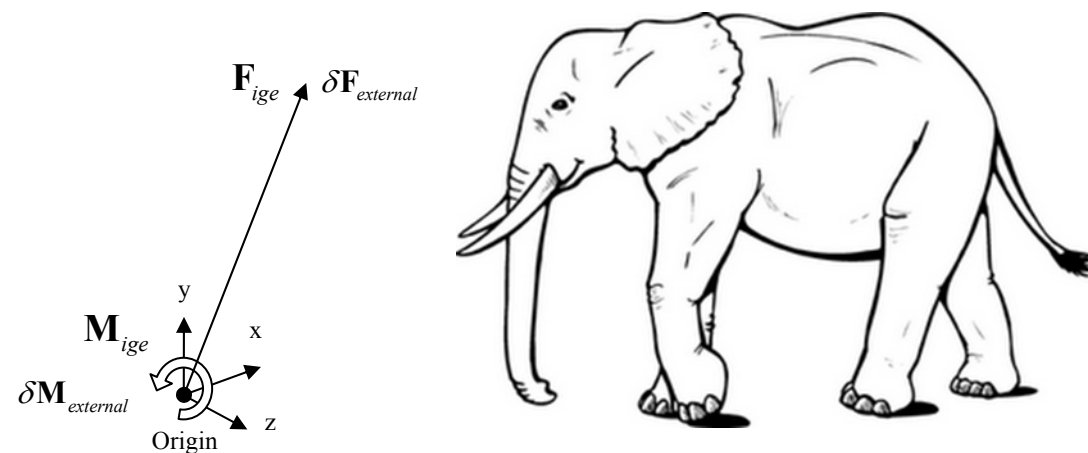


Figure 10.1. Stability criteria for a dynamic system with coplanar contact areas

The purpose of contact stability criteria is to check whether the system will slip or tip over due to an additional infinitesimal external force. The contact stability of a system does not depend on the stiffness of the internal joints (DOF) of the system and it only depends on the net properties of the system (net acceleration, angular acceleration, velocity, mass, center of mass, moment of inertia, ...). To analyze the contact stability of this system at a given frame of motion, we apply a perturbation in the external forces/moments acting on the system and evaluate the response of the system. Therefore, to simplify the explanation of the response of the system to the perturbation and avoid the discussion of system's internal motions, consider the system as one rigid body (freeze/stiffen all DOF of the system except its 6 global translational/rotational DOF).

Now let us present our general definition for contact stability of a motion: Apply a small perturbation in the external forces/moments that are applied on the rigid body (system). If the rigid body acquires a perturbation in its acceleration at that frame of motion due to that perturbation, we say that the contact of the system is unstable at that frame of motion (or just call it unstable), otherwise, we call it stable.

This is because a rigid body which has flat contact areas with the environment can only slip or tip in order to move. If the rigid body acquires a perturbation in its acceleration at that frame of motion due to a perturbation in external forces, it will definitely fall or slip (assuming that the perturbation will be present at all the times after its initial application). That is because for a rigid body, the perturbation required for the initiation of slipping is always larger than or equal to the perturbation required for continuation of slipping (static versus dynamic coefficients of friction) and the perturbation required for the initiation of tipping is also always larger than or equal to the perturbation required for the continuation of tipping (an example can be seen in Equation (3.2.18) and its explanation in Example 3.2). By the term “continuation” of falling or slipping we are referring to the “continuation” of falling or slipping until there is a change in the environmental contact areas of the system due to the slipping or falling motions.

Another example is shown in Figure 10.2 where the human avatar has several non-coplanar contact areas with the environment. All the definitions and explanations given in this section apply to system having several coplanar or non-coplanar contact areas with the environment such as this case.

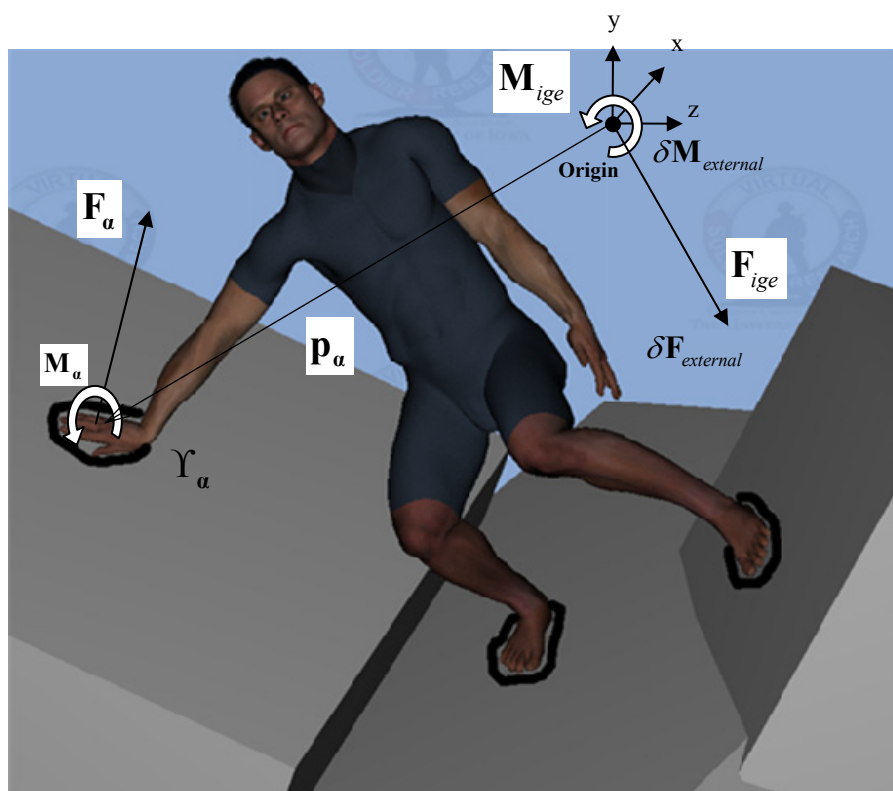


Figure 10.2. Stability criteria for a general dynamic system with non-coplanar contact areas

The system is originally affected by an arbitrary set of contact, inertial, gravitational and external forces whose sum is equal to zero due to dynamic equilibrium equations. Let us write the dynamic equilibrium equations for a sample dynamic system depicted in Figure 10.2 about the origin :

$$\begin{aligned}
 \text{Dynamic Equilibrium} &\Rightarrow \begin{cases} \mathbf{F}_{ige} + \sum \mathbf{F}_\alpha = 0 \\ \mathbf{M}_{ige} + \sum \mathbf{M}_\alpha + \sum \mathbf{p}_\alpha \times \mathbf{F}_\alpha = 0 \end{cases} \\
 &\Rightarrow \begin{cases} \mathbf{F}_{inertial} + \mathbf{F}_{gravitational} + \mathbf{F}_{external} + \sum \mathbf{F}_\alpha = 0 \\ \mathbf{M}_{inertial} + \mathbf{M}_{gravitational} + \mathbf{M}_{external} + \sum \mathbf{M}_\alpha + \sum \mathbf{p}_\alpha \times \mathbf{F}_\alpha = 0 \end{cases} \quad (10.4.1)
 \end{aligned}$$

A small perturbation in the external moments/forces is applied on it which is denoted by $\delta\mathbf{M}_{external}$ and $\delta\mathbf{F}_{external}$.

$$\Rightarrow \begin{cases} \delta\mathbf{F}_{inertial} + \delta\mathbf{F}_{gravitational} + \delta\mathbf{F}_{external} + \delta(\sum \mathbf{F}_\alpha) = 0 \\ \delta\mathbf{M}_{inertial} + \delta\mathbf{M}_{gravitational} + \delta\mathbf{M}_{external} + \delta(\sum \mathbf{M}_\alpha + \sum \mathbf{p}_\alpha \times \mathbf{F}_\alpha) = 0 \end{cases} \quad (10.4.2)$$

The system is called stable if it is able to preserve its original acceleration (keep $\delta\mathbf{M}_{inertial}$ and $\delta\mathbf{F}_{inertial}$ equal to zero) under any type of such perturbations. It is noted that for a stable system (considered as a rigid body with a known mass and gravity), a perturbation is also impossible in gravitational forces ($\delta\mathbf{F}_{gravitational} = \delta\mathbf{M}_{gravitational} = \mathbf{0}$), too. Therefore:

$$\Rightarrow \begin{cases} \underbrace{\delta\mathbf{F}_{inertial}}_0 + \delta\mathbf{F}_{gravitational} + \delta\mathbf{F}_{external} + \delta(\sum \mathbf{F}_\alpha) = 0 \\ \underbrace{\delta\mathbf{M}_{inertial}}_0 + \delta\mathbf{M}_{gravitational} + \delta\mathbf{M}_{external} + \delta(\sum \mathbf{M}_\alpha + \sum \mathbf{p}_\alpha \times \mathbf{F}_\alpha) = 0 \end{cases} \quad (10.4.3)$$

$$\Rightarrow \begin{cases} \underbrace{\delta\mathbf{F}_{gravitational}}_0 + \delta\mathbf{F}_{external} + \delta(\sum \mathbf{F}_\alpha) = 0 \\ \underbrace{\delta\mathbf{M}_{gravitational}}_0 + \delta\mathbf{M}_{external} + \delta(\sum \mathbf{M}_\alpha + \sum \mathbf{p}_\alpha \times \mathbf{F}_\alpha) = 0 \end{cases} \quad (10.4.4)$$

So, for a stable system, we need to have solutions for \mathbf{F}_α and \mathbf{M}_α in the following equations for any set of infinitesimal vectors $\delta\mathbf{M}_{external}$ and $\delta\mathbf{F}_{external}$:

$$\Rightarrow \begin{cases} \delta\mathbf{F}_{external} + \delta(\sum \mathbf{F}_\alpha) = 0 \\ \delta\mathbf{M}_{external} + \delta(\sum \mathbf{M}_\alpha + \sum \mathbf{p}_\alpha \times \mathbf{F}_\alpha) = 0 \end{cases} \quad (10.4.5)$$

On the other hand, $\sum \mathbf{F}_\alpha = -\mathbf{F}_{ige}$ and $\sum \mathbf{M}_\alpha + \sum \mathbf{p}_\alpha \times \mathbf{F}_\alpha = -\mathbf{M}_{ige}$ are vector functions of \mathbf{F}_α and \mathbf{M}_α whose values are limited in the 3D space only by the NCM and friction constraints. Consider a sample perturbation of external forces in direction \mathbf{e}_i , which results in: $\delta \mathbf{F}_{external} = |\delta \mathbf{F}_{external}| \mathbf{e}_i$, $\delta \mathbf{M}_{external} = \mathbf{0}$. For such a perturbation, Equation (10.4.5) turns into: $|\delta \mathbf{F}_{external}| + \delta(\mathbf{F}_{ige} \cdot \mathbf{e}_i) = 0$. $\mathbf{F}_{ige} \cdot \mathbf{e}_i$ is a scalar value. A change in this scalar value means the increasing or decreasing of $\mathbf{F}_{ige} \cdot \mathbf{e}_i$. It is obvious that a solution can always be found for $\delta(\mathbf{F}_{ige} \cdot \mathbf{e}_i)$ for all values of $|\delta \mathbf{F}_{external}|$ as long as $\mathbf{F}_{ige} \cdot \mathbf{e}_i$ (a function of \mathbf{F}_α and \mathbf{M}_α) is not at its local minimum or maximum value (at the time when perturbation happens). Therefore, a solution can always be found for Equation (10.4.5) as long as none of the six components of \mathbf{F}_{ige} and \mathbf{M}_{ige} is at its local minimum or maximum value.

Therefore, a system is stable at a given frame of motion, if and only if none of the six components of its net IGE (inertial, gravity, external) forces or moments is at its local minimum or maximum value.

10.5. Margins of Contact Stability of a Dynamic System

Using the insight from Section 10.4, we offer a general method to evaluate the margins of contact stability for a system having several non-coplanar contact areas with the environment. However, each contact area is assumed to be rigid, flat and non-adhesive. Similar to Section 10.4, to evaluate the margins of contact stability of the

system at a given frame of motion, consider the system as a rigid body (freeze all DOF of the system except its 6 global translation/rotation DOF).

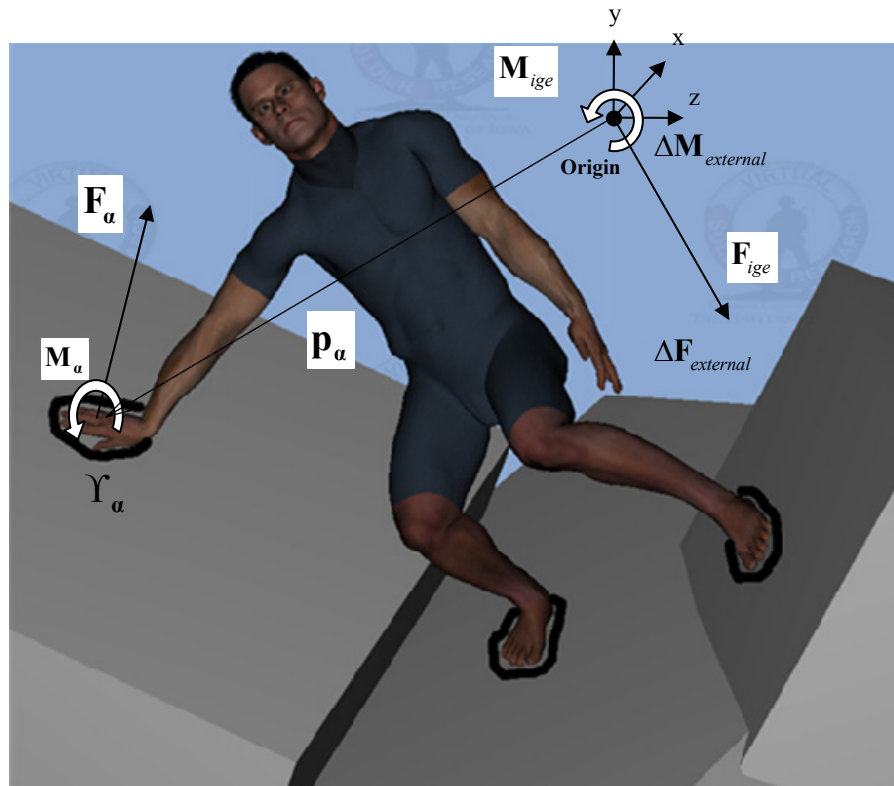


Figure 10.3. Margins of contact stability for a general dynamic system with non-coplanar contact areas

Now let us present our general definition for contact stability margins of a motion: Apply a finite amount of perturbation in the external forces/moments. Increase the amount of perturbation until the rigid body acquires a perturbation in its acceleration (a rigid body can only slip or tip in order to move). The maximum amount of perturbation in the external forces/moments in a specific direction before a change happens in the acceleration of the rigid body is referred to as the margin of contact stability of the system in that direction.

The system is originally affected by an arbitrary set of contact, inertial, gravitational and external forces whose sum is equal to zero due to dynamic equilibrium equations. Let us write the dynamic equilibrium equations for a sample dynamic system depicted in Figure 10.3 about the origin:

$$\begin{aligned} \text{Dynamic Equilibrium} &\Rightarrow \begin{cases} \mathbf{F}_{ige} + \sum \mathbf{F}_\alpha = 0 \\ \mathbf{M}_{ige} + \sum \mathbf{M}_\alpha + \sum \mathbf{p}_\alpha \times \mathbf{F}_\alpha = 0 \end{cases} \\ \Rightarrow &\begin{cases} \mathbf{F}_{inertial} + \mathbf{F}_{gravitational} + \mathbf{F}_{external} + \sum \mathbf{F}_\alpha = 0 \\ \mathbf{M}_{inertial} + \mathbf{M}_{gravitational} + \mathbf{M}_{external} + \sum \mathbf{M}_\alpha + \sum \mathbf{p}_\alpha \times \mathbf{F}_\alpha = 0 \end{cases} \quad (10.5.1) \end{aligned}$$

A perturbation in the external moments/forces is applied on it which is denoted by $\Delta \mathbf{M}_{external}$ and $\Delta \mathbf{F}_{external}$.

$$\Rightarrow \begin{cases} \Delta \mathbf{F}_{inertial} + \Delta \mathbf{F}_{gravitational} + \Delta \mathbf{F}_{external} + \Delta(\sum \mathbf{F}_\alpha) = 0 \\ \Delta \mathbf{M}_{inertial} + \Delta \mathbf{M}_{gravitational} + \Delta \mathbf{M}_{external} + \Delta(\sum \mathbf{M}_\alpha + \sum \mathbf{p}_\alpha \times \mathbf{F}_\alpha) = 0 \end{cases} \quad (10.5.2)$$

The system will be stable as long as it is able to preserve its original acceleration (keep $\Delta \mathbf{M}_{inertial}$ and $\Delta \mathbf{F}_{inertial}$ equal to zero) for given values of $\Delta \mathbf{M}_{external}$ and $\Delta \mathbf{F}_{external}$. It is noted that as long as the system remains stable, a perturbation is impossible in gravitational forces ($\Delta \mathbf{F}_{gravitational} = \Delta \mathbf{M}_{gravitational} = \mathbf{0}$), too. Therefore:

$$\Rightarrow \begin{cases} \underbrace{\Delta \mathbf{F}_{inertial} + \Delta \mathbf{F}_{gravitational}}_{\mathbf{0}} + \Delta \mathbf{F}_{external} + \Delta(\sum \mathbf{F}_\alpha) = 0 \\ \underbrace{\Delta \mathbf{M}_{inertial}}_{\mathbf{0}} + \Delta \mathbf{M}_{gravitational} + \Delta \mathbf{M}_{external} + \Delta(\sum \mathbf{M}_\alpha + \sum \mathbf{p}_\alpha \times \mathbf{F}_\alpha) = 0 \end{cases} \quad (10.5.3)$$

$$\Rightarrow \begin{cases} \underbrace{\Delta \mathbf{F}_{gravitational}}_0 + \Delta \mathbf{F}_{external} + \Delta(\sum \mathbf{F}_\alpha) = 0 \\ \underbrace{\Delta \mathbf{M}_{gravitational}}_0 + \Delta \mathbf{M}_{external} + \Delta(\sum \mathbf{M}_\alpha + \sum \mathbf{p}_\alpha \times \mathbf{F}_\alpha) = 0 \end{cases} \quad (10.5.4)$$

In order to evaluate the margins of slipping/tipping stability in a specific direction, let us denote the magnitude of perturbation by a scalar s and the direction of perturbation in the external force/moment by a unit vectors \mathbf{u}_F or \mathbf{u}_M respectively, such that $\Delta \mathbf{M}_{external} = s\mathbf{u}_M$ or $\Delta \mathbf{F}_{external} = s\mathbf{u}_F$. Therefore, to evaluate the margin of slipping/tipping stability s in that direction, we need to find the maximum allowable value for s such that a solution exists for the following equations:

$$\Rightarrow \begin{cases} \Delta \mathbf{F}_{external} + \Delta(\sum \mathbf{F}_\alpha) = 0 \\ \Delta \mathbf{M}_{external} + \Delta(\sum \mathbf{M}_\alpha + \sum \mathbf{p}_\alpha \times \mathbf{F}_\alpha) = 0 \end{cases} \quad (10.5.5)$$

$$\Rightarrow \begin{cases} s\mathbf{u}_F + \Delta(\sum \mathbf{F}_\alpha) = 0 \\ or \\ s\mathbf{u}_M + \Delta(\sum \mathbf{M}_\alpha + \sum \mathbf{p}_\alpha \times \mathbf{F}_\alpha) = 0 \end{cases} \quad (10.5.6)$$

On the other hand, $\sum \mathbf{F}_\alpha = -\mathbf{F}_{ige}$ and $\sum \mathbf{M}_\alpha + \sum \mathbf{p}_\alpha \times \mathbf{F}_\alpha = -\mathbf{M}_{ige}$ are vector functions of \mathbf{F}_α and \mathbf{M}_α whose values are limited in the 3D space only by the NCM and friction constraints. Therefore, the margins of dynamic contact stability against slipping/tipping in a specific direction \mathbf{u}_F or \mathbf{u}_M can also be found by evaluating the maximum and minimum allowable amounts of perturbations in \mathbf{F}_{ige} and \mathbf{M}_{ige} (as

functions of \mathbf{F}_α and \mathbf{M}_α) in that direction subject to NCM and friction constraints as will be explained in the next section.

10.6. Formulation for the Margins of Dynamic Stability

Consider the dynamic systems that were depicted in Figures 10.1, 10.2 and 10.3. At any time frame of motion, there is dynamic equilibrium between the inertial, gravitational and external (IGE) forces and contact forces. Let \mathbf{F}_{ige} and \mathbf{M}_{ige} be the force and moment of IGE forces at the global origin.

Definition 10.1: ***Margins of Tipping (Falling) Stability***

We define the margins of tipping (falling) stability about the positive/negative directions of horizontal axes as the maximum allowable increase/decrease in $(\mathbf{M}_{ige})_z$ and $(\mathbf{M}_{ige})_x$, such that the reaction contact forces and moments remain possible in the real world, assuming that other components of \mathbf{F}_{ige} and \mathbf{M}_{ige} remain constant.

We denote the margins of tipping (falling) stability about the positive and negative directions of the horizontal axes by: $\Delta^+(\mathbf{M}_{ige})_z, \Delta^-(\mathbf{M}_{ige})_z$ and $\Delta^+(\mathbf{M}_{ige})_x, \Delta^-(\mathbf{M}_{ige})_x$.

Definition 10.2: Margins of Slipping Stability

We define the margins of slipping stability along the positive/negative horizontal axes or about the positive/negative vertical axis as the maximum allowable increase/decrease in $(\mathbf{F}_{ige})_z$, $(\mathbf{F}_{ige})_x$ and $(\mathbf{M}_{ige})_y$, such that the reaction contact forces and moments remain possible in the real world, assuming that other components of \mathbf{F}_{ige} and \mathbf{M}_{ige} remain constant.

We denote the margins of slipping stability along the positive/negative horizontal axes by $\Delta^+(\mathbf{F}_{ige})_z, \Delta^-(\mathbf{F}_{ige})_z$ and $\Delta^+(\mathbf{F}_{ige})_x, \Delta^-(\mathbf{F}_{ige})_x$. We also denote the margins of slipping stability about the positive/negative vertical axis by $\Delta^+(\mathbf{M}_{ige})_y, \Delta^-(\mathbf{M}_{ige})_y$.

10.6.1. Individual Contact Forces and Moments as Design Variables

At any time frame of motion with \mathbf{F}_{ige} and \mathbf{M}_{ige} , a set of contact forces is required in order to maintain dynamic equilibrium, which means that any contact area is tolerating a specific net force and moment. The sum of these forces and moments should balance \mathbf{F}_{ige} and \mathbf{M}_{ige} .

When we are imposing perturbations on components of \mathbf{F}_{ige} and \mathbf{M}_{ige} to find the margins of stability, we must consider that any of the 6 components of contact forces and moments on any of the contact areas are allowed to change to find a solution for the

problem that is possible in the real world. However, in this process, the other components of \mathbf{F}_{ige} and \mathbf{M}_{ige} should be kept fixed. We offer a simple example to clarify this fact:

Consider a 2D problem in which an avatar is in a standing position with the contact surfaces of its feet and the ground having areas equal to zero (its feet cannot take moments) as shown in Figure 10.4.a. In this 2D problem the direction of all forces are assumed to be up/down and direction of all moments are perpendicular to the 2D plane. All forces and moment symbols represent the magnitude of them and are shown as scalar symbols. Without any perturbation, a possible case is shown in Figure 10.4.a. With an increase in the global moment $\Delta^+ M_{ige} = aF$, if we do not allow any change in contact forces and moments, the problem will have no solution as shown in Figure 10.4.b. But, if we allow changes in contact forces and moments, the problem will have a solution which is shown in Figure 10.4.c :

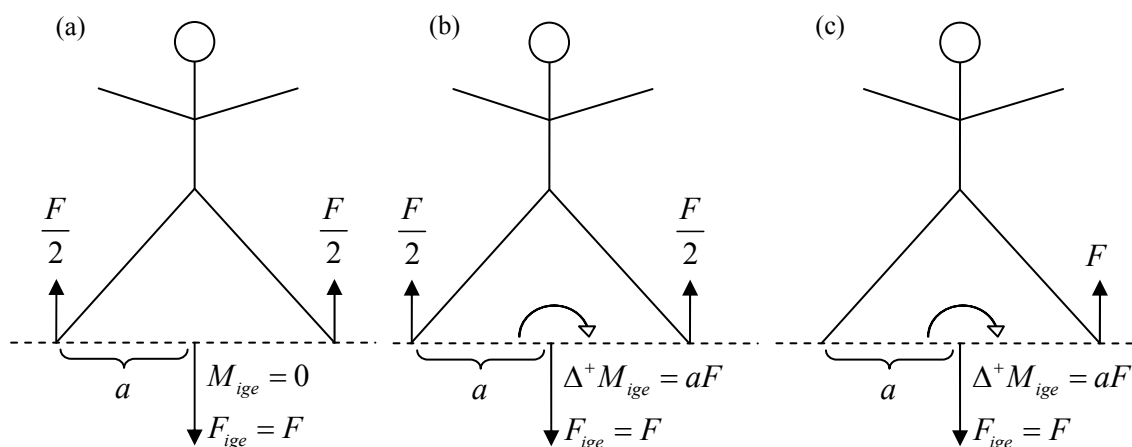


Figure 10.4. Effect of allowing changes in contact forces in determination of stability margins:
 (a) A 2D avatar in the original (unperturbed) condition
 (b) Perturbed case, preventing any change in contact forces – No Solution
 (c) Perturbed case, allowing changes in contact forces - Solvable

10.6.2. The margins of dynamic stability as linear optimization problems

In the general case (several non-co-planar and non-horizontal contact surfaces), the problem of finding the margins of stability turns into solving a linear optimization problem as shown below:

- Margins of Tipping Stability

Margins of tipping (falling) stability $\Delta^+(\mathbf{M}_{\text{ige}})_z, \Delta^-(\mathbf{M}_{\text{ige}})_z, \Delta^+(\mathbf{M}_{\text{ige}})_x$ and $\Delta^-(\mathbf{M}_{\text{ige}})_x$

can be found by maximizing (Δ^+) or minimizing (Δ^-) of $(\mathbf{M}_{\text{ige}})_z$ and $(\mathbf{M}_{\text{ige}})_x$ and subtracting them from their actual values, considering all \mathbf{F}_α and \mathbf{M}_α (contact forces and moments on contact areas) as design variables and the following linear constraints:

$$1) \quad -\mathbf{F}_{\text{ige}} = \sum \mathbf{F}_\alpha$$

$$2) \quad -\mathbf{M}_{\text{ige}} = \sum \mathbf{M}_\alpha + \sum \mathbf{p}_\alpha \times \mathbf{F}_\alpha$$

(Remove $(\mathbf{M}_{\text{ige}})_z$ or $(\mathbf{M}_{\text{ige}})_x$ equation if you are maximizing or minimizing any of them)

$$3) \quad \text{NCM Constraints (7.7.16) on } \mathbf{F}_\alpha \text{ and } \mathbf{M}_\alpha$$

$$4) \quad F_{\alpha 1}^2 + F_{\alpha 2}^2 \leq \mu^2 F_{\alpha 3}^2$$

(Instead, these approximate constraints can be used which are linear functions of \mathbf{F}_α and \mathbf{M}_α :
 $-\mu F_{\alpha 3} \leq F_{\alpha 1} \leq \mu F_{\alpha 3} \quad \text{and} \quad -\mu F_{\alpha 3} \leq F_{\alpha 2} \leq \mu F_{\alpha 3}$)

$$5) \quad -\mu R_\alpha F_{\alpha 3} \leq M'_{\alpha 3} \leq \mu R_\alpha F_{\alpha 3}$$

(Instead, these approximate constraints can be used which are linear functions of \mathbf{F}_α and \mathbf{M}_α :
 constraint (7.8.8): $-\mu \|\mathbf{E}_{\alpha i} - \mathbf{p}_\alpha\| F_{\alpha 3} \leq M_{\alpha 3} \leq \mu \|\mathbf{E}_{\alpha i} - \mathbf{p}_\alpha\| F_{\alpha 3}$)

In the above formulation, it is good to note that the NCM constraints are also linear constraints in the components of \mathbf{F}_α and \mathbf{M}_α . Therefore, one can use the simplex method to solve a general case of this problem.

If we assume that the robot has only 1 contact area and that contact area is horizontal (on the ground), the above method will yield a criterion for the margin of tipping stability similar to the ZMP method. Here, for example we maximize $(\mathbf{M}_{\text{ige}})_x$. Without loss of generality we can locate the global origin at the point of application of \mathbf{F}_1 and \mathbf{M}_1 ($\mathbf{p} = \mathbf{0}$):

$$\begin{aligned} & \text{Maximize } (\mathbf{M}_{\text{ige}})_x = -M_{1x} && \text{Subject to :} \\ 1) & \quad -\mathbf{F}_{\text{ige}} = \mathbf{F} = \text{Constant} && \Rightarrow \quad (\mathbf{F}_{\text{ige}})_y = F_y = \text{Constant} \\ 2) & \quad -(\mathbf{M}_{\text{ige}})_z = M_{1z} = \text{Constant} && \quad -(\mathbf{M}_{\text{ige}})_y = M_{1y} = \text{Constant} \\ 3) & \quad (v_{1z}, v_{1x}) = \left(-\frac{M_{1x}}{F_y}, \frac{M_{1z}}{F_y} \right) && \text{should be in the convex hull of contact area } \Upsilon_1 \text{ and } F_y \geq 0 \\ 4) & \quad F_{1z}^2 + F_{1x}^2 \leq \mu^2 F_{1y}^2 && \text{(Has no effect on the solution)} \end{aligned}$$

The above problem turns into:

$$\begin{aligned} & \text{Maximize } (v_{1z}) && \text{Subject to :} \\ 1) & \quad v_{1x} = \text{Constant} && 2) (v_{1z}, v_{1x}) \text{ should be in the convex hull } \Upsilon_1 \text{ of contact area} \end{aligned}$$

which is the same as finding the distance of the ZMP to the edges of the convex hull in the z direction (ZMP stability margins).

- Margins of Slipping Stability

Margins of slipping stability $\Delta^+(\mathbf{F}_{\text{ige}})_z, \Delta^-(\mathbf{F}_{\text{ige}})_z, \Delta^+(\mathbf{F}_{\text{ige}})_x, \Delta^-(\mathbf{F}_{\text{ige}})_x$ and $\Delta^+(\mathbf{M}_{\text{ige}})_y, \Delta^-(\mathbf{M}_{\text{ige}})_y$ can be found by maximizing or minimizing $(\mathbf{F}_{\text{ige}})_z, (\mathbf{F}_{\text{ige}})_x$ and $(\mathbf{M}_{\text{ige}})_y$ and subtracting them from their actual values, considering all \mathbf{F}_α and \mathbf{M}_α (contact forces and moments on contact areas) as design variables and the below constraints:

$$1) \quad -\mathbf{F}_{\text{ige}} = \sum \mathbf{F}_\alpha$$

(Remove $(\mathbf{F}_{\text{ige}})_z$ or $(\mathbf{F}_{\text{ige}})_x$ equation if you are maximizing or minimizing any of them)

$$2) \quad -\mathbf{M}_{\text{ige}} = \sum \mathbf{M}_\alpha + \sum \mathbf{p}_\alpha \times \mathbf{F}_\alpha$$

(Remove $(\mathbf{M}_{\text{ige}})_y$ equation if you are maximizing or minimizing it)

3) NCM Constraints (7.7.16) on \mathbf{F}_α and \mathbf{M}_α

$$4) \quad F_{\alpha 1}^2 + F_{\alpha 2}^2 \leq \mu^2 F_{\alpha 3}^2$$

(Instead, these approximate constraints can be used which are linear functions of \mathbf{F}_α and \mathbf{M}_α :

$$-\mu F_{\alpha 3} \leq F_{\alpha 1} \leq \mu F_{\alpha 3} \quad \text{and} \quad -\mu F_{\alpha 3} \leq F_{\alpha 2} \leq \mu F_{\alpha 3}$$

$$5) \quad -\mu R_\alpha F_{\alpha 3} \leq M'_{\alpha 3} \leq \mu R_\alpha F_{\alpha 3}$$

(Instead, these approximate constraints can be used which are linear functions of \mathbf{F}_α and \mathbf{M}_α :
 constraint (7.8.8):
$$-\mu \|\mathbf{E}_{\alpha i} - \mathbf{p}_\alpha\| F_{\alpha 3} \leq M_{\alpha 3} \leq \mu \|\mathbf{E}_{\alpha i} - \mathbf{p}_\alpha\| F_{\alpha 3}$$

In the above formulation, it is good to note that the NCM constraints are also linear constraints in the components of \mathbf{F}_α and \mathbf{M}_α . Therefore, one can use the simplex method to solve a general case of this problem.

10.7 Summary and Conclusion

The general NCM and friction constraints introduced in Chapter 7 play a critical role in the definition of stability concepts in this chapter. Based on these, we defined margins of tipping and slipping stabilities which are applicable for the most general cases of contact areas and are usable for both real problems such as in robot control or in simulations. We showed that the problem of finding the margins of tipping or slipping stability for the most general cases of contact areas turns into solving a linear optimization problem.

As was noted before, the ZMP stability criteria and margins are not applicable for problems in which the system's contact areas with the environment are non-coplanar. As it was shown in this chapter, the NCM stability concepts are applicable for systems with any number of contact areas with the environment, oriented arbitrarily with respect to each other (contact areas which are coplanar, non-coplanar, horizontal, inclined, parallel or non-parallel).

CHAPTER 11

GENERALIZATION OF ZMP CONSTRAINT USING NCM CONCEPTS

11.1 Introduction

In Chapter 7, we presented a general set of constraints on the equivalent reaction forces and moments (the NCM and the coulomb friction constraints). The NCM constraints are the real reasons behind the conventional ZMP constraint as proved in Theorem 8.1. The conventional ZMP constraint is only applicable when the contact areas of the dynamic system with the environment are coplanar. In this chapter, we generalize the conventional ZMP constraint so that it can apply to the most general cases when we have non-coplanar contact areas which are horizontal or inclined and parallel or non-parallel. However, in the general case of contact areas, it will be observed that besides the NCM constraints, the coulomb friction constraints also affect the ZMP constraint. The results obtained in this chapter will be specially useful for the simulation of motion tasks such as stairs climbing or uneven terrain locomotion or when the robot or the digital human leans against a wall.

11.2. Motivation for the Generalization of ZMP Constraint

It is essential for robots to move around the conventional human-centered environments that include stairs as a major terrain. But, the conventional ZMP concepts are only applicable in the cases where all contact areas are on the same plane. There has been constant research to generalize the ZMP concepts for both parallel or non-parallel

contact areas on different planes. However, as previously seen in Chapter 3, an exact, general method is still lacking to check the possibility or find the margins of stability of a dynamic motion in the general cases of contact surfaces.

NCM constraints defined in Definition 7.2 are the real theoretical reasons behind the ZMP constraint (they require the ZMP constraint to hold as a partial result). ZMP constraint expresses the natural limits on the net moment of all forces, except contact forces (which are the inertial, gravitational and external (IGE) forces). Dynamic equilibrium equations indicate that the net moment of contact forces should cancel the net moment of all other (IGE) forces. Therefore, natural limitations on the contact forces and moments (NCM constraints) will impose constraints on all other forces and moments (ZMP constraints). So, it is in fact because of the physical limitations on contact forces and moments that the ZMP constraint holds true. For example, consider a case where one of the contact areas of a walking robot can exert unlimited range of contact forces and moments on the robot (for example one of its feet is strongly glued to the ground at its moment of contact with the ground), then there will be no need for the ZMP constraint because in such a case, the possible net moment of IGE forces can have any arbitrary value and is unlimited. Therefore, this chapter offers a more in-depth look into the theoretical backgrounds for the ZMP constraints. Also, in this chapter, we use the NCM and the coulomb friction constraints to generalize the conventional ZMP constraint so that it can apply to cases when we have contact areas on different (either parallel or non-parallel) planes. In problems where the ground reaction forces and moments on individual contact areas are not calculated, it may still be preferred to use ZMP constraint

instead of NCM constraints. This generalization of ZMP constraint will benefit such problems where a robot should walk up the stairs or when a robot uses its hand to lean on the wall with its feet on the ground.

11.3. Overview of the Chapter

Section 11.4 presents the general formula to obtain constraints on the net of IGE (inertial, gravitational, external) forces and moments by using the NCM constraints. In the special case when all contact areas are on a same plane, the formula turns into the conventional ZMP constraint. In a system with the most general case of contact areas, the equations given in that section need to be solved to see if a given motion (the IGE forces and moments) are possible or not in the real world.

Section 11.5 simplifies the general formula in Section 11.4 and obtain closed form ZMP constraints by defining the ZMP constraint in two different ways for the general case of contact areas (Form I versus Form II ZMP-Like constraints).

Conventional ZMP constraint checks the possibility of IGE moments about the two horizontal axes and does not care about the moment about the vertical axis. For the general case of contact areas, all the axes become significant. Therefore, it is possible to define ZMP constraints in either 2D or 3D, for them.

Section 11.6 offers formulas for the 2D ZMP-like constraints for systems with non-coplanar but parallel contact areas.

11.4. Possibility of IGE Forces and Moments in the Real World in the Most General Case of Contact Areas

Based on the discussion in Section 8.6.1, in some problems (where GRF on individual contact areas are not calculated), it may still be preferred to use ZMP constraint. In those problems, the role of ZMP constraint is to limit the two horizontal components of \mathbf{M}_{ige} (ZMP being inside the convex hull Υ_{Total}) such that in the next step it will be possible to find unilateral reaction forces and moments on contact areas Γ_a to cancel them.

As indicated before, NCM constraints are applicable for non-coplanar contact areas (either horizontal or inclined or parallel or non-parallel) while ZMP constraint is applicable only if all contact areas are on a same plane. But, the real reasons behind the limits on \mathbf{M}_{ige} (ZMP constraint) arise from the NCM constraints (non-adhesiveness of contact areas). The theoretical basis of ZMP constraint can be derived from NCM constraints as shown in Theorem 8.1. Therefore it is possible to develop constraints on \mathbf{F}_{ige} and \mathbf{M}_{ige} (similar to ZMP) for cases where NCM constraints apply but the ZMP constraint does not apply (non-coplanar contact areas). This will be helpful in problems in which GRF on individual contact areas are not calculated as indicated in the previous paragraph.

In the most general case of contact areas (either horizontal or inclined or parallel or non-parallel or co-planar or non-coplanar), the following system of equations needs to be solved to check whether a specific \mathbf{F}_{ige} and \mathbf{M}_{ige} (the net force and moment of IGE forces at the global origin point) for a dynamic system are possible in the real world:

Given \mathbf{F}_{ige} and \mathbf{M}_{ige} , find \mathbf{F}_α and \mathbf{M}_α for each contact area ($\alpha = 1 \dots n$), such that :

$$\begin{aligned}
 1) \quad & -\mathbf{F}_{ige} = \sum \mathbf{F}_\alpha \\
 2) \quad & -\mathbf{M}_{ige} = \sum \mathbf{M}_\alpha + \sum \mathbf{p}_\alpha \times \mathbf{F}_\alpha \\
 3) \quad & \text{NCM Constraints (7.7.16) on } \mathbf{F}_\alpha \text{ and } \mathbf{M}_\alpha \\
 4) \quad & F_{\alpha 1}^2 + F_{\alpha 2}^2 \leq \mu^2 F_{\alpha 3}^2 \\
 5) \quad & -\mu R_\alpha F_{\alpha 3} \leq M'_{\alpha 3} \leq \mu R_\alpha F_{\alpha 3}
 \end{aligned} \tag{11.4.1}$$

In the above system of equations, the unknowns are \mathbf{F}_α and \mathbf{M}_α for each contact area. This system of equations needs to be solved. If a solution exists for \mathbf{F}_α and \mathbf{M}_α , then the \mathbf{F}_{ige} and \mathbf{M}_{ige} in question are possible for the dynamic system in the real world. The above problem is actually directly borrowed from Section 10.4. In that section, we found the margins of stability by maximizing or minimizing some components of \mathbf{F}_{ige} and \mathbf{M}_{ige} . Here, we just check the possibility of a given \mathbf{F}_{ige} and \mathbf{M}_{ige} in the real world. As an approximation, we replace items (4) and (5) in Equations (11.4.1) by simpler constraints which are linear functions of \mathbf{F}_α and \mathbf{M}_α :

Given \mathbf{F}_{ige} and \mathbf{M}_{ige} , find \mathbf{F}_α and \mathbf{M}_α for each contact area ($\alpha = 1 \dots n$), such that :

$$\begin{aligned}
 1) \quad & -\mathbf{F}_{ige} = \sum \mathbf{F}_\alpha \\
 2) \quad & -\mathbf{M}_{ige} = \sum \mathbf{M}_\alpha + \sum \mathbf{p}_\alpha \times \mathbf{F}_\alpha \\
 3) \quad & \text{NCM Constraints (7.7.16) on } \mathbf{F}_\alpha \text{ and } \mathbf{M}_\alpha \\
 4) \quad & -\mu F_{\alpha 3} \leq F_{\alpha 1} \leq \mu F_{\alpha 3} \quad \text{and} \quad -\mu F_{\alpha 3} \leq F_{\alpha 2} \leq \mu F_{\alpha 3} \\
 5) \quad & -\mu \|\mathbf{E}_{\alpha i} - \mathbf{p}_\alpha\| F_{\alpha 3} \leq M_{\alpha 3} \leq \mu \|\mathbf{E}_{\alpha i} - \mathbf{p}_\alpha\| F_{\alpha 3} \quad (\text{constraint (7.8.8)})
 \end{aligned} \tag{11.4.2}$$

In the above formulation, it is good to note that the NCM constraints (7.7.16) are also linear in the components of \mathbf{F}_α and \mathbf{M}_α . So, one can check the possibility of a set

of \mathbf{F}_{ige} and \mathbf{M}_{ige} for a dynamic system in the real world by checking whether there exists a solution for this linear system of equations. This should take a very short time and therefore, this check can be done at each iteration in a larger nonlinear optimization problem.

In this section, we have presented the most general method for checking the satisfaction or violation of the ZMP constraint. That is, in the most general cases of contact areas, for each case, the system of equations given in (11.4.1) or the approximate linear forms in (11.4.2) needs to be solved to see if the \mathbf{F}_{ige} and \mathbf{M}_{ige} in question are possible in the real world or not. Finding closed form solutions for these problems is a mathematical problem of finding the boundaries of vector functions subject to equality and inequality constraints. In the literature, the most related field of research that investigates such a problem is the field of “Finding the boundaries of workspace for robots”. Examples of papers in this field can be seen in Haug (1996), Abdel-Malek (1999), Hariri (2005).

In the rest of this chapter, we will find closed form solutions (find ZMP constraints) for special cases of these problems. These special cases include cases where contact areas are not coplanar, but are parallel, such as in stairs climbing or almost parallel, such as in locomotion over uneven terrains.

11.5. Using NCM Constraints to Generalize the ZMP Constraint

In this section, we try to simplify the general problem proposed in Section 11.4. In subsequent sections, we will use this simplified problem in order to find allowable ranges of \mathbf{F}_{ige} and \mathbf{M}_{ige} for which solutions for \mathbf{F}_α and \mathbf{M}_α exist. In other words, we try to use NCM constraints and friction constraints for all the contact areas and develop ZMP-Like constraints for general cases. By ZMP-Like constraints, we mean constraints that specify the possible ranges for \mathbf{F}_{ige} and \mathbf{M}_{ige} in contrast to NCM constraints which specify possible ranges for individual contact forces and moments.

Consider the general problem of several inclined and non-coplanar contact areas in Figure 11.1. This figure is a more detailed version of Figure 7.1 in Chapter 7. However, in Figure 11.1 and in the rest of this chapter, we choose the location of \mathbf{F}_α and \mathbf{M}_α for each contact area to coincide with the NCM point location for that contact area. This will not decrease the generality of the solutions obtained for IGE forces and moments and so for the ZMP-Like constraints; but it will simplify the equations for \mathbf{F}_{ige} and \mathbf{M}_{ige} . Therefore, in the rest of this chapter, and wherever the locations of \mathbf{F}_α and \mathbf{M}_α are chosen at the NCM point, \mathbf{F}_α and \mathbf{M}_α are in fact the NCM force systems for those contact area and we shall have: $\mathbf{M}_\alpha = \mathbf{M}'_\alpha$. In Figure 11.1 consider the local frame $\mathbf{e}_{a1}, \mathbf{e}_{a2}, \mathbf{e}_{a3}$ corresponding to contact area Γ_α (similar to Figure 7.1). Denote the global location of the origin of that local frame by \mathbf{o}_α . Denote the local position of the NCM point in that local frame by \mathbf{v}_α and its global location by \mathbf{w}_α . The global dynamic equilibrium equation about origin is:

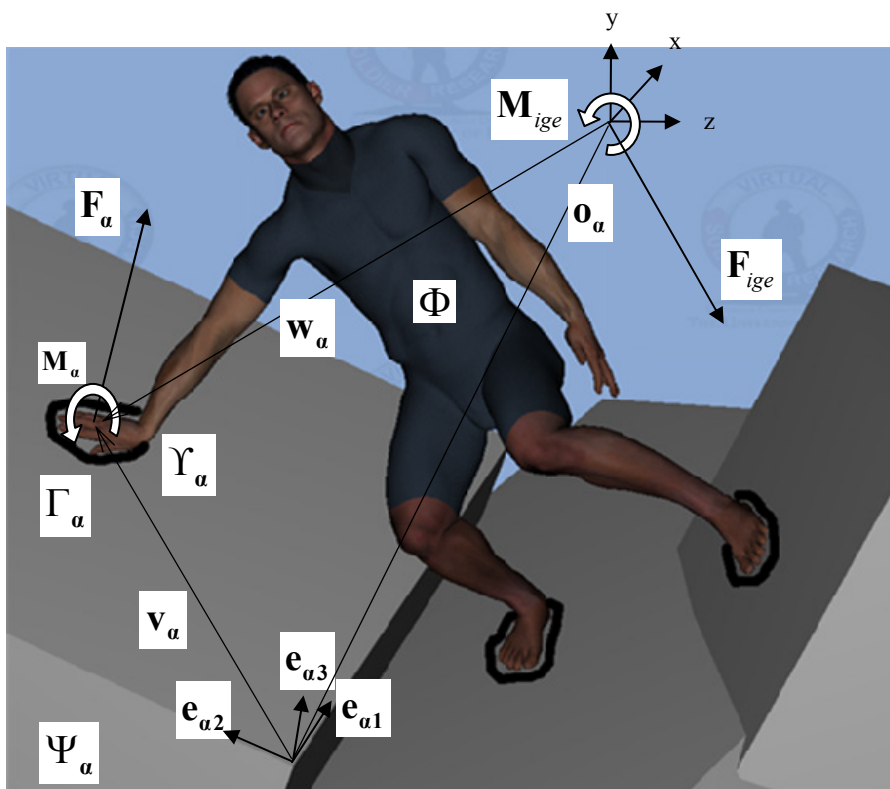


Figure 11.1. A schematic of the general problem

$$\sum \mathbf{F} = \mathbf{0} \quad \Rightarrow \quad \mathbf{F}_{ige} + \sum \mathbf{F}_a = \mathbf{0} \quad \Rightarrow \quad \mathbf{F}_{ige} = -\sum \mathbf{F}_a \quad (11.5.1)$$

$$\begin{aligned} \sum \mathbf{M} = \mathbf{0} &\Rightarrow \mathbf{M}_{ige} + \sum \mathbf{M}_a + \sum \mathbf{w}_a \times \mathbf{F}_a = \mathbf{0} \\ &\Rightarrow \mathbf{M}_{ige} = -\sum \mathbf{M}_a - \sum (\mathbf{o}_a + \mathbf{v}_a) \times \mathbf{F}_a \end{aligned} \quad (11.5.2)$$

Let us consider the following definitions:

$$\begin{aligned} F_{\alpha 1} &\triangleq \mathbf{F}_a \cdot \mathbf{e}_{a1} & F_{\alpha 2} &\triangleq \mathbf{F}_a \cdot \mathbf{e}_{a2} & F_{\alpha 3} &\triangleq \mathbf{F}_a \cdot \mathbf{e}_{a3} \\ F_{\alpha z} &\triangleq \mathbf{F}_a \cdot \mathbf{k} & F_{\alpha x} &\triangleq \mathbf{F}_a \cdot \mathbf{i} & F_{\alpha y} &\triangleq \mathbf{F}_a \cdot \mathbf{j} \\ M_{\alpha 1} &\triangleq \mathbf{M}_a \cdot \mathbf{e}_{a1} = 0 & M_{\alpha 2} &\triangleq \mathbf{M}_a \cdot \mathbf{e}_{a2} = 0 & M_{\alpha 3} &\triangleq \mathbf{M}_a \cdot \mathbf{e}_{a3} \\ M_{\alpha z} &\triangleq \mathbf{M}_a \cdot \mathbf{k} & M_{\alpha x} &\triangleq \mathbf{M}_a \cdot \mathbf{i} & M_{\alpha y} &\triangleq \mathbf{M}_a \cdot \mathbf{j} \end{aligned} \quad (11.5.3)$$

The constraints on forces and moments due to the non-adhesiveness of each convex hull Υ_a are:

$$\text{NCM Constraints (7.7.16)} \begin{cases} F_{\alpha 3} > 0 \\ \mathbf{v}_a \text{ inside } \Upsilon_a \end{cases} \quad (11.5.4)$$

$$\begin{aligned} \text{Friction Constraints (7.8.1) and (7.8.6)} & \begin{cases} \frac{F_{\alpha 1}^2 + F_{\alpha 2}^2}{F_{\alpha 3}^2} < \mu^2 \\ -\mu R_\alpha < \frac{M'_{\alpha 3}}{F_{\alpha 3}} < \mu R_\alpha \end{cases} \\ \Rightarrow \text{Friction Constraints} & \begin{cases} 0 < f_\alpha < 1 \\ -1 < m_\alpha < 1 \end{cases} \end{aligned} \quad (11.5.5)$$

: Lets define

$$\begin{cases} f_\alpha \triangleq \frac{1}{\mu} \sqrt{\frac{F_{\alpha 1}^2 + F_{\alpha 2}^2}{F_{\alpha 3}^2}} \\ m_\alpha \triangleq \frac{M_{\alpha 3}}{\mu R_\alpha F_{\alpha 3}} = \frac{M'_{\alpha 3}}{\mu R_\alpha F_{\alpha 3}} \end{cases}$$

Let us also consider the following set of definitions:

$$\begin{cases} \mathbf{e}_{af} \triangleq \sqrt{\frac{F_{\alpha 3}^2}{F_{\alpha 1}^2 + F_{\alpha 2}^2}} \left(\frac{F_{\alpha 1}}{F_{\alpha 3}} \mathbf{e}_{a1} + \frac{F_{\alpha 2}}{F_{\alpha 3}} \mathbf{e}_{a2} \right) = \frac{1}{f_\alpha \mu} \left(\frac{F_{\alpha 1}}{F_{\alpha 3}} \mathbf{e}_{a1} + \frac{F_{\alpha 2}}{F_{\alpha 3}} \mathbf{e}_{a2} \right) \\ \text{Define } 0 < \theta_\alpha < 2\pi \text{ such that: } \mathbf{e}_{af} \triangleq \text{Cos}(\theta_\alpha) \mathbf{e}_{a1} + \text{Sin}(\theta_\alpha) \mathbf{e}_{a2} \\ r_\alpha \triangleq \frac{F_{\alpha 3}}{\sum F_{\alpha 3}}, \quad \mathfrak{I}_1 \triangleq \frac{\mathbf{F}_{ige} \cdot \mathbf{e}_1}{\mathbf{F}_{ige} \cdot \mathbf{e}_3}, \quad \mathfrak{I}_2 \triangleq \frac{\mathbf{F}_{ige} \cdot \mathbf{e}_2}{\mathbf{F}_{ige} \cdot \mathbf{e}_3} \text{ for any coordinate frame } (\mathbf{e}_1, \mathbf{e}_2, \mathbf{e}_3) \end{cases} \quad (11.5.6)$$

Then:

$$\begin{aligned} \mathbf{M}_{ige} &= -\sum \mathbf{M}_a - \sum (\mathbf{o}_a + \mathbf{v}_a) \times \mathbf{F}_a \\ \Rightarrow \mathbf{M}_{ige} &= -\sum F_{\alpha 3} \left(\frac{M_{\alpha 3}}{F_{\alpha 3}} \mathbf{e}_{a3} + (\mathbf{o}_a + \mathbf{v}_a) \times \left(\sqrt{\frac{F_{\alpha 1}^2 + F_{\alpha 2}^2}{F_{\alpha 3}^2}} \mathbf{e}_{af} + \mathbf{e}_{a3} \right) \right) \\ \Rightarrow \mathbf{M}_{ige} &= -\sum F_{\alpha 3} \left(m_\alpha \mu R_\alpha \mathbf{e}_{a3} + (\mathbf{o}_a + \mathbf{v}_a) \times (f_\alpha \mu \mathbf{e}_{af} + \mathbf{e}_{a3}) \right) \end{aligned} \quad (11.5.7)$$

Considering (11.5.1), (11.5.4), (11.5.5), (11.5.6) and (11.5.7), we define two different forms for the ZMP-Like constraint problem as shown below:

A general ZMP – Like Constraint should directly or indirectly:

Form I)

Specify the Range of Feasible Values for the Vector Function \mathbf{M}_{ige} :

$$\mathbf{M}_{ige} = -\sum F_{\alpha 3} (m_{\alpha} \mu R_{\alpha} \mathbf{e}_{\alpha 3} + (\mathbf{o}_{\alpha} + \mathbf{v}_{\alpha}) \times (f_{\alpha} \mu \mathbf{e}_{\alpha f} + \mathbf{e}_{\alpha 3})) \quad (11.5.8)$$

For all feasible values of $\mathfrak{S}_1, \mathfrak{S}_2$

Form II)

Specify the Range of Feasible Values for the Vector Function \mathbf{M}_{ige} :

$$\mathbf{M}_{ige} = -\sum F_{\alpha 3} (m_{\alpha} \mu R_{\alpha} \mathbf{e}_{\alpha 3} + (\mathbf{o}_{\alpha} + \mathbf{v}_{\alpha}) \times (f_{\alpha} \mu \mathbf{e}_{\alpha f} + \mathbf{e}_{\alpha 3})) \quad (11.5.9)$$

For a specific value of $\mathfrak{S}_1, \mathfrak{S}_2$

The design variables for both Form I and Form II are \mathbf{F}_{α} and \mathbf{M}_{α} according to the original form of the problem in Equations (11.4.1) or variables that depend on \mathbf{F}_{α} and \mathbf{M}_{α} as will be seen in next sections. Also, the allowable ranges for \mathbf{M}_{ige} in both forms should be found subject to the following constraints:

$$\begin{cases} \mathbf{F}_{ige} = -\sum \mathbf{F}_{\alpha} & (11.5.10a) \\ F_{\alpha 3} > 0 & (11.5.10b) \\ v_{\alpha 3} = 0 \text{ and } (v_{\alpha 1}, v_{\alpha 2}) \text{ inside } Y_{\alpha} & (11.5.10.c) \\ 0 < f_{\alpha} < 1 & (11.5.10d) \\ -1 < m_{\alpha} < 1 & (11.5.10e) \end{cases} \quad (11.5.10)$$

Finding a solution to Form I is equal to finding a solution to Form II by ignoring constraint (11.5.10a). Therefore, it is always easier to find a solution for Form I compared to Form II. Also, note that in the conventional ZMP constraint, we actually find ranges for $\mathbf{M}_{ige} \cdot \mathbf{k}$ and $\mathbf{M}_{ige} \cdot \mathbf{i}$ (considering $(\mathbf{k}, \mathbf{i}, \mathbf{j})$ as $(\mathbf{e}_1, \mathbf{e}_2, \mathbf{e}_3)$). In that problem the solutions to Form I and Form II will be the same and equal to the solution of the conventional ZMP problem. Because in such a case, the constraint will be independent of the values for \mathfrak{S}_1 and \mathfrak{S}_2 . That is because all contact areas are on a same plane in a conventional ZMP problem and the frictional forces produce no moment about z or x axes. Unfortunately, this is only true for the conventional ZMP problem. But in any case, it is obvious that the solution to Form I will be the union of all possible solutions to Form II for all possible values of \mathbf{F}_{ige} . We will discuss the importance of solving both Form I and Form II in each of the next sections separately.

11.6. The 2D ZMP-Like Constraint for the Case of Non-Coplanar but Parallel Contact Areas

In the case of several non-coplanar, but parallel contact areas, the problem is easier to solve. So, we consider this case first. In this case, because all the planes are parallel, without any loss of generality, we can assume that all the 3 axes of all the local coordinate frames are parallel. We also define an additional reference frame $\mathbf{e}_1, \mathbf{e}_2, \mathbf{e}_3$ with its origin coinciding with the origin of the global coordinate frame. Its unit vectors are parallel to those of all the local coordinate frames. Therefore, we have

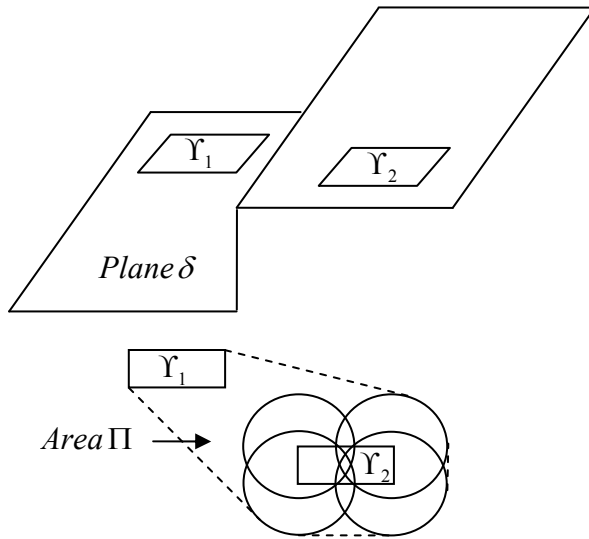
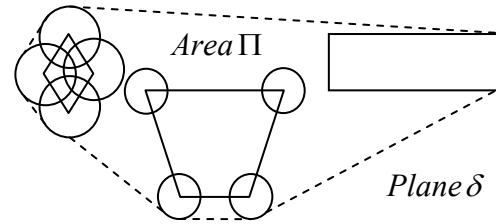
$\mathbf{e}_1 = \mathbf{e}_{\alpha 1}, \mathbf{e}_2 = \mathbf{e}_{\alpha 2}, \mathbf{e}_3 = \mathbf{e}_{\alpha 3}$ for all values of α . We also define a plane δ that passes through the global origin with the unit vector \mathbf{e}_3 perpendicular to it. We define the ZMP as a point on plane δ where the moments about planar axes $\mathbf{e}_1, \mathbf{e}_2$ are zero. We first find the “*Form I, ZMP-Like Constraint*” for this case. In this form, the allowable locations of the ZMP denoted by \mathbf{z} will be restricted by the following equation: (for simplicity of explanations in this problem, without loss of generality, assume local origins are located in positions such that $\mathbf{o}_a = o_{\alpha 3} \mathbf{e}_3 \Rightarrow o_{\alpha 1} = o_{\alpha 2} = 0$)

$$\begin{aligned}
\mathbf{M}_{ige}^{zmp} &= \mathbf{M}_{ige} - \mathbf{z} \times \mathbf{F}_{ige} = -\sum F_{\alpha 3} (m_{\alpha} \mu R_{\alpha} \mathbf{e}_{\alpha 3} + (\mathbf{o}_a + \mathbf{v}_a) \times (f_{\alpha} \mu \mathbf{e}_{af} + \mathbf{e}_{\alpha 3})) + \mathbf{z} \times \sum \mathbf{F}_a \\
\Rightarrow \underbrace{\mathbf{M}_{ige}^{zmp} \times \mathbf{e}_3}_0 &= -\sum F_{\alpha 3} (m_{\alpha} \mu R_{\alpha} \mathbf{e}_3 + (\mathbf{o}_a + \mathbf{v}_a) \times (f_{\alpha} \mu \mathbf{e}_{af} + \mathbf{e}_3)) \times \mathbf{e}_3 + \mathbf{z} \times \sum \mathbf{F}_a \times \mathbf{e}_3 \\
\Rightarrow \sum F_{\alpha 3} &(((\mathbf{o}_a + \mathbf{v}_a) \cdot \mathbf{e}_3)(f_{\alpha} \mu \mathbf{e}_{af} + \mathbf{e}_3) - (\mathbf{e}_3 \cdot (f_{\alpha} \mu \mathbf{e}_{af} + \mathbf{e}_3))(\mathbf{o}_a + \mathbf{v}_a)) \\
&\quad - [(\mathbf{e}_3 \cdot \mathbf{z}) \sum \mathbf{F}_a - (\mathbf{e}_3 \cdot \sum \mathbf{F}_a) \mathbf{z}] = 0 \\
\Rightarrow \sum F_{\alpha 3} &((o_{\alpha 3})(f_{\alpha} \mu \mathbf{e}_{af} + \mathbf{e}_3) - o_{\alpha 3} \mathbf{e}_3 - \mathbf{v}_a) - \left[\underbrace{(\mathbf{e}_3 \cdot \mathbf{z})}_{0} \sum \mathbf{F}_a - \underbrace{(\mathbf{e}_3 \cdot \sum \mathbf{F}_a)}_{\sum F_{\alpha 3}} \mathbf{z} \right] = 0 \\
\Rightarrow \mathbf{z} &= \frac{\sum F_{\alpha 3} (\mathbf{v}_a - o_{\alpha 3} \mu (f_{\alpha} \mathbf{e}_{af}))}{\sum F_{\alpha 3}} \tag{11.6.1}
\end{aligned}$$

As indicated before, to find a solution for the “*Form I, ZMP-Like Constraint*” (all possible values of \mathbf{F}_{ige}), we just need to ignore constraint (11.5.10a). Considering (11.5.10c), (11.5.10d) and (11.5.10e), the locus of \mathbf{v}_a is equal to Υ_a (according to the NCM constraints). The locus of $o_{\alpha 3} \mu (f_{\alpha} \mathbf{e}_{af})$ is achieved by sweeping f_{α} and \mathbf{e}_{af} in

their allowable ranges which is a disc of radius $o_{\alpha 3}\mu$. Therefore, the locus of $\mathbf{v}_a - o_{\alpha 3}\mu(f_\alpha \mathbf{e}_{af})$ in the global coordinate frame is the projection on plane δ of the swept area of a disc of radius $o_{\alpha 3}\mu$ on Υ_a while the center of the disc covers all the points inside the convex hull Υ_a . Therefore, the locus of $\mathbf{v}_a - o_{\alpha 3}\mu(f_\alpha \mathbf{e}_{af})$ is the convex hull of Γ_a with discs of radii $o_{\alpha 3}\mu$ located at all of its corners. \mathbf{z} according to Equation (11.6.1) is the locus of all possible weighted averages of $\mathbf{v}_a - o_{\alpha 3}\mu(f_\alpha \mathbf{e}_{af})$. Therefore, according to Lemma 8.1, the locus of \mathbf{z} is exactly the collection of all the points inside the convex hull of all the projections of contact areas Γ_a on plane δ with each contact area including a disk on each of its corners of radius $o_{\alpha 3}\mu$. We call such a convex hull by the name Area Π .

An approximate shape of Area Π is shown in Figure 11.2 for a stairs climbing case with two rectangular contact areas (two feet) and horizontal stairs. A value $\mu = 0.5$ and other relative sizes in the figure are used for deciding the radius of the disks that are drawn in the Figure 11.2. The coefficient of friction of shoe with the ground has been reported to range from 0.3 to 2 with 0.6 for a cinder track and 1.5 for grass (Jenkins, 2005). Therefore, the sizes of such disks are normally relatively large compared to the original sizes of contact areas. The exact calculated sizes for Area Π will be shown later in Figures 11.6, 11.7, 11.8, 11.10 for their corresponding problems. Figure 11.3 shows a shape of Area Π for the case of a robot having 3 arbitrary contact areas, one on plane δ and the other two at arbitrary heights (having non-zero values of $o_{\alpha 3}$).

Figure 11.2. Area Π for a stair climbing caseFigure 11.3. Area Π for 3 arbitrary contact

Definition 11.1: **Form I, 2D, ZMP-Like Constraint for Parallel Contact Areas**

For a dynamic system that has parallel contact areas with the environment, the Form I, 2D ZMP-Like constraint states that the following two statements are equivalent:

- 1- There exist possible values of $\mathfrak{S}_1, \mathfrak{S}_2$ for which the values for $\mathbf{M}_{ige} \cdot \mathbf{e}_1$ and $\mathbf{M}_{ige} \cdot \mathbf{e}_2$ are possible in the real world.
- 2- The ZMP is inside Area Π

We will compare the significance of the Form I and Form II ZMP-Like constraints at the end of this section.

Now, we try to find the “*Form II, ZMP-Like constraint*”. Starting from Equation (11.6.1), we need to consider the constraint set (11.5.10) in order to find the allowable locations of the ZMP \mathbf{z} . In this work, we only find the “*Form II, ZMP-Like constraint*” for the case of 2 contact areas and leave more general cases for future research. In such a case, Equation (11.6.1) along with constraints (11.5.10) are:

$$\text{Find the area swept by } \mathbf{z} = \frac{\sum F_{\alpha 3} (\mathbf{v}_{\alpha} - o_{\alpha 3} \mu (f_{\alpha} \mathbf{e}_{\alpha f}))}{\sum F_{\alpha 3}} \quad (11.6.2)$$

$$\text{Subject to } \left. \begin{array}{l} \mathbf{F}_{ige} = -\sum \mathbf{F}_{\alpha} \quad (11.6.3a) \\ F_{\alpha 3} > 0 \quad (11.6.3b) \\ 0 < f_{\alpha} < 1 \quad (11.6.3c) \\ v_{\alpha 3} = 0 \text{ and } (v_{\alpha 1}, v_{\alpha 2}) \text{ inside } Y_{\alpha} \quad (11.6.3d) \end{array} \right\} (11.6.3)$$

Therefore:

$$\begin{aligned} (11.6.3) \quad & \stackrel{(11.5.11)}{\Rightarrow} \mathbf{z} = \sum r_{\alpha} \mathbf{v}_{\alpha} - \sum r_{\alpha} o_{\alpha 3} \mu (f_{\alpha} \mathbf{e}_{\alpha f}) \\ \stackrel{(11.5.11)}{\Rightarrow} \mathbf{z} = \begin{Bmatrix} z_1 \\ z_2 \end{Bmatrix} = \begin{Bmatrix} \mathbf{z} \cdot \mathbf{e}_1 \\ \mathbf{z} \cdot \mathbf{e}_2 \end{Bmatrix} = \begin{Bmatrix} \sum r_{\alpha} v_{\alpha 1} - \sum o_{\alpha 3} \mu r_{\alpha} f_{\alpha} \cos(\theta_{\alpha}) \\ \sum r_{\alpha} v_{\alpha 2} - \sum o_{\alpha 3} \mu r_{\alpha} f_{\alpha} \sin(\theta_{\alpha}) \end{Bmatrix} \\ \Rightarrow \mathbf{z} = \mathbf{z}_v + \mathbf{z}_f \end{aligned} \quad (11.6.4)$$

$$\text{Where: } \mathbf{z}_v = \sum r_{\alpha} \mathbf{v}_{\alpha} = \begin{Bmatrix} \sum r_{\alpha} v_{\alpha 1} \\ \sum r_{\alpha} v_{\alpha 2} \end{Bmatrix} \quad \mathbf{z}_f = \begin{Bmatrix} -\sum o_{\alpha 3} \mu r_{\alpha} f_{\alpha} \cos(\theta_{\alpha}) \\ -\sum o_{\alpha 3} \mu r_{\alpha} f_{\alpha} \sin(\theta_{\alpha}) \end{Bmatrix}$$

$$\left. \begin{aligned}
(11.6.3a) \quad &\Rightarrow \mathbf{F}_{ige} = -\sum \mathbf{F}_a = -\sum F_{\alpha 1} \mathbf{e}_1 + F_{\alpha 2} \mathbf{e}_2 + F_{\alpha 3} \mathbf{e}_3 \\
(11.5.11) \quad &\Rightarrow \mathbf{F}_{ige} = -\sum F_{\alpha 3} (f_\alpha \mu \text{Cos}(\theta_\alpha) \mathbf{e}_1 + f_\alpha \mu \text{Sin}(\theta_\alpha) \mathbf{e}_2 + \mathbf{e}_3) \\
(11.5.11) \quad &\Rightarrow \left\{ \begin{aligned}
\mathfrak{F}_1 &= \frac{\mathbf{F}_{ige} \cdot \mathbf{e}_1}{\mathbf{F}_{ige} \cdot \mathbf{e}_3} = \frac{\sum F_{\alpha 3} f_\alpha \mu \text{Cos}(\theta_\alpha)}{\sum F_{\alpha 3}} = \sum \mu r_\alpha f_\alpha \text{Cos}(\theta_\alpha) \\
\mathfrak{F}_2 &= \frac{\mathbf{F}_{ige} \cdot \mathbf{e}_2}{\mathbf{F}_{ige} \cdot \mathbf{e}_3} = \frac{\sum F_{\alpha 3} f_\alpha \mu \text{Sin}(\theta_\alpha)}{\sum F_{\alpha 3}} = \sum \mu r_\alpha f_\alpha \text{Sin}(\theta_\alpha) \\
1 &= \sum r_\alpha
\end{aligned} \right\} (11.6.5) \\
0 &< r_\alpha < 1 \\
0 &< f_\alpha < 1 \\
v_{\alpha 3} &= 0 \quad \text{and } (v_{\alpha 1}, v_{\alpha 2}) \text{ inside } \Upsilon_\alpha
\end{aligned} \right\}$$

Therefore, the problem is simplified into:

$$\text{Find the area swept by} \quad \mathbf{z} = \mathbf{z}_v + \mathbf{z}_f \quad (11.6.6)$$

$$\text{Where:} \quad \mathbf{z}_v = \sum r_\alpha \mathbf{v}_a = \left\{ \begin{aligned} \sum r_\alpha v_{\alpha 1} \\ \sum r_\alpha v_{\alpha 2} \end{aligned} \right\} \quad \mathbf{z}_f = \left\{ \begin{aligned} -\sum o_{\alpha 3} \mu r_\alpha f_\alpha \text{Cos}(\theta_\alpha) \\ -\sum o_{\alpha 3} \mu r_\alpha f_\alpha \text{Sin}(\theta_\alpha) \end{aligned} \right\}$$

$$\text{Subject to} \left\{ \begin{aligned}
\sum \mu r_\alpha f_\alpha \text{Cos}(\theta_\alpha) &= \mathfrak{F}_1 \\
\sum \mu r_\alpha f_\alpha \text{Sin}(\theta_\alpha) &= \mathfrak{F}_2 \\
0 &< f_\alpha < 1 \\
\sum r_\alpha &= 1 \quad , \quad 0 < r_\alpha < 1 \\
v_{\alpha 3} &= 0 \quad \text{and } (v_{\alpha 1}, v_{\alpha 2}) \text{ inside } \Upsilon_\alpha
\end{aligned} \right\} \quad (11.6.7)$$

For two contact areas, without loss of generality, we can locate the global origin on the plane of convex hull Υ_1 ($o_{13} = 0$). Therefore, we have:

Find the area swept by $\mathbf{z} = \mathbf{z}_v + \mathbf{z}_f$ (11.6.8)

Where :

$$\mathbf{z}_v = \sum r_\alpha \mathbf{v}_\alpha = \begin{Bmatrix} r_1 v_{11} + r_2 v_{21} \\ r_1 v_{12} + r_2 v_{22} \end{Bmatrix} = \begin{Bmatrix} r_1 v_{11} + (1-r_1) v_{21} \\ r_1 v_{12} + (1-r_1) v_{22} \end{Bmatrix} \quad (11.6.9)$$

$$\mathbf{z}_f = \begin{Bmatrix} -o_{23} \mu r_2 f_2 \cos(\theta_2) \\ -o_{23} \mu r_2 f_2 \sin(\theta_2) \end{Bmatrix} = \begin{Bmatrix} -o_{23} \mu (1-r_1) f_2 \cos(\theta_2) \\ -o_{23} \mu (1-r_1) f_2 \sin(\theta_2) \end{Bmatrix} \quad (11.6.10)$$

$$\text{Subject to } \left. \begin{array}{l} \mu r_1 f_1 \cos(\theta_1) + \mu (1-r_1) f_2 \cos(\theta_2) = \mathfrak{Z}_1 \quad (11.6.11a) \\ \mu r_1 f_1 \sin(\theta_1) + \mu (1-r_1) f_2 \sin(\theta_2) = \mathfrak{Z}_2 \quad (11.6.11b) \\ 0 < f_1 < 1, \quad 0 < f_2 < 1, \quad 0 < r_1 < 1 \quad (11.6.11c) \\ (v_{11}, v_{12}) \text{ inside } \Upsilon_1, \quad (v_{21}, v_{22}) \text{ inside } \Upsilon_2 \quad (11.6.11d) \end{array} \right\} \quad (11.6.11)$$

In this problem, we find the area swept by \mathbf{z} for fixed values of \mathfrak{Z}_1 and \mathfrak{Z}_2 while r_1 changes between 0 and 1. Initially, let us find the area swept by \mathbf{z} for a fixed value of r_1 . In the next step, we shall sweep r_1 between 0 and 1 to find the total area swept by \mathbf{z} . Therefore, the variable parameters will be $f_1, f_2, (v_{11}, v_{12}), (v_{21}, v_{22})$. From the above equations, it is observed that \mathbf{z}_v only depends on $(v_{11}, v_{12}), (v_{21}, v_{22})$ and \mathbf{z}_f only depends on f_1, f_2 . Therefore, to find the total area swept by \mathbf{z} , we can find the areas swept by \mathbf{z}_v (denoted by Area Λ_v) and \mathbf{z}_f (denoted by Area Λ_f) separately and then add them by adding the location of each point of Area Λ_v to each point of Area Λ_f . This can be done by sweeping Area Λ_f over each point of Area Λ_v which shall be shown and discussed later. We first find the area swept by \mathbf{z}_v (denoted by Area Λ_v):

$$\text{Find the area swept by } \mathbf{z}_v = \begin{cases} r_1 v_{11} + (1-r_1) v_{21} \\ r_1 v_{12} + (1-r_1) v_{22} \end{cases} \quad (11.6.12)$$

$$\text{Subject to } \begin{cases} (v_{11}, v_{12}) \text{ inside } \Upsilon_1 & (11.6.13a) \\ (v_{21}, v_{22}) \text{ inside } \Upsilon_2 & (11.6.13b) \end{cases} \quad (11.6.13)$$

In fact, if we sweep r_1 from 0 to 1, the area swept by \mathbf{z}_v will be the convex hull of Γ_1 and Γ_2 . In a conventional ZMP problem, \mathbf{z}_r is equal to zero and this will be the area swept by \mathbf{z} (similarly, the conventional ZMP constraint states that the convex hull of the two contact areas is the allowable locations of the ZMP). But, in this more generalized problem, we need the area swept by \mathbf{z}_v for a fixed value of r_1 .

However, the problem indicated for finding Area Λ_v corresponding to a specific value of r_1 indicated by Equations (11.6.12) and (11.6.13) is exactly the same as the problem of finding Area Λ_{r_2} for a specific value of $r_2 = 1 - r_1$. In Section 8.4, it was proved that the Area Λ_{r_2} for a specific value of $r_2 = 1 - r_1$ can be found using the following procedure:

For two general polygons Υ_1 and Υ_2 , Λ_{r_2} can be found by the following procedure:

- 1- Consider (v_{11}, v_{12}) to be fixed on a corner E of polygon Υ_1 . Vary (v_{21}, v_{22}) on all corners of polygon Υ_2 and plot the locations of \mathbf{z}_v denoted by D_i .
- 2- Draw copies of area Υ_1 scaled by r_1 with corner E located at all points D_i .
- 3- The area swept by \mathbf{z}_v (denoted by Area Λ_v) will be equal to the convex hull of all the areas drawn in step 2.

Example 11.1: Constructing Areas Λ_v for Two Contact Areas: a Pentagon and a Triangle

Consider area Υ_1 to be a pentagon and area Υ_2 to be a triangle located at positions shown in Figure 11.4. The corresponding Areas Λ_v for different values of r_1 are shown:

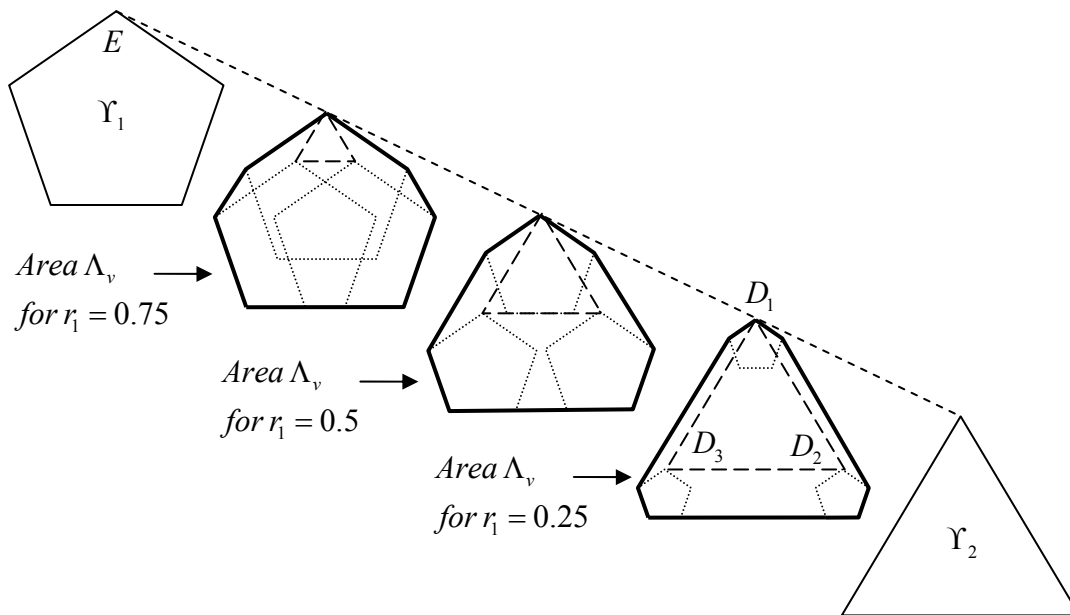


Figure 11.4. Constructing Areas Λ_v for different values of r_1 for two contact areas

Now, we find the area swept by \mathbf{z}_f :

$$\text{Find the area swept by } \mathbf{z}_f = \begin{cases} -o_{23}\mu(1-r_1)f_2\cos(\theta_2) \\ -o_{23}\mu(1-r_1)_2f_2\sin(\theta_2) \end{cases} \quad (11.6.14)$$

$$\text{Subject to } \begin{cases} \mu r_1 f_1 \cos(\theta_1) + \mu(1-r_1)f_2\cos(\theta_2) = \mathfrak{Z}_1 & (11.6.15a) \\ \mu r_1 f_1 \sin(\theta_1) + \mu(1-r_1)f_2\sin(\theta_2) = \mathfrak{Z}_2 & (11.6.15b) \\ 0 < f_1 < 1, \quad 0 < f_2 < 1 & (11.6.15c) \end{cases} \quad (11.6.15)$$

Therefore:

$$(11.6.14) \quad \Rightarrow \quad z_{f_1}^2 + z_{f_2}^2 = (o_{23}\mu(1-r_1)f_2)^2$$

$$\stackrel{(11.6.15.3)}{\Rightarrow} \quad 0 \leq z_{f_1}^2 + z_{f_2}^2 \leq (o_{23}\mu(1-r_1))^2 \quad (11.6.16)$$

$$(11.6.15) \quad \Rightarrow \quad \begin{cases} -\mu(1-r_1)f_2\cos(\theta_2) + \mathfrak{T}_1 = \mu r_1 f_1 \cos(\theta_1) \\ -\mu(1-r_1)f_2\sin(\theta_2) + \mathfrak{T}_2 = \mu r_1 f_1 \sin(\theta_1) \end{cases}$$

$$\stackrel{*o_{23}}{\Rightarrow} \quad \begin{cases} -o_{23}\mu(1-r_1)f_2\cos(\theta_2) + o_{23}\mathfrak{T}_1 = o_{23}\mu r_1 f_1 \cos(\theta_1) \\ -o_{23}\mu(1-r_1)f_2\sin(\theta_2) + o_{23}\mathfrak{T}_2 = o_{23}\mu r_1 f_1 \sin(\theta_1) \end{cases}$$

$$\stackrel{(11.6.14)}{\Rightarrow} \quad \begin{cases} z_{f_1} + o_{23}\mathfrak{T}_1 = o_{23}\mu r_1 f_1 \cos(\theta_1) \\ z_{f_2} + o_{23}\mathfrak{T}_2 = o_{23}\mu r_1 f_1 \sin(\theta_1) \end{cases}$$

$$\Rightarrow \quad (z_{f_1} + o_{23}\mathfrak{T}_1)^2 + (z_{f_2} + o_{23}\mathfrak{T}_2)^2 = (o_{23}\mu r_1 f_1)^2$$

$$\stackrel{(11.6.15.3)}{\Rightarrow} \quad 0 \leq (z_{f_1} + o_{23}\mathfrak{T}_1)^2 + (z_{f_2} + o_{23}\mathfrak{T}_2)^2 \leq (o_{23}\mu r_1)^2 \quad (11.6.17)$$

Inequality (11.6.16) constrains \mathbf{z}_f to be inside a disk of radius $o_{23}\mu(1-r_1)$ centered at the origin. Inequality (11.6.17) constrains \mathbf{z}_f to be inside a disk of radius $o_{23}\mu r_1$ centered at $(-o_{23}\mathfrak{T}_1, o_{23}\mathfrak{T}_2)$. Therefore, the area swept by \mathbf{z}_f (allowable values for \mathbf{z}_f) is the intersection of these two disks which we denote by Area Λ_f .

The area swept by \mathbf{z}_f depends on the values of $\mathfrak{T}_1, \mathfrak{T}_2, r_1, o_{23}, \mu$ which are all fixed values except for r_1 which is temporarily fixed, but will be swept later between 0 and 1 to find the total area swept by \mathbf{z} . The shapes for Areas Λ_f for some fixed values of $\mathfrak{T}_1, \mathfrak{T}_2, r_1, o_{23}, \mu$ are shown in Figure 11.5.

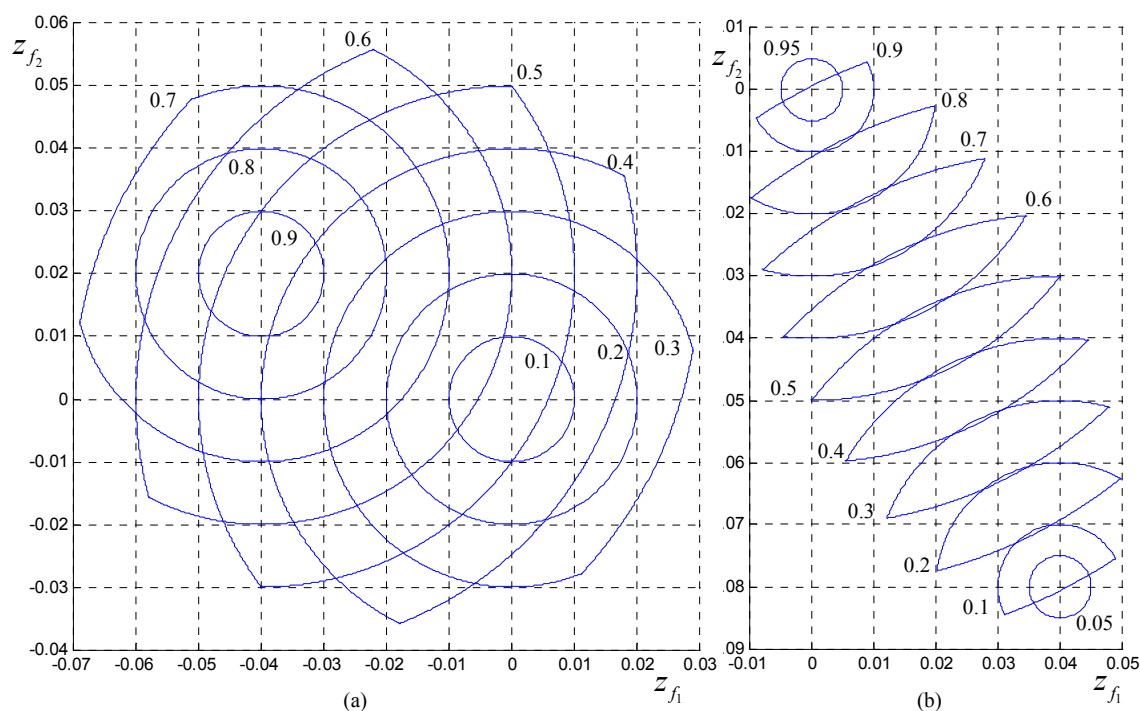


Figure 11.5. Shapes for Areas Λ_f for $\sigma_{23} = 0.2$, $\mu = 0.5$, $r_1 = 0, 0.1, \dots, 1$ as labeled in figures with
 (a) $\zeta_1 = 0.2$, $\zeta_2 = -0.1$ and (b) $\zeta_1 = -0.2$, $\zeta_2 = 0.4$

Now remember that $\mathbf{z} = \mathbf{z}_v + \mathbf{z}_f$. As indicated before, to find the total area swept by \mathbf{z} which we denote by Area Λ , we should add the location of each point of Area Λ_v to each point of Area Λ_f . This can be done by sweeping Area Λ_f over each point of Area Λ_v . Assuming Area Λ_v to be a polygon with n corners (see Figure 11.4), Area Λ can be constructed by choosing a desired step value $\Delta r_1 \leq 1$ and using the following procedure:

Algorithm 11.1:

- 1- Let $r_1 = 0$
- 2- Draw Λ_v as described before (see Figure 11.4)
- 3- Select the suitable shape of Area Λ_f from (a figure similar to) sample Figure 11.5.
- 4- At each corner of Area Λ_v , locate a copy of Area Λ_f such that the origin of the coordinate system in Figure 11.5 coincides with the corner.
- 5- Let $r_1 = r_1 + \Delta r_1$. If $r_1 \leq 1$ then go to step 2.
- 6- The area swept by \mathbf{z} which we denote by Area Λ will be the convex hull of all the copies of Areas Λ_f drawn in the previous steps.

Definition 11.2: ***Form II, 2D, ZMP-Like Constraint for Parallel Contact Areas***

For a dynamic system that has parallel contact areas with the environment, at each instant of motion the values for \mathfrak{S}_1 and \mathfrak{S}_2 are known. The Form II, 2D ZMP-Like constraint states that the two below statements are equivalent:

- 1- The values for $\mathbf{M}_{ige} \cdot \mathbf{e}_1$ and $\mathbf{M}_{ige} \cdot \mathbf{e}_2$ are possible in the real world.
- 2- The ZMP is inside the Area Λ that corresponds to those values of $\mathfrak{S}_1, \mathfrak{S}_2$.

A program in Visual Basic has been written by the authors, which:

- 1- Plots Area Λ by sweeping all the variable parameters in their allowable ranges using several nested For-Next loops and If-Then statements (for checking inequality constraints) and assignments (for imposing equality constraints) to find the location of \mathbf{z} for each combination of possible values of variables and plotting a single point at that location.
- 2- Draws Areas Λ_f using the procedure described in Algorithm 11.1. It is observed in the results that Areas Λ_f drawn in this step exactly define the boundaries of the area swept by \mathbf{z} (Area Λ) in Step 1. This can be considered as a validation for the accuracy of the procedure described in Algorithm 11.1.

This program currently assumes that contact areas Υ_1 and Υ_2 are both parallel rectangles of same sizes. For a stair climbing case shown previously in Figure 11.2, assume that contact areas Υ_1 and Υ_2 have same lengths of 0.2 meters and widths 0.05 meters with the distance between their centers in the forward and sideways directions equal to 0.3 and 0.15 respectively. Areas Λ are plotted by this program for the same values of parameters as in Figures 11.5.a and 11.5.b and are shown in Figures 11.6 and 11.7 respectively. As it is seen from these figures, Areas Λ_f that are borrowed from Figures 11.5.a and 11.5.b and drawn according to Algorithm 11.1 in Figures 11.6 and 11.7, exactly define the boundaries of the area swept by \mathbf{z} (Area Λ) which confirms the validity of Algorithm 11.1.

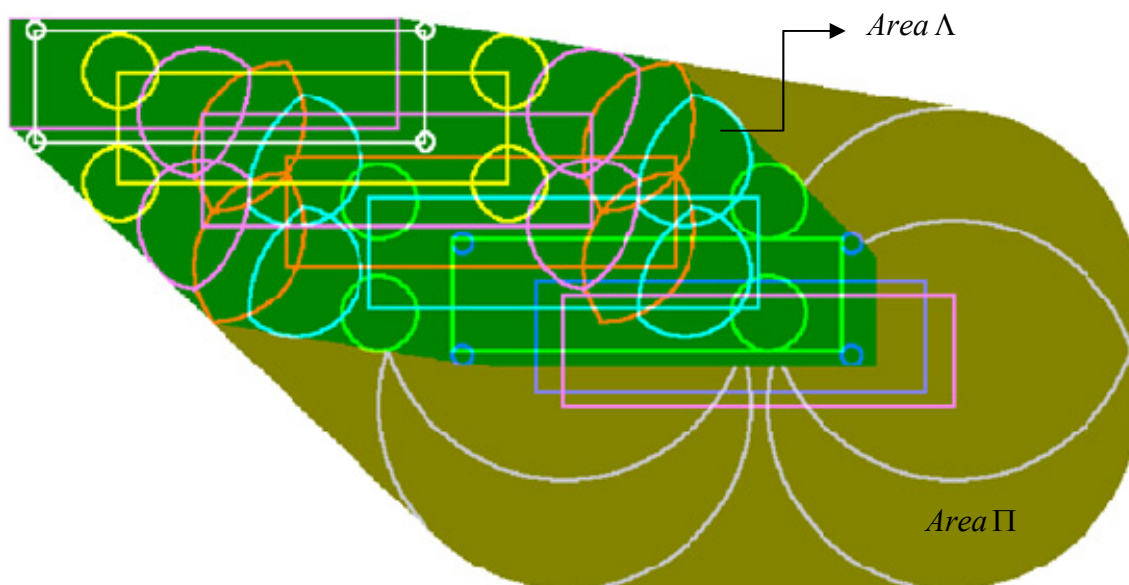


Figure 11.6. Shapes for Area Π (dark yellow) and Area Λ (green) for $o_{23} = 0.2$, $\mu = 0.5$, $\mathfrak{S}_1 = 0.2$, $\mathfrak{S}_2 = -0.1$. Areas Λ_f are the same as calculated in Figure 11.5.a.

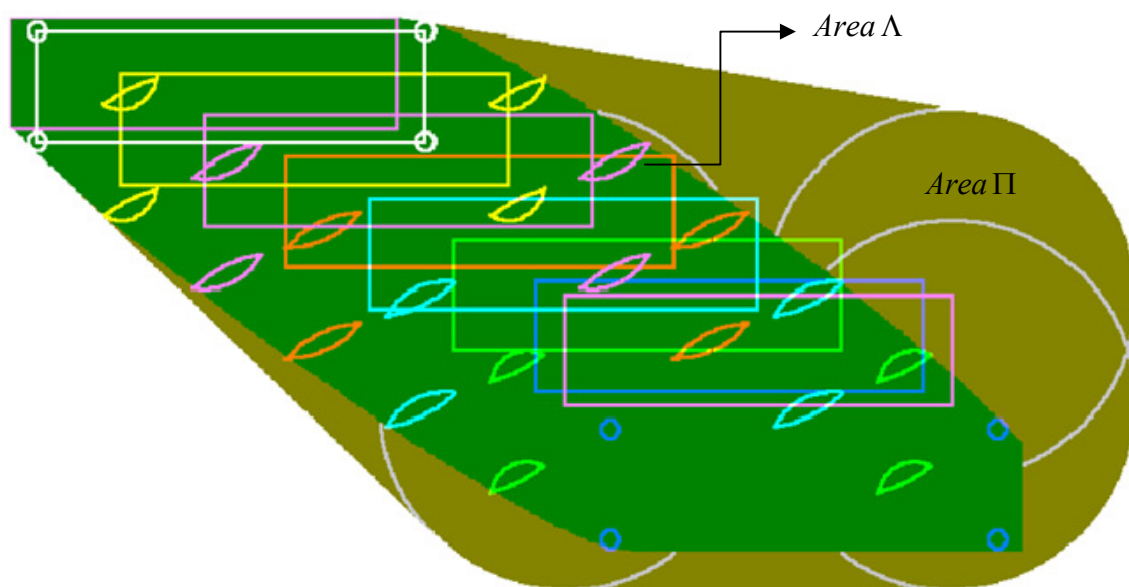


Figure 11.7. Shapes for Area Π (dark yellow) and Area Λ (green) for $o_{23} = 0.2$, $\mu = 0.5$, $\mathfrak{S}_1 = -0.2$, $\mathfrak{S}_2 = 0.4$. Areas Λ_f are the same as calculated in Figure 11.5.b.

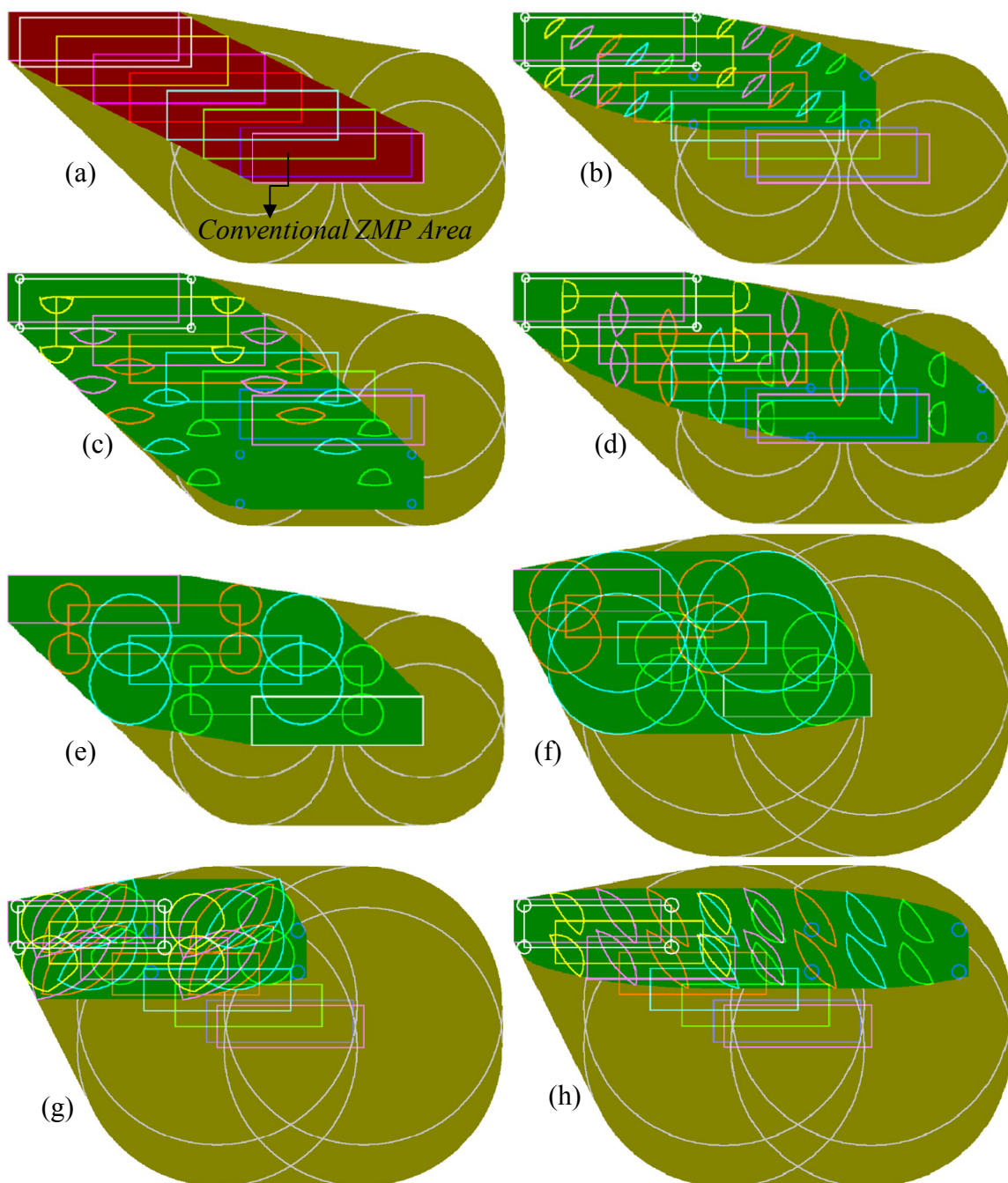


Figure 11.8. The conventional ZMP area (red) is shown in (a). Shapes for Area Π (dark yellow) and Area Λ (green) for different values of $o_{23}, \mu, \zeta_1, \zeta_2$ are shown in figures (b) to (h). In (b) to (e), we have

$$o_{23} = 0.2, \mu = 0.5 \text{ and (b) } \zeta_1 = 0.32, \zeta_2 = -0.32, \text{ (c) } \zeta_1 = 0, \zeta_2 = -0.4, \text{ (d) } \zeta_1 = -0.4, \zeta_2 = 0, \text{ (e) } \zeta_1 = 0, \zeta_2 = 0.$$

$$\text{In (f) to (h), we have } o_{23} = 0.2, \mu = 1 \text{ and (f) } \zeta_1 = 0, \zeta_2 = 0, \text{ (g) } \zeta_1 = 0.4, \zeta_2 = -0.5, \text{ (h) } \zeta_1 = -0.7, \zeta_2 = -0.5.$$

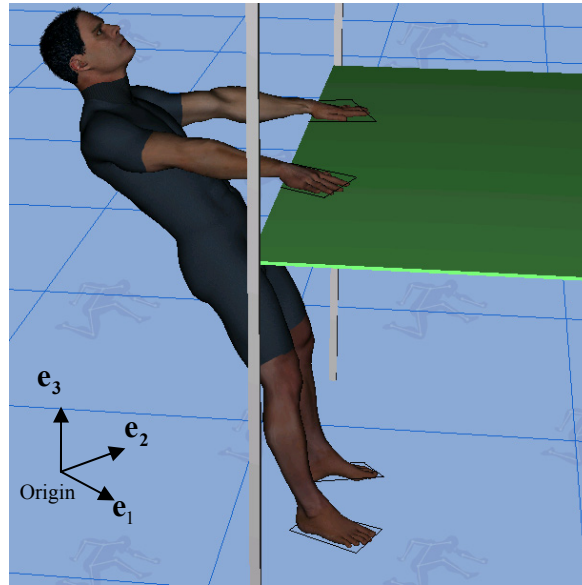


Figure 11.9. Avatar having non-coplanar contact areas

For a more clear explanation of how the non-coplanarity of the contact areas can transform the conventional ZMP area and turn it into Area Π and Area Λ , consider the avatar shown in Figure 11.9. It has 4 separate contact areas with the environment. Its two feet soles are on the ground. Its two hand palms have contact with a rigid and unmovable table. The origin is assumed to be located on the ground and therefore the plane δ will be the ground. The value for o_{α_3} for the 2 contact areas on the hand palms will be equal to the elevation of the table. Consider respectively Γ_1 and Γ_2 as the contact areas of the feet with the ground and the hands with the table. Assume that Γ_1 and Γ_2 are rectangles having same lengths of 0.15 and widths 0.4 with the distance between their centers in the forward and sideways directions equal to 0.05 and 0 respectively. Let $o_{23} = 1.2$ (height of the table) and $\mu = 0.5$ (coefficient of friction). The shapes of Area Π and Area Λ for different values of \mathfrak{S}_1 and \mathfrak{S}_2 are shown in Figure 11.10.

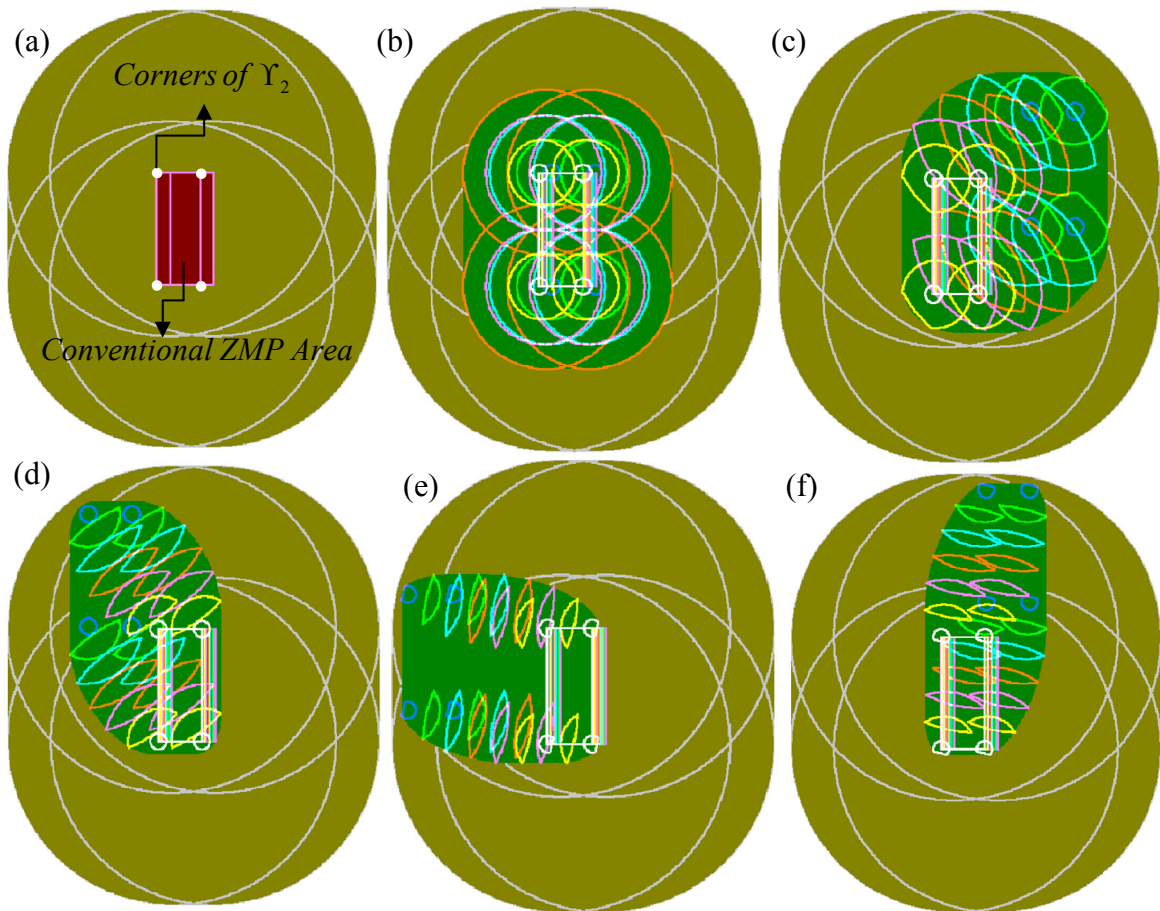


Figure 11.10. The conventional ZMP area (red) is shown in (a). Shapes for Area Π (dark yellow) and Area Λ (green) for $\sigma_{23} = 1.2$, $\mu = 0.5$ and different values of \mathfrak{S}_1 , \mathfrak{S}_2 are shown in Figures (b) to (f).

Values of \mathfrak{S}_1 , \mathfrak{S}_2 in each figure are: (b) $\mathfrak{S}_1 = 0$, $\mathfrak{S}_2 = 0$, (c) $\mathfrak{S}_1 = 0.25$, $\mathfrak{S}_2 = -0.2$, (d) $\mathfrak{S}_1 = 0.25$, $\mathfrak{S}_2 = -0.35$, (e) $\mathfrak{S}_1 = 0.45$, $\mathfrak{S}_2 = -0.1$, (f) $\mathfrak{S}_1 = -0.1$, $\mathfrak{S}_2 = -0.45$.

The radius of the disks on the corners of the contact areas Γ_1 and Γ_2 in Area Π will be equal to $\sigma_{\alpha 3}\mu$ which is $\sigma_{\alpha 3}\mu = 0.6$ at its hands (Γ_2) and zero at its feet (Γ_1). Now, let us show Area Π and Area Λ in their real positions in the world. Consider the avatar in a static posture without external loads. In that case, we shall have $\mathfrak{S}_1 = 0$, $\mathfrak{S}_2 = 0$ and the corresponding Area Π and Area Λ were shown in Figure 11.10.b. Also, in such a case, the location of the ZMP will be the projection of the avatar's center of gravity on

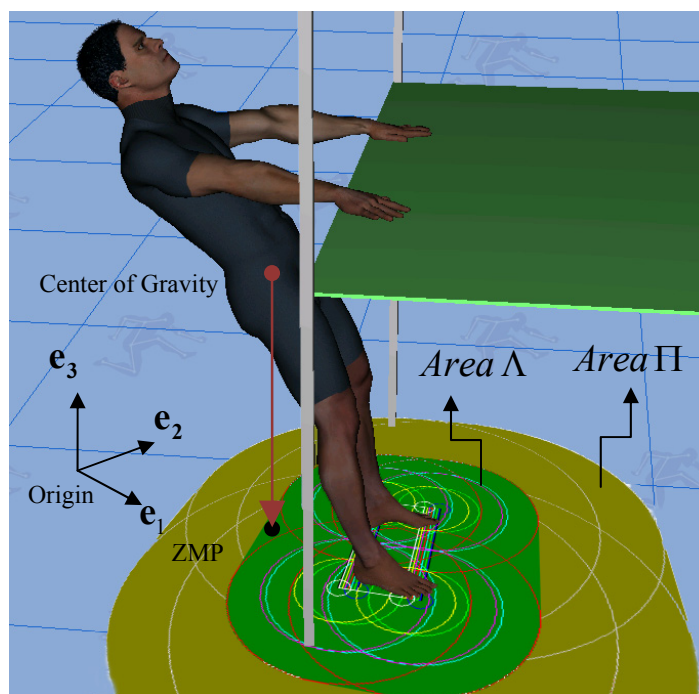


Figure 11.11. Avatar being able to lean back without falling due to non-coplanar contact areas

the ground (plane δ). For this case, Area Π and Area Λ are borrowed from Figure 11.10.b and are shown in their real positions in the world in Figure 11.11.

If it was not for the elevation of the table (o_{α_3}) or for the friction forces at the palms (μ) Area Π and Area Λ would have been equal to the conventional ZMP area as shown in Figure 11.10.a. The ZMP would have been out of both Area Π and Area Λ and the posture shown was impossible (zero acceleration was impossible), and the avatar would have to have an acceleration (have to be falling) in such a situation. But due to the elevation of the table and the existence of friction, Area Π and Area Λ are different from the conventional ZMP area and the avatar is able to lean back without falling.

Finally, we summarize the benefits of Form I (Area Π) vs. Form II (Area Λ) ZMP-Like constraints (see Definitions 11.1, 11.2 and Figures 11.8, 11.10) :

The significance and the benefits of the Form I ZMP-Like constraints are:

- 1- Similar to the conventional ZMP constraint, the shape of Area Π only depends on the shape and location of contact areas and does not depend on the value of \mathbf{F}_{ige} .
- 2- It is much easier to construct Area Π compared to Area Λ
- 3- If the ZMP is outside Area Π , we can conclude that the motion is impossible in the real world for all \mathfrak{S}_1 and \mathfrak{S}_2 (\mathbf{F}_{ige}) according to Definition 11.1.
- 4- It is the union of all Areas Λ for all possible values of \mathbf{F}_{ige} in the real world.

The weak aspects of Form I ZMP-Like constraints are:

- 1- If the ZMP is inside Area Π , we cannot be sure whether the values for $\mathbf{M}_{ige} \cdot \mathbf{e}_1$ and $\mathbf{M}_{ige} \cdot \mathbf{e}_2$ are possible or not for the current \mathbf{F}_{ige} . We can just be sure that there exist values of \mathbf{F}_{ige} (\mathfrak{S}_1 and \mathfrak{S}_2) for which they are possible in the real world.

The significance and the benefits of Form II ZMP-Like constraints are:

- 1- We can be sure whether the values for $\mathbf{M}_{ige} \cdot \mathbf{e}_1$ and $\mathbf{M}_{ige} \cdot \mathbf{e}_2$ are possible or not for the current \mathbf{F}_{ige} based on the ZMP being inside or outside Area Λ

The weak points of Form II ZMP-Like constraints are:

- 1- Unlike the conventional ZMP constraint, the shape of Area Π does not only depend on the shape and location of contact areas. It also depends on the value of \mathbf{F}_{ige} ($\mathfrak{S}_1, \mathfrak{S}_2$). It means that unlike the conventional ZMP constraint, the shape of Area Π changes for different accelerations or different external forces.
- 2- It is much harder to construct Area Λ compared to Area Π

If we assume all the contact areas to be coplanar, the Form I and Form II ZMP-Like constraints will both become same as the conventional ZMP constraint and also independent of $\mathfrak{S}_1, \mathfrak{S}_2$. Area Π and Area Λ will both be equal to the convex hull of all contact points. That is because we shall have $o_{\alpha 3} = 0$ for all contact areas and the value of \mathbf{z} (location of ZMP) in Equation (11.6.1) will be independent of the frictional forces. In other words that is because in a conventional ZMP problem, the frictional forces produce no moment about planar axes ($\mathbf{e}_1, \mathbf{e}_2$).

The ZMP-Like constraints given in this section can be used to check the possibility or find the margins of stability of robot motion in robot control problems in all cases where we have one or more contact areas on several inclined or horizontal planes as long as all planes are parallel such as when a robot wants to climb stairs (either horizontal stairs as in Figure 11.12.a or inclined but parallel stairs as in Figure 11.12.c) or for example, when the hand of a robot has contact with the surface of a table parallel to the inclined ground as shown in Figure 11.12.b.

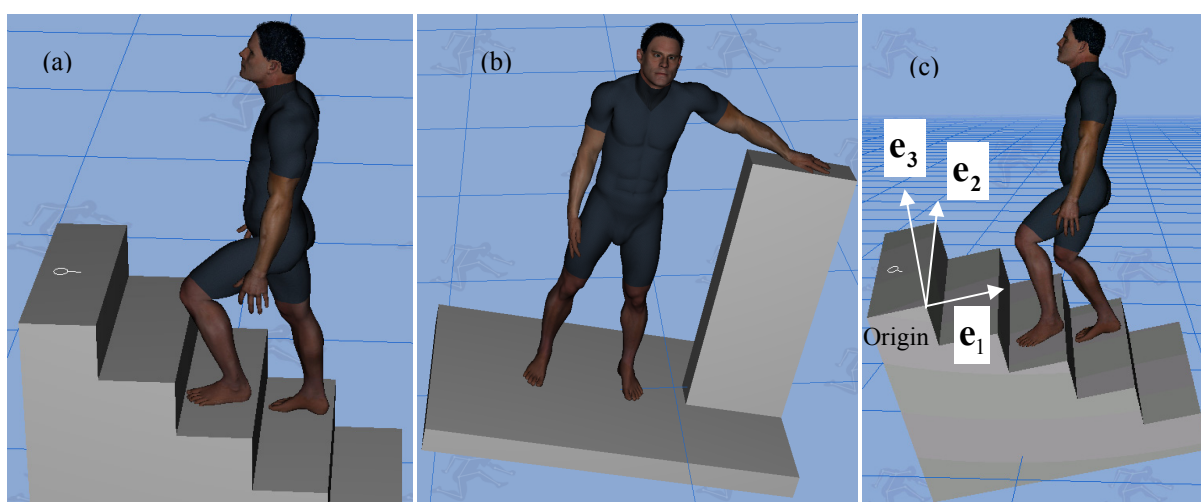


Figure 11.12. Samples of the applicability of the proposed ZMP-Like constraints in the analysis of motions:
 (a) Horizontal stairs (b) Parallel external contact areas (c) Inclined stairs

11.7. ZMP-like Constraints in the General Case of Non-Coplanar, Inclined Contact Areas

In general, deriving the range for \mathbf{M}_{ige} for the Form I or Form II ZMP-Like constraints defined by (11.5.8) and (11.5.9) is the mathematical problem of finding the boundaries of vector functions subject to equality and inequality constraints. In the literature, the most related field of research that investigates such a problem is the field of “Finding the boundaries of workspace for robots”. Examples of papers in this field can be seen in Haug (1996), Abdel-Malek (1999), Hariri (2005). We leave the usage of these general approaches for Finding ZMP-Like constraints as the future topic of research.

However, we have already presented the most general method for checking the violation or satisfaction of the ZMP constraint or finding the ZMP stability margins. That is, in the most general cases of contact areas, for each case, the system of equations given in (11.4.1) or the approximate form that is linear in unknowns (11.4.2) needs to be solved to see if for the \mathbf{F}_{ige} and \mathbf{M}_{ige} in question are possible or not (They are possible if and only if there is a solution for the system of equations). Also, to find tipping or slipping stability margins in the most general cases, the method in Section 10.6 can be used.

11.8. Summary and Conclusion

In this chapter, we presented a general formulation to check the possibility of a given motion (with a given \mathbf{F}_{ige} and \mathbf{M}_{ige}) which can replace ZMP constraint for systems

with any general case of environmental contact areas. The general formulations for finding closed form solutions that resemble the form of the conventional ZMP constraint were also presented. For systems with non-coplanar contact areas (unlike coplanar), the suggested ZMP constraints are dependent on frictional elements. The actual closed form solutions were calculated and depicted which are equivalent to the ZMP constraint for the cases of parallel contact areas. These are new results because the conventional ZMP constraints are only applicable to cases of coplanar contact areas. A new software was also developed which finds these new constraints numerically and compares them with analytical results in order to validate the suggested method.

CHAPTER 12
SUMMARY, CONCLUSIONS AND FUTURE RESEARCH

12.1 Summary and Conclusions

• **Part I – Background of Research:**

Part I of this work consisting of Chapters 1, 2 and 3 included the introduction and background material for this research:

In Chapter 2, we introduced the basics of the predictive dynamics method. It was shown that the kinematic and dynamic calculations can be performed with complete mathematical certainty, if and only if the ratios for the partitioning of environment contact forces are given (if all the external forces are known in the general sense). However, this is not true for a digital human, if it has more than one contact area with the environment. In that case, the equivalent ground reaction force and moment exerted on each contact area of the digital human with the environment are indeterminate.

Chapter 3 was a review of the ZMP concepts existing in the literature by using a simple example. It was shown that in the real world, the ZMP constraint is never violated during any motion of a dynamic system including unstable or falling motions. It was also shown that ZMP stability margins and stability criterion are very different from the ZMP constraint and their role is to evaluate the stability of a given motion. Some conclusions were as follows:

- 1- The ZMP constraint transforms two equations of the general dynamic equilibrium (out of the 6 force and moment equilibrium equations for the whole system) into inequalities by removing from the equations the contact

forces acting on the system. These equations represent the dynamic equilibrium of all the moments exerted on the whole system about the horizontal axes.

- 2- The ZMP constraint specifies the range of values for the tipping (horizontal) components of the net moment of the IGE forces (about any fixed point such as the origin) that are possible in the real world for a dynamic system.

- **Part II- ZMP Method:**

Part II of this work consisting of Chapters 4, 5 and 6 was a study of the ZMP method for modeling environmental contact:

Chapter 4 presented a theoretical study of the ZMP method. It presented an important theorem (Theorem 4.1) which showed the relation between the ZMP constraint and the unilaterality of ground reaction forces. It was shown that an additional constraint requiring the vertical component of the IGE forces to be downwards needs to be imposed besides the ZMP constraint to ensure the unilaterality of ground reaction forces. Theorem 4.1 shows that the ZMP method used in predictive dynamics is a legitimate method for producing motions that are possible in the real world. However, an assumption was used for the calculation (partitioning) of ground reaction forces in the ZMP method which was not mathematically proved and was based on observations from limited experimental data. This assumption was partially evaluated in Section 4.6 to show its backgrounds and was further evaluated in Section 7.10 to show its deficiencies. In

that chapter, the ZMP concepts in predictive dynamics were also used to design general algorithms which modeled the exact changes of the transient ground contact areas during the motion and calculate ground reaction forces for modeling tasks in the predictive dynamics environment.

In Chapter 5 and 6, the modules based on the ZMP method introduced in Sections 4.3 and 4.4 are used to model the motion of a human (soldier) performing several military tasks: aiming, kneeling, going prone and aiming in prone position. To model the dynamic tasks, new methods in collision avoidance were used which appear in Appendix A. In Appendix A, we presented new theorems on optimization-based collision avoidance that use other finite primitives besides the conventional spheres to model objects or limbs. This new capability was needed to model self and environment collision avoidance in this research.

- **Part III- NCM Method:**

Part III of this work consisting of Chapters 7 to 11 was a study of the NCM method for modeling environmental contact:

Chapter 7 was a theoretical chapters in which we introduced the new concept of Normal Contact Moment (NCM) point and constraints for each of the contact areas with the environment. This chapter presented a general set of constraints on the equivalent reaction force systems (forces and moments) of non-adhesive contact areas by defining a point called NCM point. That general set of constraints was composed of NCM constraints and some suggested constraints on the frictional forces and moments which

use the NCM point definition. The NCM constraints are necessary and sufficient for modeling the unilaterality of distributed contact forces. Therefore, the unilaterality of distributed contact forces can be modeled completely by the NCM constraints. Based on the NCM point location, we presented new constraints on the frictional contact moment of a contact area. NCM constraints along with those proposed coulomb friction constraints can completely model the non-adhesiveness of a contact area.

Chapter 8 was another theoretical chapter in which (NCM) constraints were compared to the ZMP constraint. This chapter presented a relationship between the location of the ZMP and NCM points for the case of coplanar contact areas. Based on that, the following conclusions were made:

- 1- ZMP constraint is just a result of NCM constraints and is weaker than them. So, the ZMP constraint cannot ensure that calculated GRF in the ZMP method are possible in the real world. NCM constraints need to be used to ensure that.
- 2- The linear, uniform partitioning assumption used in the ZMP method in fact causes all the calculated GRF except maybe one to have values that are mathematically impossible in the real world.
- 3- The experimental data support the ZMP method only for the ratio of the vertical component of GRF (not for the remaining 5 components). This is just a logical physical phenomenon that would have resulted automatically, if the NCM constraints had been used (it is embedded in the NCM constraints).
- 4- ZMP constraint applies only to the cases in which the system's contact with the environment is in one plane only. Unlike ZMP constraint, NCM

constraints are applicable for the most general cases of contact areas (coplanar or non-coplanar contact areas which are horizontal or inclined or parallel or non-parallel).

In Chapter 9, the previous military tasks modeled in Chapters 5 and 6 by using the ZMP method are remodeled using the NCM method and the results are compared. In that chapter, we introduced algorithms that re-partition the GRF values obtained by the ZMP method such that the values are possible in the real world (satisfy the NCM constraints). As an example, the algorithm was implemented for the “Going Prone” task and a previously simulated “Walking” task. The conclusions were:

- 1- It was proved mathematically in Chapter 8 and validated in Chapter 9 that:
At least one component of the calculated GRF is impossible in the real world for all ground contact areas, except may be for one contact area in the ZMP method.
- 2- It was proved mathematically in Chapter 4 and validated in Chapter 9 that:
Satisfaction of ZMP constraint ensures that it is possible to find unilateral contact forces on the given contact areas to cancel the given IGE forces for the dynamic system. That is because we could find GRF that are possible in the real world by re-partitioning them.
- 3- The torques obtained after re-partitioning seem to be lower than the original torques. However, the optimality of the initial motion from the ZMP method seem to stay almost unaffected after re-partitioning. Therefore, although the

motion obtained in the ZMP method is possible and almost optimal, the GRF need to be re-partitioned in order to obtain realistic values.

- 4- The re-partitioning (NCM method) does not ensure that the re-partitioned GRF are optimal or match the experimental data. These issues also depend on the original simulation and the constraints used there to predict a motion task. However, it seems that the results of the re-partitioning for the walking task considerably improved similarity of the GRF ratios with the experimental data.

In Chapter 10, we introduce the NCM stability margins. we defined margins of tipping and slipping stabilities which are applicable for the most general cases of contact areas and are usable for both real problems such as in robot control or in simulations. We showed that the problem of finding the margins of tipping or slipping stability for the most general cases of contact areas turns into solving a linear optimization problem. The ZMP stability criteria and margins are not applicable for problems in which the system's contact areas with the environment are non-coplanar. As it was shown in this chapter, the NCM stability concepts are applicable for systems with any number of contact areas with the environment, oriented arbitrarily with respect to each other (contact areas which are coplanar, non-coplanar, horizontal, inclined, parallel or non-parallel).

In Chapter 11, the NCM constraints are used to generalize the ZMP constraint. In this chapter, we presented a general formulation to check the possibility of a given motion which can replace ZMP constraint for systems with any general case of

environmental contact areas. The general formulations for finding closed form solutions that resemble the form of the conventional ZMP constraint were also presented. The actual closed form solutions were calculated and depicted for the cases of parallel contact areas. A new software was also developed which finds these new constraints numerically and compares them with analytical results in order to validate the suggested method.

12.2 Future Research

Currently, two separate optimization problems are solved to achieve the predictive dynamics results. In the first optimization problem (ZMP method), the design variables are only the joint angle profiles. In the second optimization problem (NCM method), the joint angle profiles are prescribed values borrowed from the ZMP method and the indeterminate equivalent ground reaction forces and moments are the only design variables. As a result this procedure only applies to tasks where environmental contact areas are coplanar.

As future research, the NCM method can eventually enable the modeling of tasks in the predictive dynamics environment in which the contact areas are non-coplanar. In that case, the ZMP method and constraints should be completely abandoned. The alternative method will be to solve a single, more complicated optimization problem in which the design variables are the joint angle profiles and the indeterminate equivalent ground reaction forces and moments at the same time. Environmental contact definitions should be more general and include the position and orientation of environmental contact

planes. Generalizations in the calculations of gradients with respect to new additional design variables will also be necessary. NCM constraints should be used to solve the problem (which ensure ZMP constraint to hold for the coplanar case of contacts).

The benefit of the alternative method is that:

- A- It will be applicable to systems with any arbitrary case of contact areas with the environment (coplanar or non-coplanar contact areas which are horizontal or inclined or parallel or non-parallel).
- B- Friction constraints can be imposed with any desired coefficient of friction. In the current method, in the second optimization, they are set equal to values that were required to generate the motion using the ZMP method (in the first optimization).
- C- In the current method, the motion is prescribed in the second optimization and is unaffected by the NCM method. In the alternative method, the motion will also be affected by the NCM method.

The major drawbacks of the alternative method are:

- A- We will have a lot more number of design variables than the current method ($6 * (\text{number of contact areas} - 1)$ new design variables at each time grid point).
- B- The partitioning of GRF is performed subject to all the unnecessary constraints which only depend on the kinematics and are independent of the GRF partitioning.

The above issues may seriously slow down the convergence rate and affect the efficiency of the optimization procedure.

Future research can also include enhancement of the proposed theorems and implementations (task simulations). Several examples are stated below:

- 1- It is still possible to generalize the ZMP constraints and validate the results further than the current stage. Finding the closed form solutions for ZMP constraint problem is the mathematical problem of finding the boundaries of vector functions subject to equality and inequality constraints. In the literature, the most related field of research that investigates such a problem is the field of “Finding the boundaries of workspace for robots”. Examples of papers in this field can be seen in Haug (1996), Abdel-Malek (1999), Hariri (2005).
- 2- Refinement of motion tasks, which include, but are not limited to:
 - A- Testing the “Minimum Movement (Displacement)” performance measure, developed by the author of the thesis.
 - B- Decreasing the number of design variables in the motion tasks. (General modules for decreasing the design variables are developed and initial implementation has been done for “Aiming While Standing”.)
 - C- A more complete validation of the simulated dynamic tasks. (Validation for “Going Prone” is completed but for the other dynamic tasks, only their predicted NPOA (natural point of aim) is validated.)

- 3- Derviving closed form solutions for the proposed NCM contact stability criteria and stability margins for systems with non-coplanar contact areas with the environment.

APPENDIX A
OPTIMIZATION-BASED COLLISION AVOIDANCE USING SPHERES, FINITE
CYLINDERS AND FINITE PLANES

A.1 Introduction

A digital human must avoid the collision of the body segments with other non-adjacent body segments as well as with the objects in the environment while performing a task. In this appendix, we develop mathematical models for constraints that can avoid these collisions. The digital human body segments and the obstacles in the environment are modeled using surrogate geometries. The body segments are represented by using one or more spheres rigidly attached to a local reference frame so that these spheres move as the body segments move. The objects in the environment are modeled using one or more of the five primitive geometries: spheres, infinite cylinders, infinite planes, finite cylinders, and finite planes. A generic collision avoidance strategy is developed to avoid spheres with all the five primitive geometries used for representing obstacles.

We use gradient based optimization strategy for predicting the motion of the digital human avatar while performing a task. One of the requirements of a gradient based optimization is use of constraint functions and objective functions with continuous gradients of at least first order. This is equivalent to a requirement for the elements to have smooth surfaces (no edges). But finite cylinders and finite planes do not have smooth edges. Hence, we present a method to smooth out the edges of finite cylinders and planes and consider these modified elements instead, so that the constraint gradients are continuous.

A.2. Literature Review

The computation of distance between two mathematical objects finds many applications in robotics. Most of the effort in robotics in the field of collision avoidance involves the path planning optimization for mobile robots where the path of the robot is normally modified by optimization in order to avoid collision. Using spheres to model obstacles has also been popular in the field of path planning in flying spacecrafts (Singh, 2001, 2002). There have also been several studies which use spheres for modeling objects. For a human avatar, modeled as a robot with multiple branches, the design variables which affect self collision are the joint angles. For obstacle collision avoidance, the global translation/rotation of the avatar is also added to those variables. For example Johnson (2010) uses spheres to model a digital human. This model is used in the prediction of static postures to prevent the digital human from collision with obstacles (obstacle avoidance) as well as with itself (self avoidance).

Colbaugh et al. (1989) used simple geometric primitives to represent the robot arms and its environment for a planar manipulator. The obstacles were represented by circles surrounded by a surface of influence, and the links were modeled by straight lines. A redundancy resolution scheme was proposed to achieve obstacle avoidance. This approach was extended to the 3-D workspace of redundant manipulators in Shadpey et al. (1994, 1995) and Glass et al. (1995).

Using spheres to model links and obstacles for collision avoidance has an important advantage. The advantage is that the optimization constraint that needs to be satisfied to avoid collision between 2 spheres is simply: $d^2 \geq (r_1 + r_2)^2$, where d is the

distance between the spheres' centers and r_1 and r_2 are the radii of the spheres. This constraint is simple to calculate and if the motions of the 2 spheres are functions of q_i , then this constraint is also a C^∞ function of q_i (the class of functions with continuous p th-order derivatives is denoted by C^p).

By using available optimization softwares, collision avoidance can be integrated as a constraint among others. Indeed, one may consider writing these constraints using any available proximity distance algorithm which returns signed proximity distances separating two bodies; see the recent exhaustive books by van den Bergen (2004) and Ericson (2005).

However, while using the gradient-based optimization software, the gradients of the objective function and the constraints need to be continuous with respect to the design variables (generally robot joint angles and joint angle trajectories' parameters). Some of the works in the field of collision avoidance, model the surface of objects by many flat surfaces such as polyhedrons. The proximity distance between polyhedrons does not have continuous gradients with respect to the parameters. Continuity properties of the distance have been merely discussed or even assumed in previous works. For example, in Lee (2001) and Choset (1997), where the obstacle avoidance problem has been addressed in a 2D case, it has been claimed that the distance between convex objects is smooth and thus the gradient is continuous. The latter assertion is not always valid unless one object is strictly convex, and the former depends on the continuity properties of both objects' surfaces. It is only in Rusaw (2001) that the non-differentiability (and non-convexity) of

the distance between convex bodies is well addressed and used with non-smooth analysis in the context of sensory-based planning.

A recent paper (Escande, 2007) claims to be the first to treat the problem of ensuring continuous distance's gradients. It suggests a solution to get rid of the non-differentiability. They build offline strictly convex bounding volume that can be considered as a smooth 'rounding' of the polyhedron convex hull. However, even in this work, the edges between any 2 polyhedrons are not smoothed out. They don't actually need to perform such an operation, as they consider the collision of polyhedrons one by one with each other during the motion.

A.3. Formulations

In this appendix, we introduce a new method for obstacle avoidance by combining parts of the surfaces of differentiable primitives (sphere, infinite cylinder, infinite plane) and creating new compound primitives (finite cylinder, finite plane, finite one-sided plane, box). We should make sure that these surface parts are joined together at boundaries with equal slopes, which means that these joints should cause no edge on the surface of the compound primitive. The distance between the two primitives or compound primitives is always calculated by a single scalar constraint function. Theorem A.3 at the end of this appendix states that if two objects have convex surfaces without any edges (C^1 surfaces), then the derivative of minimum distance between them with

respect to q_i is a continuous function of q_i . Hence, the proposed method is suitable for use as a constraint in the gradient based optimization solver.

In Sections A.3.1 and A.3.2, we present the formula for collision avoidance constraints. In each case, f is the value of the constraint that should be kept positive to avoid collision. Also, the position vectors defined in the following section are considered to be the functions of the design variables, q_i . If the primitive is associated with a fixed obstacle in space, the position vectors of all points on such primitives are constant vectors and hence, the gradients of the position vectors of all such points with respect to design variables are zero.

A.3.1. Constraints for Collision Avoidance Between Two Primitives

All calculations in this section for each vector is independent of the location and orientation of its reference frame. So, they hold true for any orientation or position of the global frame with respect to them (They can correspond to any location/orientation of their reference frame). Therefore, reference frames are not shown in the figures.

A.3.1.1. Sphere-to-Sphere Collision Avoidance Constraint

As shown in Figure A.1, A and B are the centers of the spheres with radii r_1 and r_2 respectively. Let d denote the distance between A and B. Let the global position vector of the points A and B be given by $\mathbf{G}_A = (X_A \ Y_A \ Z_A)^T$ and $\mathbf{G}_B = (X_B \ Y_B \ Z_B)^T$. Assume that spheres A and B are attached to two coordinate frames denoted respectively in the D-H table as coordinate frame number m in branch i and coordinate frame number n in branch

j. Assume that the global coordinate frame in the D-H table is numbered as coordinate frame 0. Let the local position vector of the points A and B be given by $\mathbf{L}_A = (x_A \ y_A \ z_A)^T$ and $\mathbf{L}_B = (x_B \ y_B \ z_B)^T$. The constraint function that should be kept positive to avoid collision and its gradients with respect to the design variables can be calculated as:

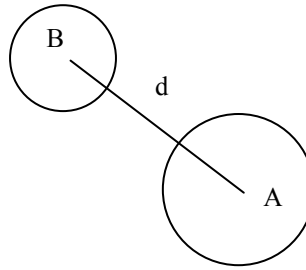


Figure A.1. Sphere-to-Sphere collision

$$f = d^2 - (r_1 + r_2)^2 \quad \Rightarrow \quad f = (\mathbf{G}_A - \mathbf{G}_B) \cdot (\mathbf{G}_A - \mathbf{G}_B) - (r_1 + r_2)^2 \geq 0 \quad (A.3.1)$$

$$\Rightarrow \quad \frac{\partial f}{\partial q_k} = 2 \left(\frac{\partial \mathbf{G}_A}{\partial q_k} - \frac{\partial \mathbf{G}_B}{\partial q_k} \right) \cdot (\mathbf{G}_A - \mathbf{G}_B) \quad (A.3.2)$$

Calculation of f :

$$(A.3.1) \Rightarrow \quad f = (\mathbf{G}_A - \mathbf{G}_B) \cdot (\mathbf{G}_A - \mathbf{G}_B) - (r_1 + r_2)^2 \geq 0$$

$$\begin{cases} \mathbf{G}_A = (X_A \ Y_A \ Z_A)^T = [{}^0T_{n,i}] (x_A \ y_A \ z_A)^T = [{}^0T_{m,i}] \mathbf{L}_A \\ \mathbf{G}_B = (X_B \ Y_B \ Z_B)^T = [{}^0T_{m,j}] (x_B \ y_B \ z_B)^T = [{}^0T_{n,j}] \mathbf{L}_B \end{cases} \quad (A.3.3)$$

$$\text{where } \begin{cases} {}^0T_{m,i} = {}^0T_{1,i} {}^1T_{2,i} \cdots {}^{m-1}T_{m,i} \\ {}^0T_{n,j} = {}^0T_{1,j} {}^1T_{2,j} \cdots {}^{n-1}T_{n,j} \end{cases}$$

Calculation of $\frac{\partial f}{\partial q_k}$ is more complex. It is a function of $\frac{\partial \mathbf{G}_A}{\partial q_k}$ and $\frac{\partial \mathbf{G}_B}{\partial q_k}$. In a

branched D-H structure, each joint q_k may belong at the same time to several different branches. Therefore, for example in the branch i , let q_k be denoted by $q_{s,i}$ and in branch

j , let it be denoted by $q_{t,j}$. Therefore, the calculation of $\frac{\partial f}{\partial q_k}$ is done using the following

procedure:

$$(A.3.2) \Rightarrow \frac{\partial f}{\partial q_k} = 2 \left(\frac{\partial \mathbf{G}_A}{\partial q_k} - \frac{\partial \mathbf{G}_B}{\partial q_k} \right) \cdot (\mathbf{G}_A - \mathbf{G}_B)$$

$$\begin{cases} \mathbf{G}_A = [{}^0T_{m,i}] \mathbf{L}_A \\ \mathbf{G}_B = [{}^0T_{n,j}] \mathbf{L}_B \end{cases} \Rightarrow \begin{cases} \frac{\partial \mathbf{G}_A}{\partial q_k} = \left[\frac{\partial {}^0T_{m,i}}{\partial q_{s,i}} \right] \mathbf{L}_A \\ \frac{\partial \mathbf{G}_B}{\partial q_k} = \left[\frac{\partial {}^0T_{n,j}}{\partial q_{t,j}} \right] \mathbf{L}_B \end{cases} \quad (A.3.4)$$

$$\text{where } \begin{cases} {}^0T_{m,i} = {}^0T_{1,i} {}^1T_{2,i} \cdots {}^{m-1}T_{m,i} \\ {}^0T_{n,j} = {}^0T_{1,j} {}^1T_{2,j} \cdots {}^{n-1}T_{n,j} \end{cases} \Rightarrow \begin{cases} \frac{\partial {}^0T_{m,i}}{\partial q_{s,i}} = {}^0T_{1,i} \cdots {}^{s-2}T_{s-1,i} \frac{\partial {}^{s-1}T_{s,i}}{\partial q_{s,i}} {}^sT_{s+1,i} \cdots {}^{m-1}T_{m,i} \\ \frac{\partial {}^0T_{n,j}}{\partial q_{t,j}} = {}^0T_{1,j} \cdots {}^{t-2}T_{t-1,j} \frac{\partial {}^{t-1}T_{t,j}}{\partial q_{t,j}} {}^tT_{t+1,j} \cdots {}^{n-1}T_{n,j} \end{cases} \quad (A.3.5)$$

$${}^{s-1}T_{s,i} = \begin{pmatrix} C_{s,i} & -S_{s,i} C \alpha_{s,i} & S_{s,i} S \alpha_{s,i} & a_{s,i} C_{s,i} \\ S_{s,i} & C_{s,i} C \alpha_{s,i} & -C_{s,i} S \alpha_{s,i} & a_{s,i} S_{s,i} \\ 0 & S \alpha_{s,i} & C \alpha_{s,i} & d_{s,i} \\ 0 & 0 & 0 & 1 \end{pmatrix}, \quad \frac{\partial {}^{s-1}T_{s,i}}{\partial q_{s,i}} = \begin{pmatrix} -S_{s,i} & -C_{s,i} C \alpha_{s,i} & C_{s,i} S \alpha_{s,i} & -a_{s,i} S_{s,i} \\ C_{s,i} & -S_{s,i} C \alpha_{s,i} & S_{s,i} S \alpha_{s,i} & a_{s,i} C_{s,i} \\ 0 & 0 & 0 & 0 \\ 0 & 0 & 0 & 0 \end{pmatrix}$$

where : $S_{s,i} \equiv \text{Sin}(q_{s,i})$, $C_{s,i} \equiv \text{Cos}(q_{s,i})$

$$\Rightarrow \frac{\partial {}^{s-1}T_{s,i}}{\partial q_{s,i}} = [Q_{Rot}] [{}^{s-1}T_{s,i}] \quad \text{Where: } [Q_{Rot}] = \begin{pmatrix} 0 & -1 & 0 & 0 \\ 1 & 0 & 0 & 0 \\ 0 & 0 & 0 & 0 \\ 0 & 0 & 0 & 0 \end{pmatrix}$$

$$\Rightarrow \frac{\partial f}{\partial q_k} = 2 \left(\left[\frac{\partial {}^0T_{m,i}}{\partial q_{s,i}} \right] \mathbf{L}_A - \left[\frac{\partial {}^0T_{n,j}}{\partial q_{t,j}} \right] \mathbf{L}_B \right) \cdot (\mathbf{G}_A - \mathbf{G}_B) \quad (A.3.6)$$

$$\text{where } \begin{cases} \frac{\partial {}^0T_{m,i}}{\partial q_{s,i}} = {}^0T_{1,i} \cdots {}^{s-2}T_{s-1,i} [Q_{Rot}] {}^{s-1}T_{s,i} {}^sT_{s+1,i} \cdots {}^{m-1}T_{m,i} & \text{for } 1 \leq s \leq m \\ \frac{\partial {}^0T_{n,j}}{\partial q_{t,j}} = {}^0T_{1,j} \cdots {}^{t-2}T_{t-1,j} [Q_{Rot}] {}^{t-1}T_{t,j} {}^tT_{t+1,j} \cdots {}^{n-1}T_{n,j} & \text{for } 1 \leq t \leq n \end{cases}$$

Now, remember that in branch i , q_k was denoted by $q_{s,i}$ and in branch j , it was denoted by $q_{t,j}$. To calculate the vector $\frac{\partial f}{\partial q_k}$ efficiently, we separate it into the following

two terms which contain the gradients of the locations of the first and the second spheres:

$$\Rightarrow \frac{\partial f}{\partial q_k} = 2 \underbrace{\left(\left[\frac{\partial {}^0T_{m,i}}{\partial q_{s,i}} \right] \mathbf{L}_A \right)}_{\text{Term1}} \cdot (\mathbf{G}_A - \mathbf{G}_B) - 2 \underbrace{\left(\left[\frac{\partial {}^0T_{n,j}}{\partial q_{t,j}} \right] \mathbf{L}_B \right)}_{\text{Term2}} \cdot (\mathbf{G}_A - \mathbf{G}_B) \quad (A.3.7)$$

For efficient calculation, components of “Term 1” should be calculated by varying s from 1 to m considering that $q_{s,i}$ corresponds to component k of the vector “Term 1”. Components of “Term 2” should be calculated separately by varying t from 1 to n considering that $q_{t,j}$ corresponds to component k of the vector “Term 2”. Then, the vector $\frac{\partial f}{\partial q_k}$ can be calculated by adding “Term1” and “Term 2”. For efficiency of

computation, the formulas obtained for gradients in Sections A.3.1.2 and A.3.1.3 also need to be separable into two terms which contain the gradients of the locations of the first object and the second object, same as is done in this section.

A.3.1.2. Sphere-to-Infinite Cylinder Collision Avoidance Constraint

As shown in Figure A.2, d is the minimum distance between the center of the sphere and the axis of the cylinder. A is the center of the sphere with radius r_1 . B is any point on the cylinder's axis with radius r_2 . Let the global position vector of the points A and B be given by $\mathbf{G}_A = (x_A \ y_A \ z_A)^T$ and $\mathbf{G}_B = (x_B \ y_B \ z_B)^T$. Assume that sphere A and cylinder B are attached to two coordinate frames denoted respectively in the D-H table as coordinate frame number m in branch i and coordinate frame number n in branch j . Assume that the global coordinate frame in the D-H table is numbered as coordinate frame 0. Let the local position vector of the points A and B be given by $\mathbf{L}_A = (x_A \ y_A \ z_A)^T$ and $\mathbf{L}_B = (x_B \ y_B \ z_B)^T$. \mathbf{u} is the expression of the unit vector along the cylinder's axis in the global reference frame. \mathbf{L}_u is its expression in the cylinder's local coordinate frame n . Therefore, \mathbf{W} , the vector connecting point A to point B, can be written as:

$$\mathbf{W} = \mathbf{G}_B - \mathbf{G}_A$$

Now, define a vector \mathbf{h} such that: $\mathbf{h} \equiv \mathbf{W} \times \mathbf{u}$ (A.3.8)

Since \mathbf{u} is a unit vector: $|\mathbf{h}|^2 = \mathbf{h} \cdot \mathbf{h} = |\mathbf{W}|^2 \sin^2 \theta = |\mathbf{d}|^2$ (A.3.9)

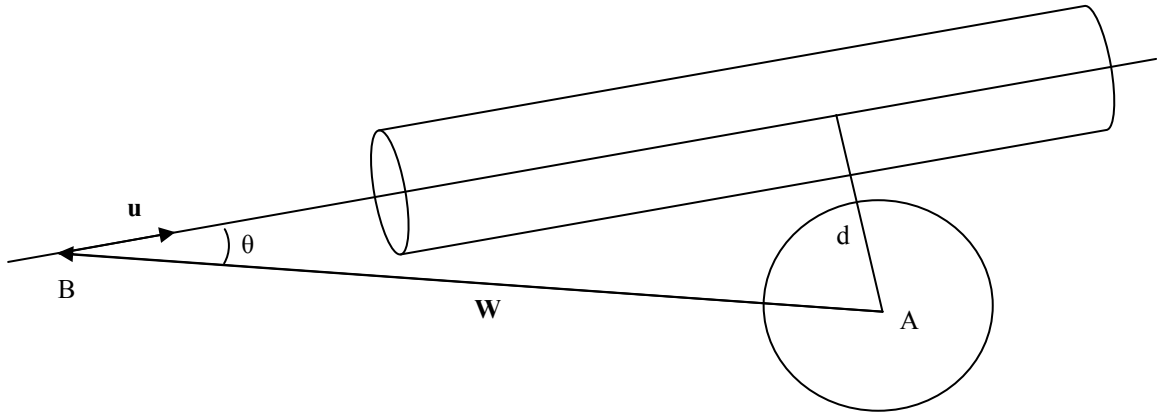


Figure A.2. Collision avoidance of a sphere with an infinite cylinder

Hence, the constraint function and the gradients can thus be calculated as:

$$f = |\mathbf{d}|^2 - (r_1 + r_2)^2 = \mathbf{h} \cdot \mathbf{h} - (r_1 + r_2)^2 \geq 0 \quad (A.3.10)$$

$$\frac{\partial f}{\partial q_k} = 2 \frac{\partial \mathbf{h}}{\partial q_k} \cdot \mathbf{h} \quad (A.3.11)$$

Calculation of f :

$$(A.3.10) \quad \Rightarrow \quad f = \mathbf{h} \cdot \mathbf{h} - (r_1 + r_2)^2 \geq 0$$

$$\text{Same as (A.3.3):} \quad \mathbf{G}_A = [{}^0T_{m,i}] \mathbf{L}_A, \quad \mathbf{G}_B = [{}^0T_{n,j}] \mathbf{L}_B \quad (A.3.12)$$

$$\mathbf{u} = [{}^0T_{n,j}] \mathbf{L}_u \quad \mathbf{W} = \mathbf{G}_B - \mathbf{G}_A, \quad \mathbf{h} = \mathbf{W} \times \mathbf{u}$$

Similar to what was done in Section A.3.1.1, we also need to separate $\frac{\partial f}{\partial q_k}$ into

two terms which contain the gradients of the locations of the first object (sphere) and the second object (cylinder):

$$(A.3.4) \Rightarrow \quad \frac{\partial \mathbf{G}_A}{\partial q_k} = \left[\frac{\partial^0 T_{m,i}}{\partial q_{s,i}} \right] \mathbf{L}_A, \quad \frac{\partial \mathbf{G}_B}{\partial q_k} = \left[\frac{\partial^0 T_{n,j}}{\partial q_{t,j}} \right] \mathbf{L}_B \quad \text{Also: } \frac{\partial \mathbf{u}}{\partial q_k} = \left[\frac{\partial^0 T_{n,j}}{\partial q_{t,j}} \right] \mathbf{L}_u$$

$$\mathbf{W} = \mathbf{G}_B - \mathbf{G}_A \Rightarrow \quad \frac{\partial \mathbf{W}}{\partial q_k} = \frac{\partial \mathbf{G}_B}{\partial q_k} - \frac{\partial \mathbf{G}_A}{\partial q_k} = \left[\frac{\partial^0 T_{n,j}}{\partial q_{t,j}} \right] \mathbf{L}_B - \left[\frac{\partial^0 T_{m,i}}{\partial q_{s,i}} \right] \mathbf{L}_A \quad (A.3.13)$$

$$(A.3.8) \Rightarrow \quad \mathbf{h} = \mathbf{W} \times \mathbf{u} \quad \Rightarrow \quad \frac{\partial \mathbf{h}}{\partial q_k} = \frac{\partial \mathbf{W}}{\partial q_k} \times \mathbf{u} + \mathbf{W} \times \frac{\partial \mathbf{u}}{\partial q_k}$$

$$\Rightarrow \quad \frac{\partial \mathbf{h}}{\partial q_k} = \left(\left[\frac{\partial^0 T_{n,j}}{\partial q_{t,j}} \right] \mathbf{L}_B - \left[\frac{\partial^0 T_{m,i}}{\partial q_{s,i}} \right] \mathbf{L}_A \right) \times \mathbf{u} + \mathbf{W} \times \left(\left[\frac{\partial^0 T_{n,j}}{\partial q_{t,j}} \right] \mathbf{L}_u \right) \quad (A.3.14)$$

$$(A.3.11) \quad \Rightarrow \quad \frac{\partial f}{\partial q_k} = 2 \frac{\partial \mathbf{h}}{\partial q_k} \cdot \mathbf{h}$$

Therefore:

$$\frac{\partial f}{\partial q_k} = 2 \left[\left(\left[\frac{\partial^0 T_{n,j}}{\partial q_{t,j}} \right] \mathbf{L}_B - \left[\frac{\partial^0 T_{m,i}}{\partial q_{s,i}} \right] \mathbf{L}_A \right) \times \mathbf{u} + \mathbf{W} \times \left(\left[\frac{\partial^0 T_{n,j}}{\partial q_{t,j}} \right] \mathbf{L}_u \right) \right] \cdot \mathbf{h} \quad (A.3.15)$$

$$\Rightarrow \frac{\partial f}{\partial q_k} = 2 \underbrace{\left[\left(\left[\frac{\partial^0 T_{n,j}}{\partial q_{t,j}} \right] \mathbf{L}_B \right) \times \mathbf{u} + \mathbf{W} \times \left(\left[\frac{\partial^0 T_{n,j}}{\partial q_{t,j}} \right] \mathbf{L}_u \right) \right] \cdot \mathbf{h}}_{\text{Term1}} - 2 \underbrace{\left[\left(\left[\frac{\partial^0 T_{m,i}}{\partial q_{s,i}} \right] \mathbf{L}_A \right) \times \mathbf{u} \right] \cdot \mathbf{h}}_{\text{Term2}} \quad (A.3.16)$$

A.3.1.3. Sphere-to-Infinite Plane Collision Avoidance Constraint

As shown in Figure A.3, d is the minimum distance from the center of the sphere to the plane. A is the sphere's center with radius r_1 . B is any point on the mid-plane of the plane with thickness $2t_2$. Let the global position vectors of the points A and B be given as

$\mathbf{G}_A = (X_A \ Y_A \ Z_A)^T$ and $\mathbf{G}_B = (X_B \ Y_B \ Z_B)^T$. Assume that sphere A and plane B are attached

to two coordinate frames denoted respectively in the D-H table as coordinate frame number m in branch i and coordinate frame number n in branch j . Assume that the global coordinate frame in the D-H table is numbered as coordinate frame 0. Let the local

position vector of the points A and B be given by $\mathbf{L}_A = (x_A \ y_A \ z_A)^T$ and $\mathbf{L}_B = (x_B \ y_B \ z_B)^T$. \mathbf{u} is the expression of the unit vector perpendicular to the plane in the global frame. \mathbf{L}_u is its expression in the plane's local coordinate frame n . \mathbf{W} is the vector connecting A to B. The constraint function f that should be kept positive to avoid collision and its gradients with respect to the design variables can be calculated as:

$$\mathbf{W} = \mathbf{G}_B - \mathbf{G}_A \quad d = \mathbf{W} \cdot \mathbf{u}$$

$$f = d^2 - (r_1 + t_2)^2 = (\mathbf{W} \cdot \mathbf{u})^2 - (r_1 + t_2)^2 \geq 0 \quad (A.3.17)$$

$$\frac{\partial f}{\partial q_k} = 2(\mathbf{W} \cdot \mathbf{u}) \left(\frac{\partial \mathbf{W}}{\partial q_k} \cdot \mathbf{u} + \mathbf{W} \cdot \frac{\partial \mathbf{u}}{\partial q_k} \right) \quad (A.3.18)$$

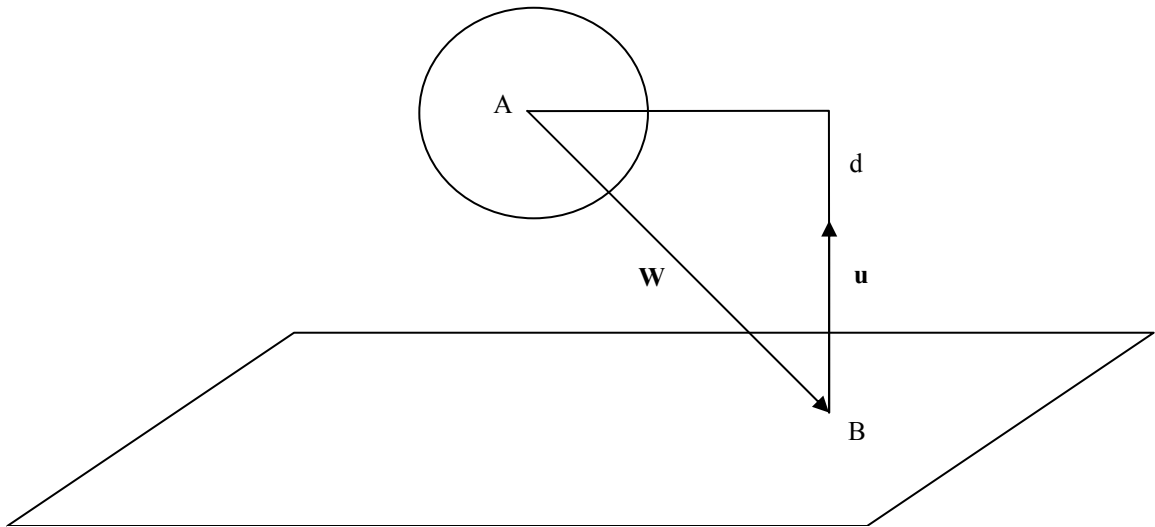


Figure A.3. Collision avoidance of a sphere with an infinite plane

Calculation of f :

$$(A.3.17) \Rightarrow f = (\mathbf{W} \cdot \mathbf{u})^2 - (r_1 + t_2)^2 \geq 0$$

Same as (A.3.3): $\mathbf{G}_A = [{}^0T_{m,i}] \mathbf{L}_A$, $\mathbf{G}_B = [{}^0T_{n,j}] \mathbf{L}_B$

$$\mathbf{u} = [{}^0T_{n,j}] \mathbf{L}_u, \quad \mathbf{W} = \mathbf{G}_B - \mathbf{G}_A \quad (A.3.19)$$

Similar to what was done in Section A.3.1.1, we also need to separate $\frac{\partial f}{\partial q_k}$ into

two terms which contain the gradients of the locations of the first object (sphere) and the second object (plane):

$$(A.3.4) \Rightarrow \frac{\partial \mathbf{G}_A}{\partial q_k} = \left[\frac{\partial {}^0T_{m,i}}{\partial q_{s,i}} \right] \mathbf{L}_A, \quad \frac{\partial \mathbf{G}_B}{\partial q_k} = \left[\frac{\partial {}^0T_{n,j}}{\partial q_{t,j}} \right] \mathbf{L}_B, \quad \frac{\partial \mathbf{u}}{\partial q_k} = \left[\frac{\partial {}^0T_{n,j}}{\partial q_{t,j}} \right] \mathbf{L}_u$$

$$\mathbf{W} = \mathbf{G}_B - \mathbf{G}_A \Rightarrow \frac{\partial \mathbf{W}}{\partial q_k} = \frac{\partial \mathbf{G}_B}{\partial q_k} - \frac{\partial \mathbf{G}_A}{\partial q_k} = \left[\frac{\partial {}^0T_{n,j}}{\partial q_{t,j}} \right] \mathbf{L}_B - \left[\frac{\partial {}^0T_{m,i}}{\partial q_{s,i}} \right] \mathbf{L}_A \quad (A.3.20)$$

$$(A.3.18) \Rightarrow \frac{\partial f}{\partial q_k} = 2(\mathbf{W} \cdot \mathbf{u}) \left(\frac{\partial \mathbf{W}}{\partial q_k} \cdot \mathbf{u} + \mathbf{W} \cdot \frac{\partial \mathbf{u}}{\partial q_k} \right)$$

Therefore:

$$\frac{\partial f}{\partial q_k} = 2d \left[\left(\left[\frac{\partial {}^0T_{n,j}}{\partial q_{t,j}} \right] \mathbf{L}_B - \left[\frac{\partial {}^0T_{m,i}}{\partial q_{s,i}} \right] \mathbf{L}_A \right) \cdot \mathbf{u} + \mathbf{W} \cdot \left(\left[\frac{\partial {}^0T_{n,j}}{\partial q_{t,j}} \right] \mathbf{L}_u \right) \right]$$

$$\Rightarrow \frac{\partial f}{\partial q_k} = 2d \underbrace{\left[\left(\left[\frac{\partial {}^0T_{n,j}}{\partial q_{t,j}} \right] \mathbf{L}_B \right) \cdot \mathbf{u} + \mathbf{W} \cdot \left(\left[\frac{\partial {}^0T_{n,j}}{\partial q_{t,j}} \right] \mathbf{L}_u \right) \right]}_{\text{Term1}} - 2d \underbrace{\left[\left(\left[\frac{\partial {}^0T_{m,i}}{\partial q_{s,i}} \right] \mathbf{L}_A \right) \cdot \mathbf{u} \right]}_{\text{Term2}} \quad (A.3.21)$$

A.3.1.4. Infinite Cylinder-to-Infinite Cylinder Collision Avoidance Constraint

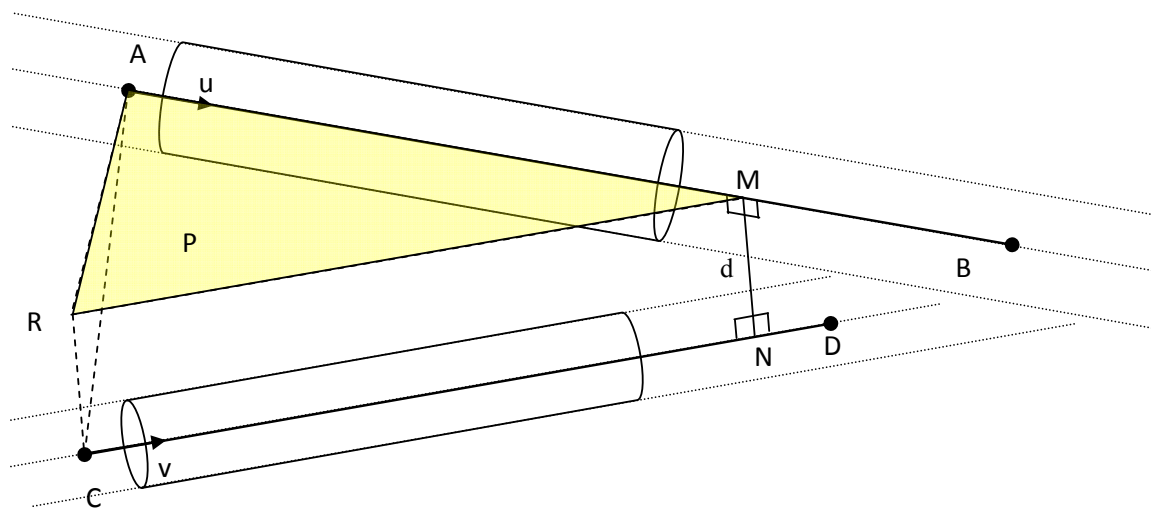


Figure A.4. The collision avoidance of two infinite cylinders

As shown in Figure A.4, d is the minimum distance between the axes of the cylinders. A and B are any two points on the first cylinder's axis with radius r_1 . C and D are any two points on the second cylinder's axis with radius r_2 . Let the global position vector of the points A, B, C and D be given by $\mathbf{G}_A, \mathbf{G}_B, \mathbf{G}_C$ and \mathbf{G}_D . Assume that cylinder AB and cylinder CD are attached to two coordinate frames denoted respectively in the D-H table as coordinate frame number m in branch i and coordinate frame number n in branch j . Assume that the global coordinate frame in the D-H table is numbered as coordinate frame 0. Let the local position vector of the points A, B, C and D be given by $\mathbf{L}_A, \mathbf{L}_B, \mathbf{L}_C$ and \mathbf{L}_D . \mathbf{u} and \mathbf{v} are respectively the expression of the unit vectors along the axis of cylinders AB and CD in the global frame. \mathbf{L}_u and \mathbf{L}_v are respectively their

expressions in the cylinders' local coordinate frames m and n . Let $\mathbf{w} = \mathbf{u} \times \mathbf{v}$. Therefore,

$$\text{we shall have: } \mathbf{w} = \frac{\overline{MN}}{\|\overline{MN}\|}$$

Create a plane containing line AB and with a perpendicular unit vector \mathbf{w} and call it the plane P . Select point R on plane P such that $\overline{RC} \perp P$. Then, we shall have:

$$\left. \begin{array}{l} P \perp \overline{RC} \\ P \perp \overline{MN} \\ RC \parallel P \end{array} \right\} \Rightarrow \left\{ \begin{array}{l} \overline{RC} \parallel \overline{MN} \\ \|\overline{RC}\| = \|\overline{MN}\| \end{array} \right. \Rightarrow \overline{RC} = \overline{MN}$$

$$\overline{AC} \cdot \overline{RC} = \|\overline{RC}\|^2 \Rightarrow \overline{AC} \cdot \overline{MN} = \|\overline{MN}\|^2 \Rightarrow \|\overline{MN}\| = \overline{AC} \cdot \mathbf{w}$$

$$\Rightarrow d^2 = \|\overline{MN}\|^2 = \overline{AC} \cdot (\mathbf{u} \times \mathbf{v}) \quad , \quad \overline{AC} = \mathbf{G}_C - \mathbf{G}_A \quad (A.3.22)$$

$$\frac{\partial d^2}{\partial q_k} = \frac{\partial \overline{AC}}{\partial q_k} \cdot (\mathbf{u} \times \mathbf{v}) + \overline{AC} \cdot \left(\frac{\partial \mathbf{u}}{\partial q_k} \times \mathbf{v} \right) + \overline{AC} \cdot \left(\mathbf{u} \times \frac{\partial \mathbf{v}}{\partial q_k} \right)$$

$$\text{Same as (A.3.4): } \left\{ \begin{array}{l} \frac{\partial \mathbf{G}_A}{\partial q_k} = \left[\frac{\partial^0 T_{m,i}}{\partial q_{s,i}} \right] \mathbf{L}_A \\ \frac{\partial \mathbf{u}}{\partial q_k} = \left[\frac{\partial^0 T_{m,i}}{\partial q_{s,i}} \right] \mathbf{L}_u \\ \frac{\partial \mathbf{G}_C}{\partial q_k} = \left[\frac{\partial^0 T_{n,j}}{\partial q_{t,j}} \right] \mathbf{L}_C \\ \frac{\partial \mathbf{v}}{\partial q_k} = \left[\frac{\partial^0 T_{n,j}}{\partial q_{t,j}} \right] \mathbf{L}_v \end{array} \right. \quad (A.3.23)$$

$$\Rightarrow \frac{\partial d^2}{\partial q_i} = \left(\left[\frac{\partial^0 T_{n,j}}{\partial q_{t,j}} \right] \mathbf{L}_C - \left[\frac{\partial^0 T_{m,i}}{\partial q_{s,i}} \right] \mathbf{L}_A \right) \cdot (\mathbf{u} \times \mathbf{v}) + \overline{AC} \cdot \left(\left[\frac{\partial^0 T_{m,i}}{\partial q_{s,i}} \right] \mathbf{L}_u \times \mathbf{v} \right) + \overline{AC} \cdot \left(\mathbf{u} \times \left[\frac{\partial^0 T_{n,j}}{\partial q_{t,j}} \right] \mathbf{L}_v \right)$$

$$\Rightarrow \frac{\partial d^2}{\partial q_i} = \underbrace{\left[\overline{AC} \cdot \left(\left[\frac{\partial^0 T_{m,i}}{\partial q_{s,i}} \right] \mathbf{L}_u \times \mathbf{v} \right) - \left[\frac{\partial^0 T_{m,i}}{\partial q_{s,i}} \right] \mathbf{L}_A \cdot (\mathbf{u} \times \mathbf{v}) \right]}_{\text{Term1}}$$

$$+ \underbrace{\left[\overline{AC} \cdot \left(\mathbf{u} \times \left[\frac{\partial^0 T_{n,j}}{\partial q_{t,j}} \right] \mathbf{L}_v \right) + \left[\frac{\partial^0 T_{n,j}}{\partial q_{t,j}} \right] \mathbf{L}_C \cdot (\mathbf{u} \times \mathbf{v}) \right]}_{\text{Term2}} \quad (A.3.24)$$

A.3.2. Constraints for Collision Avoidance Between Two Compound Primitives

The primitives presented in Section A.3.1 can also be combined to produce compound primitives like finite cylinders (smoothed) and finite planes (smoothed) with constraints that have C^1 continuity. The constraints used for such compound primitives are discussed in this section.

A.3.2.1. Sphere-to-Finite Cylinder Collision Avoidance Constraint

First, the region of the location of the sphere with respect to the finite cylinder as shown in Figure A.5 is determined by evaluating the scalar products of vectors \mathbf{a} , \mathbf{b} with vector \mathbf{c} using Table A.1. Based on the region, the value and all the gradients of the collision avoidance constraint are set equal to one of the following constraints:

At Region 1: Sphere-to-Infinite Cylinder

At Regions 2,3 : Sphere-to-Sphere

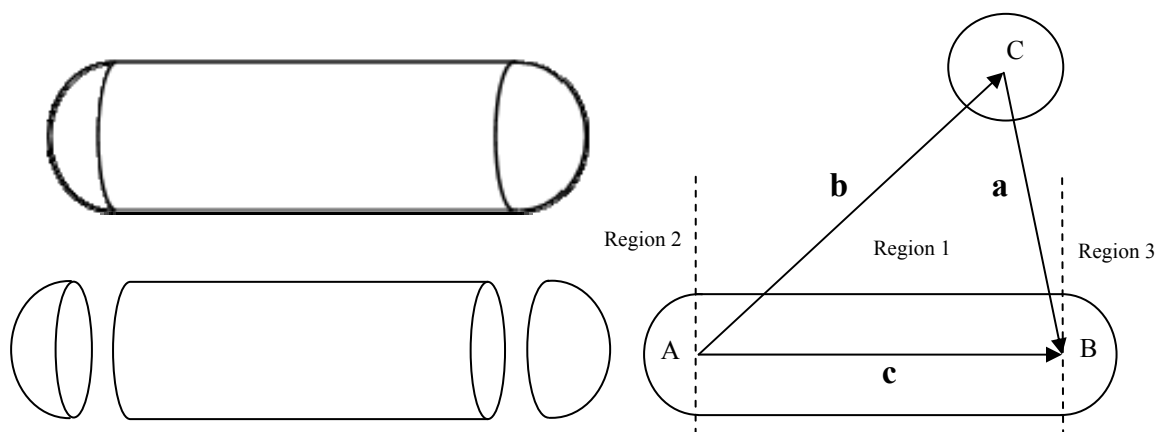


Figure A.5. Smoothed finite cylinder, regions defined around it and its collision avoidance with a sphere

Region Number	a.c	b.c
1	+	+
2	+	-
3	-	+

Table. A.1. Determining region of the location of the sphere with respect to the finite cylinder

A.3.2.2. Sphere-to-Finite Plane Collision Avoidance Constraint

First, the region of the location of the sphere with respect to the finite plane as shown in Figures A.6 and A.7 is determined by evaluating the scalar product of vectors $\mathbf{a}, \mathbf{b}, \mathbf{c}, \mathbf{d}$ with vectors \mathbf{u}, \mathbf{v} using Table A.2. Based on the region, value and gradients of the collision avoidance constraint are set equal to one of the following constraints:

At Region 1: Sphere-to-Infinite Plane

At Regions 6, 7, 8, 9: Sphere-to-Sphere

At Regions 2, 3, 4, 5: Sphere-to-Infinite Cylinder

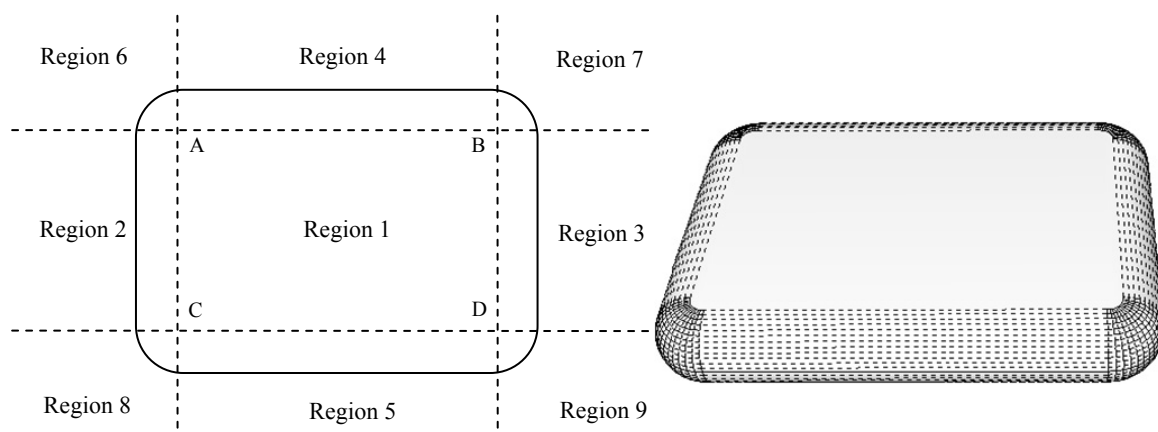


Figure A.6. Smoothed finite plane with the regions defined around it

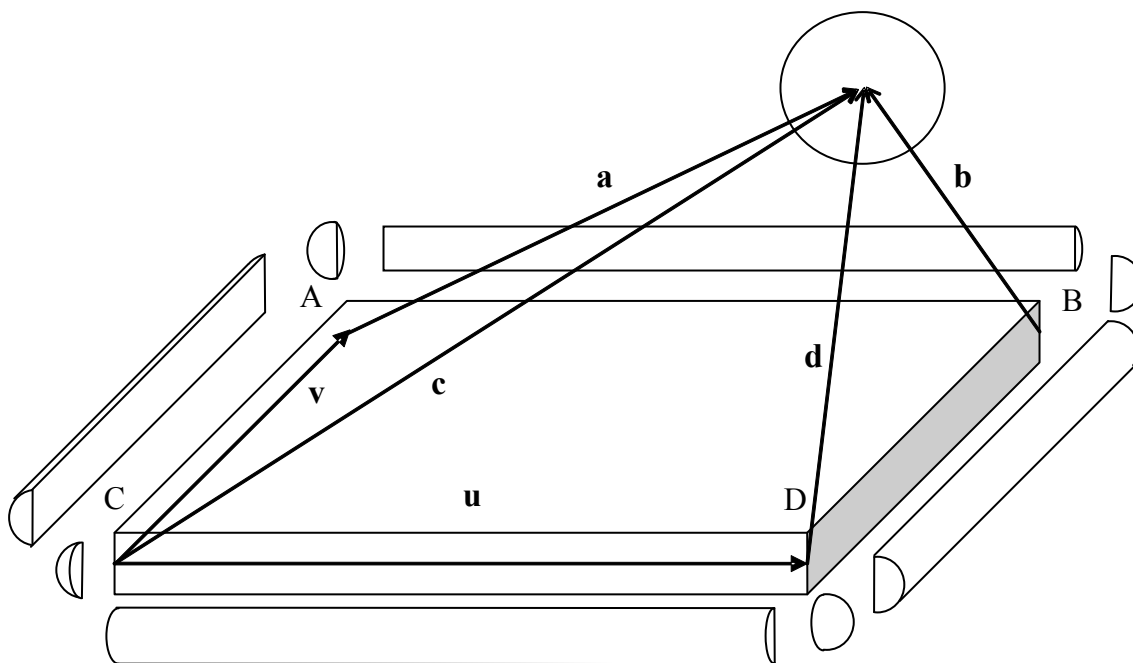


Figure A.7. Finite plane (smoothed) to sphere collision avoidance

Region #	$a.u$	$b.u$	$c.u$	$d.u$	$a.v$	$b.v$	$c.v$	$d.v$
1	+	-	+	-	-	-	+	+
2	-	-	-	-	-	-	+	+
3	+	+	+	+	-	-	+	+
4	+	-	+	-	+	+	+	+
5	+	-	+	-	-	-	-	-
6	-	-	-	-	+	+	+	+
7	+	+	+	+	+	+	+	+
8	-	-	-	-	-	-	-	-
9	+	+	+	+	-	-	-	-

Table. A.2. Determining region of the location of the sphere with respect to the finite plane

A.3.2.3. Finite Cylinder-to-Finite Cylinder Collision Avoidance Constraint

In brief, this problem turns into:

- 1- Find the minimum distance between the two line segments AB, CD.
- 2- Calculate the gradient of that minimum distance.

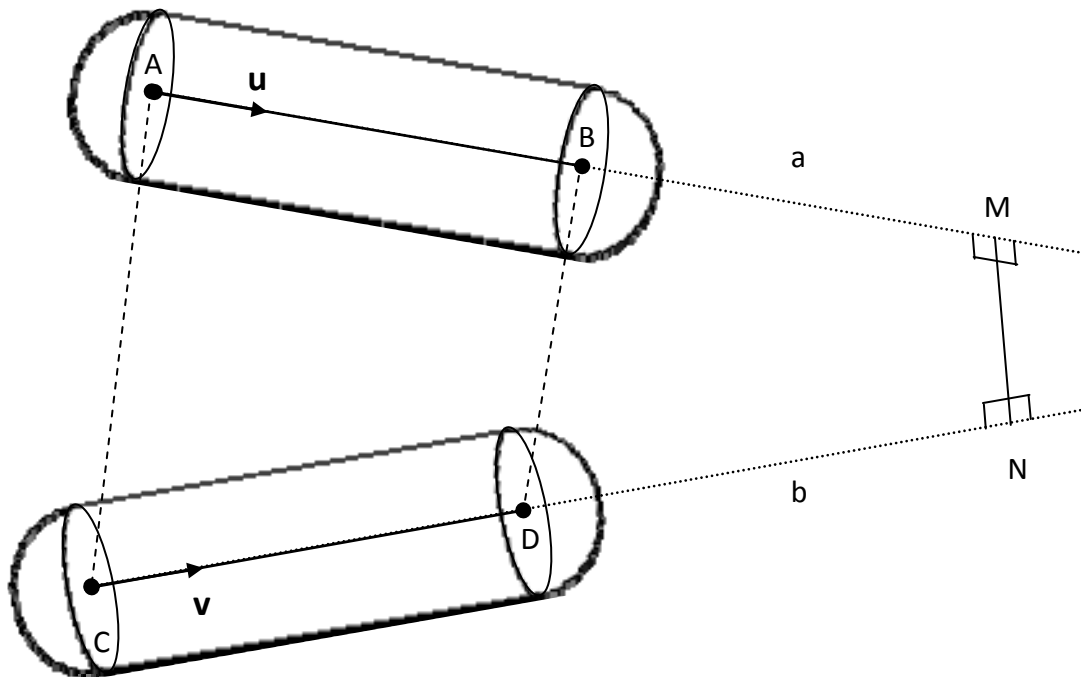


Figure A.8. The collision avoidance of two finite cylinders

CASE 1)

Minimum distance of the two infinite lines passing through A, B and C, D occurs on points between A, B on AB and points C, D on CD. Below, we calculate the requirements for this case to occur:

$$\left. \begin{array}{l} \vec{M} = \vec{A} + a\mathbf{u} \\ \vec{N} = \vec{C} + b\mathbf{v} \end{array} \right\} \Rightarrow \overline{MN} = \vec{A} + a\mathbf{u} - \vec{C} - b\mathbf{v} \quad (A.3.25)$$

$$\text{Minimizing } \|\overline{MN}\| : \begin{cases} \frac{\partial \|\overline{MN}\|^2}{\partial a} = 0 & \Rightarrow \mathbf{u} \cdot (\vec{A} + a\mathbf{u} - \vec{C} - b\mathbf{v}) = 0 \\ \frac{\partial \|\overline{MN}\|^2}{\partial b} = 0 & \Rightarrow \mathbf{v} \cdot (\vec{A} + a\mathbf{u} - \vec{C} - b\mathbf{v}) = 0 \end{cases}$$

$$\Rightarrow \begin{cases} a - (\mathbf{u} \cdot \mathbf{v})b = \mathbf{u} \cdot \vec{C} - \mathbf{u} \cdot \vec{A} \\ (\mathbf{u} \cdot \mathbf{v})a - b = \mathbf{v} \cdot \vec{C} - \mathbf{v} \cdot \vec{A} \end{cases} \Rightarrow \begin{cases} a = \frac{k_2 - k_1 k_3}{1 - k_1^2} \\ b = \frac{k_1 k_2 - k_3}{1 - k_1^2} \end{cases} \quad (A.3.26)$$

$$\text{Where: } \begin{cases} k_1 = \mathbf{u} \cdot \mathbf{v} \\ k_2 = \mathbf{u} \cdot \overline{AC} \\ k_3 = \mathbf{v} \cdot \overline{AC} \end{cases}$$

For the minimum distance of the two infinite cylinders to occur on points between A, B on AB and points C, D on CD, we should have:

$$\begin{cases} 0 < a < \|\overline{AB}\| \\ 0 < b < \|\overline{CD}\| \end{cases} \quad (A.3.27)$$

CASE 2)

This case should be studied, if the requirements for Case 1 do not exist. In this case, we should perform the four operations listed below without calculating the gradients. Whichever case has the minimum distance, we should set the constraint value equal to that distance and calculate the gradients from the formula for that case:

1. Collision Detection of Sphere A to Finite Cylinder CD
2. Collision Detection of Sphere B to Finite Cylinder CD
3. Collision Detection of Sphere C to Finite Cylinder AB
4. Collision Detection of Sphere D to Finite Cylinder AB

A.3.2.4. Finite Cylinder-to-Finite Plane Collision Avoidance Constraint

In brief, these cases need to be considered:

CASE 1)

The only possibility for the minimum distance to occur between the cylindrical part of the finite cylinder Q and the planar part of finite plane P is that the axis of the finite cylinder Q intersects the mid-plane of the finite plane P . This case is depicted in Figure A.9 and can be checked via the following formulation:

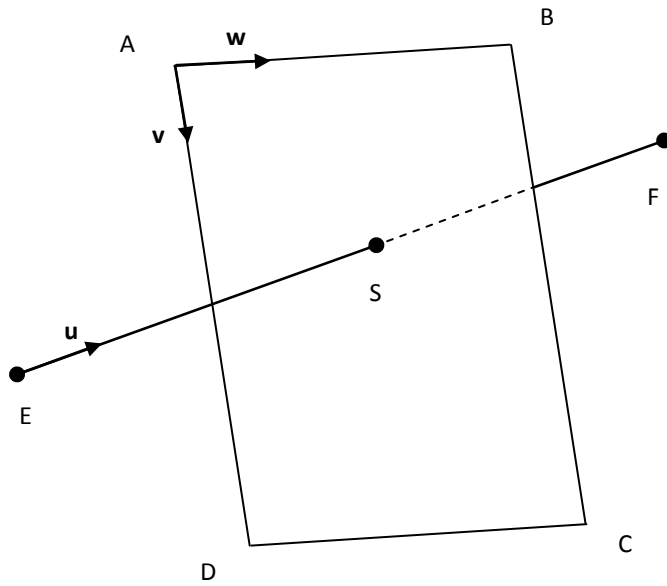


Figure A.9. The collision avoidance of a finite cylinders with a finite plane

$$\left. \begin{aligned} \vec{S} &= k_2 \mathbf{v} + k_3 \mathbf{w} + \vec{A} \\ \vec{S} &= \vec{E} + k_1 \mathbf{u} \end{aligned} \right\} \Rightarrow \vec{E} + k_1 \mathbf{u} = k_2 \mathbf{v} + k_3 \mathbf{w} + \vec{A} \quad (A.3.28)$$

$$\begin{bmatrix} u_x & -v_x & -w_x \\ u_y & -v_y & -w_y \\ u_z & -v_z & -w_z \end{bmatrix} \begin{Bmatrix} k_1 \\ k_2 \\ k_3 \end{Bmatrix} = \begin{Bmatrix} A_x - E_x \\ A_y - E_y \\ A_z - E_z \end{Bmatrix} \Rightarrow \begin{Bmatrix} k_1 \\ k_2 \\ k_3 \end{Bmatrix} = \begin{bmatrix} u_x & -v_x & -w_x \\ u_y & -v_y & -w_y \\ u_z & -v_z & -w_z \end{bmatrix}^{-1} \begin{Bmatrix} A_x - E_x \\ A_y - E_y \\ A_z - E_z \end{Bmatrix} \quad (A.3.29)$$

In order for the line to intersect the mid-plane of the finite plane, we should have:

$$\begin{cases} 0 \leq k_1 \leq \|\vec{EF}\| \\ 0 \leq k_2 \leq \|\vec{BC}\| \\ 0 \leq k_3 \leq \|\vec{AB}\| \end{cases} \quad (A.3.30)$$

In this case, the minimum distance between the finite cylinder Q and the finite plane P is equal to $-\left(r + \frac{t}{2}\right)$ where r is the radius of the finite cylinder and t is the thickness of the finite plane. Also, the distance gradient is zero with respect to all design variables.

CASE 2)

1. Decompose the finite plane B into sets $W = \{4 \text{ spheres}\}$, $V = \{4 \text{ cylindrical parts of finite cylinder}\}$. For whichever element of V that the minimum distance occurs on the lines (same as Section A.3.2.3, Case 1), calculate that distance and ignore the spheres at the end of the cylindrical part for all the rest of calculations. For other elements of V, ignore the cylindrical part and calculate distances as (Section A.3.2.3, CASE 2).
2. Decompose the finite cylinder A into 2 spheres and ignore the cylindrical part. If any sphere is located in Region1 of finite plane B, calculate the distance.

At the end, the case with the minimum distance determines the value and gradients of the constraint.

A.3.2.5. Finite Plane-to-Finite Plane Collision Avoidance Constraint

There is no condition that the minimum distance occurs between the plane parts of both finite planes. In brief, the method given below is proposed to handle such a case:

1. Ignore the planar part of finite plane, A (only consider the additional finite planes and spheres used for smoothing its edges), decompose it into 4 finite cylinders and perform 4 instances of (finite cylinder and finite plane B) collision avoidance without calculating the gradients.
2. Ignore the planar part of finite plane B (only consider the additional finite planes and spheres used for smoothing its edges), decompose it into sets $W = \{4 \text{ spheres}\}$, $V = \{4 \text{ cylindrical parts of finite cylinder}\}$. If any sphere of W is located in Region 1 of finite plane A, calculate the distance. If the axis of any member of V intersects the mid-plane of finite plane A, stop and calculate according to (Section A.3.2.3, CASE 1).

At the end, the case with the minimum distance determines the value and gradients of the constraint.

A.4. Test Results

We test the proposed obstacle avoidance constraints within the framework of predictive dynamics and observe the results:

Simulation 1: The results of using the self avoidance modules in the predictive dynamics code is shown in Figure A.10. The segments of the human avatar are filled with spheres. The task shown below is a complicated task that requires the avatar to kneel down and touch the right knee with left hand and touch the left midfoot with its right hand. This task cannot be simulated correctly unless self-avoidance constraint is properly modeled and implemented in the predictive dynamics code.



Figure A.10. The test task with sphere to sphere self collision avoidance

Simulation 2: This task requires the avatar to move its hand from sphere A located at the top of a table to sphere B at the bottom of the table. Figure A.11 shows the result of the simulation without using any collision avoidance constraints.

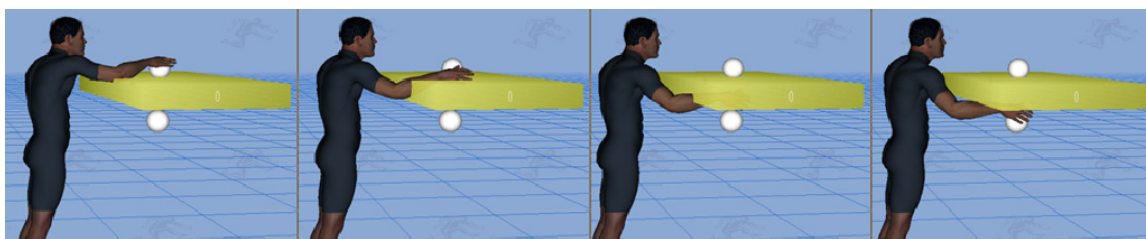


Figure A.11. Result of simulation without imposing obstacle avoidance constraints

Simulation 3: This task also requires the avatar to move its hand from sphere A located at the top of the table to sphere B located at the bottom of the table. The table is modeled as a finite plane. The right arm is filled with 7 spheres and so, 7 sphere-to-finite plane collision avoidance constraints are imposed during the motion. The cost function minimized for this motion is a combination of dynamics effort and total displacement. Figure A.12 shows the result of using the mentioned collision avoidance constraints.

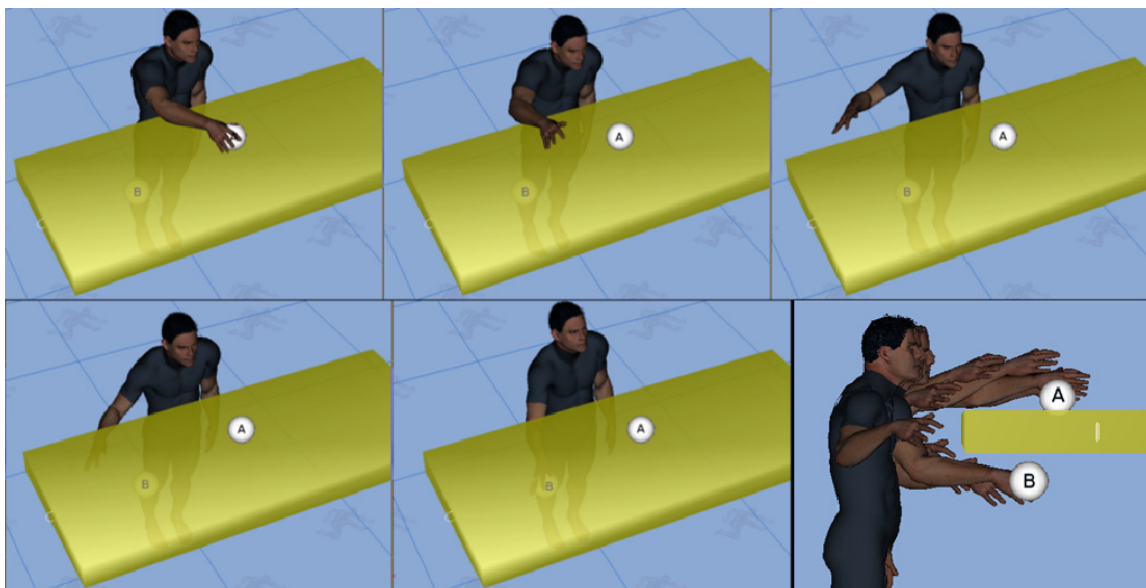


Figure A.12. Result of simulation after imposing obstacle avoidance constraints

A.5. Conclusion

In this appendix, it was proved that any shape may be used for object definition in optimization-based collision avoidance as long as the shape's surface is convex and has no edges (C^1 surface) so that the gradients of the obstacle avoidance constraint (minimum distance between the surfaces) are continuous. Finite cylinders and finite planes have edges which violates the continuity requirements. These edges of the finite cylinder and finite plane can be smoothed out by combining their surfaces with parts of the surfaces of spheres and cylinders as was shown in Sections A.3.2.1 and A.3.2.2. We call these objects compound primitives. Implementation of other compound objects as shown in Figure A.13 can be considered as topics of future research.

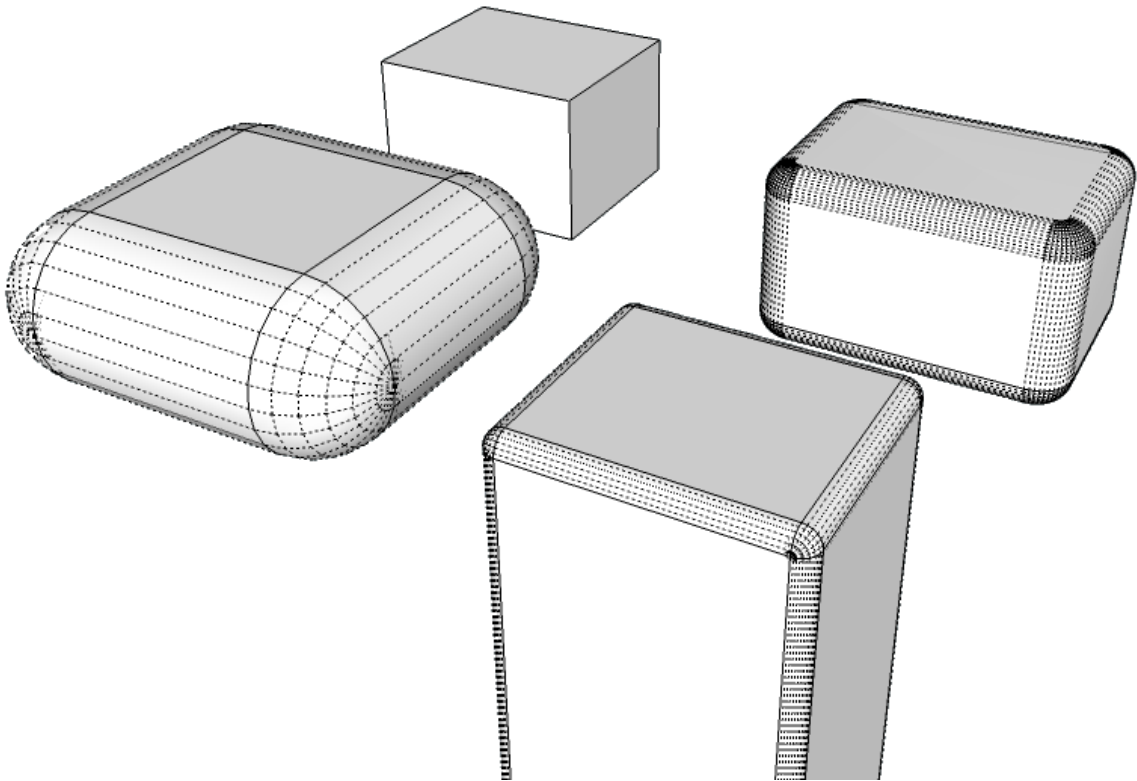


Figure A.13. An edged box (unsuitable), a finite plane, a 1-sided finite plane, a box (smoothed)

A.5. Theorems on Optimization-Based Collision
Avoidance

Definition Set A.1: ***Witness Points of Minimum Distance***

P and Q are rigid bodies whose motions are functions of q_i ($i = 1 \dots n$). Witness points of minimum distance between these two rigid bodies called A, B are defined as the points respectively on P, Q between which the minimum distance of P, Q occurs at any q_i . We denote the global position of points A, B at any q_i by $\mathbf{A}(q_i)$ and $\mathbf{B}(q_i)$.

$A'_{q_{i_0}}$ and $B'_{q_{i_0}}$ are defined as the footprint points of A, B on P, Q for $q_i = q_{i_0}$. $A'_{q_{i_0}}$ and $B'_{q_{i_0}}$ are points attached to the surfaces of P, Q which move with P, Q. We denote the global position of $A'_{q_{i_0}}$ and $B'_{q_{i_0}}$ by $\mathbf{A}'_{q_{i_0}}(q_i)$ and $\mathbf{B}'_{q_{i_0}}(q_i)$. Since $A'_{q_{i_0}}$ and $B'_{q_{i_0}}$ are the footprints of A, B at $q_i = q_{i_0}$, the following conditions hold:

$$\left\{ \mathbf{A}'_{q_{i_0}}(q_{i_0}) = \mathbf{A}(q_{i_0}) \quad , \quad \mathbf{B}'_{q_{i_0}}(q_{i_0}) = \mathbf{B}(q_{i_0}) \right\} \quad (A.6.1)$$

Theorem A.1: ***Continuity of the Minimum Distance***

Using Definition Set A.1, the minimum distance between any 2 rigid bodies P, Q is a continuous function of q_i .

Proof:

The footprints of A, B at $q_i = q_{i_0}$ shown by $\mathbf{A}'_{q_{i_0}}(q_i)$ and $\mathbf{B}'_{q_{i_0}}(q_i)$ are continuous functions of q_i due to the rules of rigid body motion. The minimum distance between P, Q at $q_i = q_{i_0}$ is called $d_{q_{i_0}}$, and therefore:

$$\begin{aligned} \forall \Delta q_i : d_{q_{i_0}} &= \|\overline{AB}\| = \|\mathbf{B}'_{q_{i_0}}(q_{i_0}) - \mathbf{A}'_{q_{i_0}}(q_{i_0})\| \leq \|\mathbf{B}'_{q_{i_0} + \Delta q_i}(q_{i_0}) - \mathbf{A}'_{q_{i_0} + \Delta q_i}(q_{i_0})\| \\ \lim_{\Delta q_i \rightarrow 0} d_{q_{i_0} + \Delta q_i} &= \lim_{\Delta q_i \rightarrow 0} \|\mathbf{B}'_{q_{i_0} + \Delta q_i}(q_{i_0} + \Delta q_i) - \mathbf{A}'_{q_{i_0} + \Delta q_i}(q_{i_0} + \Delta q_i)\| \geq d_{q_{i_0}} \end{aligned} \quad (A.6.2)$$

The minimum distance between P, Q at $q_i = q_{i_0} + \Delta q_i$ is equal to $d_{q_{i_0} + \Delta q_i}$ and so:

$$d_{q_{i_0} + \Delta q_i} = \|\overline{AB}\| = \|\mathbf{B}'_{q_{i_0} + \Delta q_i}(q_{i_0} + \Delta q_i) - \mathbf{A}'_{q_{i_0} + \Delta q_i}(q_{i_0} + \Delta q_i)\| \quad (A.6.3)$$

$$d_{q_{i_0} + \Delta q_i} = \|\mathbf{B}'_{q_{i_0} + \Delta q_i}(q_{i_0} + \Delta q_i) - \mathbf{A}'_{q_{i_0} + \Delta q_i}(q_{i_0} + \Delta q_i)\| \leq \|\mathbf{B}'_{q_{i_0}}(q_{i_0} + \Delta q_i) - \mathbf{A}'_{q_{i_0}}(q_{i_0} + \Delta q_i)\|$$

$$\lim_{\Delta q_i \rightarrow 0} d_{q_{i_0} + \Delta q_i} \leq \lim_{\Delta q_i \rightarrow 0} \|\mathbf{B}'_{q_{i_0}}(q_{i_0}) - \mathbf{A}'_{q_{i_0}}(q_{i_0})\| = d_{q_{i_0}} \quad (A.6.4)$$

And therefore:

$$(A.6.2) \text{ and } (A.6.4) \Rightarrow \lim_{\Delta q_i \rightarrow 0} d_{q_{i_0} + \Delta q_i} = d_{q_{i_0}} \quad (A.6.5)$$

Theorem A.2: ***Continuity of the Witness Point Locations***

Using Definition Set A.1, if P has a convex surface and Q has a strictly convex surface, then the locations of A, B are continuous function of q_i .

Proof:

For any q_i :

$$(A.3) \Rightarrow d_{q_i} = \|\mathbf{B}'_{q_i}(q_i) - \mathbf{A}'_{q_i}(q_i)\| \leq \|\mathbf{B}'_{q_i+\Delta q_i}(q_i) - \mathbf{A}'_{q_i+\Delta q_i}(q_i)\| \quad (A.6.6)$$

and

$$d_{q_i+\Delta q_i} = \|\mathbf{B}'_{q_i+\Delta q_i}(q_i + \Delta q_i) - \mathbf{A}'_{q_i+\Delta q_i}(q_i + \Delta q_i)\| \leq \|\mathbf{B}'_{q_i}(q_i + \Delta q_i) - \mathbf{A}'_{q_i}(q_i + \Delta q_i)\| \quad (A.6.7)$$

Since $\|\mathbf{B}'_{q_i}(q_i) - \mathbf{A}'_{q_i}(q_i)\|$ and $\|\mathbf{B}'_{q_i+\Delta q_i}(q_i) - \mathbf{A}'_{q_i+\Delta q_i}(q_i)\|$ are continuous functions of q_i according to Theorem A.1, then there exists some $0 < \alpha < 1$ such that:

$$\begin{aligned} \|\mathbf{B}'_{q_i}(q_i + \alpha\Delta q_i) - \mathbf{A}'_{q_i}(q_i + \alpha\Delta q_i)\| &= \|\mathbf{B}'_{q_i+\Delta q_i}(q_i + \alpha\Delta q_i) - \mathbf{A}'_{q_i+\Delta q_i}(q_i + \alpha\Delta q_i)\| \geq d_{q_i+\alpha\Delta q_i} \\ \lim_{\Delta q_i \rightarrow 0} d_{q_i+\alpha\Delta q_i} &= \lim_{\Delta q_i \rightarrow 0} d_{q_i} = \lim_{\Delta q_i \rightarrow 0} \|\mathbf{B}'_{q_i}(q_i + \alpha\Delta q_i) - \mathbf{A}'_{q_i}(q_i + \alpha\Delta q_i)\| \\ \Rightarrow \lim_{\Delta q_i \rightarrow 0} d_{q_i+\Delta q_i} &= \lim_{\Delta q_i \rightarrow 0} \|\mathbf{B}'_{q_i+\Delta q_i}(q_i + \alpha\Delta q_i) - \mathbf{A}'_{q_i+\Delta q_i}(q_i + \alpha\Delta q_i)\| \quad (A.6.8) \end{aligned}$$

Because P is convex, one can pass a planar surface through $\mathbf{A}'_{q_i}(q_i + \alpha\Delta q_i)$ and $\mathbf{A}'_{q_i+\Delta q_i}(q_i + \alpha\Delta q_i)$ such that all points on that surface belong to P. Also, since Q is strictly convex, one can pass a spherical cap through $\mathbf{B}'_{q_i}(q_i + \alpha\Delta q_i)$ and $\mathbf{B}'_{q_i+\Delta q_i}(q_i + \alpha\Delta q_i)$ with the convex side of the cap towards the plane that we have passed through P such that all points on that cap belong to Q.

But as shown in Figure A.14, and if $|\Delta q_i| \ll 1$ the minimum distance between P,

Q ($\lim_{\Delta q_i \rightarrow 0} d_{q_i+\alpha\Delta q_i}$) is equal to the value calculated in Equation (A.6.8), if and only if:

$$\begin{cases} \lim_{\Delta q_i \rightarrow 0} \mathbf{A}'_{q_i}(q_i + \alpha\Delta q_i) = \lim_{\Delta q_i \rightarrow 0} \mathbf{A}'_{q_i+\Delta q_i}(q_i + \alpha\Delta q_i) \\ \lim_{\Delta q_i \rightarrow 0} \mathbf{B}'_{q_i}(q_i + \alpha\Delta q_i) = \lim_{\Delta q_i \rightarrow 0} \mathbf{B}'_{q_i+\Delta q_i}(q_i + \alpha\Delta q_i) \end{cases} \quad (A.6.9)$$

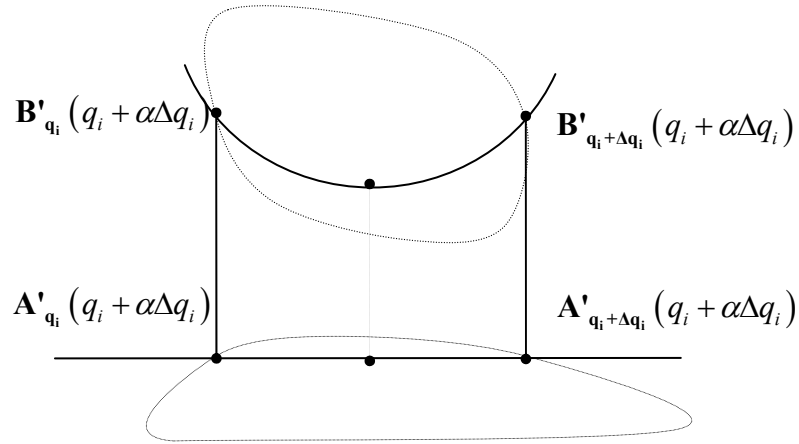


Figure A.14. Continuity of witness points positions as a result of surface convexity

On the other hand, $\mathbf{A}'_{q_i}(q_i)$ and $\mathbf{B}'_{q_i}(q_i)$ are continuous functions of q_i due to the rules of rigid body motion as stated in Theorem A.1 and therefore:

$$\left\{ \begin{array}{l} \lim_{\Delta q_i \rightarrow 0} \mathbf{A}'_{q_i}(q_i + \alpha \Delta q_i) = \mathbf{A}'_{q_i}(q_i) = \mathbf{A}(q_i) \\ \lim_{\Delta q_i \rightarrow 0} \mathbf{A}'_{q_i + \Delta q_i}(q_i + \alpha \Delta q_i) = \lim_{\Delta q_i \rightarrow 0} \mathbf{A}'_{q_i + \Delta q_i}(q_i + \Delta q_i) = \lim_{\Delta q_i \rightarrow 0} \mathbf{A}(q_i + \Delta q_i) \end{array} \right. \quad (A.6.10)$$

$$\left\{ \begin{array}{l} \lim_{\Delta q_i \rightarrow 0} \mathbf{B}'_{q_i}(q_i + \alpha \Delta q_i) = \mathbf{B}'_{q_i}(q_i) = \mathbf{B}(q_i) \\ \lim_{\Delta q_i \rightarrow 0} \mathbf{B}'_{q_i + \Delta q_i}(q_i + \alpha \Delta q_i) = \lim_{\Delta q_i \rightarrow 0} \mathbf{B}'_{q_i + \Delta q_i}(q_i + \Delta q_i) = \lim_{\Delta q_i \rightarrow 0} \mathbf{B}(q_i + \Delta q_i) \end{array} \right. \quad (A.6.11)$$

Therefore:

$$\left. \begin{array}{l} (A.6.9) \text{ and } (A.6.10) \Rightarrow \lim_{\Delta q_i \rightarrow 0} \mathbf{A}(q_i + \Delta q_i) = \mathbf{A}(q_i) \\ (A.6.9) \text{ and } (A.6.11) \Rightarrow \lim_{\Delta q_i \rightarrow 0} \mathbf{B}(q_i + \Delta q_i) = \mathbf{B}(q_i) \end{array} \right\} \Rightarrow \mathbf{A}(q_i), \mathbf{B}(q_i) \text{ are continuous}$$

For an alternative proof for Theorem A.2, you can see Escande (2007).

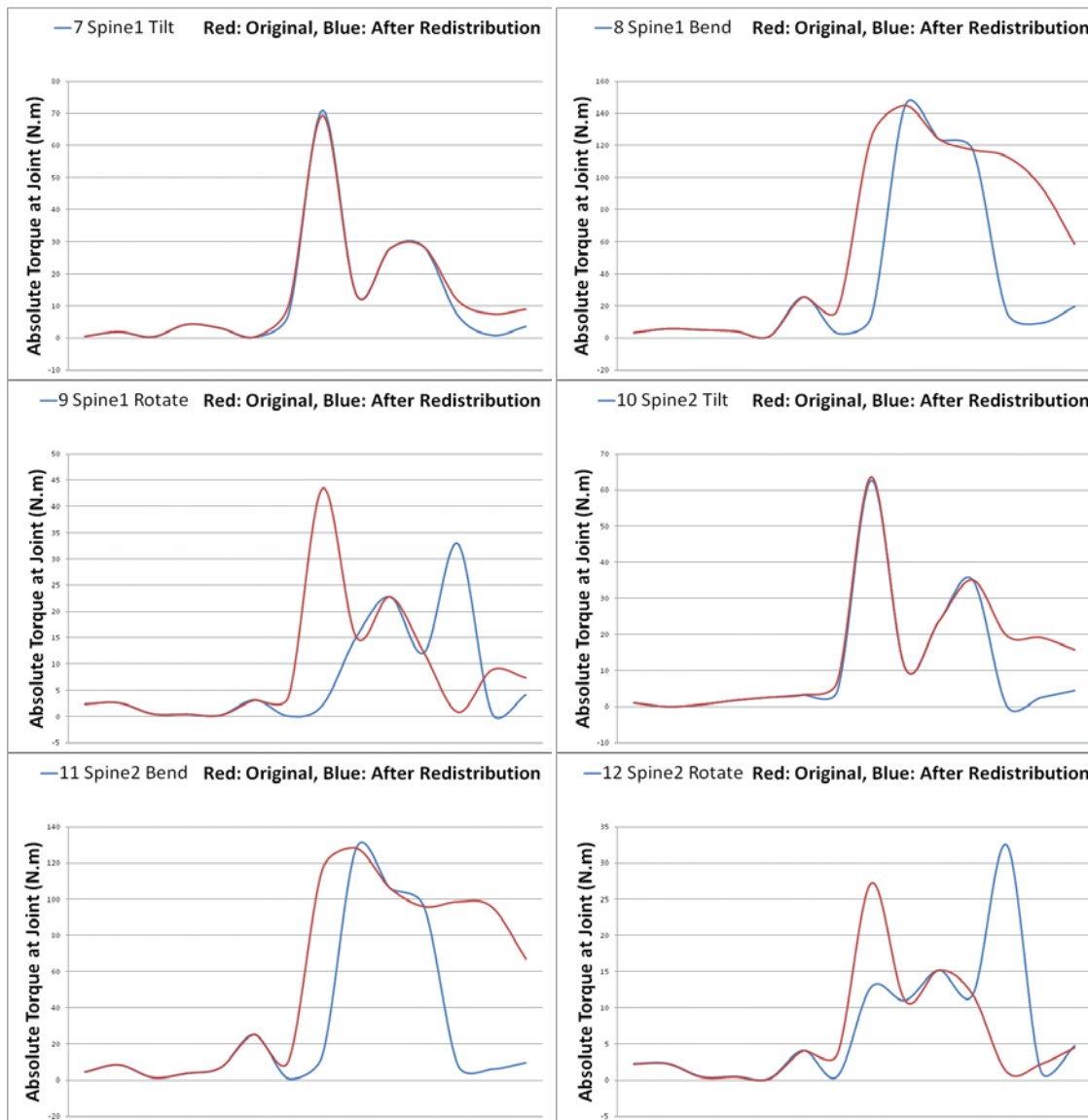
Theorem A.3: *Differentiability of the Minimum distance*

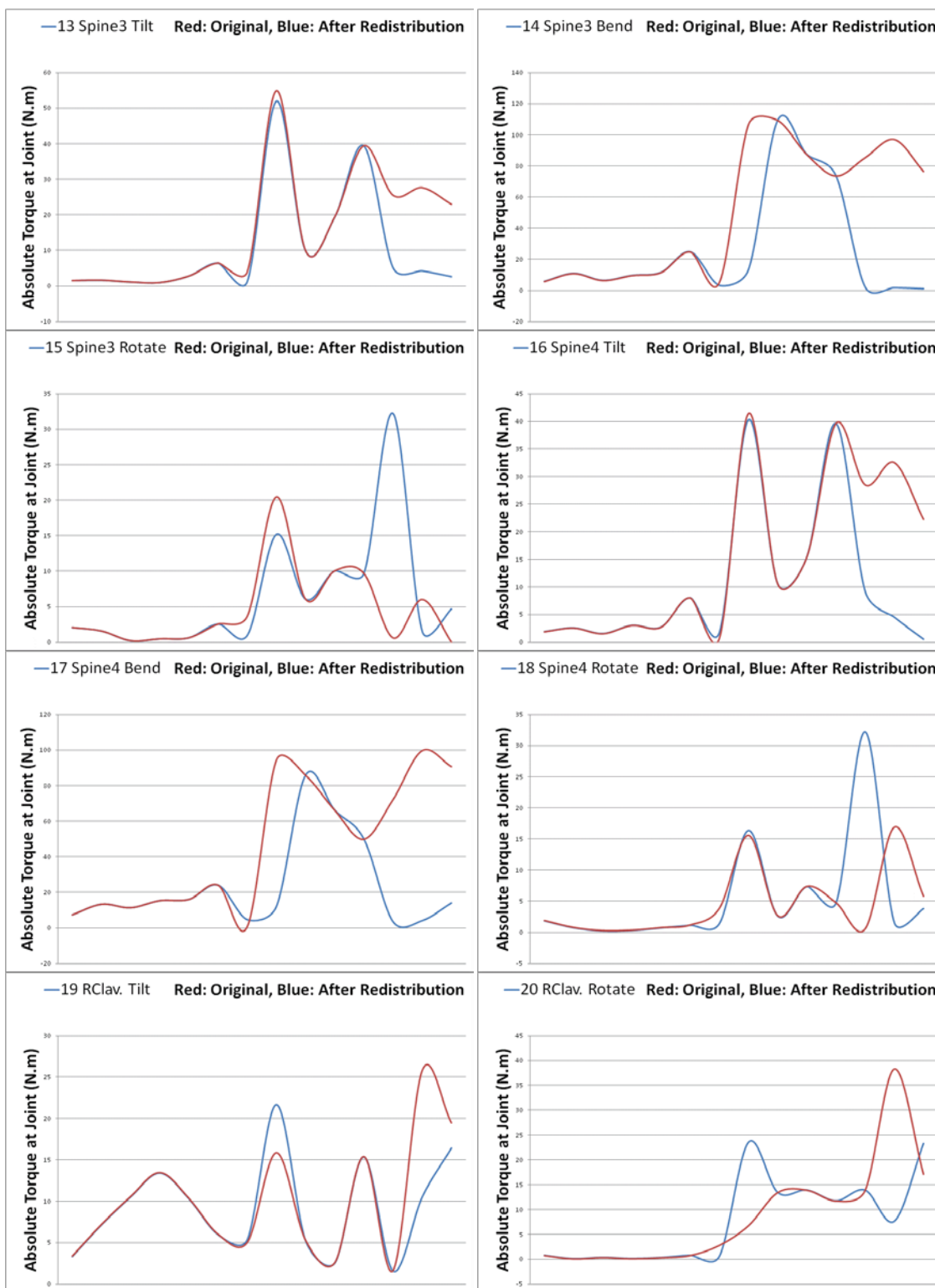
If P has a C^1 convex surface and Q has a C^1 strictly convex surface, then the minimum distance between P, Q is a C^1 function of q_i

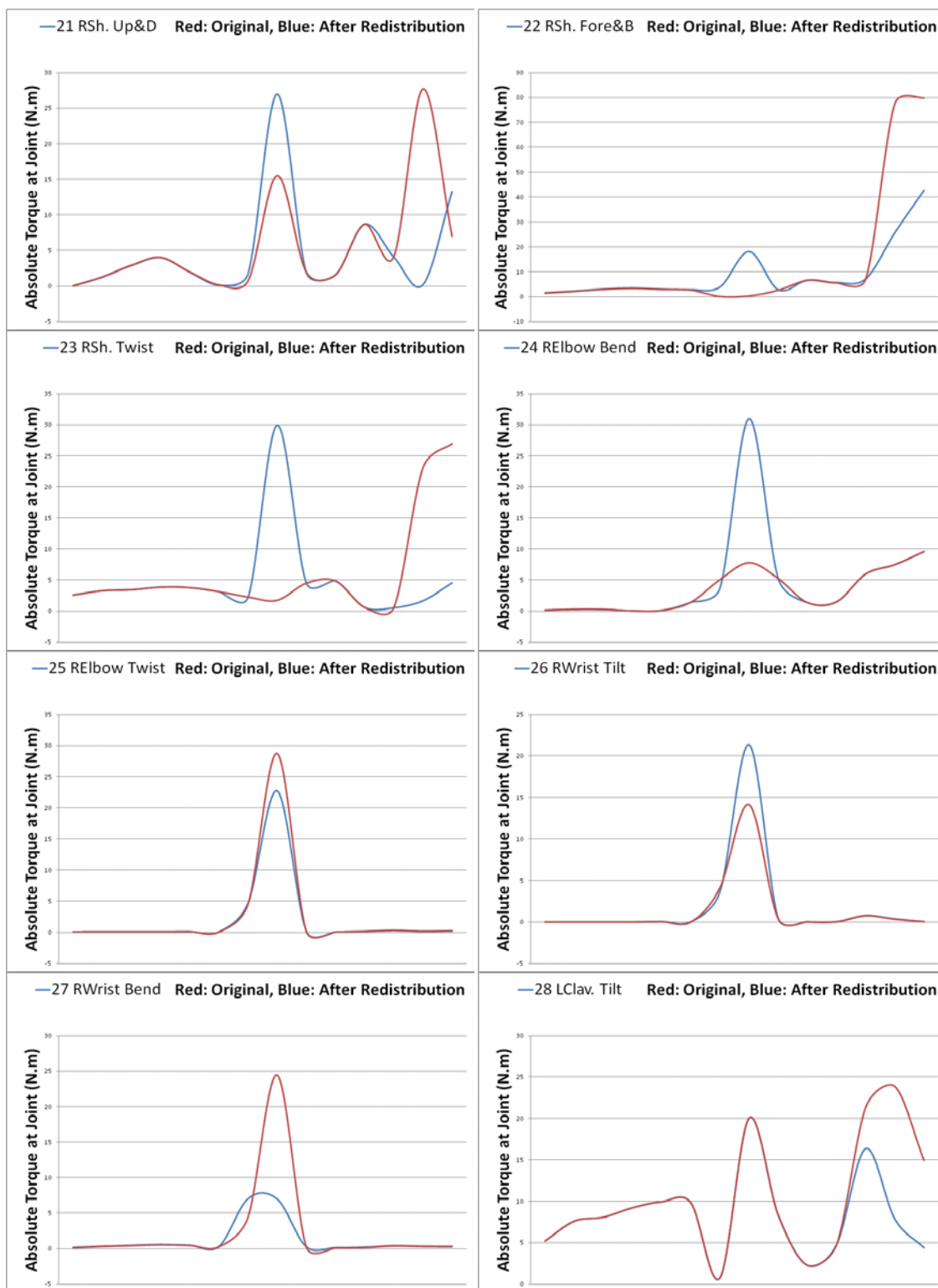
Proof:

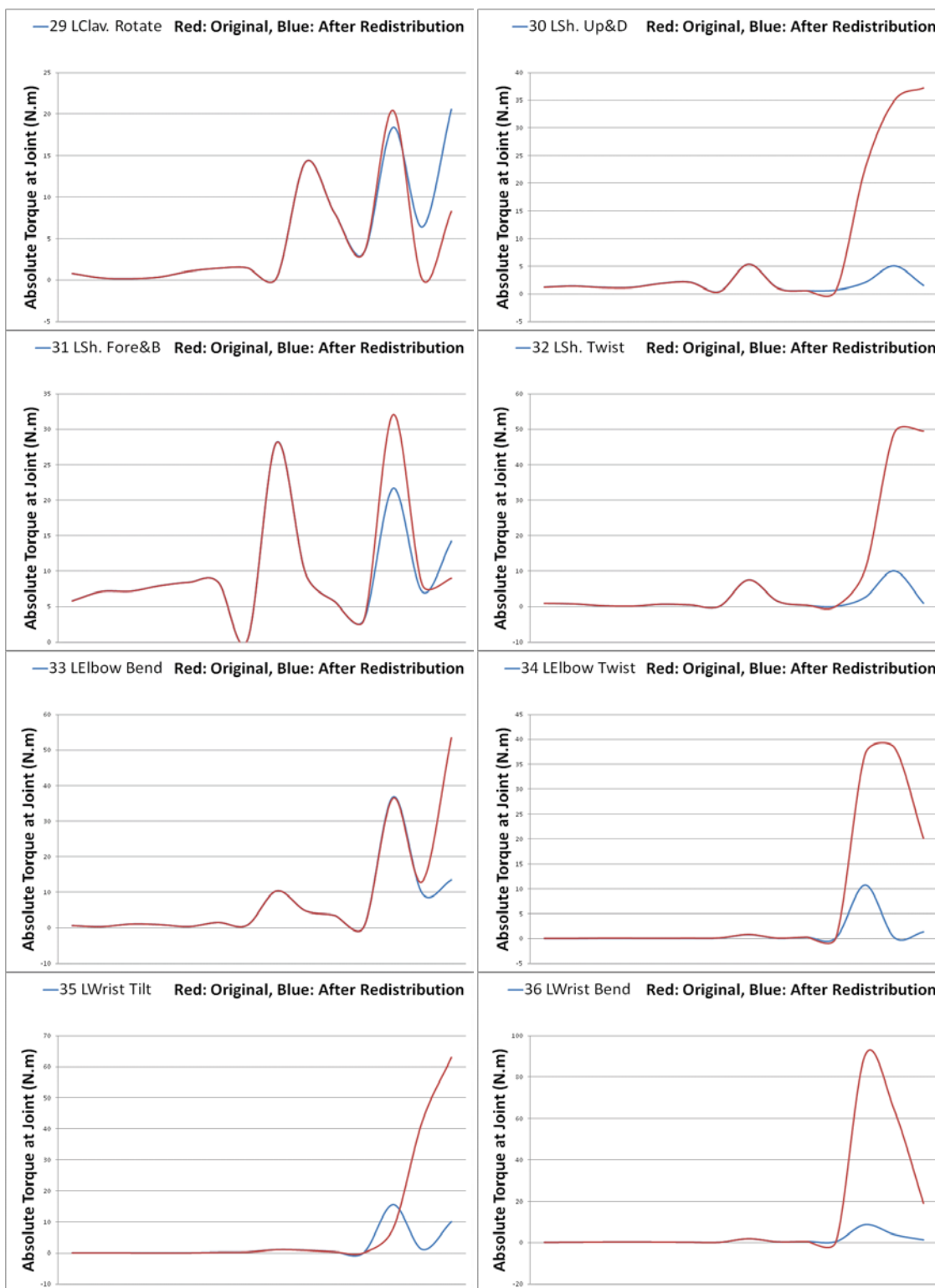
According to Theorem A.2, the witness points A, B move on continuous paths on P, Q during the motion. These paths are C^1 , because they are located on P, Q. Therefore $\mathbf{A}(q_i)$ and $\mathbf{B}(q_i)$ and therefore the minimum distance between P, Q are also C^1 functions of q_i .

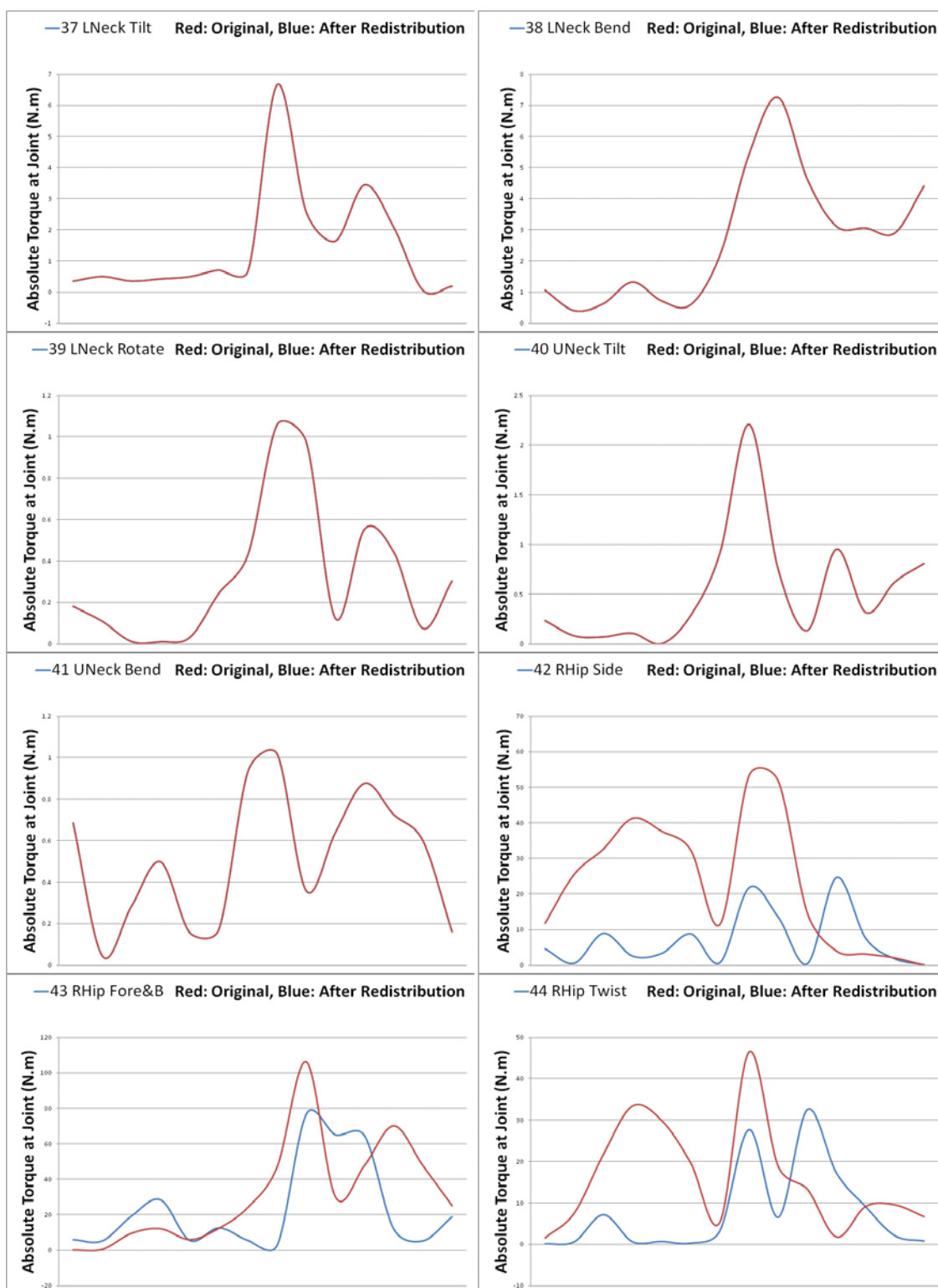
APPENDIX B

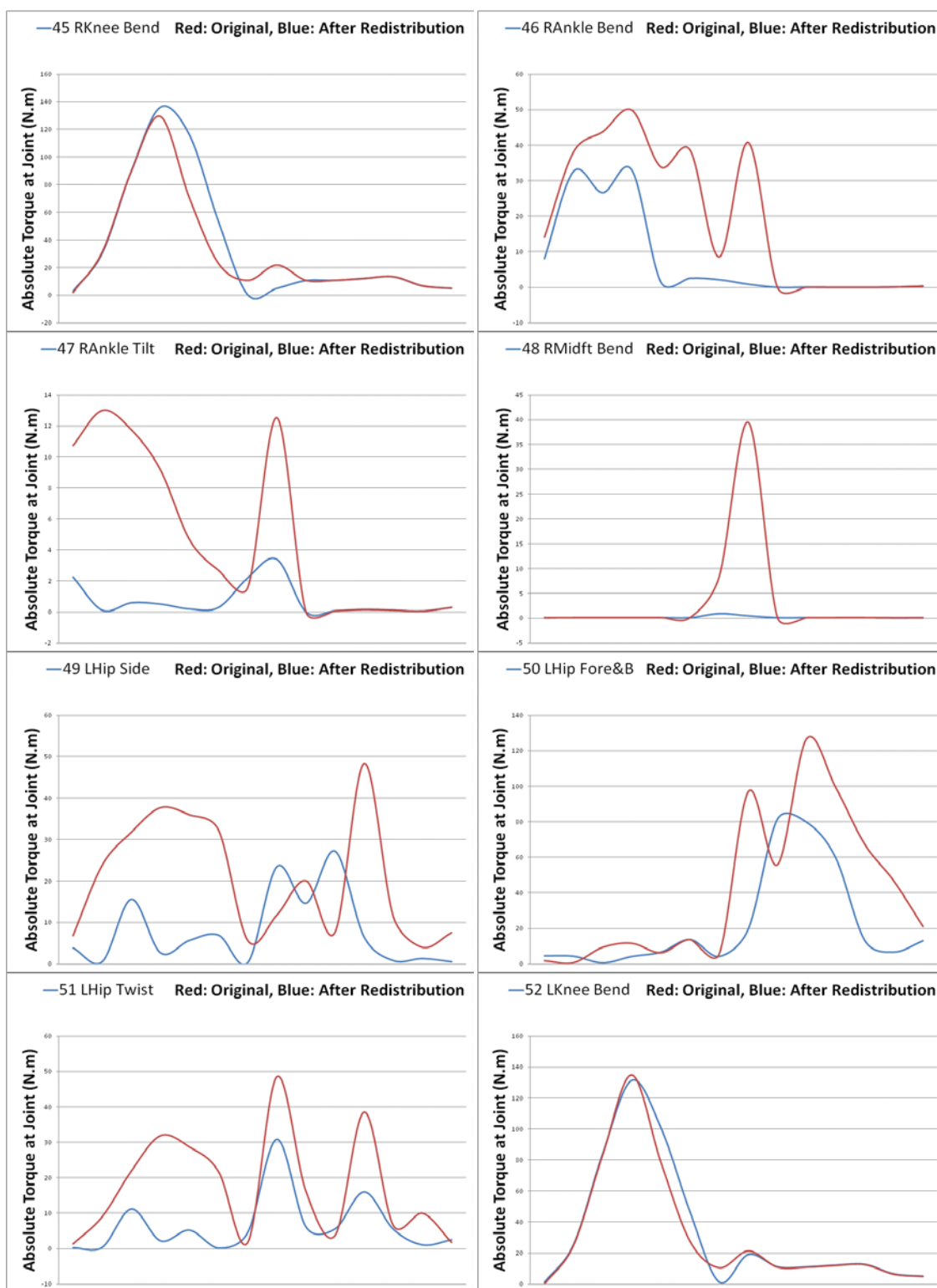
COMPARISON OF JOINT TORQUES BEFORE AND AFTER RE-PARTITIONING
IN THE SAMPLE TASK IN CHAPTER 9

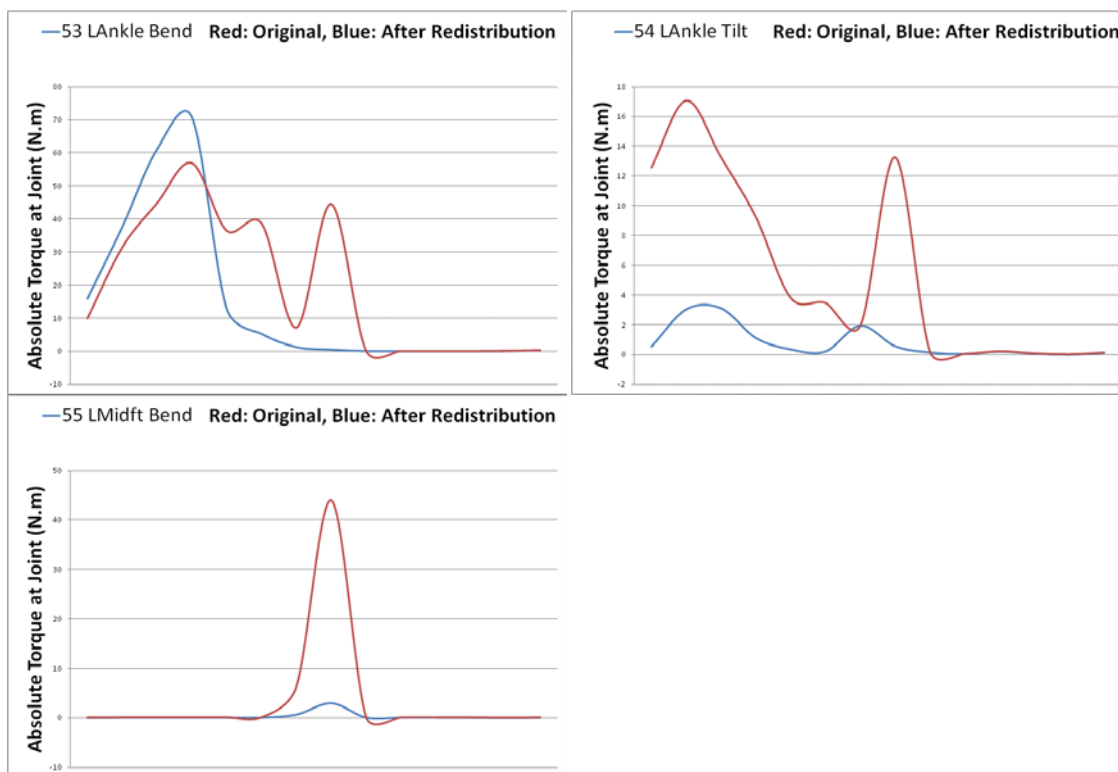






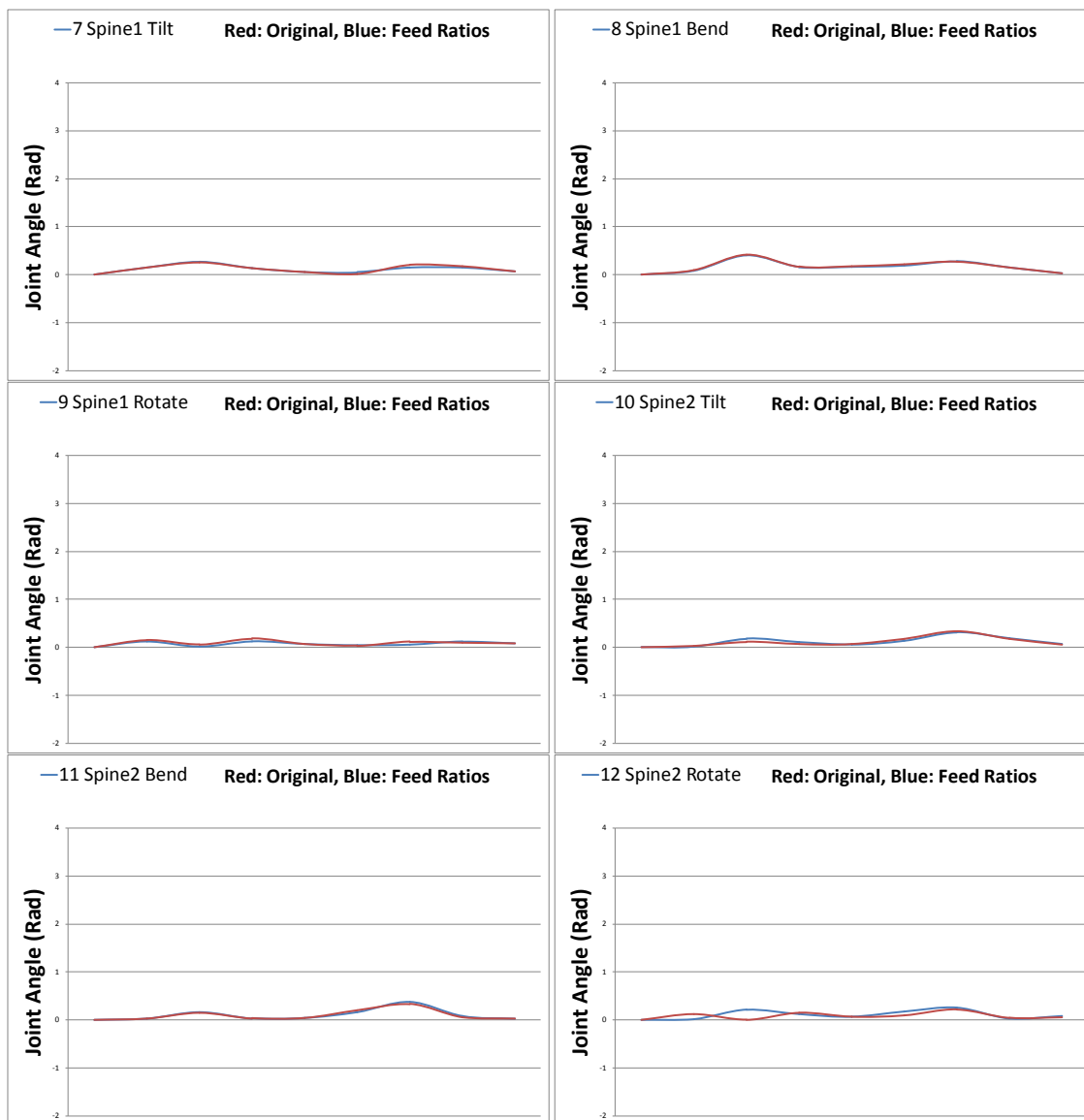


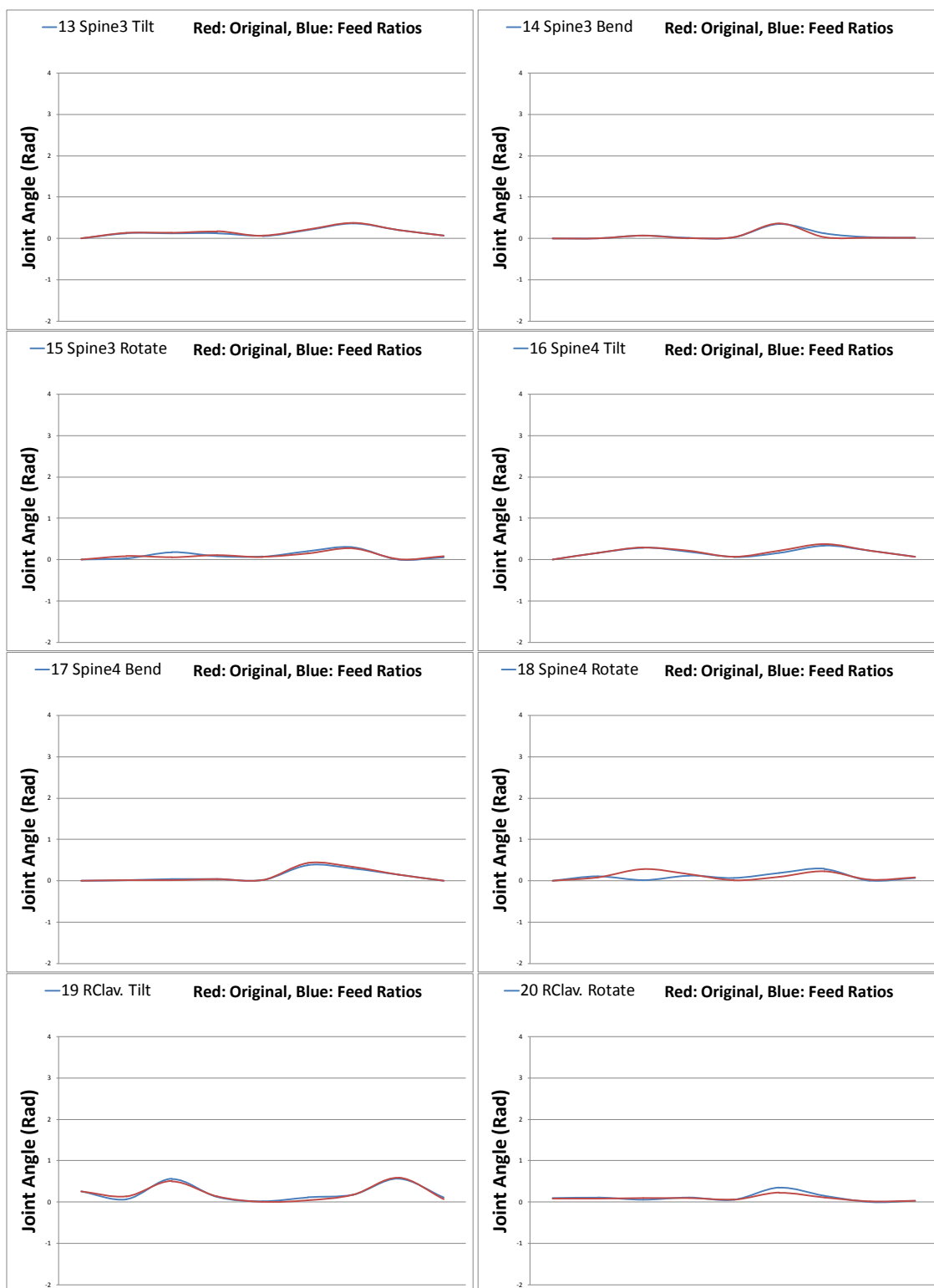


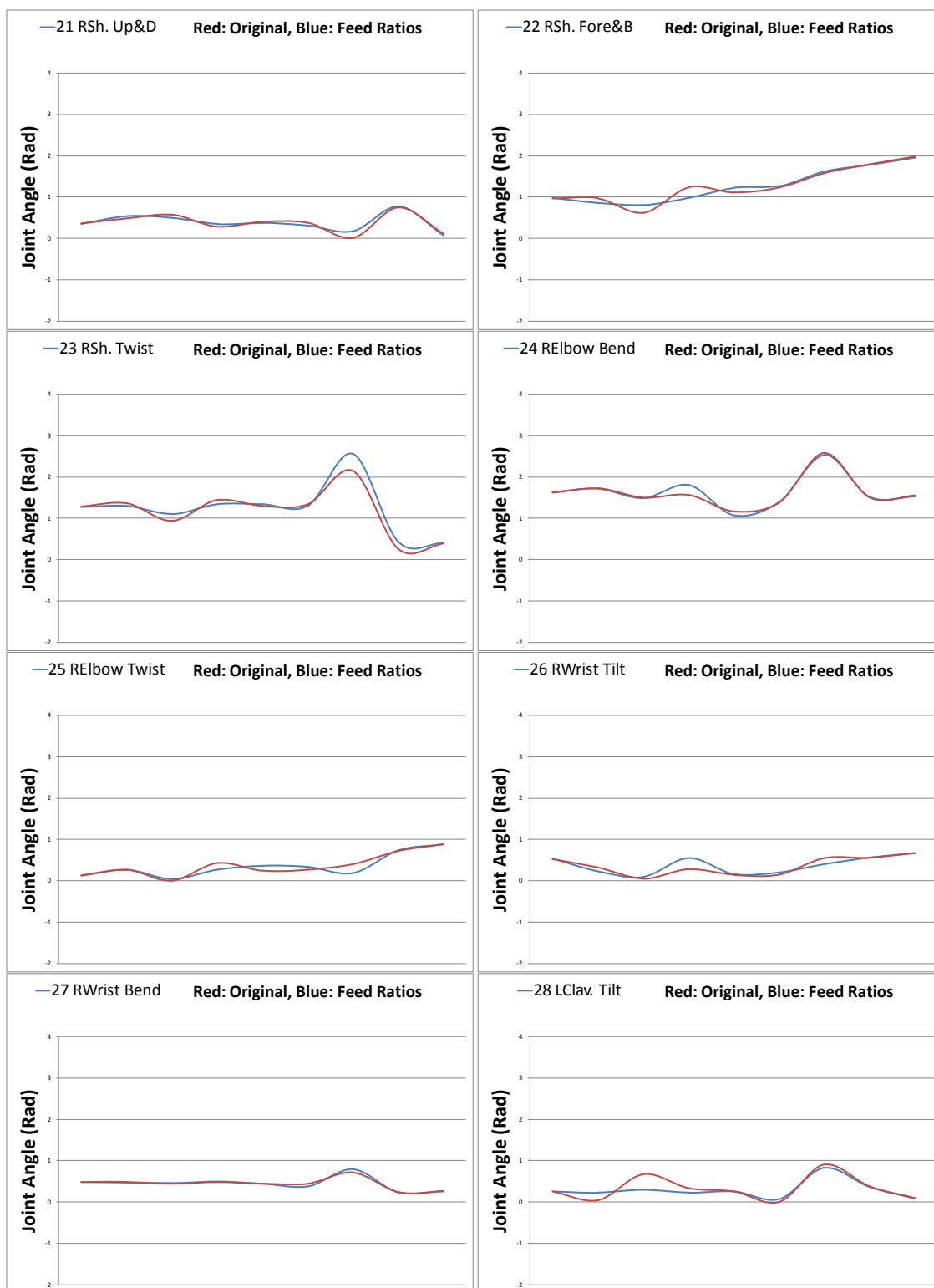


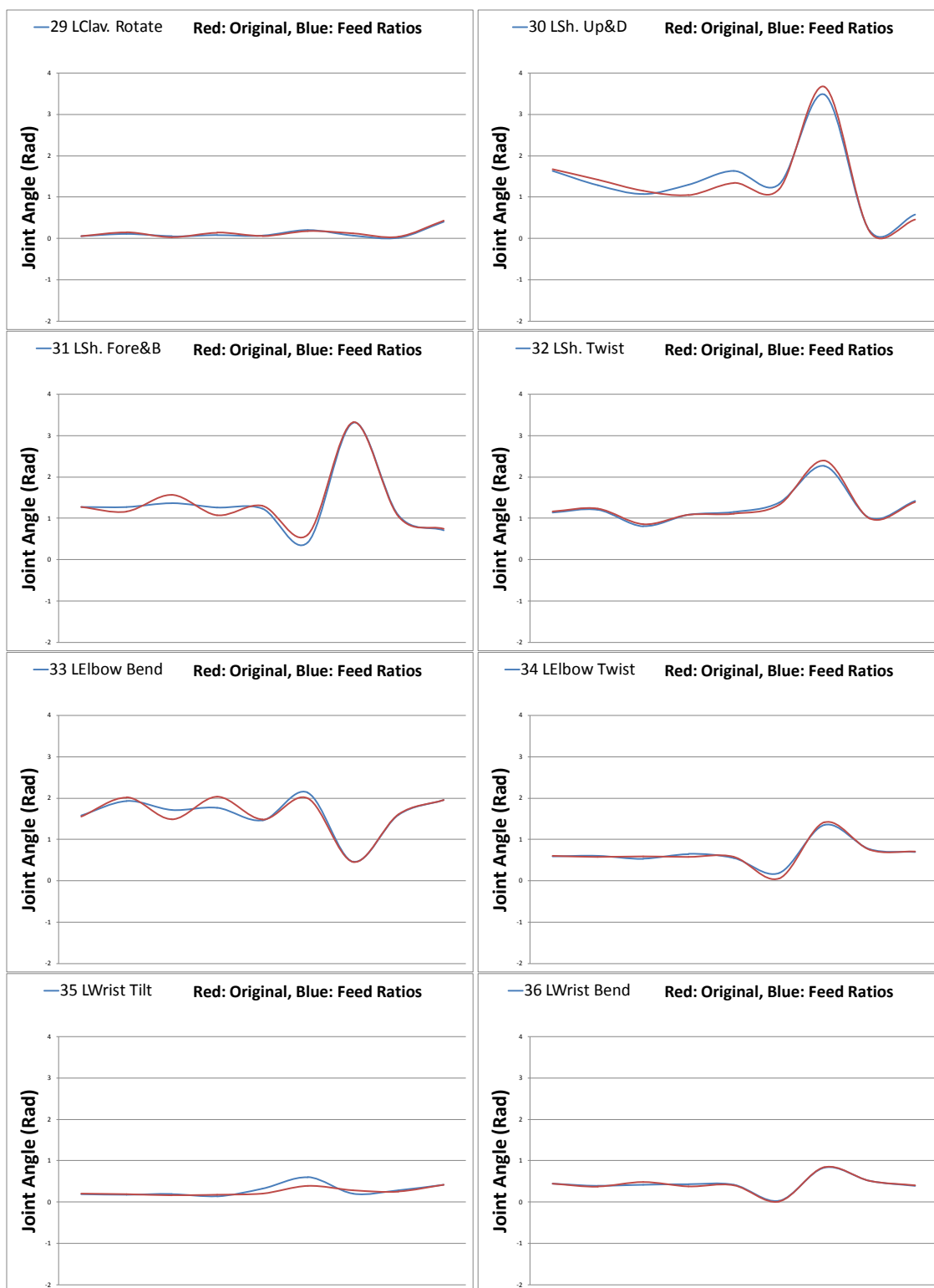
APPENDIX C

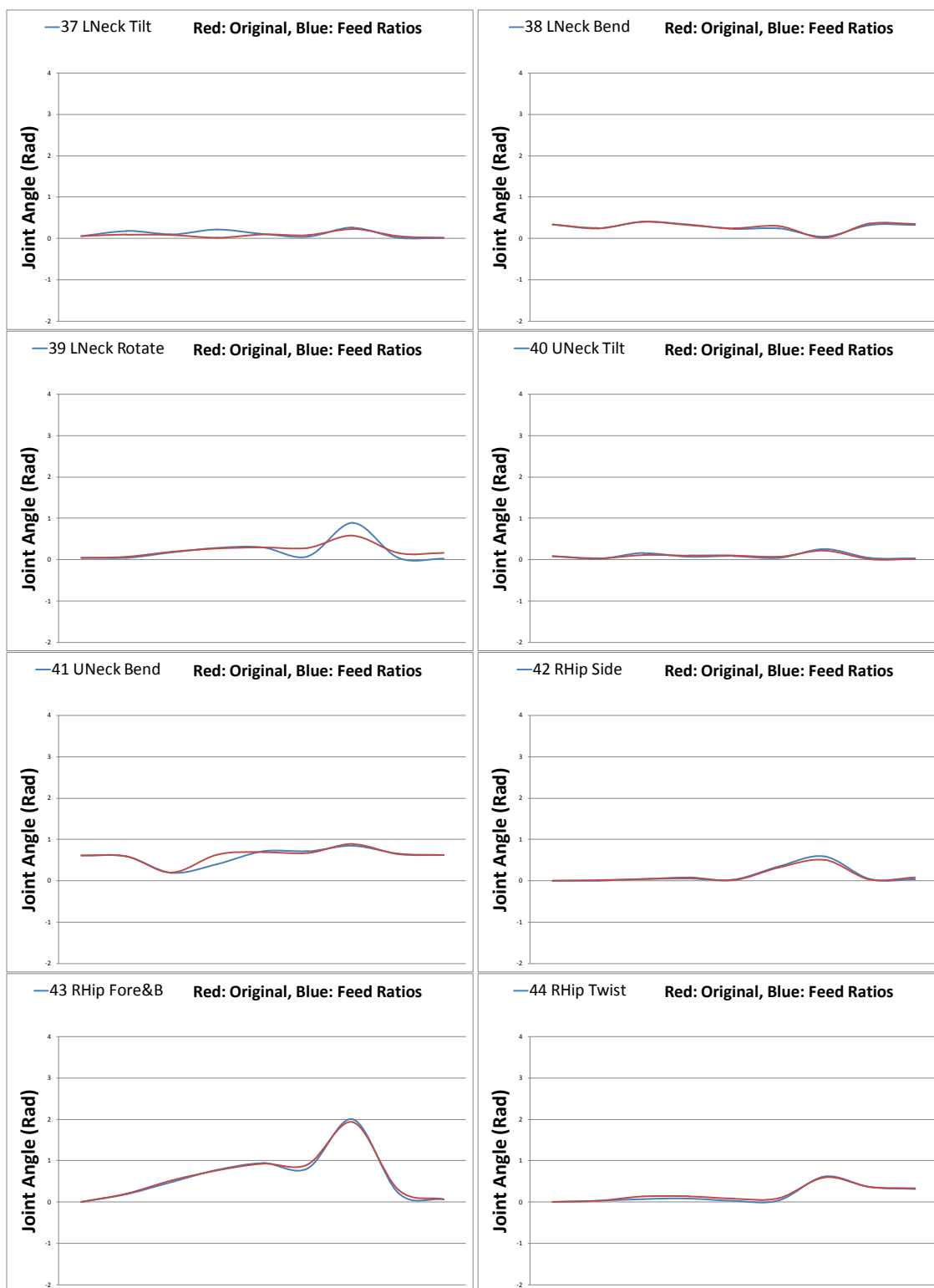
KINEMATIC EFFECTS OF FEEDING THE GRF RATIOS OF NCM METHOD BACK
 INTO THE ZMP METHOD IN THE GOING PRONE TASK (CHAPTER 9)

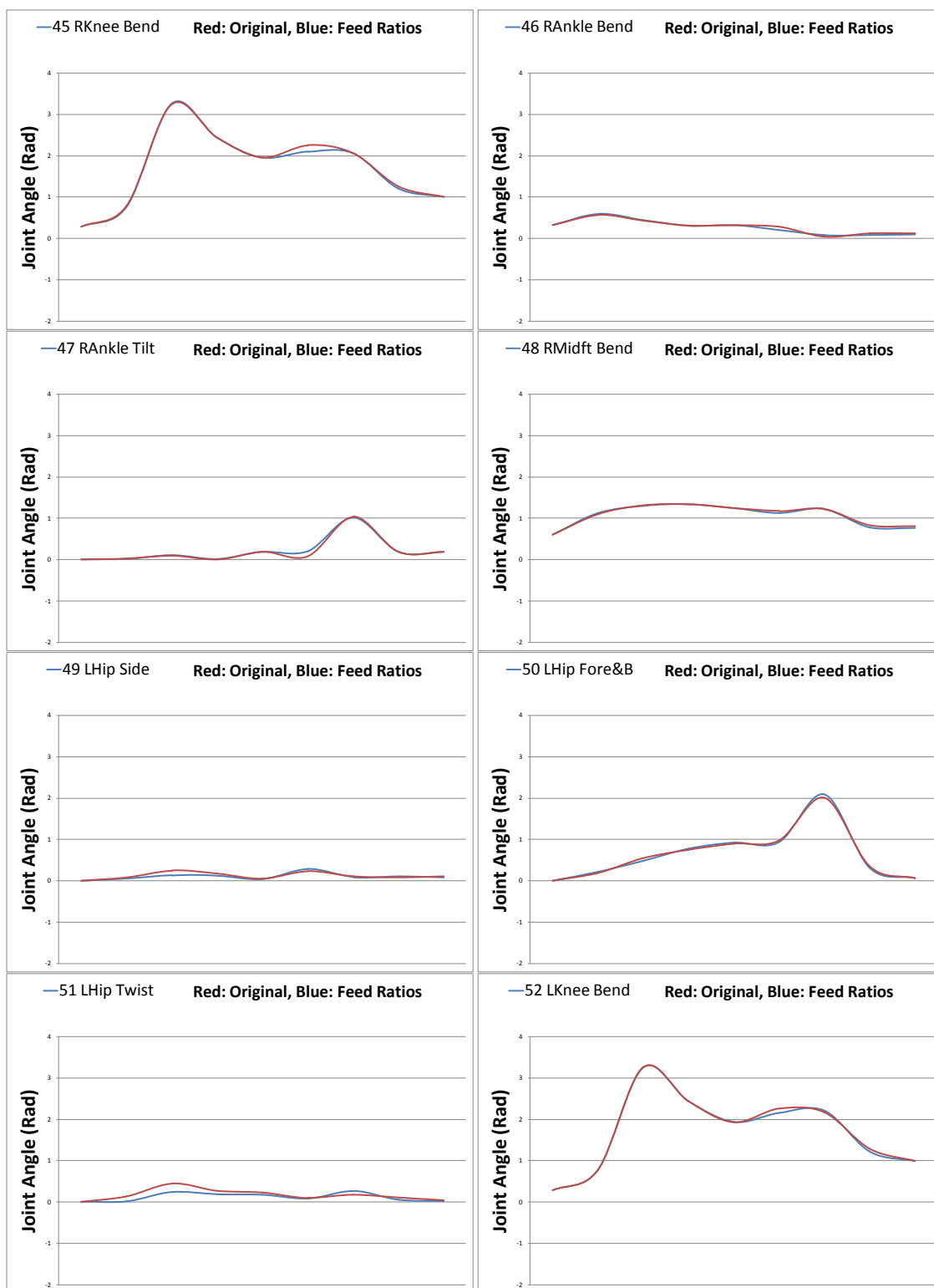


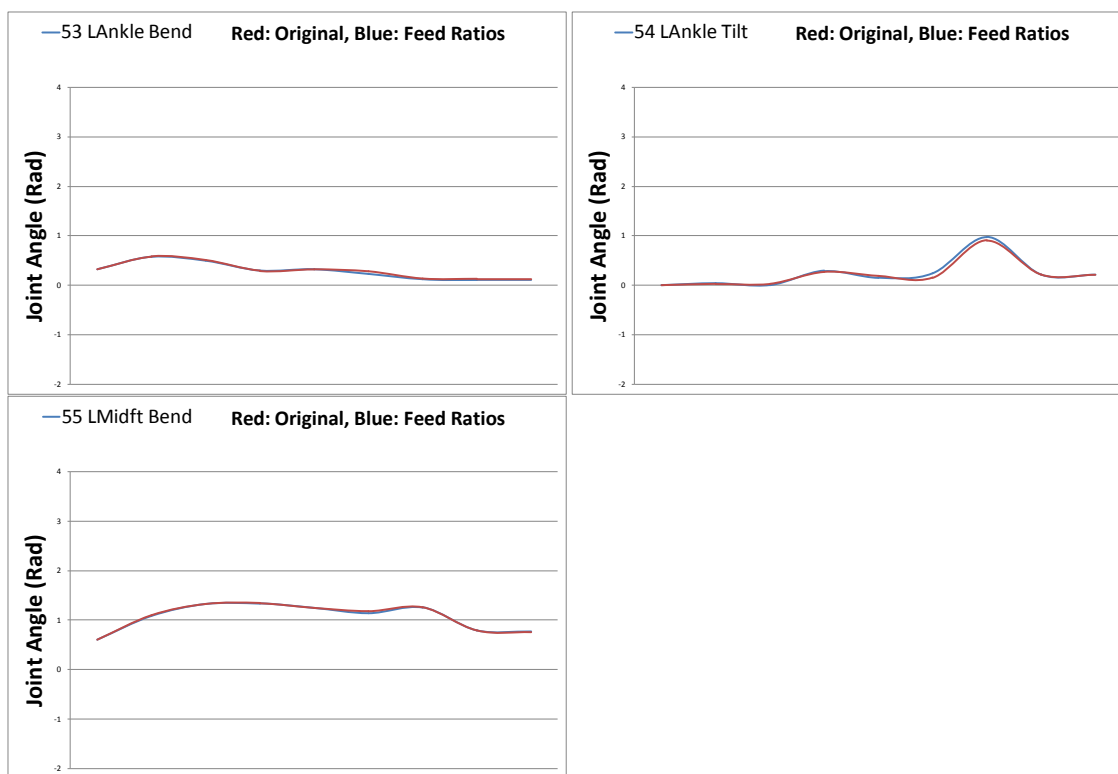












APPENDIX D

GRF RATIOS FOR WALKING IN NCM VERSUS EXPERIMENTAL DATA

Definition of the Set or Array Component		Time Grid #1	Time Grid #2	Time Grid #3	Time Grid #4	Time Grid #5	Time Grid #6	Time Grid #7	Time Grid #8	Time Grid #9
Right Foot Contact Force System at Force Plate Support	Fy	602.30	576.10	530.30	463.00	377.30	282.10	190.10	110.80	44.40
	Fz	101.50	110.40	115.60	114.50	105.20	88.20	65.70	41.40	18.40
	Mx	53.20	51.70	49.00	45.10	39.30	31.40	21.50	11.00	1.10
Left Foot Contact Force System at Force Plate Support	Fy	87.10	192.60	304.10	404.20	476.60	521.70	552.90	579.80	599.60
	Fz	37.30	-4.20	-43.70	-74.00	-91.90	-102.7	-110.5	-114.2	-110.5
	Mx	22.30	13.10	7.60	13.50	12.00	17.70	20.20	24.30	28.20
Position of ZMP Along z		0.29	0.36	0.42	0.49	0.54	0.59	0.65	0.71	0.76
ZMP to Right Foot Along z		0.16	0.23	0.29	0.36	0.41	0.46	0.52	0.58	0.63
ZMP to Left Foot Along z		0.55	0.48	0.42	0.35	0.30	0.24	0.19	0.13	0.08
Right Foot Mx at ZMP		96.06	131.18	156.54	170.23	160.01	137.59	103.34	65.06	25.20
Left Foot Mx at ZMP		-29.45	-88.46	-133.0	-146.2	-152.6	-133.0	-109.6	-78.54	-45.21
Ratio of dz for Left Foot		0.22	0.32	0.41	0.51	0.58	0.66	0.73	0.81	0.89
Ratio of Fy for Left Foot		0.13	0.25	0.36	0.47	0.56	0.65	0.74	0.84	0.93
Ratio of Fz for Left Foot		0.27	-0.04	-0.61	-1.83	-6.91	7.08	2.47	1.57	1.20
Mx/Fy for Left Foot at ZMP		0.16	0.23	0.30	0.37	0.42	0.49	0.54	0.59	0.57

Table D.1. Experimental Data (Winter, 2009)

- Note:

The presented values in walking tables (NCM Method, Experimental Data, ZMP Method) are only for double support phase of walking. For plotting ratios, additional values of 0 and 1 were also considered to exist for Fy and Fz ratios when the ratio of dz is equal to 0 and 1, for plotting. Because 0 and 1 ratios correspond to single support phase, where all the IGE force/moment is supported (canceled) by one foot.

Definition of the Set or Array	Component	Value at Time Grid #1	Value at Time Grid #2	Value at Time Grid #3	Value at Time Grid #4	Value at Time Grid #5	Value at Time Grid #6	Value at Time Grid #7
Right Foot Contact Force System at the Midpoint of Right Foot (From Table 9.14)	Fx	-48.148	30.083	-39.065	3.309	12.099	17.145	13.130
	Fy	834.730	167.981	122.917	80.247	65.779	76.128	43.668
	Fz	362.561	98.070	107.724	101.531	98.669	114.192	65.502
	Mx	0.403	-0.492	-0.472	-0.300	-5.592	-6.381	-3.526
	My	1.915	0.111	-20.467	-5.577	-3.810	2.015	7.826
	Mz	5.257	6.186	6.128	4.001	1.500	3.358	1.939
Left Foot Contact Force System at the Midpoint of Left Foot (From Table 9.14)	Fx	-9.023	-37.602	34.899	-7.283	-20.818	-36.645	-49.819
	Fy	110.834	148.229	310.851	468.869	595.522	693.734	831.089
	Fz	-99.226	-29.976	-84.453	-123.095	-165.240	-226.010	-222.754
	Mx	11.416	14.447	27.800	37.757	31.828	1.972	-0.811
	My	14.807	12.055	-19.458	-4.960	-0.512	-4.537	-4.123
	Mz	3.547	8.345	7.163	6.626	11.471	16.779	20.048
ZMP Location	x	0.070	0.046	0.065	0.075	0.082	0.089	0.096
	y	0.000	0.000	0.000	0.000	0.000	0.000	0.000
	z	0.051	0.335	0.498	0.591	0.653	0.697	0.731
Location of Midpoint of Right Foot	x	-0.075	-0.075	-0.075	-0.075	-0.075	-0.075	-0.074
	y	0.054	0.054	0.060	0.067	0.074	0.082	0.090
	z	-0.006	0.060	0.059	0.059	0.059	0.061	0.065
Location of Midpoint of Left Foot	x	0.078	0.078	0.078	0.078	0.078	0.077	0.077
	y	0.074	0.073	0.067	0.062	0.056	0.052	0.047
	z	0.696	0.762	0.762	0.761	0.759	0.757	0.755
Distance of Midpoint of Right Foot From ZMP	dx	-0.145	-0.121	-0.140	-0.150	-0.157	-0.164	-0.170
	dy	0.054	0.054	0.060	0.067	0.074	0.082	0.090
	dz	-0.057	-0.275	-0.439	-0.533	-0.594	-0.636	-0.666
Distance of Midpoint of Left Foot From ZMP	dx	0.008	0.032	0.013	0.003	-0.005	-0.012	-0.019
	dy	0.074	0.073	0.067	0.062	0.056	0.052	0.047
	dz	0.645	0.427	0.264	0.169	0.106	0.060	0.024
Mx for Right Foot at ZMP		47.886	45.729	53.455	42.454	33.470	42.051	25.571
Mx for Left Foot at ZMP		-60.092	-48.839	-54.248	-41.662	-31.501	-39.801	-20.934
Ratio of dz for Left Foot		0.081	0.392	0.624	0.759	0.848	0.914	0.965
Ratio of Fy for Left Foot		0.117	0.469	0.717	0.854	0.901	0.901	0.950
Ratio of Fz for Left Foot		-0.377	-0.440	-3.629	5.708	2.482	2.021	1.417
Mx/Fy for Left Foot at ZMP		0.057	0.272	0.435	0.529	0.509	0.552	0.586

Table D.2. Results of Repartitioning of GRF Using NCM Method (Continuation of Table 9.14)

REFERENCES

- [1] Abdel-Malek, K., Yeh, H. J., and Khairallah, N., 1999, "Workspace, Void, and Volume Determination of the General 5DOF Manipulator"; *Mechanics of Structures and Machines*, Vol. 27, No. 1, pp. 91-117
- [2] Alexander, T. and Conradi, J., 2011, "On the Applicability of Digital Human Models for Personal Equipment Design", *HCI International 2011*.
- [3] Anderson, D., 2002, "The Natural Point of Aim stance - Better Shooting"; *American Handgunner*, May 2002
- [4] Arakawa, T., Fukuda, T., 1997, "Natural motion generation of biped locomotion robot using hierarchical trajectory generation method consisting of GA, EP layers"; Paper presented at the *IEEE Int'l Conf. on Robotics and Automation*
- [5] Arampatzis, A., Bruggemann, G.-P., 1998, "A mathematical high bar – human body model for analyzing and interpreting mechanical energetic processes on the high bar"; *Journal of Biomechanics* 31, Elsevier, 1998, 1083-1092
- [6] Bachar, Y., 2004, "Developing Controllers for Biped Humanoid Locomotion"; MSc thesis, University of Edinburgh
- [7] Bae, H., 2001, "A Study on the Stair Walking of Lower Power Biped Robot"; *KJEE/IEEK/ICASE Joint Conference.*, pp. 105- 109
- [8] Balaz, T., Racek, F., Řehor, Z., Melsa, P., 2007, "Valuation of shooter position using high speed camera"; *In Proceedings 8th Symposium on Weapon Systems*, UO Brno, 2.- 3.5.2007, ISBN 978-80-7231-248-1
- [9] Balkcom, D.J., Trinkle, J.C., 2002, "Computing wrench cones for planar rigid body contact tasks"; *Int. J. Robotics Research*, vol.21, no.12, pp.1053- 1066
- [10] Bhatt, R., Xiang, Y., Kim, J., Mathai, A., Penmatsa, R., Chung, H. J., Kwon, H. J., Patrick, A., Rahmatalla, S., Marler, T., Beck, S., Yang, J., Arora, J. S., Abdel-Malek, K., Obusek, J. P., 2008, "Dynamic Optimization of Human Stair-Climbing Motion"; *SAE Digital Human Modeling Conference*, June 2008, Pittsburgh, PA
- [11] Brabcova, K., Macko, M., 2005, "Shooting gun motion: mathematical models"; In *Proceedings of the 2005 Conference on computational and mathematical methods on science and engineering CMMSE-2005*. Alicante, University of Alicante, Spain, June 2005. ISBN 84-609-4844-7, pp. 68-78.

- [12] Buss, S. R., 2003, “3-D Computer Graphics: A Mathematical Introduction with OpenGL”; *Cambridge University Press*, May 19, 2003.
- [13] Choset, H., Mirtich, B., and Burdick, J., 1997, “Sensor based planning for a planar rod robot: Incremental construction of the planar Rod-HGVG”; *IEEE International Conference on Robotics and Automation*, vol. 4
- [14] Colbaugh, R., Seraji, H., and Glass, K., 1989, “Obstacle avoidance of redundant robots using configuration control”; *Int. J. Robot. Res.* 6, 721–744
- [15] Dasgupta, A., Nakamura, Y., 1999, “Making feasible walking motion of humanoid robots from human motion capture data”; Paper presented at the *IEEE International Conference on Robotics and Automation*
- [16] Elizondo, D., 2006, “The Linear Separability Problem: Some Testing Methods”; *IEEE Transactions on Neural Networks*, vol. 17, no. 2, March 2006
- [17] Ericson, C., 2005, “Real-time collision detection”; *The Morgan Kaufmann Series in Interactive 3D Technology*, D. H. Eberly, Ed. Morgan Kaufmann Publishers
- [18] Escande, A., Miossec, S., and Kheddar, A., 2007, “Continuous gradient proximity distance for humanoids free-collision optimized-postures”; *IEEE-RAS 7th International Conference on Humanoid Robots*
- [19] Foley, J. D., 1996, "Computer Graphics: Principles and Practice"; *Addison-Wesley Professional*, page 490.
- [20] Garcia, A., Estremera, J., and Gonzalez de Santos, P., 2002, "A classification of stability margins for walking robots"; *In Proc. of the 2002 Int. Symp. on Climbing and Walking Robots*.
- [21] Gienger, M., Löffler, K., Pfeiffer, F., 2001, “Towards the design of a biped jogging robot”; *IEEE Int. Conf. Robot. Autom.* pp. 4140–4145
- [22] Glass, K., Colbaugh, R., Lim, D., and Seraji, H., 1995, “Real-time collision avoidance for redundant manipulators”; *IEEE Trans. Rob. Autom.* 11:(10)
- [23] Goswami, A., 1999, “Postural stability of biped robots and the Foot-Rotation Indicator (FRI) point”; *Int. J. of Robotics Research*, 18(6):523–533.
- [24] Goswami, A., Kallem, V., 2004, “Rate of change of angular momentum and balance maintenance of biped robots”; *Proc, IEEE Intl. Conf. on Robotics and Automation*, vol. 4, pp. 3785-3790

- [25] Granieri, J.P. and Crabtree, J. and Badler, N.I., 1995, "Production and playback of human figure motion for 3D virtual environments", *Proceedings of Virtual Reality Annual International Symposium*, 1995.
- [26] Harada, K., Kajita, S., Kaneko, K., Hirukawa, H., 2003, "ZMP Analysis for Arm/Leg Coordination"; *Proc. IEEE/RSJ Int. Conf. on Intelligent Robots and Systems*, October 2003
- [27] Hariri, M., 2005, "Boundaries of the Workspace for Serial Robots Considering Orientation Components", M. Sc. Thesis in Mechanical Engineering, Shiraz University, Shiraz, Iran
- [28] Haug, E. J., Luh, C. M., Adkins, F. A., and Wang, J. Y., 1996, "Numerical Algorithms for Mapping Boundaries of Manipulator Workspaces"; *ASME Journal of Mechanical Design*, 118, pp. 228-234
- [29] Hirai, K., Hirose, M., Haikawa, Y., Takenaka, T., 1998, "The Development of Honda Humanoid Robot"; *IEEE Int. Conf. on Robotics and Automation*, Leuven, Belgium, pp. 1321-1326
- [30] Hirose, M., Haikawa, Y., Takenaka, T., Hirai, K., 2001, "Development of humanoid robot ASIMO"; *IEEE/RSJ Int. Conf. Intell. Robots Syst. – Workshop 2*
- [31] Hirukawa, H., Hattori, S., Harada, K., Kajita, S., Kaneko, K., Kanehiro, F., Fujiwara, K., Morisawa, M., 2006, "A Universal Stability Criterion of the Foot Contact of Legged Robots- Adios ZMP"; *Proceedings of the IEEE International Conference on Robotics and Automation*, May 2006, Orlando, Florida
- [32] Huang, Q., Yokoi, K., Kajita, S., Kaneko, K., Arai, H., Koyachi, N., Tanie, K., 2001, "Planning walking patterns for a biped robot"; *IEEE Trans. Robot. Autom.* 17(3), 280–289
- [33] Hurmuzlu, Y., G' enot, F., and Brogliato, B., 2001, "Modeling, stability and control of biped robots: A general framework"; *INRIA research report 4290*
- [34] Jenkins, S. P. R., 2005, "Sports Science Handbook: A-H"; *Multi-Science publishing*, 400 pages
- [35] Jindrich , D. L., Full, R. J., 2002, "Dynamic stabilization of rapid hexapedal locomotion"; *The Journal of Experimental Biology* 205, 2803–2823 (2002)
- [36] Johnson, R., Fruehan, C., Schikore, M., Marler, T. and Abdel-Malek, K., 2010, "New developments with collision avoidance for posture prediction"; *3rd International Conference on Applied Human Factors and Ergonomics (AHFE)* 17-20 July, 2010 Miami, Florida

- [37] Kalakrishnan, M., Buchli, J., Pastor, P., Mistry, M., Schaal, S., 2011, “Learning, planning, and control for quadruped locomotion over challenging terrain”; *The International Journal of Robotics Research* 30(2) 236–258
- [38] Kaneko, K., Kajita, S., Kanehiro, F., Yokoi, K., Fujiwara, K., Hirukawa, H., Kawasaki, T., Hirata, M., Isozumi, T., 2002, “Design of advanced leg module for humanoid robotics project of METI”; *IEEE Int. Conf. Robot. Autom.* pp. 38–45
- [39] Kim, J.H., Xiang, Y., Bhatt, R., Yang, J., Chung, H.J., Patrick, A., Mathai, A.J., Arora, J.S., Abdel-Malek, K., 2008, “General Biped Motion and Balance of a Human Model”; *SAE Digital Human Modeling Conference*, June 2008, Pittsburgh, PA
- [40] Kim, J.Y., Park, I.W., Oh, J.H., 2009, “Realization of Dynamic Stair Climbing for Biped Humanoid Robot Using Force/Torque Sensors”; *J Intell Robot Syst* 56:389–423
- [41] Kunkel, P., Inversion Geometry (Title of Web Page as Listed on the Site) <http://whistleralley.com/inversion/inversion.htm> (accessed November 20, 2011).
- [42] Lee, J. Y. and Choset, H., 2001, “Sensor-based construction of a retract-like structure for a planar rod robot”; *IEEE Transactions on Robotics and Automation*, vol. 17, no. 4, pp. 435–449
- [43] Lim, S., 2007, “Dynamic Stair Walking of Biped Humanoid Robots”; *Journal of Mechanical Science and Technology*, Volume 21, Number 6, 970-975
- [44] Macko, M., Balaz, T., and Racek, F., 2009, “A determination of the significant points on sporting shooter body for comparison of the computing and measuring shooter movement”; *In Proceedings of the 11th WSEAS international conference on Mathematical methods and computational techniques in electrical engineering (MMACTEE'09)*
- [45] Moosavian, S. Ali. A., Dabiri, A., 2010, “Dynamics and Planning for Stable Motion of a Hexapod Robot”; *IEEE/ASME International Conference on Advanced Intelligent Mechatronics*, Montréal, Canada, July 6-9, 2010
- [46] Pang, J., Trinkle, J., 2000, “Stability characterizations of rigid body contact problems with Coulomb friction”; *Zeitschrift für Angewandte Mathematik und Mechanik*, vol.80, no.10, pp.643-663
- [47] Park, I.W., Kim, J.Y., Lee, J., Oh, J.H., 2006, “Online free walking trajectory generation for biped humanoid robot KHR-3(HUBO)”; *IEEE Int. Conf. Robot. Autom.* (Orlando) pp. 1231–1236

- [48] Pratt, D.R. and Barham, P.T. and Locke, J. and Zyda, M.J. and Eastman, B. and Moore, T. and Biggers, K. and Douglass, R. and Jacobsen, S. and Hollick, M., 1994, "Insertion of an articulated human into a networked virtual environment", *Proceedings of the Fifth Annual Conference on AI, Simulation, and Planning in High Autonomy Systems*, 1994.
- [49] Ren, L., Jones, R., Howard, D., 2005, "Dynamic analysis of load carriage biomechanics during level walking"; *Journal of Biomechanics* 38 (4), 853–863
- [50] Ren, L., Jones, R., Howard, D., 2007, "Predictive modelling of human walking over a complete gait cycle"; *Journal of Biomechanics* 40 (2007) 1567–1574
- [51] Rusaw, S., 2001, "Sensor-based motion planning in SE(2) and SE(3) via nonsmooth analysis"; *Oxford University Computing Laboratory*, Tech. Rep
- [52] Saida, T., Yokokoji, Y. and Yoshikawa, T., 2003, "FSW (feasible solution of wrench) for Multi-legged Robots"; *Proc. IEEE Int. Conf. on Robotics and Automation*, pp.3815-3820
- [53] Sardain, P., Bessonnet, G., 2004, "Forces acting on a biped robot. Center of pressure-zero moment point"; *IEEE Transactions on Systems, Man and Cybernetics*, Part A, vol. 34, no. 5, pp. 630-637
- [54] Shadpey, F., Tessier, C., Patel, R.V., and Robins, A., 1994, "A trajectory planning and obstacle avoidance system for kinematically redundant manipulators"; *CASI Conference on Astronautics*, Ottawa, ON, November 1994
- [55] Shadpey, F., Tessier, C., Patel, R.V., Langlois, B., and Robins, A., 1995, "A trajectory planning and object avoidance system for kinematically redundant manipulators: An experimental evaluation"; *AAS/AIAA American Astrodynamic Conference*, August 1995, Halifax, NS, Canada
- [56] Singh, G., 2002, "Collision-avoidance assured path-planning for Starlight interferometer"; *International Symposium Formation Flying Mission and Technologies* Toulouse, France
- [57] Singh, G., Hadaegh, F.Y., 2001, "Collision Avoidance Guidance for Formation Flying Applications"; *AIAA Guidance, Navigation, and Control Conference*, Montreal, Quebec, Canada
- [58] Sugahara, Y., Kawase, M., Mikuriya, Y., Hosobata, T., Sunazuka, H., Hashimoto, K., Lim, H., Takanishi, A., 2004, "Support torque reduction mechanism for biped locomotor with parallel mechanism"; *IEEE/RSJ Int. Conf. Intell. Robots Syst.* pp. 3213–3218

- [59] Takanishi, A., Ishida, M., Yamazaki, Y., Kato, I., 1985, “The realization of dynamic walking by the biped walking robot WL-10RD”; *Int. Conf. Adv. Robot.* (ICAR’85) pp. 459–466
- [60] Trinkle, J., Pang, J., Sudarsky, S., Lo, G., 1997, “On dynamic multi-rigid-body contact problems with Coulomb friction”; *Zeitschrift für Angewandte Mathematik und Mechanik*, vol.77, no.4, pp.267-279
- [61] U.S. Marine Corps., 2001, “Rifle marksmanship (Marine Corps Reference Publication, MCRP 3-01A)”; Albany, GA: Author; *Department of the Navy Headquarters*, Washington, DC, 29 March 2001.
- [62] U.S. Army, 1974, “Rifle Marksmanship (Field Manual 23-8)”; Fort Benning, GA: Author; *Department of the Army Headquarters*, Washington, DC.
- [63] U.S. Army, 2011, “Rifle Marksmanship M16-/M4-Series Weapons (FM 3-22.9)”; Fort Benning, GA: Author; *Department of the Army Headquarters*, Washington, DC, 10 February 2011.
- [64] van den Bergen, G., 2004, “Collision detection in interactive 3D environments”; ser. The Morgan Kaufmann Series in Interactive 3D Technology, D. H. Eberly, Ed. *Morgan Kaufmann Publishers*.
- [65] Vitek, R., 2008, “Influence of the small arm barrel bore length on the angle of jump dispersion”; *Mathematics And Computers In Science And Engineering Proceedings of the 7th WSEAS international conference on System science and simulation in engineering*, Venice, Italy, 2008, ISBN ~ ISSN:1790-2769 , 978-960-474-027-7, 114-118
- [66] Vukobratović, M., Borovac, B., Surla, D., Stokić, D., 1997, “Biped Locomotion : Dynamics, Stability, Control and Application”; *Springer-Verlag, Mathematik und Mechanik*, vol.77, no.4, pp.267-279
- [67] Vukobratović, M., Borovac, B., 2004, “Zero-moment point – thirty five years of its life”; *International Journal of Humanoid Robotics*, 1(1), 157-173
- [68] Vukobratović, M., Stepanenko, J., 1972, “On the stability of anthropomorphic systems”; *Math. Biosci.* 15, 1–37
- [69] Winter, D.A., 1990, “The Biomechanics and Motor Control of Human Movement”; second ed. *Wiley*, New York
- [70] Winter, D.A., 2009, “The Biomechanics and Motor Control of Human Movement”; fourth ed. *Wiley*, New York

- [71] Wysocki, F. and Fowlkes, D., 1994, "Team Target Engagement Simulator Advanced Technology Demonstration", *Proceedings of the Individual Combatant Modeling and Simulation Symposium*.
- [72] Xiang, Y., Arora, J.S., Rahmatalla, S., Bhatt, R., Marler, T., Abdel-Malek, K. 2009, "Human Lifting Simulation using Multi-objective Optimization Approach"; *Multibody Systems Dynamics*, DOI 10.1007/s11044-009-9186-y.
- [73] Xiang, Y., Chung, H. J., Mathai, A., Rahmatalla, S., Kim, J., Marler, T., Beck, S., Yang, J., Arora, J. S., Abdel-Malek, K., 2007, "Optimization-based Dynamic Human Walking Prediction"; *SAE Digital Human Modeling Conference*, June 2007, Seattle, WA
- [74] Xiang, Y., Arora, J.S., and Abdel-Malek, K. 2008 "Optimization-based motion prediction of mechanical systems: sensitivity analysis"; *Structural and Multidisciplinary Optimization*, 2008